Hybrid Flow through Microchannels for Blood Cell Separation

Anas Zakaria Alazzam

A Thesis
In the Department
of
Mechanical and Industrial Engineering

Presented in Partial Fulfillment of the Requirements
For the Degree of Doctor of Philosophy at
Concordia University
Montreal, Quebec, Canada

April 2010

Library and Archives
Canada

Published Heritage
Branch

395 Wellington Street
Ottawa ON K1A 0N4
Canada

Bibliothèque et
Archives Canada

Direction du
Patrimoine de l'édition

395, rue Wellington
Ottawa ON K1A 0N4
Canada

Your file Votre référence
ISBN: 978-0-494-67350-8
Our file Notre référence
ISBN: 978-0-494-67350-8

NOTICE:

The author has granted a non-exclusive license allowing Library and Archives Canada to reproduce, publish, archive, preserve, conserve, communicate to the public by telecommunication or on the Internet, loan, distribute and sell theses worldwide, for commercial or non-commercial purposes, in microform, paper, electronic and/or any other formats.

The author retains copyright ownership and moral rights in this thesis. Neither the thesis nor substantial extracts from it may be printed or otherwise reproduced without the author's permission.

AVIS:

L'auteur a accordé une licence non exclusive permettant à la Bibliothèque et Archives Canada de reproduire, publier, archiver, sauvegarder, conserver, transmettre au public par télécommunication ou par l'Internet, prêter, distribuer et vendre des thèses partout dans le monde, à des fins commerciales ou autres, sur support microforme, papier, électronique et/ou autres formats.

L'auteur conserve la propriété du droit d'auteur et des droits moraux qui protège cette thèse. Ni la thèse ni des extraits substantiels de celle-ci ne doivent être imprimés ou autrement reproduits sans son autorisation.

In compliance with the Canadian Privacy Act some supporting forms may have been removed from this thesis.

While these forms may be included in the document page count, their removal does not represent any loss of content from the thesis.

Conformément à la loi canadienne sur la protection de la vie privée, quelques formulaires secondaires ont été enlevés de cette thèse.

Bien que ces formulaires aient inclus dans la pagination, il n'y aura aucun contenu manquant.

Canada

Signatures page

Abstract

Hybrid Flow through Microchannels for Blood Cell Separation

Anas Zakaria Alazzam, Ph.D.
Concordia University, 2010

Cancer is considered to be the second cause of death in the Canada and other parts of the world. Separation of cancer cells from blood for early detection of cancer improves prognostics of survivals for most of types of cancer. In this thesis, design and fabrication of microdevices for living cell separation based on dielectrophoresis phenomena is presented. A novel microfluidic device for continuous separation of malignant cells from blood is fabricated and experimentally tested. The separation of breast cancer cells from blood using the microdevice is performed experimentally and reached close to 100% accuracy with a flow rate 0.1 mL/hr. Parallel configuration of the presented microdevice is recommended to increase the separation speed which will enable point-of-care tests.

The effects of dielectrophoretic manipulation and carbon nanotubes on living cells are also investigated in the present work. The changes in genes expression due to the exposure to AC field of 10 kHz and 100 kHz and carbon nanotubes treatment are studied using microarray analysis. Results show that 75% of the studied genes were altered by the exposure to 10 KHz field and only 25% of the genes were slightly altered by the 100 kHz exposure. As a result, higher AC frequency in range of 100 kHz is recommended for dielectrophoretic applications. Moreover, important genes are reported to be altered by carbon nanotubes.

Due to the fact that dielectrophoretic separation of living cells requires knowledge of the strength and distribution of electric field, analytical solutions for dielectrophoretic force over non-uniform interdigitated electrodes and for moving dielectrophoretic phenomenon are derived. Novel method to approximate the function that describes the potential profile between adjacent electrodes is reported. Excellent agreement is found by comparing the analytical solution with numerical and experimental results. A number of designs for the microfluidic chip were completed and experimental work carried out with living cells form cell lines being separated from blood. The experimental results suit the analytical findings and the method could be used in clinical studies.

Acknowledgment

In the first place I would like to express my gratitude and thanks to my supervisors Dr. Rama Bhat and Dr. Ion Stiharu who were abundantly helpful and offered priceless assistance, guidance and support throughout this study. I am grateful to Dr. Rama Bhat for his advice and constant encouragement and I owe my deepest gratitude to Dr. Ion Stiharu for his constructive comments, crucial contribution and willingness to meet and discuss throughout the course of the thesis.

Special thanks for Dr. Ala-Eddin Al Moustafa and Dr. Amber Yasmeen for the assistance, help and all the facilities they provided in Jewish General Hospital during my experiments.

It is a pleasure to thank those who made this thesis possible, my beloved parents, brothers, sisters, my wife Hadil and my daughter Daleen. Thank you all for your moral support and truly without your encouragement this work would have been impossible. Exceptional thanks to Daleen for being my motivation to finish and to Hadil for her understanding and support.

I am indebted to my friends and colleagues for their help and support. Thank you all and special thanks to Vahé, Alfin Leo , Dacian, Mohammad Aljarrah, Mohammad AlKhaleel and Mohammad Sababheh.

This thesis is dedicated to my wonderful parents, Zakaria and Aysheh. Thank you for all the love, guidance, support and encouragement that you have always given me.

I love you!

Table of Contents

List of Acronyms

AC	Alternating Current
AsPFF	Asymmetrical Pinched Flow Fractionation
AutoCAD	Autodesk Computer Aided Design or Drafting
BPE	Bovine Pituitary Extract
cDNA	Complementary Deoxyribonucleic Nucleic Acid
COMSOL	Finite Element Analysis Solver and Simulation Software
cm	Centimeter, 10^{-2} meter
CNT	Carbon NanoTubes
DC	Direct Current
DEP	Dielectrophoresis or Dielectrophoretic
DNA	Deoxyribonucleic Nucleic Acid
dpi	Dots per inch
EDL	Electrical Double Layer
EDTA	EthyleneDiamineTetraacetic Acid
EpCAM	Epithelial Cell Adhesion Molecule
F_{DEP}	Dielectrophoretic Force
F_{Drag}	Drag Force
FEA	Finite Element Analysis
FFF	Fluid Flow Fractionation
F_{sed}	Sedimentation Force
GAPDH	Glyceraldehyde 3-phosphate dehydrogenase
HNBE	Human Normal Bronchial Epithelial

hr	Hour
Hz	Hertz
KHz	Kilo-Hertz, 10^3 Hz
KSF	Keratinocyte Serum Free
m	Meter
MATLAB	MATrix LABoratory
MEMS	Micro-Electro-Mechanical System
MHz	Mega Hertz, 10^6 Hertz
mL	Milliliter, 10^{-3} Liter
mm	Millimeter, 10^{-3} Meter
mRNA	Messenger RiboNucleic Acid
mS/m	Milli-Siemens per meter
MUMPs	Multi-User MEMS-Processes
MWCNT	Multi-Walled Carbon NanoTubes
nDEP	Negative Dielectrophoresis or Dielectrophoretic
N-S	Navier-Stokes
PBS	Phosphate Buffered Saline
PCR	Polymerase Chain Reaction
pDEP	Positive Dielectrophoresis or Dielectrophoretic
PDMS	PolyDiMethylSiloxane
PFF	Pinched Flow Fractionation
RBC	Red Blood Cell
RNA	RiboNucleic Acid

RPMI	Roswell Park Memorial Institute medium
RT	Reverse Transcription
siRNA	Small interfering RiboNucleic Acid
SWCNT	Single-Walled Carbon NanoTubes
UV	UltraViolet light
WBC	White Blood Cell
2D	Two Dimensional
3D	Three Dimensional
µL	Micro-Liter, 10^{-6} Liter
µm	Micro-Meter, 10^{-6} meter

List of Symbols

Å	Angstrom
A, a	constant
A_o	Fourier constant
A_m	Fourier constant
B,b	Constant
C,c	Constant
C_{mem}	Membrane capacitance
d	The distance between adjacent electrodes
D	Constant
e	electric charge
E	Electric Field
f	Frequency
F	Force
$\boldsymbol{f_{CM}}$	Calusius-Mossotti factor
$\boldsymbol{F(x)}$	Function of the variable x
g	The gap between the electrodes
$\boldsymbol{G(y)}$	Function of the variable y
H,h	Constant represents the height of the channel
i	Unit vector in x-direction
j	Unit vector in y-direction
K	Constant of the separation
K_b	Boltzmann constant

L	Length of the unit segment
n	Constant
$\boldsymbol{n_0}$	Ion density
P	Pressure
pH	Measure of acidity
r	Radius
S	Siemens , SI unit for electrical conductance
t	Time
T	Temperature
Th	Thickness of the electrodes layer
$\boldsymbol{u}$	Velocity vector component
U	Fluid velocity
$\boldsymbol{v}$	Velocity vector component
V	Voltage
w	Width of the electrode
$\boldsymbol{w}$	Velocity vector component
x	x-direction of the Cartesian coordinate system
$\bar{\boldsymbol{x}}$	Normalized x-direction of the Cartesian coordinate system
y	y-direction of the Cartesian coordinate system
$\bar{\boldsymbol{y}}$	Normalized y-direction of the Cartesian coordinate system
z	z-direction of the Cartesian coordinate system
Z	Valence
$\boldsymbol{\alpha}$	Constant

°C	Degree Celsius
β	Constant
∞	Infinity
π	Pi
ε_0	Dielectric Vacuum constant
ε_m	Suspending medium dielectric constant
ε_p^*	Complex permittivity of particle
ε_m^*	Complex permittivity of medium
ρ_e	Charge density (charge per unit volume)
ρ_f	Fluid density
μ_f	Fluid viscosity
σ	Surface tension
σ_M	Medium conductivity
θ	Represents an angle
φ	Potential distribution function
δ	Constant
ζ	Vector component of $\boldsymbol{\nabla} E^2$
ω	Angular frequency
$\boldsymbol{\nabla}$	gradient operator
$\cong$	Approximately equals to
$\frac{\partial}{\partial x}$	First partial derivative with respect to x

$\frac{\partial}{\partial y}$	First partial derivative with respect to y
$\frac{\partial^2}{\partial x^2}$	Second partial derivative with respect to x
$\frac{\partial^2}{\partial y^2}$	Second partial derivative with respect to y

List of Biological Terms

MDA231	Breast cancer cells "line MDA231" have been isolated from human breast cancer patients as continuous culture in University of Texas, Medicine Department of Anderson Hospital and Tumor Institute [217]. The cell line is used as in vitro models for breast cancer cells. The MDA231 line consists of identical cells that have been multiplied from the same cells
EDTA	EthyleneDiamineTetraacetic Acid that is widely used in biological applications
Trypsin	Trypsin is a pancreatic serine protease that is used to detach adherent cells from the cell culture dish wall during the process of harvesting cells to re-suspend them in medium
RPMI 1640	Cells medium used to culture cells was developed at Roswell Park Memorial Institute medium (RPMI)
FBS	Fetal bovine serum the rich of proteins and used in cell culturing were cells can grow and divide

PBS	Phosphate buffered saline is a buffer solution that is used in biological applications
Ficoll-Paque	Ficoll is a registered trademark that is part of Ficoll-Paque which is commonly used in biology laboratories to separate blood to its components using centrifugation
RLT	A buffer that is commonly used for lyzis of cells and tissues before the RNA isolation

List of Figures

List of Tables

Chapter 1 : Literature Review

1.1. Introduction

With a better understanding of the molecular origins of diseases, medical diagnostics depends heavily on affordable and reliable technologies that enable microscale molecular analysis. Progress in genomics and proteomics has made it possible to identify genes and gene products that influence numerous disease states. Certain medical assays are performed on living cells in order to diagnose diseases. For example, large number of cells from the blood stream are counted on or tested for specific properties after they are separated from the other cells and plasma. The specimen of blood is mixed with either markers or substances that enable the un-clustering of the cells. Centrifugation process separates the cells into layers of different type based on their mass density. Despite the fact that the process is time consuming and laborious, the above method is used by far most frequently in medical bio-assays. Cells that are similar in size might require a longer process for separation. However, cells subjected to sustained compressive force due to centrifugation effect usually get structurally damaged.

Separation through cytometry is also used at a much reduced scale in medical bio-assays as in medical research. Cells from a specimen are targeted with optical markers which are photonically detected by color detectors. Detection of micro particles up to 20 different types of cells could be performed, when they capture different optical markers according to their properties.

Both methods are practical, effective but they are both harsh on the cells. Either cells get structurally damaged or chemically altered, or sometimes both. The drawback is that if the above methods are intensively used, the possibility to re-culture the collected cells is significantly reduced. Lately, the progress made in the biological assays performed on a very small number of cells necessitates the requirement of cells separation through non-damaging methods.

Recently there is a trend to develop cell assay technologies that are capable of separating, trapping and detecting bioparticles in a single device [2, 3].

The recent progress in the field of microfabrication makes it possible to integrate and perform complex functions on living cells on a single chip. Lab-on-a-chip microdevices bring the enormous advantage of tiny sample size, rapid and accurate results and the ability to be implemented on point-of-care devices. Such devices hold promising future applications for biological operations [4, 5].

1.2. Separation of microparticles, cells and blood components

Numerous researchers have reported their studies in the area of blood cells separation [6, 7]. Studies of the physical properties of cells were carried out to find new separation techniques specially those which can be performed on a small volume of blood samples. Microfluidic devices with the capability to separate, sort and detect specific bioparticles are considered strong candidates for the future bio-instruments for cell assay [8, 9].

Separation of blood cells and extraction of plasma are important steps in disease diagnostics, clinical chemistry tests, immunoassay tests and cell biology research. Plasma has been isolated from blood with different hematocrit "volume percentage of cells" using microfluidic devices. These devices are mainly based on the size exclusion or Zweifach–Fung principle [10].

The phenomenon that occurs at the bifurcation point when the cells have tendency to travel in the daughter channel which has a higher flow rate compared to the other daughter channel is called Zweifach–Fung effect or "bifurcation Law". On the other hand, size-exclusion process could be also based on a filtration. The blood passes through a porous interface so that the plasma and the cells with size smaller than the pore size pass through while the rest of cells are trapped.

Zweifach–Fung based microfluidic devices have been introduced for plasma extraction. Plasma was extracted from sheep blood samples with different hematocrit using a network of bifurcated microchannels [7, 11]. The plasma "skimming" process has been studied using different geometries of the separation device. These geometries include microchannel bends [12, 13] and corner-edge [14]. The effect of the feeding velocity, hematocrit, bend angle and the flow rate ratio between the cell collector and the plasma channel were studied.

Another method that enables separation of plasma from blood uses size exclusion. Microfilters have been designed, fabricated and used to trap blood cells and prevent them from passing to the plasma rich mixture [15-17]. Filters were fabricated from Si using reactive ion etching and photolithography.

Other methods of plasma separation have been reported. Platelet rich plasma has been separated using water-soluble polymers. This new technique was performed by studying the effect of various water-soluble polymers on the process of platelet rich plasma separation. Different polymers have been mixed each time with whole blood and the process of blood separation was observed. The effect of sixteen different polymers were studied and reported in [18].

Recent cell separation microdevices use hydrodynamic, antigen-antibodies, magnetic, and electrokinetic forces on cells. Different cells experience different forces which are used to direct them to special locations in the separation device. Microdevices use the hydrodynamics force to sort different size microbeads and cells have been reported. Aligning of different size particles using pinched channel or what is called Pinched Flow Fractionation (PFF) technique has been proposed [19, 20].

In PFF method the liquid rich in particles enters through one of the two inlets and one outlet of the Y-shape pinched microchannel, while the free-particle liquid enters from the second inlet. Particles are concentrated on one side of the channel by the free-particle liquid. After the liquid and particles pass though the pinched area they enter a broadened segment of the channel. The particles position across the channel according to their size; the large particles are forced to the center of the channel while the small particles are forced to the microchannel sidewalls (Figure 1.1).

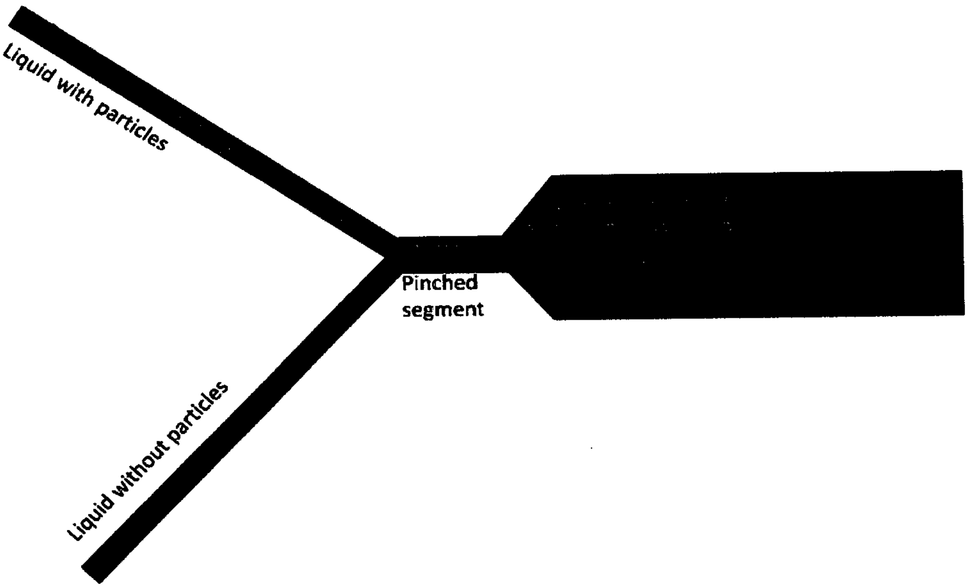

Figure 1.1: Principle of pinched flow fractionation.

PFF scheme has been improved by changing the broadened segment with an asymmetrical branched channel [20]. The new asymmetrical pinched flow fractionation (AsPFF) scheme consists of a twelve symmetrical microchannel that replaces the broad segment of PFF. AsPFF has been successfully used to separate micro-particles and red blood cells (RBC).

The interaction force between antigen and antibody make it possible to separate specific bioparticles from a mixture. Epithelial Cell Adhesion Molecule (EpCAM) is an antigen that is expressed on almost all cancer cells that originate from epithelial cells and is identified as foreign bodies (antigen) by the body's immune system.

Anti-EpCAm antibodies have a strong ability to bond with EpCAM protein. A microchannel with anti-EpCAM antibodies fixed at its wall has been used to diagnose and separate breast cancer cells [21]. As the blood sample flows in the microchannel the breast cancer cells are trapped by the anti-EpCAM antibodies on the microchannel wall while the rest of the blood cells continue moving with the stream.

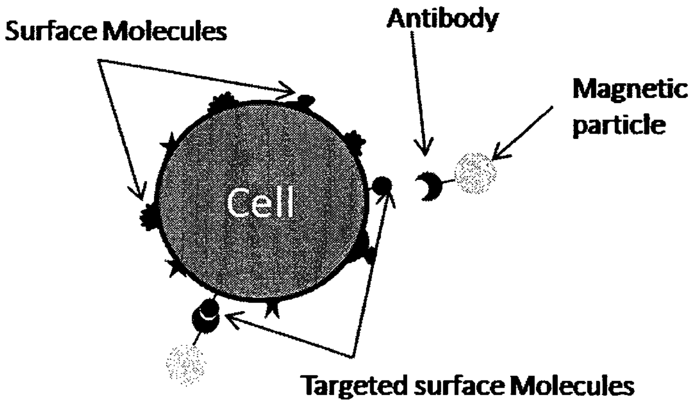

Figure 1.2: Schematic diagram of cell labeling process.

Microsystems that make use of magnetic forces have also been used in cell manipulation and analysis. Separation of cells with specific surface markers attached to magnetic microparticles has been reported using magnetic cell sorting system [22]. Cells are marked using matching antibodies attached to magnetic particles which bond to specific surface molecules on the epithelium of the cells (Figure 1.2). The effect of antibody binding capacity of a cell as well as the interaction of particle-magnetic field and the cell diameter were studied [23].

RBCs consist of hemoglobin, a composite protein containing iron atoms. White blood cells (WBCs) do not contain hemoglobin which makes them to react differently to magnetic field from the way RBCs do. Magnetophoretic microseparator using the constitutive properties of blood cells have been designed and fabricated [24, 25]. The separator has one inlet and three outlets and ferromagnetic wire along the center of the microchannel.

External magnetic field was applied normal to the microchannel creating a magnetic force that drives the red blood cells (paramagnetic) to flow away from the center of the main channel. The magnetic force draws the white blood cells (diamagnetic) toward the center of the channel where the ferromagnetic wire is located. The main microchannel was divided into three narrow channels connected to the outlets. Red blood cells (RBCs) flow through the two side narrow channels while the white blood cells flow through the central narrow channel.

Magnetophoretic manipulation of magnetic particles has been electrically controlled using dielectrophoresis phenomena [26]. Parallel electrodes subjected to AC electric signal enable dielectrophoresis while the DC signal enables magnetophoretic occurrence simultaneously to transport particles in-plane and out-of-plane electrically.

The electrical properties of cells depend on the cell size, shape and physiological status. Different types of cells might have different electrical properties. Variety of cells and particles were separated using dielectrophoresis phenomena [27-29].

Dielectrophoresis (DEP) as a separation method was first time described by Pohl as the motion of neutral, polarisable particles subjected to non-uniform electrical fields [30, 31]. Non uniform electrical field is created using an array of metallic electrodes with a certain arrangement [32, 33] or by implementing insulator areas between distant side electrodes [34, 35].

Dielectrophoresis has been extensively used for cell separation in microdevices because it uses the natural properties of cells [36-38]. DEP is considered one of the noninvasive and rapid separation techniques. In addition, cell separation using dielectrophoretic phenomenon holds application promises in disease diagnostics and in medical research through the implementation of practical microdevices [39, 40].

Presently there is an enormous interest in developing microfluidic lab-on-chip devices for biological and clinical purposes [41]. DEP microdevices are considered one of the most important methods in cells assay since they can conveniently be electrically manipulated [42]. DEP is used in focusing, separation and fractionation of cells and microorganisms at small scales which makes the method ideal for point-of-care devices.

The attraction and induced motion of cells or microorganisms towards the area of high electric field (field maxima) is called positive dielectrophoresis (pDEP). On the other hand, negative dielectrophoresis (nDEP) is the phenomenon in which the cells collect in low electric field division of the separation chamber (field minima).

Table 1.1: Dimensions and properties of selected cells

Cell Line	Radius (μm)	Membrane Capacitance (mF/m^2)	Crossover frequency* (KHz)	Response at 25KHz	References
Erythrocytes	2.8	11.6±2.14	69.3	nDEP	[6, 27, 43, 44]
Lymphocytes	3.5	13.6±1.94	47.3	nDEP	[6, 27, 43]
Granulocytes	4.7	16.7±2.41	28.7	nDEP	[6, 45]
Monocytes	4.6	15.24±1.04	32.1	nDEP	[6, 45]
MDA231	6.2	35.61±4.91	10.1	pDEP	[6, 27]
MDA435	7.7	29.97±7.20	9.7	pDEP	[6, 27, 44]
MDA468	7.2	28.41±1.42	11.0	pDEP	[6, 27]
HL-60	5.8	15.0±1.90	25.9	nDEP	[6, 27]
Ds19	5.9	17.4±2.00	21.9	pDEP	[27]

* calculated at conductivity of medium of 10 mS/m

Cell sizes and membrane capacitances have been discussed and measured using DEP based microdevices (Table 1.1). The frequency at which the change from positive to negative DEP occurs is called the crossover frequency (Figure 1.3). The crossover frequency of several human cells has been determined using microelectronic chip array [46].

The crossover frequencies of micro-beads and human blood erythrocytes have been determined experimentally using interdigitated and intercastellated electrodes. The behavior of the cells and beads has been studied visually over a wide range of frequencies and different conductivity media. The work concluded that positive DEP forces acting on large size cells in flow are weak and retaining devices are not very suitable for DEP separation [47].

The DEP separation of diluted blood in fluidic chamber was studied in order to determine the response of the cells under different frequencies. Moreover, DEP force has been measured using optical tweezers [48]. The tweezers worked as a force sensor for analyzing the particle movement and determine its crossover frequency.

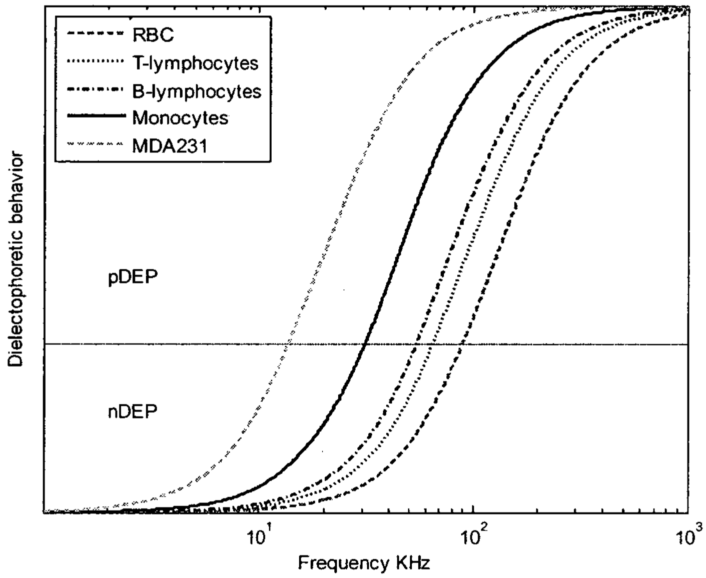

Figure 1.3: Dielectrophoretic behavior of selected cells under different frequencies (conductivity of medium =10 mS/m)

Different geometries of electrodes have been used in DEP microdevices. These include quadrupole electrodes, interdigitated castellated electrodes, parallel electrodes, 3D irregular shape electrodes and spiral electrodes [49].

The response of the human breast cancer cells (MDA231) has been inspected using spiral shape electrodes [50]. The MDA231 cells have been studied under different conductivity of medium and wide range of frequencies.

Different three dimensional (3D) electrode structures have been used to separate bioparticles. Viable and nonviable yeast cells mixture has been separated and focused in a small part of the channel for cytometry and other bio-applications [40, 51, 52]. However, full and accurate systematical study on the influence of the configuration of the electrodes on the performance of the device has not been reported in the open literature.

Sequential dielectrophoretic field-flow separation method was described using 3D irregular shape (hump-like) electrodes. The 3D electrodes work as walls for the separation channel and at the same time create DEP force [40, 51]. The reported design used DEP force to trap targeted cells in a dead zones inside the separation chamber. The rest of cells are focused by the DEP in the center of the channel and keep moving with the fluid stream.

Column-like electrodes with square cross section were used to trap cells in a dead zone between the pillars in order to hold them against the flow stream [52]. The four ports separation chamber has the capability to change the dead zone location by changing the inlet-outlet ports. The captured cells in the dead zones were rinsed out by changing the inlet and the outlet ports that creates flow stream in the dead zone.

Parallel electrodes on printed circuit board device have been used to isolate single type of cells from complex cell population mixture. The electric field generated by the device can generate a cylindrical shape dielectrophoresis cage that is capable of entrapping cells. Separation of white blood cells from erythrocytes mixture has been achieved by entrapping cells using dielectrophoresis (DEP) cages and dragging these cages between the electrodes [53].

Annular electrodes on polyimide substrate have been introduced to trap and control cells and particles using nDEP [54]. The separation channel was formed by drilling holes in on the polyimide substrate with metals.

Elliptic-shaped microelectrodes attached to the circumference of the channel have been employed to focus cells in the center of the channel [55] using nDEP. On the other hand, pDEP was used to focus particles and cells at the center of the channel using planar electrodes [56].

The influence of DEP on a large variety of cells and microorganism has been investigated. These include Rod-shaped viruses [57], human leukocyte [45], Duadi and NCI-H929 cell line [43], live bacteria in water [58], C174 myeloma [59] and yeast cells [60].

DEP microdevices have been described to have the potential for early detection of cancerous cells in blood. DEP based microdevices have been reported for differentiating between the oral squamous cell carcinoma and the normal keratinocyte cells [61].

Human oral squamous cell carcinoma cell line H357 and human HPV-16 transformed keratinocyte cell line UP have been used in the study. Number of cells accumulating over the electrodes because of the DEP force has been recorded after 1 min of applying the AC potential. The dielectric properties of the cells were calculated by fitting the experiment data to a single shell model. Significant difference in membrane capacitance has been found between the two cell lines used in the study.

Different methods of cell separation based on DEP have been studied and reported. DEP separation methods can be classified into four main categories; DEP retention (DEP affinity), DEP migration and the two continuous DEP separation methods; DEP deflection and DEP field flow fraction (FFF). DEP retention is performed by creating strong electric field that traps the targeted cells at the electrode edges and stop their movement due to the media flow. Other cells that experience nDEP will continue their movement along with the stream [27, 28, 62, 63].

Interdigitated castellated electrodes are the most used geometry in DEP applications [37, 64, 65]. Castellated electrodes are considered as distinctive electrodes in DEP retention as they offer a long trapping electric field.

Castellated electrodes can be directly opposite or staggered with an offset (Figure 1.4). In case of directly opposite electrodes (parallel), the cells that experience pDEP will collect in the area of high electric field between the electrode faces. Alternatively, cells that experience nDEP will be focused in the internal corners of the electrodes where the electric field is minimal. For offset electrodes the cells under pDEP will be gathering on the line connecting the electrodes face-tips and cells with nDEP will be accumulating between the electrodes corners.

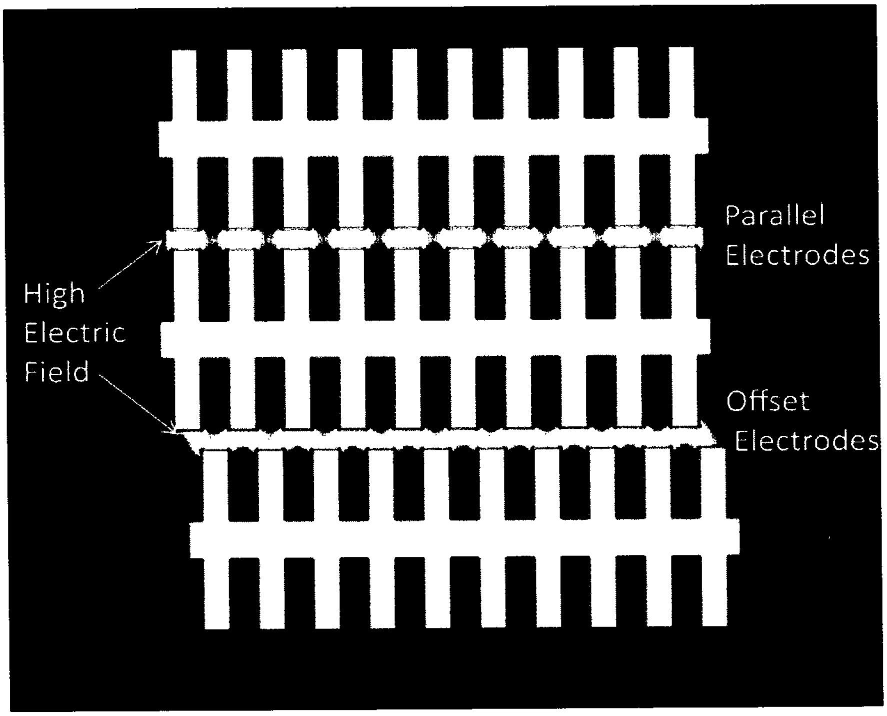

Figure 1.4: The geometry of castellated electrodes (white area)

Other geometries for the electrodes have been used and reported. Optically addressable projection array has the advantage of being non-contact type cell-electrodes and have been used for DEP manipulation of cells [66].

Uniform electric fields have been generated using parallel electrodes. Non-uniform fields have been optically induced by altering the conductivity of selected spots of photoconductive layers inserted between electrodes. The electric fields change significantly when the photoconductive layers are subjected to light. The reported optical method has used the laser as light source to influence the electric field between the electrodes.

DEP migration process is performed by forcing cells using DEP force to migrate to different parts of the separation chamber to be collected in a next step.

Quadrupole microelectrodes (Figure 1.5) are considered the ideal geometry for DEP migration method [42]. Cells that experience pDEP will move toward the edge of the electrodes and cells that experience nDEP will move toward the center.

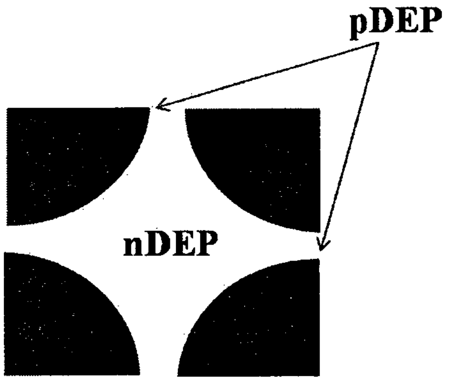

Figure 1.5: Schematic diagram of quadrupole electrodes

Quadrupole electrodes have been reported for DEP manipulation of cells and particles. Quadrupole electrodes were used to study the mobility coefficient of the polystyrenecarboxylate particles [67] and to create electrically switched single-cell traps [68].

Continuous DEP deflecting separation of cells is performed by redirecting the movement of targeted cells toward specific outlet that is different from the outlet of other cells. DEP deflection separation has been reported using different layer of electrodes [69-71]. Electrodes inclined toward the center of the channel have been employed to separate platelets from diluted whole blood [72]. The separation process was improved by including two purification steps in the separation chamber.

Red and white blood cells have been separated from diluted blood. Cells were separated using planar interdigitated electrode array making a certain angle with the direction of the flow [73]. The planar electrodes have been chosen to have an angle of 11° with the direction of the fluid flow. Optimizing the sizes of the electrodes, the gap between the electrodes and the angle that the electrodes make with the flow have been reported to affect the separation process. Modified interdigitated electrodes lined up perpendicular to the flow direction were used to align different micro-beads in different lanes [74]. The triangular shape electrodes create gradient electric field between electrodes that used to separate different size beads in different tracks.

DEP force is increased by implementing two layers of electrodes on top and bottom sides of the separation channel. Open ended barrier like electrodes on top and bottom sides of the separation chamber have been introduced to redirect targeted particles to move along the electrodes [75]. Other particles with different velocities penetrate the barriers and flow straight towards the channel outlet.

Separation chamber with saw-tooth pattern walls work at the same time as electrodes has been employed to separate cells using DC electrophoretic and dielectrophoretic field gradient [76]. Moreover, path lines for particles movements were used to study the transportation and separation of particles in none converging saw tooth channel. The particles blocking and trapping phenomena at specific were found to be affected by single dimensionless parameter [77]. This parameter was found to be function of the particle dielectrophoretic and electrokinetic mobility, the applied voltage and the spacing between the electrodes.

Cells have the tendency to settle to the bottom in a vertical channel because of the difference between their density and that of the suspension medium. Arrays of electrodes fabricated at the bottom of the microchannel are used to create dielectrophoresis force opposite to the sedimentation force. Different cells levitate to different equilibrium height above the electrodes due to the difference in forces acting on the cells. This phenomenon is called dielectrophoretic field-flow fraction (DEP FFF) [78-81].

For a standard pressure driven flow, the flow will have a parabolic shape (Figure 1.6). Different cells will have different elevations in the separation chamber and different velocities. This phenomenon has been used to separate different kinds of cells including cancer cells [44, 82], human leukocytes cells [83] and stem cells [84].

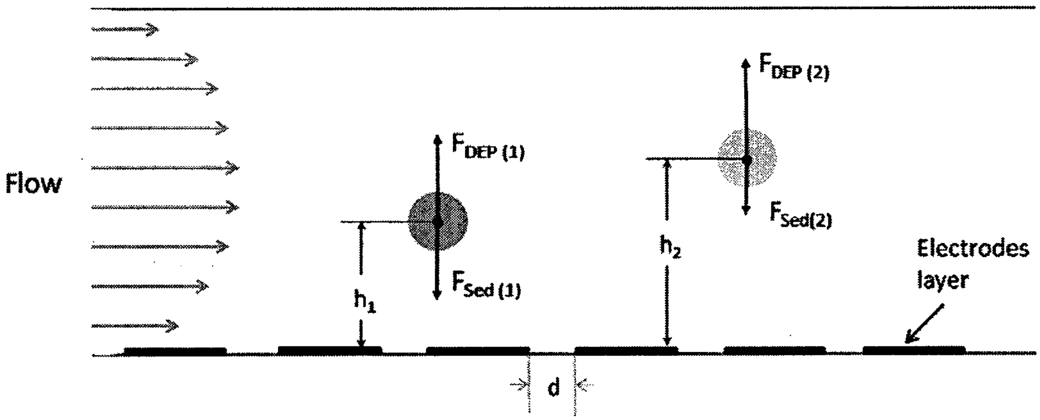

Figure 1.6: Dielectrophoretic field-flow-fraction principle

Enrichment of stem cells from mix of erythrocytes and digest-generated cell debris has been introduced using interdigitated electrode array on polyimide substrate [84]. One inlet and two outlet separation chamber has been used to enrich the stem cells in the mixture. The outlets were located in the upper and lower parts of the separation chamber. Stem cells experience nDEP flow close to the upper part of the separation chamber far from the electrode layer and exit from the outlet located in the upper part. Other cells and debris experience pDEP and exit from the outlet located in the lower part of the separation chamber. Stem cells enrichment has reached up to 14-folds.

The trajectory of cell above interdigitated electrodes for FFF based device was found to be wavy if the ratio between the levitation height (h) and the average electrode and spacing distance (d) is less than 0.6 and to be uniformly constant height if the ratio is greater than 0.6 [85]. This phenomenon causes imprecise sorting of the cells and particles. Solution for this problem was reported by designing the electrodes parallel to the direction of the flow stream.

The applications of DEP force go beyond the separation of particles and cells. DEP has been used in separation of specific band of DNA using parallel straight Au electrodes [86]. Au electrodes on silicon substrate have been created using microcontact printing with distance and electrode width varying between 1-80 μm. DNA bands have been reported to accumulate on the electrode edges where the electric field is maximal. Moreover, transporting of cells in a microchannel has been reported using DEP based device [87]. Sequentially activation of single electrode from an array of electrodes has been used to transport cells without using fluid flow. Microdevices using DEP force and capable of sorting cells by modifying their trajectory has been proposed [88]. Miniaturized array of electrodes on the bottom of the microchannel were used to concentrate the cells on a small section of the stream.

Similar microfluidic devices for moving particles from one side of the microfluidic chip to the opposite side have been proposed [89, 90]. Particles were pushed from one side of the channel to the opposite side by DEP force. Applications of these devices include switching particles from one medium to another or concentrating particles in one side of the channel of the device.

Sorting of yeast cells in a simple microchannel and planar electrodes has been performed using negative dielectrophoresis [91]. The behavior of the cells under different frequencies and medium conductivity was reported. Guiding efficiency was reported to be decreasing with increasing the flow rate of the cells.

Capacitor-like 3D filter chips with two planar electrodes made from stainless steel mesh have been fabricated and tested using yeast cells [40]. The filtration process has been improved through employing dielectrophoretic force to the standard filtration process.

Labeling targeted cells with certain particles to increase their dielectrophoretic response compared to other cells can improve and the principle could enhance the efficiency of cell sorting process [92]. Bacteria cells labeled with specific particles differ in polarization from non-label cells and have been sorted using quadrupole electrodes.

Combination of DEP with other forces increase the performance of DEP based devices. Electro-osmotic flow has been reported to induce circulation of particles above the electrodes and increase number of cells captured by DEP [93].

Single-cell or single-particle traps using ring-dot or quadrupole electrodes had been built and reported [68, 94, 95]. Single-cell trap electrodes using pDEP can be used for capturing, imaging, analysis and sorting of single-cell. The functions and the performances of the traps were tested successfully using beads and cells suspended in low conductivity sucrose medium.

Multi-target or multi-task DEP based microfluidic chips that can be used for cell assays and tests contribute to advancement of efficient lab-on-chip devices [96]. DEP based microdevices have been reported for continuous bacterial cell concentrating and gene detection [97], blood cell trapping and lysing [98] and for filtering, sorting, trapping and detection of bioparticles on a single microfluidic chip [99].

Integrated circuits as part of microfluidic chips have been used to trap and move particles and living cells along predetermined paths. The programmable integrated circuit consists of array of pixels that are individually controlled. The chip is capable of trapping and moving droplets, mixing two droplets and splitting one droplet into two [100].

1.3. Blood cells in medium and microdevices

Blood flow mechanics has been experimentally and numerically studied using 2D and 3D computer simulation [101, 102]. Based on particles method for blood flow between two parallel plates, particles as "nodes" were used to represent blood content and the domain as a single or as a set of particles. This model has been used to study the deformation of RBC as they flow through a narrow area. The aggregation of RBC and platelets was also studied [103, 104].

The deformation of cells is defined as the ability of cells to deform in order to pass small capillaries of the microcirculation [105]. While the phenomenon in which cells in vitro have the tendency to stack themselves with cells of their own type is called cell aggregation [106].

Electrical properties like the surface electric charge of the RBCs have been found to be influenced by its aggregation, deformation and disaggregation [107, 108].

Quantitative estimation for the electrical and mechanical properties and cells aggregation were measured using electro-optical techniques. Electro-optical method consists of observing the time for orientation when electrical field is applied and disorientation time of RBC after switching off the field.

Aggregability of RBC has been found to be influenced by the cell geometry and the electric charges arrangement on their surface. Glycocalyx which is the outer component of a cell membrane was found to be one of the main influencing factors for the electric charge distribution over the cell surface.

RBCs aggregation size has been studied as a function of the inter-erythrocytic force. A considerable degree of the RBC aggregation and the inter-erythrocytic force was found [109].

Human RBCs under normal conditions have a regular biconcave disk shape. Theoretical shapes of the RBC contour were fitted including the effect of curvature elasticity based on microscope images for the RBC [110].

The biconcave shape of resting RBC can be lost by the effect of the environmental conditions such as pH, chemical agent such as adenosine-derived nucleotide, $C_{10}H_{16}N_5O_{13}P_3$ (ATP) content and the amount of charge on the cell membrane [111-114]. At low pH values the RBC membrane was found to contract producing stomatocytosis and to expand at high pH values producing echinocytosis. RBC shapes have been found to stay normal in pH ranging from 6.3-7.9 and become abnormal beyond those values.

RBC deformation and orientation inside a microchannel has been studied by measuring the RBC deformation index across the channel height by using high speed camera. RBCs were found to congregate at the center of the flow [115].

The effect of WBCs, platelets and RBCs content ratio in blood on the blood flow through a microchannel has been experimentally studied. Transit time for a specific volume of blood to pass through a standard microchannel has been investigated [116]. Different hematocrit blood samples will have different transit time and for the same conditions of flow and the same hematocrit no connection between the human age and the transit time was found.

1.4. Blood components and properties

Blood circulates in the blood vessels of the body to provide energy and oxygen to the cells and the living being. Blood consists of plasma with suspended cells. In theory, Blood contains red blood cells (erythrocytes), white blood cells (leukocytes) and platelets. The total volume of the blood in the adult person is about 5 liters which is almost 8% of the total weight.

Plasma is the fluid portion of the blood in which the blood cells and platelets are normally suspended making up about 55% of total blood volume. The pH value of the blood ranges from 7.35 to 7.45 and it has a relative viscosity of 4.5 to 5.5 depending on blood hematocrit.

Centrifugal action separates the blood cells and the plasma into two parts; cells part at the bottom and plasma at the top. The upper portion of the cells part is called "puffy coat". Puffy coat contains most of the white blood cells and platelets.

A cubic millimeter of blood contains 5.1-5.8 million RBCs in males and 4.3-5.2 million cells in females, and 5,000-10,000 WBCs, and not more than 450,000 platelets cell [117, 118].

Red blood cells (RBCs) which are responsible for carrying the oxygen through the body have a biconcave disc shape with a 7.5 μm diameter and 2.5 μm thickness (Figure 1.7) and they have a circulating life of about 120 days. RBC contains hemoglobin which is a complex iron containing protein.

White blood cells (WBCs) are larger than the RBCs and have nuclei. WBCs are mainly divided into five main types: neutrophils, eosinophils, basophils and the two granular type monocytes and lymphocytes. WBCs are responsible for protecting the body from the strange substances and cells.

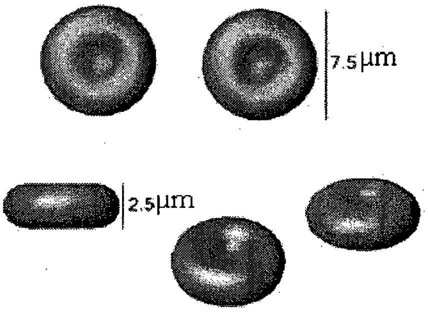

Figure 1.7: Human Red Blood Cells representative diagram

Neutrophils WBCs are the most WBCs found in the blood, and they form 54% - 62% of the whole WBC mass. Monocytes cells are the largest WBCs. Platelets are disk like cytoplasmic body and they are the smallest blood cells and play an important role in blood clotting.

1.5. Microchannels fabrication

Microdevices such as microchannels are usually fabricated by a deposition and etching process. Etch type microchannels are fabricated usually in glass or silicon and for embossing-based microchannel the base material is polymers or rubber.

Glass microchannels with semi-circular cross section are fabricated using etching process [119]. Silicon based microchannels with circular cross-section can be fabricated by bonding two semi-circular microchannels produced by isotropic etching [120] (Figure 1.12). Rectangular cross-section microchannels are made-up using Multi-User MEMS Processes (MUMPs) [121]. MUMPs based microchannels are usually made from glass or polysilicon.

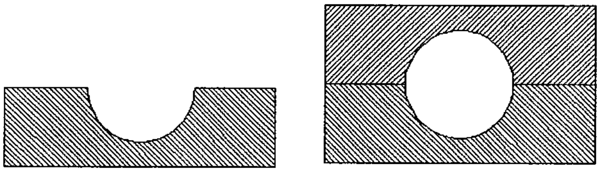

Figure 1.8: Schematic diagram for the fabrication of circular cross-section microchannel

Polymer based microchannels with different shapes are fabricated by embossing. Embossing silicon die has been created using etching process [122]. Miniaturized die has been used to create rectangular cross section microchannels using hot embossing process. Ni-Co based mold has been used in the process [123]. UV laser ablation micromachining has been used to fabricate microchannels based differently. Different substrate materials were used to study the effect of the substrate material on the morphology of the microchannels [124].

1.6. Fluid transportation in microchannel

Some small forces in the macro scale become extremely significant and relatively large at micro-scale level. Electrostatic force and surface tension are two examples of such forces. Surface tension is the property of a fluid surface that causes it to act like an elastic sheet. Interfacial forces rule such phenomena such as the wetting or non-wetting of solids by liquids.

The angle at which a fluid interface meets the solid surface is called the contact angle. Change in contact angle due to an applied potential difference between the solid and the electrolyte (fluid) is called electro-wetting. The relation between the surface tension and the applied voltage is parabolic and is expressed by Lippmann's equation which takes the form [125-127]:

$$\sigma_{sl} = \sigma_{sl0} - \frac{C}{2}(V - V_0)^2 \tag{1}$$

where V is the applied voltage, σ_{sl} is the surface tension between the solid surface and the liquid surface, σ_{sl0} is the maximum surface tension (at $V=V_0$) and C is the capacitance per unit area for electrical double layer. The subscript **s** is for solid and **l** for liquid. One can obtain the basic electrowetting equation by using Young's Equation [128] and Lippman's equation. Young's equation can be obtained by balancing the forces at the contact angle (Figure 1.9).

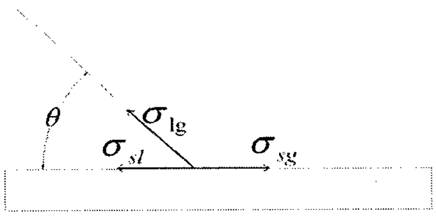

Figure 1.9: Schematic diagram for the force balance at the contact angle

$$\cos(\theta) = \frac{\sigma_{sg} - \sigma_{sl}}{\sigma_{\lg}} \tag{2}$$

where θ is the contact angle and the subscript **s** is for solid, **l** for liquid and **g** for gas (vapor) . Substituting (1) in (2) gives:

$$\cos(\theta(V)) = \frac{\sigma_{sg} - \sigma_{sl0}}{\sigma_{\lg}} + \frac{C}{2\sigma_{\lg}}(V - V_0)^2 \tag{3}$$

Several electrowetting based microdevices have been reported. Micromotor [125], switch-gate [129] and micropump [130] have been fabricated and tested. Continuous fluid motion in microchannel is achievable by creating surface tension difference in fluid-solid interface (Figure 1.10 a). Array of electrodes are used to reach continuous motion of the fluid (Figure 1.10b).

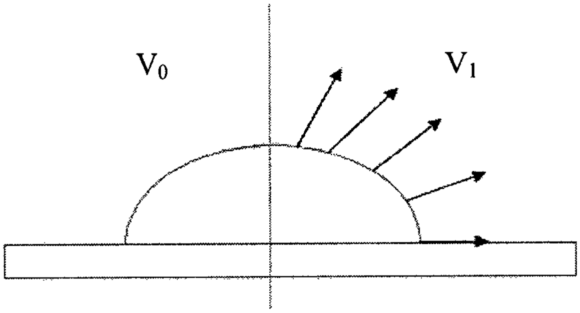

(a) Droplet with an activated right electrode and deactivated left electrode.

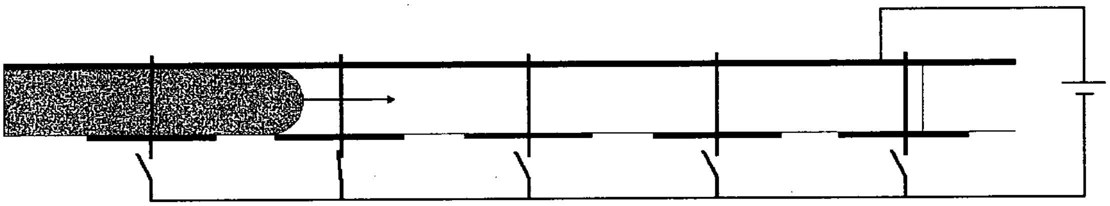

(b) Schematic diagram for the continuous electrowetting motion.

Figure 1.10: Continuous electrowetting fluid motion in microchannel using array of electrodes

For a polar fluid in contact with a solid surface, the surface of the solid yields an electric charge drawing the fluid ions toward the surface while fluid particles with the same charge emigrate away from the surface (Figure 1.11 a). This phenomenon creates a very thin layer called Stern layer [128] (Figure 1.11 b). Stern layer affects the distribution of charges in the liquid which creates a thicker layer called “diffuse layer”. Stern layer and the diffuse layer together are called Electrical Double Layer EDL (Figure 1.11 c).

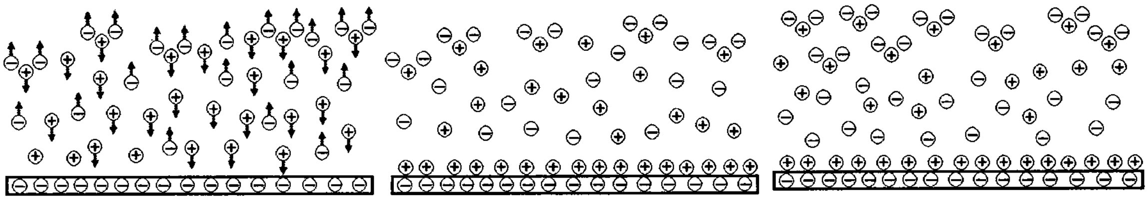

(a) Movement of the charges and ions **(b) Stern layer** **(c) Stern and diffuse layers (EDL)**

Figure 1.11: Sketch of the Electrical Double Layer (EDL)

Since the diffuse layer has a net charge, applying an electrical field will influence its movement. Motion of the fluid under the influence of an applied electric field is called Electro-osmosis phenomenon (Figure 1.12).

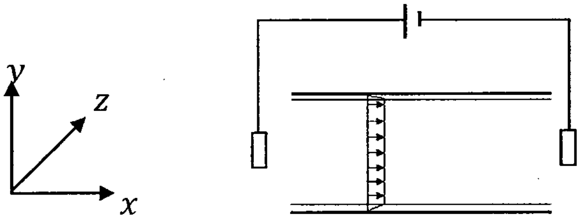

Figure 1.12: Schematic representation of the flow in a channel subjected to difference potential.

The body force per unit volume (F) due to the induced electrical field is given by equation (4). From the electrostatic theory the relation between the EDL potential (ψ) and the net charge per unit volume (ρ_e) is given by equation (5) [131-133].

$$F = E_x \rho_e(y, z) \tag{4}$$

$$\frac{\partial^2\psi}{\partial y^2}+\frac{\partial^2\psi}{\partial z^2}=-\frac{1}{\varepsilon}\rho_e \tag{5}$$

where E_x is the applied external electrical field and ψ is the electrical potential.

Assuming the equilibrium Boltzmann distribution as follows:

$$n_i = n_0\exp\left(-\frac{z_i e\psi}{k_b T}\right) \tag{6}$$

where Z is the valence, e is the electronic charge , k_b is the Boltzmann constant, n_0 is ion density in molar unit (bulk concentration) and T is the absolute temperature .

The net electric charge is given by

$$\rho_e = e\left(Z_+n_+ + Z_-n_-\right) \tag{7}$$

From equations (6) and (7)

$$\rho_e = -2Zen_0\sinh\left(\frac{Ze\psi}{k_b T}\right) \tag{8}$$

Substituting equation (8) in equation (5) yields to Poisson-Boltzmann equation which is written as:

$$\frac{\partial^2\psi}{\partial y^2}+\frac{\partial^2\psi}{\partial z^2}=-\frac{2Zen_0}{\varepsilon}\sinh\left(\frac{Ze\psi}{k_b T}\right) \tag{9}$$

For a two-dimensional laminar incompressible flow through a uniform cross sectional area channel, the equation of motion is given by.

$$\rho_f\frac{\partial U}{\partial t}+\rho_f(U.\nabla)U = -\nabla P + F + \mu_f\nabla^2 U \tag{10}$$

where U is the fluid velocity, ρ_f is the density, μ_f is the viscosity, P is the pressure, t is the time and F is a force term.

For a fully developed steady flow the terms ($\frac{\partial U}{\partial t}$, $(U.\nabla)U$) cancel out and the pressure term becomes function of x only $\left(\frac{dP}{dy}=\frac{dP}{dz}=0, \frac{dP}{dx}=Const\right)$ which yields:

$$\frac{\partial^2 u}{\partial y^2}+\frac{\partial^2 u}{\partial z^2}=\frac{1}{\mu_f}\frac{dP}{dx}-\frac{1}{\mu_f}F_x \tag{11}$$

where x, y, z are the Cartesian coordinates and u is the velocity in x-direction. For zero pressure gradient and pure body force (F) due to the induced electrical field (E_x), the equation of the flow due to the electro-osmosis effect is given by [134, 135].

$$\frac{\partial^2 u}{\partial y^2}+\frac{\partial^2 u}{\partial z^2}=-\frac{1}{\mu_f}E_x\rho_e(y,z) \tag{12}$$

Flow of fluid due to pressure difference in microchannels is very similar to that in the macro scale [136]. Fluid flow equations in microchannels are given by Navier-Stokes equations and the continuity equation (equations 10 and 13). Navier-Stokes equations ignore the molecular nature of fluid and it is applicable to numerous flow situations.

$$\frac{\partial \rho}{\partial t}+\frac{\partial(\rho u)}{\partial x}+\frac{\partial(\rho v)}{\partial y}+\frac{\partial(\rho w)}{\partial z}=0 \tag{13}$$

As in the case of the electro-osmotic driven flow, pressure driven flow with zero body force is given by

$$\frac{\partial^2 u}{\partial y^2}+\frac{\partial^2 u}{\partial z^2}=\frac{1}{\mu_f}\frac{dp}{dx} \tag{14}$$

The effect of mixing between the electroosmotic and the pressure forces (kinematics) to drive fluid in microchannels with rectangular cross-section has been studied [38, 39, 41]. The equation of motion for electroosmotic-pressure driven flow in microchannels for steady, two dimensional and fully developed flow is given by

$$\frac{\partial^2 u}{\partial y^2}+\frac{\partial^2 u}{\partial z^2}=\frac{1}{\mu_f}\frac{dP}{dx}-\frac{1}{\mu_f}E_x\rho_e(y,z) \tag{15}$$

This equation is solved analytically or using finite difference method or finite element method.

Among the discussed methods to transport fluid and cells in microchannels, pressure driven flow seems to be the most suitable and the most reliable for DEP applications. Other methods might affect the distribution of the electric field and therefore affect the separation process.

This investigation used pressure to control the flow of medium and cells in the microdevice due to the simplicity compared to other methods. The cross section of the separation microdevice affects the flow profile of the cells in the device and therefore affects the separation process. The effect of the microchannel cross section on the separation process for fully developed pressure driven flow is discussed in the next chapter.

1.7. Layout of the thesis

In the last year, 171,000 new cases of cancer were expected to happen and 75,300 patients to die in Canada from the disease. Lung and breast cancer were found to be the main causes of cancer death in women. Statistical reports indicated a rise in cancer cases among young women. Early detection of cancer improves prognostics of survival for most types of cancer. Current cancer detection techniques in general are costly, time consuming and patients might need days to get the results. A point-of-care testing device for early detection of cancer cells will improve the chance to cure the disease in tumor stage before spreading in the body. Moreover, such a device might be used in the follow up of patients that have been treated with chemotherapy. This thesis included in the first chapter a comprehensive literature review about separation of cells and particles in microdevices. The second and third sections of the chapter discussed the size, shape and physical properties of blood cells. However, in the last section of the chapter the transportation of living cells and particles in microdevices and the fabrication of microchannels were discussed.

The movement of cells and medium in the proposed microfluidic were controlled using a syringe pump. Fluid transportation in different cross sections microchannels are presented in chapter two. The effect of the cross section of the microchannel on the separation process was studied using trapezoidal, semi circular and rectangular microchannels.

Separation of the cells in the microdevice was performed using dielectrophoresis phenomena. In order to indicate the parameters that affect the separation process and to create a model for the cell movement in the separation device, a mathematical formulation for the dielectrophoretic force is needed. Analytical solutions for two applications use dielectrophoresis phenomena are reported in chapter three. Electric potential, electric field and the gradient of the strength of electric field distribution functions were found analytically using Fourier series. A mathematical formulation for non uniform interdigitated electrodes and moving dielectrophoresis are reported in the chapter.

The targeted separation speed by this work should ensure a separation speed that enables point of care tests. Therefore, several parameters in the separation device should be optimized in order to increase the speed and the accuracy of the separation. The effect of the shape and size of the electrode layer on the separation process are discussed in chapter four. The fabrication process of the separation device is also presented in the chapter.

This work has also been directed towards searching ways through which the separation speed could be improved. One possibility was seen as treating cells with carbon nanotubes. The effect of carbon nanotubes on the dielectric properties of the cell and their biocompatibility and toxicity were investigated and results are presented in chapter five. Microarray analysis were used to study the modifications happened in the genes of human bronchial epithelial cells due to treating them with carbon nanotubes.

The experimental setup of the separation process, the preparation of medium and cells before the separation and the separation accuracy and speed are discussed in chapter six. However, knowing the fact that there is a need to re-culture the cells after the separation process for further studies, therefore the separation device should ensure minimal changes in the cells. The viability of the cells after the separation and the effect of the electric field exposure on living cells were studied using microarray analysis. The results are reported in chapter six of the thesis.

The last chapter of the thesis includes the summary and the contributions of this work. Possible future works are also presented in the chapter.

Chapter 2 : Pressure Driven Flow in Microchannels

2.1. Introduction:

Interest in the MicroElectroMechanical Systems (MEMS) and Microfluidic devices has expanded rapidly during the past decades. Microfluidic devices are being used in a wide variety of applications mainly within the area of biomedical devices. This increase in demand for microfluidics requires full understanding of fluid flow in microchannels which form the basis for microfluidic devices. The present trend in microfluidics application is on integration of the fluid flow system with the microstructures, micro-electronics including the controls and micro-optics. However, a major issue in such devices is the flow through the microchannels, aspect that is dealt in this work.

Understanding the behavior of flow in microfluidic devices is a significant key to push forward the microdevices design process and plays an important role in improving the process of microfluidic control. Microchannels of different cross sections have been integrated and assembled in various configurations within microfluidic devices.

Two main procedures are used to model the fluid flow through channels, the first approach deals with the fluid as a collection of molecules where the fluid properties are defined at every point in the space and time. Molecular based model leads to complicated nonlinear ordinary differential equations such as Euler's and Burnett's equations.

The second model deals with the fluid as a continuum. Continuum model gives approximate results because the fluid is assumed to be continuous and its properties such as pressure, density and velocity are defined as averages over elements that are sufficiently small. Navier-Stokes (N-S) model is the most used continuum model and it is applicable to several flow situations. Liquids however, do not have a well advanced molecular-based theory in microchannels as that for dilute gases [137]. So they are good candidates for N-S model.

Reynolds number is one of the significant criteria used to determine the transition of flow from the laminar to turbulent region. The fluid flows in layers that do not mix with each other in the laminar region while in turbulent region the fluid velocity and pressure fluctuate randomly. Fluids flowing in microchannels have a typical value of Reynolds number that fall in the laminar region and for many applications Reynolds number will be close to 1.

Transition from laminar to turbulent region in microchannels with a hydraulic diameter of few micrometers occurs at different values of Reynolds numbers as in normal size channels. It is difficult to indicate the transition point from laminar to turbulent in smooth microchannels [138]. Behavior of liquids in round glass microtubes with diameter ranging from 50 to 247 μm have been experimentally studied [139]. The results show that the behavior of fluid flow in microtubes with diameters above 50 μm is very similar to the ones in macroscale channels and the transition from laminar to turbulent occurs at Reynold's numbers in the range of 1,800-2,300. Similar results have been observed using glass and silicon microchannels with a hydraulic diameter ranging from 45.5 to 83.1 μm [140, 141]. The work concludes that for Reynolds numbers below 1000 the flow was laminar and it became fully turbulent at Reynolds number greater than 3000.

Experimental results of flow behavior of water, methanol and isopropanol in microtubes show similarity with the macroscale fluid flow characteristics [142-144].

Stainless steel and fused silica microtubes with round and rectangular cross section with a hydraulic diameter down to 15 μm have been used in the studies. As the hydraulic diameter of the channel goes down close to the molecular size, less similarity was observed with the predictions of the conventional theory [143].

The early transition from laminar to turbulent in microchannels with a hydraulic diameter of few micrometers was found to be strongly dependent on the surface roughness and channel surface geometry in microchannels [145, 146]. Regardless of the fact that transition from laminar to turbulent occurs at high Reynolds numbers, most of the microfluidic applications perform at Reynolds numbers that do not exceed 100. For example, mixing of two fluids is still a challenge in microchannels due to the difficulty to reach high Reynolds numbers that cross the laminar region. Current researches are looking for other techniques to mix fluids at low Reynolds numbers such as using different cross section of channels and implementing partial obstructions in the channel.

Many fluid flow investigations have studied microchannels of different cross-section. Circular, rectangular and trapezoidal microchannels have been used extensively due to the simplicity of manufacturing and cost [136]. Circular cross-section microchannels have been used to study the heat transfer characteristics [142], the transition to turbulent in microchannel [139] and to investigate flow properties such as pressure drop and flow rates [143, 144]. Rectangular cross-section microchannels have been used for wide range of applications such as studying the electroosmotic and electrokinetic effects in microchannels [147-149] , flow characteristics [150-152] and bio-applications [153].

The effect of the electrical double layer (EDL) on pressure driven flow have been numerically studied based on Poisson–Boltzmann equation. EDL near the wall of the rectangular microchannel have reported to limit the motion of ions near the channel wall and therefore of the liquid molecules. The velocity distribution and the flow rate in the rectangular cross section microchannel have been found to be significantly affected by the EDL in case of low concentration solution and high zeta potential fluid. Increasing in the friction coefficient and decreasing in flow rate have been reported as the zeta potential of solid/liquid interfaces increases [147, 148].

Experimental results for laminar liquid and vapor flow in rectangular microchannels with smooth surfaces have shown good agreement with the conventional values that come from the analytical solution of Navier-Stokes equation. Surface roughness has been described as the reason for the earlier transition from laminar to turbulent region in rectangular cross section microchannels [150].

Due to the simplicity of manufacturing, many studies have used silicon based trapezoidal cross section microchannels. Trapezoidal microchannels have been reported to study the flow rate, pressure drop and to measure the friction factor across the microchannel [154-156].

In order to understand of the effect of the microchannel cross-section on the DEP separation, one has to study the fluid flow behavior in microchannels of different cross-sections. Moreover, the profile of flow would indicate the speed of certain micro-particles that are suspended in the transported fluid.

The flow pattern of liquid in semi circular, rectangular and the widely used trapezoidal microchannels have been studied numerically using finite element method

[147, 157, 158]. The flow profiles in microchannels under same conditions but different cross-sections have been discussed. Since the width (diameter) of the semi-circular shape is twice the height (radius), the width of the microchannels under discussion has been taken to be double the height for the three different cross-sectional microchannels.

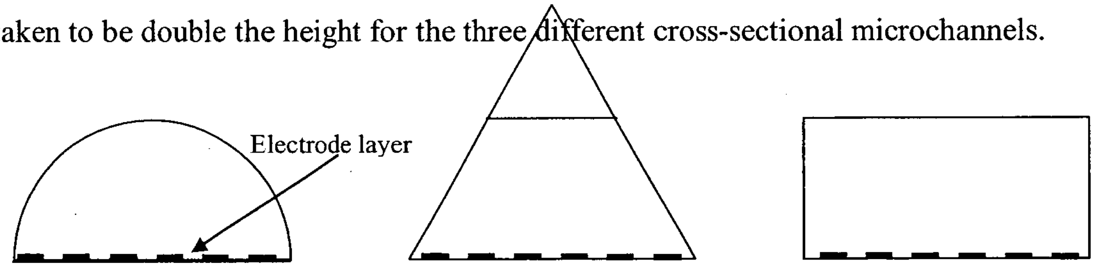

Figure 2.1: Circular, trapezoidal and rectangular cross-sectional microchannels

2.2. Governing equations

It is quite common to use N-S equations and the mass continuity to describe the fluid flow in micro and macro channels. The fluid flow in a closed microchannel is given by the N-S equations as follows:

$$\rho \frac{\partial \boldsymbol{u}}{\partial t} + \rho(\boldsymbol{u}.\nabla)\boldsymbol{u} = -\nabla \boldsymbol{P} + F + \mu\nabla^2\boldsymbol{u} \tag{16}$$

Since the fluid flow is in one direction, there are no components for the velocity normal to the x direction$\left(\mathbf{u} = \mathrm{u}(\mathrm{y},\mathrm{z})\right)$. The body force F is assumed to be negligible and the flow is assumed to be fully developed and steady. Therefore, equation (16) can be simplified to the form:

$$\frac{\partial^2 u}{\partial y^2} + \frac{\partial^2 u}{\partial z^2} = \frac{1}{\mu}\frac{dp}{dx} \tag{17}$$

The boundary conditions are the no-slip conditions on the wall of the channel.

$$u(y,z) = 0 \; on \; the \; boundaries \tag{18}$$

Equation (17) has further been studied using finite element method and commercial software based on conventional fluid theory. Pressure difference across the microchannel, $\left(\frac{dp}{dx}\right)$, equals to 1 and viscosity μ of water was assumed in the study.

2.3. Results and discussion

DEP separation methods such as DEP retention and DEP migration require cells to pass close to the electrode layer to be affected by the generated DEP force. Moreover, in order to hold the cells against the fluid stream, the drag force that acts on the cell must be less than or equal to the DEP force. Full knowledge of the effect of the microchannel cross section is needed in order to improve DEP separation of cells. The effect of the cross section of the microchannel on the velocity profile is studied in this section. The profiles of the normalized velocity with respect to the maximum velocity for semi-circular, rectangular and trapezoidal cross-sectional microchannels are shown in Figure 2.2.

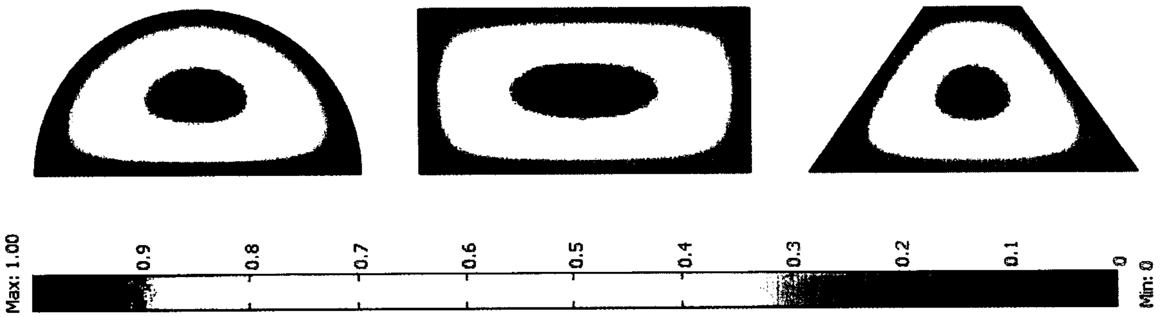

Figure 2.2: Velocity profile for circular, rectangular and trapezoidal cross-sectional microchannels

In order to study the effect of the cross-section on the separation process, the velocity profile in the microchannel has been divided into three different regions. The first region is called dead zone where the normalized velocity is less than 0.1. The second region is the neutral zone where the normalized velocity between 0.1 and 0.5. The last region is the rapid zone where the normalized velocity is greater than 0.5. The three different zones in the microchannels under discussion are shown in Figure 2.3.

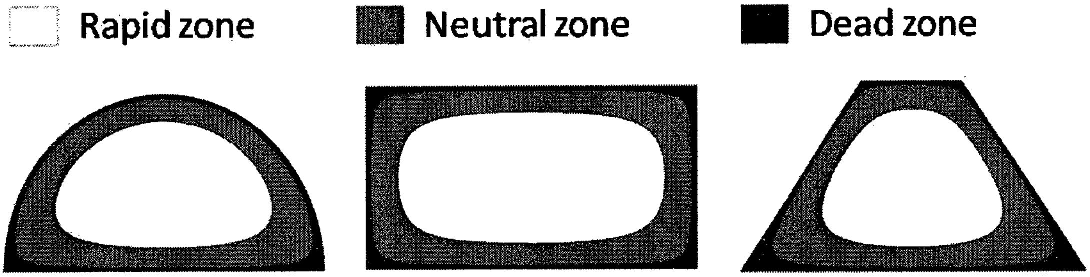

Figure 2.3: Zones under discussion for circular, rectangular and trapezoidal cross-sectional microchannels

Cells in the dead zone travel with very low velocity compared to the cells at the center of the channel to reach almost zero at the boundaries of the microchannel. The area of the dead zone for semi-circular microchannel is about 11% of the total area while it is around 12% for the rectangular microchannel and it reaches more than 14% in the trapezoidal microchannel.

The slowly moving cells in the dead zone make it difficult for the targeted cells to reach the electrode layer and to be separated. Moreover, the part of the dead zone at the corners of the microchannel occupies fraction of the electrodes that slows down the separation process.

Most of the cells are expected to move in the rapid zone because of the high speed. Therefore, rapid zone is considered the most important one among the three zones. The area-ratio of the rapid zone to the total area of the microchannel and the electrodes coverage by the zone are two significant factors in selecting a certain cross-sectional microchannel for separation purposes.

The rapid zone for semi-circular microchannel occupies about 48% of the total area and it covers around 67% of the electrode layer. Meanwhile, the rapid zone for rectangular microchannel is around 50% of the total area and it covers more than 79% of the electrodes while trapezoidal microchannel has a rapid zone that is less than 45% of the total area and occupies around 52% of the electrodes.

Based on the percentage of the rapid zone and the electrodes coverage, rectangular cross-sectional microchannels are considered the ideal choice for DEP separation. Rectangular cross-sectional microchannel has a small dead zone and a rapid zone that occupies large part of the microchannel which ensures uniform distribution of the cells in the microchannel. Moreover, the rapid zone covers large part of the electrode layer which means that more cells will be affected by DEP force generated by the electrodes.

Semi-circular cross-sectional microchannel comes as a second choice for DEP separation. Semi-circular microchannel has the lowest area-ratio dead zone because it has only two corners. Furthermore, the rapid zone of the semi-circular microchannel is greater than that for trapezoidal microchannel. Moreover, it occupies larger part of the electrodes compared to the area occupied by the rapid zone of the trapezoidal microchannel.

The flow rate in the separation microchannel has a direct impact on the separation speed. The Flow rate for the three microchannels under discussion and at the same conditions is shown in Figure 2.4.

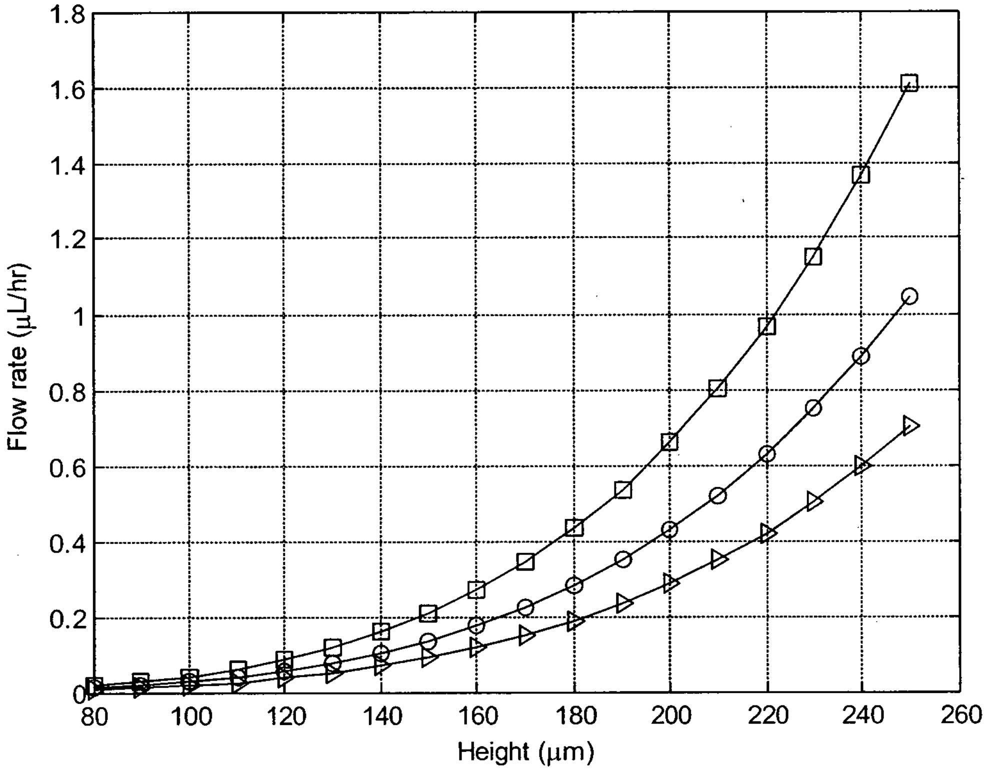

Figure 2.4: Flow rate vs. the channel height for circular, rectangular and trapezoidal cross-sectional microchannels where the width of the microchannel was assumed to be two times the height $\left(\frac{1}{\mu}\frac{dp}{dx} = 10^3\right)$.

Flow rate in rectangular cross-sectional microchannel has been found to be higher than the flow rate in the semi-circular and trapezoidal cross-sectional microchannels under the same pressure difference. This is due to the large size of the rectangular cross-sectional microchannel compared to the other two cross-sectional microchannels. Based on the flow rate under constant pressure difference, rectangular cross-sectional microchannel comes as first choice in order to yield rapid separation of cells.

The separation of living cells in microfluidic devices requires good knowledge of the cells and medium behavior in such devices. Moreover, in order to construct path lines and to create models for the cells movement in DEP devices, all forces act on the cell during the separation process need to be calculated. This includes the drag force due to the cell movement and DEP force created by the electrodes layer. A mathematical solution for electrical potential, electric field and DEP force created by non uniform interdigitated electrodes is derived in the next chapter. In addition, a mathematical formulation for electric field and DEP force for moving dielectrophoretic phenomenon are also provided based on Fourier series.

Chapter 3 : Analytical solution for dielectrophoretic force generated by non-uniform interdigitated electrode array and for moving dielectrophoresis applied to living cells separation.

3.1. Introduction

Around 18 century, it was discovered that diseases are caused by microorganisms. Since 1835 when Agostino Bassi proved that a disease of silkworm was caused by a fungal infection [159] until today researchers are trying to study the microorganisms under specific conditions. These investigations have lately gone down to molecular level.

The large number of a variety of cells, all coexisting in a living organism, make it impossible screening of each individual cell. However, within a specimen of freely moving cells, it may be possible to study a reduced number of particular cells that should be extracted, and separated from the other cells in the specimen.

The term "Cell separation" has been widely used in the literature in order to express the process of purification of single cell line from a mixture of cells. Cell separation is an important tool in disease diagnostics and research, stem cell research and cell biology.

Cell separation methods can be classified into two main categories based on the separation principle; separation based on the physical properties of the cells and biochemical characteristics based separation. Magnetic cell separation [22, 160], electrokinetic separation [79, 161-163] and density gradient centrifugation [164, 165] are techniques used based on the physical properties of the cells in order to separate them. On the other hand, separation of cells using the reaction between antigens with specific genes expressed on the cell membrane is an example of biochemical separation method [166].

Each of the presently used methods has advantages and disadvantages and specific method is used for specific purpose.

However, until today, there is no standard technique available to obtain 100% pure population of viable particular cell line from inhomogeneous cell mixture. The purity of a certain cell line is defined as the percentage of the cells of the same characteristics in the separated cell population. Purity of the separated cells is not the only important feature in selecting a separation process. Viability of the cells after the separation, recovery, cost, speed and simplicity of the process are other elements that play an important role in selecting certain separation process versus another.

Recovery denotes the fraction of the targeted cells separated to the total number of targeted cells initially present in the sample. Viability is a generic term that indicates several assessments on the condition of the cells after they are subjected to a procedure compared to the conditions before the procedure is applied and it might be considered the most important assessment criteria in any separation procedure.

The most often used technique which is also the least expensive to determine the cell viability is through dye exclusion. A dye solution is added to the cells and is kept for a few minutes. A few dyes have been used for this assay and the most used dyes are Trypan blue and Erythrosine B. The cell membrane of nonviable cells is permeable and the dye will penetrate the cell wall, while viable cells will have impermeable or less permeable membrane and they will not take the dye color. A significant difference of color between the viable and non-viable cells can be seen under regular inverted microscope. The fraction of the cells that did not take the dye to the total number of cells indicates the viability of the cells.

In order to indicate the viability or recovery of the separation method, the number of the cells has to be determined before and after the separation. Cells counting methods are classified in direct and indirect techniques. The hemocytometer is the most commonly used direct method to count the cells.

The haemocytometer consists of thick glass including two identical counting chambers on both sides and specially made glass as shown in Figure 3.1. Each counting chamber consists of 9 large squares each measuring 1×1 mm. The center square is divided into 25 small squares. The volume between the glass slide grid and a glass coverslip is 10^{-4} mL. The number of cells in each chamber is calculated by multiplying the number of cells counted in the fine squared mesh times 10^4 times the sample volume in milliliters as the sample is diluted ten thousand times before counting.

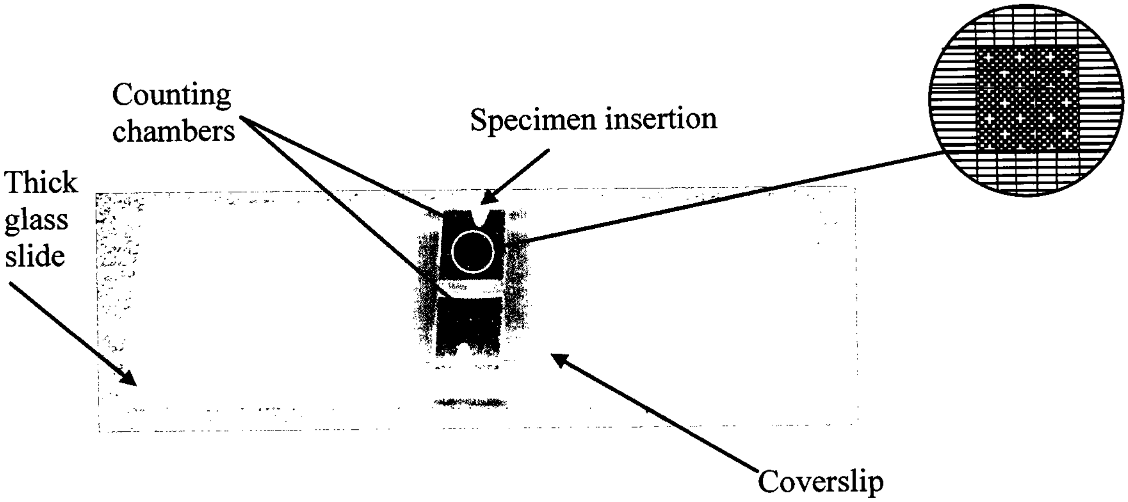

Figure 3.1 : Haemocytometer

In order to increase the accuracy of counting, the average number of cells in both counting chamber is used in the calculation. On the other hand, an example of indirect method of cells counting is using the protein content in the cells. The number of cells in a sample is found by calculating the protein content of the sample divided by the expected protein content of a single cell.

Electrokinetics phenomena are a family of different effects that occur in fluid containing particles including living cells. Electrokinetics phenomena have impressive applications in separation of biological molecules and particles and transporting of fluid in microchannels. The two main parts of electrokinetics phenomena used in the separation of biological molecules and cells are the electrophoresis and dielectrophoresis phenomena.

Electrophoresis is the movement of charged particles under the influence of electric field. If the particle is positively charged it will move toward the electrode with the negative polarity (Figure 3.2 (a)). Alternatively, the particle will move toward the positive polarity electrode if it holds negative charges (Figure 3.2 (b)).

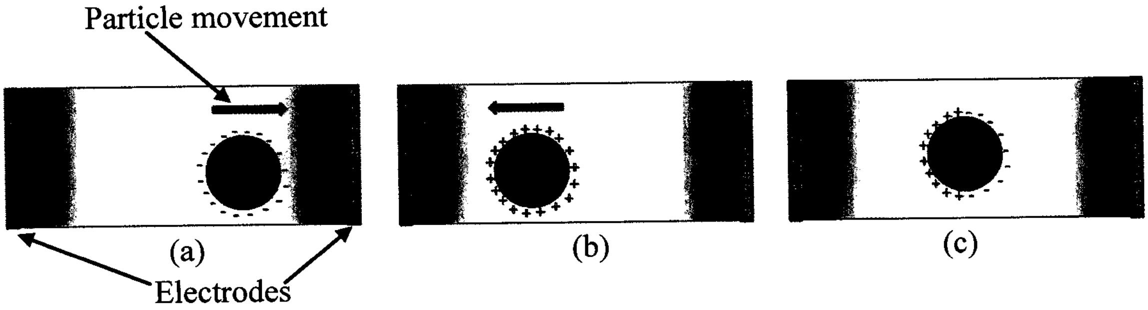

Figure 3.2: Electrophoresis phenomenon and movement of different charged particles.

Electrophoresis is widely used in protein gel electrophoresis separation including Western Blot biological test. If the cell or the molecule has no charge, the net force acting on it due to the uniform electrical field is equal to zero and no movement will occur (Figure 3.2 (c)).

Dielectrophoresis (DEP) is the second electrokinetics phenomenon. DEP was defined first time by Pohl [31] as the motion of neutral, polarisable particle subjected to non-uniform electrical field (Figure 3.3). Particle in similar situation will experience a force whose magnitude and direction depend on the amplitude and frequency of the applied AC electric field and the dielectric properties of the particle and its submersion medium[31].

Dielectrophoresis phenomena have been exclusively used in microdevices for cell separation [27, 36-38] because it uses the natural properties of cells. Moreover, dielectrophoresis is considered one of the noninvasive and rapid separation techniques. In addition, cell separation using dielectrophoresis phenomena holds promise for disease diagnostics and other biological applications of microdevices [39, 46]. Different types of cells have been separated from mixture of cells using DEP based microdevices including yeast cells, lymphocytes and cancer cells [27, 69, 83].

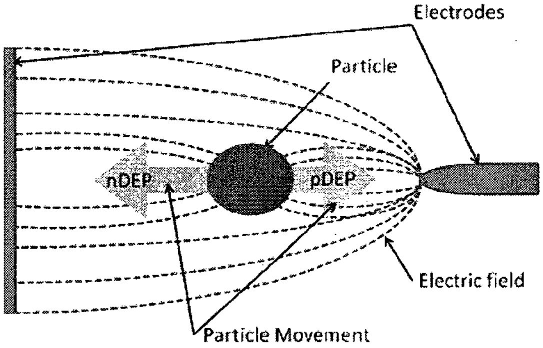

Figure 3.3: Dielectrophoresis phenomena

The expression of dielectric force acting on a spherical polarisable cell placed in a non-uniform electrical field and immersed in a medium is given by the equation [42, 71].

$$\boldsymbol{F}_{DEP} = \pi \varepsilon_0 \varepsilon_m r^3 Re[f_{CM}] \nabla(E.E) \tag{19}$$

where ε_0 is the vacuum dielectric constant, ε_m is the suspending medium dielectric constant, r is the particle radius, Re$[f_{CM}]$ is the real part of Clausius-Mossotti factor and $\boldsymbol{E}$ represents the peak electric field. Clausius-Mossotti factor f_{CM} is defined as [167]

$$f_{CM}(\varepsilon_p^*, \varepsilon_m^*, \omega) = \frac{\varepsilon_p^*(\omega) - \varepsilon_m^*(\omega)}{\varepsilon_p^*(\omega) + 2\varepsilon_m^*(\omega)} \tag{20}$$

where ε_p^* and ε_m^* are the frequency dependent complex permittivity of the particle and of the suspending medium respectively, and ω is the angular frequency. The complex permittivity $\varepsilon^*(\omega)$ depends on the dielectric constant ε and the conductivity of the medium σ_M and defined as

$$\varepsilon^*(\omega) = \varepsilon - j\frac{\sigma_M}{\omega} \tag{21}$$

where $j = \sqrt{-1}$. The real part of Clausius-Mossotti $\mathrm{Re}[f_{CM}]$ is a function of the particle and the suspending medium [27], and it can be written as :

$$\mathrm{Re}[f_{CM}] = \left(\frac{f^2 - f_0^2}{f^2 + 2f_0^2}\right) \tag{22}$$

In the above equation f represents the applied AC electric frequency and f_0 is the crossover frequency (the frequency when $\mathrm{Re}[f_{CM}] = 0$). The crossover frequency can be expressed as:

$$f_0 = \frac{\sigma_M}{\sqrt{2}\pi r C_{mem}} \tag{23}$$

where C_{mem} is the membrane capacitance of the particle, the cell in the present case.

If the real part of Clausius-Mossotti factor is negative, the particle will experience a repulsive force from the charged electrodes. This phenomenon is called negative dielectrophoresis (nDEP). On the other hand the particle will experience positive dielectrophoresis (pDEP) if the real part of Clausius-Mossotti factor has a positive value (Figure 3.3).

The main principle used to separate different types of particles or different cells from a mixture using dielectrophoresis is to ensure pDEP for some cells and nDEP for other cells. The design of the separation chamber should take into consideration that the frequency of the applied AC and the conductivity of the medium should ensure a dielectrophoretic response for the targeted cells that is opposite to dielectrophoretic response of the rest of the cells.

3.2. Problem description for non-uniform interdigitated electrodes

One of the designs that divides the separation chamber into high and low electric field regions is the non-uniform interdigitated electrodes as illustrated in Figure 3.4.

In order to compute the force on the particle created by the electric field or to develop models for particle movement in the separation chamber, a formulation for the electric field is required. The electric field is given by Gauss's law as follow.

$$\nabla . \boldsymbol{E} = \frac{\rho}{\varepsilon_0} \tag{24}$$

where ρ is the total electric charge density. In the present case the charge density including both free and bound charge is zero. Equation (24) becomes

$$\nabla . \boldsymbol{E} = 0 \tag{25}$$

The quasi-electrostatic form of Maxwell's equation relates the electric field with the electric potential in the equation.

$$\boldsymbol{E} = -\nabla \varphi \tag{26}$$

where φ represents the electric potential. Substitution of equation (26) into (25) yields

$$\frac{\partial^2\varphi}{\partial x^2}+\frac{\partial^2\varphi}{\partial y^2}=0 \tag{27}$$

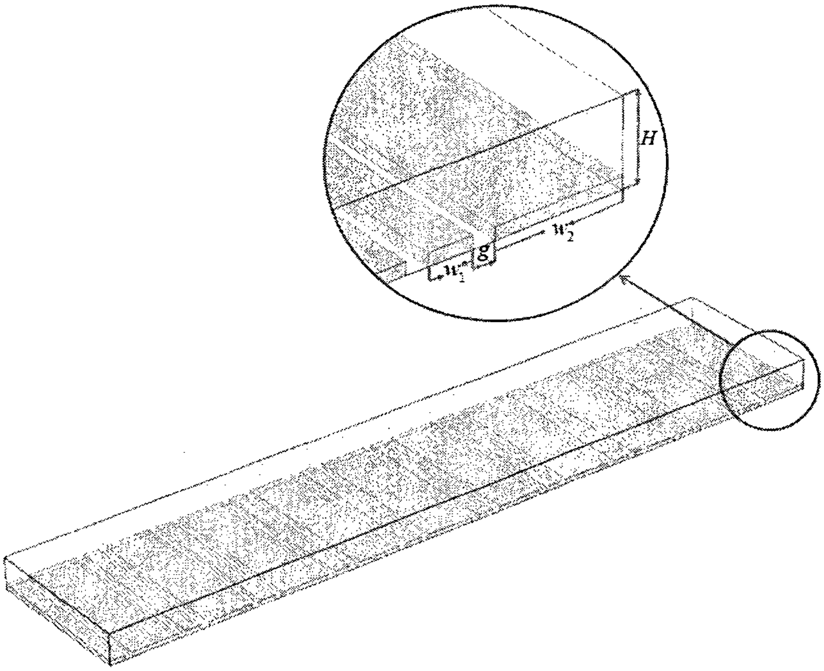

Figure 3.4: The schematic diagram shows the non-uniform interdigitated electrodes and the channel of the separation chamber of finite height *H*.

Figure 3.4 shows the diagram of the geometry under discussion. This design is similar to the widely used interdigitated electrodes but in the present case the electrode sizes are different. From the symmetry of electrode, the unit segment in Figure 3.5 is used to simplify the problem.

The boundary conditions applied for Laplace equation (27) are

1) Potential of value V_0 on one of the electrodes.

$$\varphi(x,0)=V_0 \qquad 0\le x\le\frac{w_1}{2} \tag{28}$$

2) Potential of value $-V_0$ on adjacent electrodes.

$$\varphi(x,0)=-V_0 \qquad \frac{w_2}{2}\le x\le 1 \tag{29}$$

3) The gradient normal to the surface between the electrodes is zero, (insulated surface).

$$\frac{\partial\varphi}{\partial\bar{y}}(x,0)=0 \qquad \frac{w_1}{2}\leq x\leq\frac{w_2}{2} \tag{30}$$

The length of the unit segment is assumed to be L, where

$$\mathrm{L}=\frac{\mathrm{w}_1}{2}+\mathrm{g}+\frac{\mathrm{w}_2}{2} \tag{31}$$

In order to normalize the equation with respect to the coordinates, the following dimensionless parameters are employed

$$\bar{x}=\frac{x}{L} \tag{32}$$

$$\bar{y}=\frac{y}{H} \tag{33}$$

Substituting (32) and (33) into (27) yields:

$$\frac{\partial^2\varphi}{L^2\partial\bar{x}^2}+\frac{\partial^2\varphi}{H^2\partial\bar{y}^2}=0 \tag{34}$$

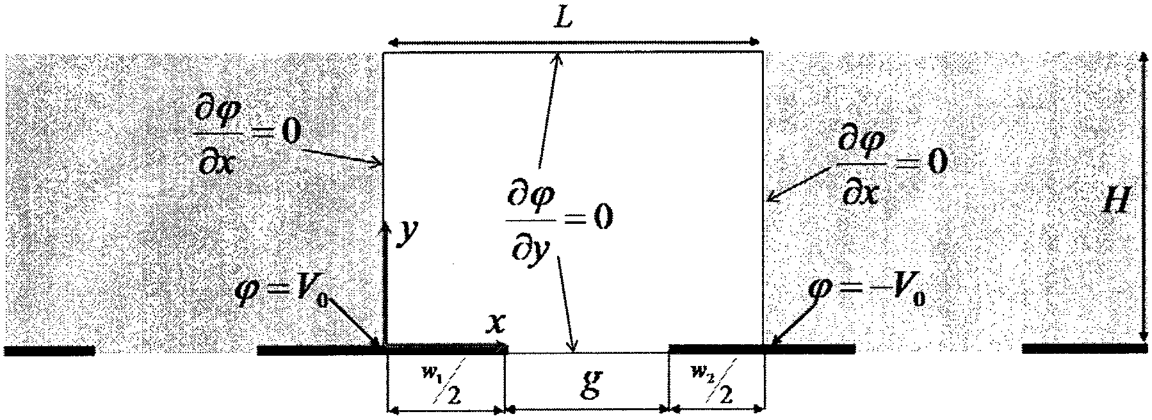

Figure 3.5: The unit segment and the boundary conditions used to simplify the problem

Using the non-dimensional parameters in (32) and (33), the boundary conditions become.

$$\varphi(\bar{x},0)=V_0 \qquad 0\leq\bar{x}\leq\alpha_1 \tag{35}$$

$$\varphi(\bar{x},0) = -V_0 \qquad \alpha_2 \leq \bar{x} \leq 1 \tag{36}$$

$$\varphi(\bar{x},0) = \varphi_g(\bar{x}) \qquad \alpha_1 \leq \bar{x} \leq \alpha_2 \tag{37}$$

where:

$$\alpha_1 = \frac{w_1}{2L} \tag{38}$$

$$\alpha_2 = \frac{g + \left(\frac{w_1}{2}\right)}{L} \tag{39}$$

and $\varphi_g(\bar{x})$ represent the electrical potential distribution function between the two adjacent electrodes. Using the symmetry between the adjacent unit segments, the following conditions are assumed

$$\frac{\partial \varphi}{\partial \bar{x}}(0,\bar{y}) = 0 \tag{40}$$

$$\frac{\partial \varphi}{\partial \bar{x}}(1,\bar{y}) = 0 \tag{41}$$

The height of the microfluidic chamber for cell separation is finite and the boundary condition in the upper part of the chamber needs to be included in the solution. Since the upper part of the separation chamber is generally covered with an insulated layer of glass or Polydimethylsiloxane (PDMS) which has a low electrical conductivity [168]. The potential gradient across the upper part is set to zero.

$$\frac{\partial \varphi}{\partial \bar{y}}(\bar{x},1) = 0 \tag{42}$$

The boundary condition (42) is believed to be the exact state at the upper part of the separation chamber.

3.3. Solution of the governing equations

By using the separation of variables techniques, the solution is assumed to take the form.

$$\varphi(\bar{x},\bar{y}) = C + F(\bar{x})G(\bar{y}) \tag{43}$$

where $F(\bar{x})$ is function of the normalized dimension $\bar{x}$ only, while $G(\bar{y})$ is function of $\bar{y}$ only and C is a constant. The derivatives of (43) are

$$\varphi_{\bar{x}}(\bar{x},\bar{y}) = F_{\bar{x}}(\bar{x})G(\bar{y}) \tag{44}$$

$$\varphi_{\overline{xx}}(\bar{x},\bar{y}) = F_{\overline{xx}}(\bar{x})G(\bar{y}) \tag{45}$$

$$\varphi_{\bar{y}}(\bar{x},\bar{y}) = F(\bar{x})G_{\bar{y}}(\bar{y}) \tag{46}$$

$$\varphi_{\overline{yy}}(\bar{x},\bar{y}) = F(\bar{x})G_{\overline{yy}}(\bar{y}) \tag{47}$$

Substituting equations (45) and (47) into (34) yields

$$\frac{F_{\overline{xx}}(\bar{x})G(\bar{y})}{L^2} + \frac{F(\bar{x})G_{\overline{yy}}(\bar{y})}{H^2} = 0 \tag{48}$$

Dividing equation (48) by $F(\bar{x})G(\bar{y})$ where $F(\bar{x})G(\bar{y}) \neq 0$, gives

$$\frac{F_{\overline{xx}}(\bar{x})}{L^2F(\bar{x})} + \frac{G_{\overline{yy}}(\bar{y})}{H^2G(\bar{y})} = 0 \tag{49}$$

Rearrangement of equation (49) yields

$$\frac{F_{\overline{xx}}(\bar{x})}{F(\bar{x})} = -\frac{L^2G_{\overline{yy}}(\bar{y})}{H^2G(\bar{y})} \tag{50}$$

The two sides of the equation cannot be equal unless both are equal to a constant. Because of the nature of the boundary conditions a positive constant will lead to trivial solution. The two ordinary differential equations that come from equation (50) are solved as follows.

$$\frac{F_{\overline{xx}}(\bar{x})}{F(\bar{x})} = -K^2 \tag{51}$$

Rearrangement of the terms of equation (51) gives:

$$F_{\overline{xx}}(\bar{x}) + K^2 F(\bar{x}) = 0 \tag{52}$$

Assuming the solution to be in the form:

$$F(\bar{x}) = a_i e^{\delta_i \bar{x}} \tag{53}$$

Substituting equation (53) into (52) yields:

$$a_i {\delta_i}^2 e^{\delta_i \bar{x}} + K^2 a_i e^{\delta_i \bar{x}} = 0 \tag{54}$$

Solution of equation (54) for δ_i gives:

$$\delta_1 = -Ki \tag{55}$$

$$\delta_2 = -Ki \tag{56}$$

where K is the separation constant and $i = \sqrt{-1}$. Equation (53) becomes:

$$F(\bar{x}) = a_0 \cos(K\bar{x}) + a_1 \sin(K\bar{x}) \tag{57}$$

Following the same steps to solve the right side of equation (50), the solution is

$$\frac{L^2 G_{\overline{yy}}(\bar{y})}{H^2 G(\bar{y})} = K^2 \tag{58}$$

$$G(\bar{y}) = b_0 e^{\frac{KH}{L}\bar{y}} + b_1 e^{\frac{-KH}{L}\bar{y}} \tag{59}$$

Substitution of (57) and (59) into (43) yields:

$$\varphi(\bar{x}, \bar{y}) = C + (a_0 \cos(K\bar{x}) + a_1 \sin(K\bar{x})) \left(b_0 e^{\frac{KH}{L}\bar{y}} + b_1 e^{\frac{-KH}{L}\bar{y}} \right) \tag{60}$$

Substituting the boundary condition (40) into (60) gives:

$$(-a_0 \mathrm{K} \sin(0) + a_1 K cos(0)) G(\bar{y}) = 0 \tag{61}$$

Equation (61) has non-trivial solution only if

$$a_1 = 0 \tag{62}$$

Equation (60) becomes:

$$\varphi(\bar{x},\bar{y}) = C + \left(a_0\cos(K\bar{x})\right)\left(b_0 e^{\frac{KH}{L}\bar{y}} + b_1 e^{\frac{-KH}{L}\bar{y}}\right) \tag{63}$$

Substitution of the condition (42) gives:

$$\left(a_0\cos(K\bar{x})\right)\left(b_0\frac{KH}{L}e^{\frac{KH}{L}} - \frac{KH}{L}b_1 e^{\frac{-KH}{L}}\right) = 0 \tag{64}$$

Equation (64) has a non-trivial solution if

$$b_0\frac{KH}{L}e^{\frac{KH}{L}} - \frac{KH}{L}b_1 e^{\frac{-KH}{L}} = 0 \tag{65}$$

Rearrangement the terms of equation (65) gives:

$$b_0 = e^{\frac{-2KH}{L}}b_1 \tag{66}$$

Equation (60) becomes:

$$\varphi(\bar{x},\bar{y}) = C + \left(a_0\cos(K\bar{x})\right)\left(b_1 e^{\frac{-2KH}{L}} e^{\frac{KH}{L}\bar{y}} + b_1 e^{\frac{-KH}{L}\bar{y}}\right) \tag{67}$$

which can be written as

$$\varphi(\bar{x},\bar{y}) = C + \left(\mathrm{C}_1\cos(K\bar{x})\right)\left(e^{\frac{KH(\bar{y}-2)}{L}} + e^{\frac{-KH}{L}\bar{y}}\right) \tag{68}$$

where the constant $\mathrm{C}_1 = a_0 b_1$

Substitution of the condition (41) into (68) yields:

$$\left(\mathrm{C}_1\mathrm{K}\sin(K)\right)\left(e^{\frac{KH(\bar{y}-2)}{L}} + e^{\frac{-KH}{L}\bar{y}}\right) = 0 \tag{69}$$

which has nontrivial solution only if

$$\sin(K) = 0 \tag{70}$$

Solving equation (70) gives:

$$K = n\pi \tag{71}$$

The solution in (68) becomes:

$$\varphi(\bar{x},\bar{y}) = C + \sum_{n=1}^{\infty} \mathrm{C_n}\left(\cos(n\pi\bar{x})\right)\left(e^{\frac{n\pi H}{L}(\bar{y}-2)} + e^{\frac{-n\pi H}{L}\bar{y}}\right) \tag{72}$$

To understand the nature of the potential between the adjacent electrodes one needs to solve Laplace's equation between the electrodes in the configuration described in Figure 3.6 .The equation expresses the potential in the gap between the two adjacent electrodes with the boundary conditions as illustrated.

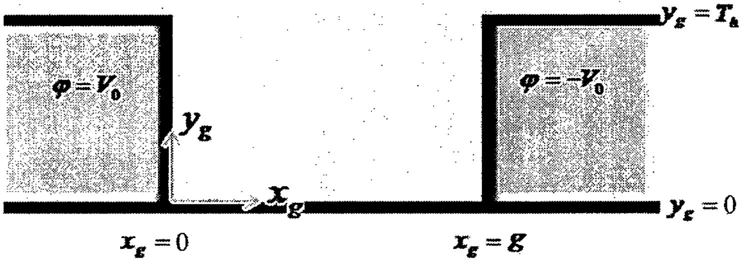

Figure 3.6: Schematic diagram shows the gap between the two adjacent electrodes with the coordinate system used to solve the problem. The electrodes are assumed of finite thickness $\mathbf{T_h}$

$$\frac{\partial^2\varphi_g}{\partial x_g^2} + \frac{\partial^2\varphi_g}{\partial {y_g}^2} = 0 \tag{73}$$

$$\varphi_g(0, y_g) = V_0 \qquad\qquad y_g \leq T_h \tag{74}$$

$$\varphi_g(g, y_g) = -V_0 \qquad y_g \leq T_h \tag{75}$$

Since the electrodes are deposited on an insulated layer. The following boundary condition is implied:

$$\frac{\partial \varphi_g}{\partial y_g}(x_g, 0) = 0 \tag{76}$$

where φ_g represents the electric potential in the gap between the adjacent electrodes describe in the unit segment (Figure 3.5), x_g and y_g are the coordinate system inside the gap (Figure 3.6). To normalize the coordinates in equation (73) with respect to the geometry, the following dimensionless parameters are proposed:

$$\bar{x}_g = \frac{x_g}{g} \tag{77}$$

$$\bar{y}_g = \frac{y}{T_h} \tag{78}$$

where T_h represent the hight of the electrode and g is the gap between the two adjacent electrodes. The dimensionless form of equation (73) with the boundary conditions becomes:

$$\frac{\partial^2 \varphi_g}{g^2 \partial \bar{x}_g^2} + \frac{\partial^2 \varphi_g}{T_h^2 \partial \bar{y}_g{}^2} = 0 \tag{79}$$

$$\varphi_g(0, \bar{y}_g) = V_0 \qquad \bar{y}_g \leq 1 \tag{80}$$

$$\varphi_g(1, \bar{y}_g) = -V_0 \qquad \bar{y}_g \leq 1 \tag{81}$$

$$\frac{\partial \varphi_g}{\partial \bar{y}_g}(\bar{x}_g, 0) = 0 \tag{82}$$

Based on the separation of variables principles, the solution of equation (79) is assumed to take the form

$$\varphi_g(\bar{x}_g, \bar{y}_g) = F_g(\bar{x}_g) G_g(\bar{y}_g) \tag{83}$$

where $F_g(\bar{x}_g)$ is a function of the variable $\bar{x}_g$ only, $G_g(\bar{y}_g)$ is function of $\bar{y}_g$ only.

Substituting (83) into (79) yields:

$$\frac{F_g'' G_g}{g^2} + \frac{F_g G_g''}{T_h^2} = 0 \tag{84}$$

where F_g'' is the second derivative of $F_g(\bar{x}_g)$ with respect to $\bar{x}_g$ and G_g'' is the second derivative of $G_g(\bar{y}_g)$ with respect to $\bar{y}_g$.

Dividing equation (84) by $F_g G_g$ where $F_g G_g \neq 0$ gives

$$\frac{F_g''}{g^2 F_g} + \frac{G_g''}{T_h^2 G_g} = 0 \tag{85}$$

Rearrangement of (85) yields:

$$\frac{F_g''}{F_g} = -\frac{g^2 G_g''}{T_h^2 G_g} \tag{86}$$

This is true only when both sides of (86) equal to a constant

$$\frac{F_g''}{F_g} = -\frac{g^2 G_g''}{T_h^2 G_g} = K_g^2 \; or \; -K_g^2 \tag{87}$$

For the case of negative constant

$$\frac{g^2 G_g''}{T_h^2 G_g} = K_g^2 \tag{88}$$

$$\frac{F_g''}{F_g} = -K_g^2 \tag{89}$$

Arrangement of (88) and (89) yields

$$G_g{}'' - \frac{T_h^2 K_g^2}{g^2} G_g = 0 \tag{90}$$

$$F_g{}'' + -K_g^2 F_g \tag{91}$$

The solutions of (90) and (91) are

$$G_g\left(\bar{y}_g\right) = C_{3g} cos\left(\frac{T_h K_g}{g}\bar{y}_g\right) + C_{4g} sin\left(\frac{T_h K_g}{g}\bar{y}_g\right) \tag{92}$$

$$F_g\left(\bar{x}_g\right) = C_{1g} e^{\left(K_g \bar{x}_g\right)} + C_{2g} e^{\left(-K_g \bar{x}_g\right)} \tag{93}$$

where C_{1g}, C_{2g}, C_{3g} and C_{4g} are constants. Substituting the boundary condition (76) yields

$$\left(C_{1g} e^{K_g \bar{x}_g} + C_{2g} e^{-K_g \bar{x}_g}\right)\left(C_{4g}\frac{T_h K_g}{g}\right) = 0 \tag{94}$$

This gives

$$C_{4g} = 0 \tag{95}$$

The solution in (83) can be expressed as:

$$\varphi_g\left(\bar{x}_g, \bar{y}_g\right) = \left(C_{5g} e^{K_g \bar{x}_g} + C_{6g} e^{-K_g \bar{x}_g}\right)\left(cos\left(\frac{T_h K_g}{g}\bar{y}_g\right)\right) \tag{96}$$

where the constants $C_{5g} = C_{1g}C_{3g}$ and $C_{6g} = C_{2g}C_{3g}$. Substituting the boundary conditions (80) and (81) yields

$$V_0 = \left(C_{5g} + C_{6g}\right)\left(cos\left(\frac{T_h K_g}{g}\bar{y}_g\right)\right) \tag{97}$$

$$-V_0 = \left(C_{5g} e^{K_g} + C_{6g} e^{-K_g}\right)\left(cos\left(\frac{T_h K_g}{g}\bar{y}_g\right)\right) \tag{98}$$

The dimensionless variable $\bar{y}_g$ ranges inside the gap between the two electrodes from 0 to 1. The maximum value for the term $cos\left(\frac{T_h K_g}{g}\bar{y}_g\right)$ is 1 while the minimum value is:

$$cos\left(\frac{\pi T_h}{d}\right) \tag{99}$$

The deposited electrodes are usually less than or in the range of one nanometer thickness where the gap between the electrodes is in the range of several micrometers to less than a millimeter. In the present work, the electrodes were assumed to have negligible thickness that approach zero. Therefore, equations (97) and (98) can be approximated as

$$V_0 = C_{5g} + C_{6g} \tag{100}$$

$$-V_0 = C_{5g}e^{K_g} + C_{6g}e^{-K_g} \tag{101}$$

Solving (100) and (101) for $C_{5g}$and C_{6g} gives

$$C_{5g} = \frac{V_0(1 + e^{-K_g})}{e^{-K_g} - e^{K_g}} \tag{102}$$

$$C_{6g} = \frac{-V_0(1 + e^{K_g})}{e^{-K_g} - e^{K_g}} \tag{103}$$

The potential between the adjacent electrodes can be expressed by:

$$\varphi_g(\bar{x}_g) = \left(\frac{V_0}{e^{-K_g} - e^{K_g}}\right)\left((1 + e^{-K_g})e^{K_g\bar{x}_g} - (1 + e^{K_g})e^{-K_g\bar{x}_g}\right) \tag{104}$$

The solution in equation (104) describes the potential between the adjacent electrodes while equation (72) expresses the electric potential over the electrodes as shown in Figure 3.5. At the interface between the two domains the separation constants K and K_g were assumed to have the same value and for simplicity n in case of K_g was assumed to be 1. Using this assumption the value of K_g becomes:

$$K_g = \pi \tag{105}$$

In order to write the conditions (35), (36) and the potential profile between the adjacent electrodes (105) as one condition at the bottom of the separation chamber

(Figure 3.5), the Fourier cosine series formulation is used. The Fourier cosine series is given as

$$\varphi(\bar{x},0) = A_0 + \sum_{m=1}^{\infty} A_m cos(m\pi\bar{x}) \qquad 0 \leq \bar{x} \leq 1 \tag{106}$$

where the constants A_0 and A_m are the constants of Fourier series and are calculated as it follows:

$$A_0 = \int_0^1 \varphi(\bar{x},0)d\bar{x} \tag{107}$$

$$A_m = 2\int_0^1 \varphi(\bar{x},0)cos\left(\frac{m\pi\bar{x}}{1}\right)d\bar{x} \tag{108}$$

Since the dimensionless variable $\bar{x}_g$ is different from the dimensionless variable $\bar{x}$ that is used in the unit segment described in Figure 3.5, the relation between the two dimensionless variables is necessary in order to calculate the constants of Fourier series. The relation between the two dimensionless parameters is given as:

$$\bar{x} = (\alpha_2 - \alpha_1)\bar{x}_g + \alpha_1 \tag{109}$$

The constant A_0 is calculated along the unit segment using the formula (107)

$$A_0 = \int_0^{\alpha_1} V_0 d\bar{x} + \int_{\alpha_1}^{\alpha_2} \varphi_g(\bar{x})d\bar{x} + \int_{\alpha_2}^{1} (-V_0)d\bar{x} \tag{110}$$

which can be rewritten as:

$$A_0 = \int_0^{\alpha_1} V_0 d\bar{x} + (\alpha_2 - \alpha_1)\int_0^1 \varphi_g(\bar{x}_g)d\bar{x}_g + \int_{\alpha_2}^{1} (-V_0)d\bar{x} \tag{111}$$

Calculating the integrals in (111), yields

$$A_0 = V_0\alpha_1 + -V_0(1-\alpha_2) \tag{112}$$

Rearrangement of (112) gives

$$A_0 = V_0(\alpha_1 + \alpha_2 - 1) \tag{113}$$

The constant A_m is calculated using (108), which gives:

$$A_m = 2\left(\int_0^{\alpha_1} V_0 cos(m\pi\bar{x})d\bar{x} + \int_{\alpha_1}^{\alpha_2} \varphi_g(\bar{x})cos(m\pi\bar{x})d\bar{x} + \int_{\alpha_2}^{1}(-V_0)cos(m\pi\bar{x})d\bar{x}\right) \tag{114}$$

The integrals in equation (114) are calculated separately as follows:

$$\int_0^{\alpha_1} V_0 cos(m\pi\bar{x})d\bar{x} = \frac{V_0 sin(m\pi\alpha_1)}{m\pi} \tag{115}$$

$$\begin{gathered}\int_{\alpha_1}^{\alpha_2} \varphi_g(\bar{x})cos(m\pi\bar{x})d\bar{x} = \\ (\alpha_2-\alpha_1)\int_0^1 \varphi_g(\bar{x}_g)cos\left(m\pi\left((\alpha_2-\alpha_1)\bar{x}_g+\alpha_1\right)\right)d\bar{x}_g = \\ V_0(\alpha_2-\alpha_1)\left[\begin{array}{c}\dfrac{m\pi(1-e^{k_g})(\alpha_2-\alpha_1)\left(sin(m\pi\alpha_2)+sin(m\pi\alpha_1)\right)}{\left(m^2\pi^2(\alpha_2-\alpha_1)^2+{k_g}^2\right)(e^{k_g}-1)}+ \\ \dfrac{k_g(1+e^{k_g})\left(cos(m\pi\alpha_1)-cos(m\pi\alpha_2)\right)}{\left(m^2\pi^2(\alpha_2-\alpha_1)^2+{k_g}^2\right)(e^{k_g}-1)}\end{array}\right]\end{gathered} \tag{116}$$

$$\int_{\alpha_2}^{1}(-V_0)cos(m\pi\bar{x})d\bar{x} = \frac{-V_0}{m\pi}\left(sin(m\pi)-sin(m\pi\alpha_2)\right) = \frac{V_0}{m\pi}sin(m\pi\alpha_2) \tag{117}$$

$$A_m = 2\left[\begin{array}{c} \frac{V_0 sin(m\pi\alpha_1)}{m\pi} + \\ V_0(\alpha_2-\alpha_1)\left(\begin{array}{c} \frac{m\pi(1-e^{k_g})(\alpha_2-\alpha_1)(sin(m\pi\alpha_2)+sin(m\pi\alpha_1))}{(m^2\pi^2(\alpha_2-\alpha_1)^2+{k_g}^2)(e^{k_g}-1)} + \\ \frac{k_g(1+e^{k_g})(cos(m\pi\alpha_1)-cos(m\pi\alpha_2))}{(m^2\pi^2(\alpha_2-\alpha_1)^2+{k_g}^2)(e^{k_g}-1)} \end{array}\right) + \\ \frac{V_0}{m\pi} sin(m\pi\alpha_2) \end{array}\right] \tag{118}$$

Rearrangement of (118) gives:

$$\begin{aligned} A_m = \left(\frac{2V_0}{m\pi}\right)\Bigg(&\left(1-\frac{1}{\left(1+\left(\frac{k_g}{m\pi(\alpha_2-\alpha_1)}\right)^2\right)}\right)(sin(m\pi\alpha_2)+sin(m\pi\alpha_1)) \\ &+\frac{(1+e^{k_g})}{\left(m\pi(\alpha_2-\alpha_1)+\frac{{k_g}^2}{m\pi(\alpha_2-\alpha_1)}\right)(e^{k_g}-1)}(cos(m\pi\alpha_1)-cos(m\pi\alpha_2))\Bigg) \end{aligned} \tag{119}$$

Using Fourier series, the boundary conditions (35), (36) and (37) are written as one condition in the following equation.

$$\varphi(\bar{x},0) = A_0 + \textstyle\sum_{m=1}^{\infty} A_m cos(m\pi\bar{x}) \tag{120}$$

Substitution the condition (120) in equation (72) gives

$$\varphi(\bar{x},0) = C + \sum_{n=1}^{\infty} C_n(\cos(n\pi\bar{x}))\left(e^{\frac{-2n\pi H}{L}}+1\right) = A_0 + \sum_{m=1}^{\infty} A_m cos(m\pi\bar{x}) \tag{121}$$

Solving equation (121) for C and C_n yields

$$C = A_0 \tag{122}$$

$$C_n = \frac{A_m}{\left(e^{\frac{-2n\pi H}{L}}+1\right)} \tag{123}$$

The profile of the electric potential inside the unit segment that used in the solution is given by the equation

$$\varphi(\bar{x},\bar{y}) = A_0 + \sum_{n=1}^{\infty} \frac{A_m}{\left(e^{\frac{-2n\pi H}{L}} + 1\right)} \left(\cos(n\pi\bar{x})\right) \left(e^{\frac{n\pi H}{L}(\bar{y}-2)} + e^{\frac{-n\pi H}{L}\bar{y}}\right) \tag{124}$$

The separation chamber consists of numerous symmetrical unit segments in certain arrangement. Each unit segment is a mirror-like to the next unit along (Figure 3.7). The solution in (124) expresses the potential in one unit segment. To find the potential anywhere in the chamber, one has to correlate the unit segment with the coordinate system along the chamber. The relationship between the dimensionless value $\bar{\mathrm{x}}$ and the coordinate system in the chamber is shown in Figure 3.7. The following relation between the two systems of coordinates is assumed.

$$\bar{\mathrm{x}} = \frac{2\tan^{-1}\left(\tan\frac{\pi\mathrm{X}}{2\mathrm{L}}\right)}{\pi} \tag{125}$$

where *X* is the coordinate along the separation chamber presumptuous the first unit segment starts with the first point of the separation chamber (Figure 3.7). The potential inside the separation chamber is given as:

$$\varphi(X,\bar{y}) = A_0 + \sum_{n=1}^{\infty} \frac{A_m}{\left(e^{\frac{-2n\pi H}{L}} + 1\right)} \left(\cos\left((2\mathrm{n})\tan^{-1}\left(\tan\frac{\pi\mathrm{X}}{2\mathrm{L}}\right)\right)\right) \left(e^{\frac{n\pi H}{L}(\bar{y}-2)} + e^{\frac{-n\pi H}{L}\bar{y}}\right) \tag{126}$$

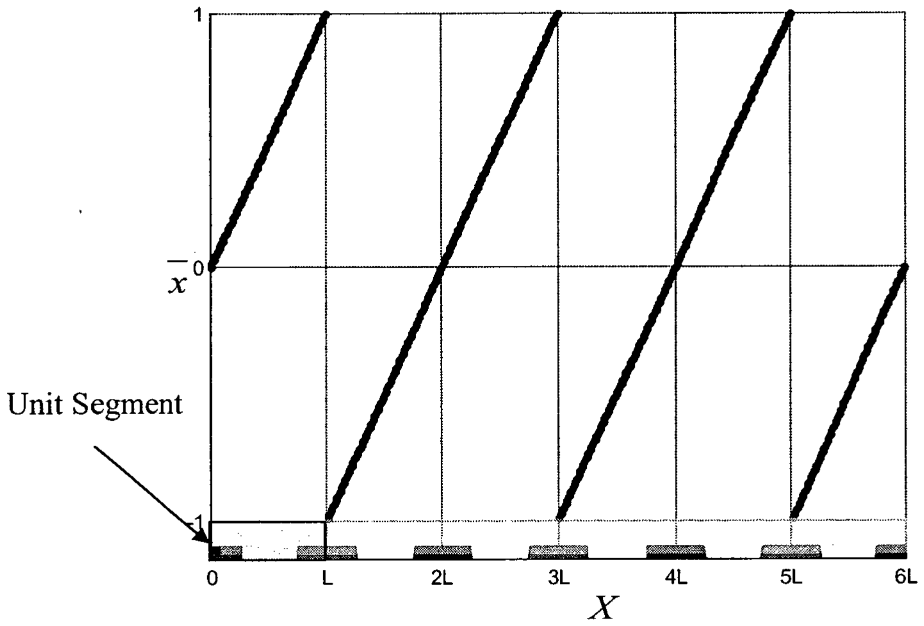

Figure 3.7: The arrangement of the unit segments and the variation of the coordinates in the separation chamber

The electric field is further calculated based on equations (26) and (124) as follows:

$$E(\bar{x},\bar{y}) = -\nabla\varphi(\bar{x},\bar{y}) \tag{127}$$

$$E(\bar{x},\bar{y}) = E_x(\bar{x},\bar{y})i + E_y(\bar{x},\bar{y})j \tag{128}$$

where $E_x(\bar{x},\bar{y})$ and $E_y(\bar{x},\bar{y})$ are the components of the electric field vector and i is the unit vector in $\bar{x}$-direction and j is the unit vector in $\bar{y}$-direction. The vector components E_x and E_y are given as:

$$E_x(\bar{x},\bar{y}) = \sum_{n=1}^{\infty}\left(\frac{n\pi A_m}{L\left(e^{\frac{-2n\pi H}{L}}+1\right)}\right)\left(\sin(n\pi\bar{x})\right)\left(e^{\frac{n\pi H}{L}(\bar{y}-2)} + e^{\frac{-n\pi H}{L}\bar{y}}\right) \tag{129}$$

$$E_y(\bar{x},\bar{y}) = \sum_{n=1}^{\infty}\left(\frac{n\pi A_m}{L\left(e^{\frac{-2n\pi H}{L}}+1\right)}\right)\left(\cos(n\pi\bar{x})\right)\left(e^{\frac{-n\pi H}{L}\bar{y}} - e^{\frac{n\pi H}{L}(\bar{y}-2)}\right) \tag{130}$$

The square of the electric field that found in (128) is given as:

$$E^2(\bar{x},\bar{y}) = E_x^2 + E_y^2 \tag{131}$$

The gradient of the square of the electric field which is part of the DEP force expressed in (19) is found as follows:

$$\nabla E^2 = \left(2E_x\frac{\partial E_x}{\partial x} + 2E_y\frac{\partial E_y}{\partial x}\right)i + \left(2E_x\frac{\partial E_x}{\partial y} + 2E_y\frac{\partial E_y}{\partial y}\right)j \tag{132}$$

Equation (132) can be written as:

$$\nabla E^2 = \frac{1}{L}\left(2E_x\frac{\partial E_x}{\partial \bar{x}} + 2E_y\frac{\partial E_y}{\partial \bar{x}}\right)i + \frac{1}{H}\left(2E_x\frac{\partial E_x}{\partial \bar{y}} + 2E_y\frac{\partial E_y}{\partial \bar{y}}\right)j \tag{133}$$

The derivatives $\frac{\partial E_x}{\partial \bar{x}}, \frac{\partial E_y}{\partial \bar{x}}, \frac{\partial E_x}{\partial \bar{y}}$ and $\frac{\partial E_y}{\partial \bar{y}}$ are calculated as follows:

$$\frac{\partial E_x}{\partial \bar{x}} = \sum_{n=1}^{\infty}\left(\frac{(n\pi)^2 A_m}{L\left(e^{\frac{-2n\pi H}{L}}+1\right)}\right)\cos(n\pi\bar{x})\left(e^{\frac{n\pi H}{L}(\bar{y}-2)} + e^{\frac{-n\pi H}{L}\bar{y}}\right) \tag{134}$$

$$\frac{\partial E_y}{\partial \bar{x}} = \sum_{n=1}^{\infty}\left(\frac{(n\pi)^2 A_m}{L\left(e^{\frac{-2n\pi H}{L}}+1\right)}\right)\sin(n\pi\bar{x})\left(e^{\frac{n\pi H}{L}(\bar{y}-2)} - e^{\frac{-n\pi H}{L}\bar{y}}\right) \tag{135}$$

$$\frac{\partial E_x}{\partial \bar{y}} = \sum_{n=1}^{\infty}\left(\frac{(n\pi)^2 H A_m}{L^2\left(e^{\frac{-2n\pi H}{L}}+1\right)}\right)\left(\sin(n\pi\bar{x})\right)\left(e^{\frac{n\pi H}{L}(\bar{y}-2)} - e^{\frac{-n\pi H}{L}\bar{y}}\right) \tag{136}$$

$$\frac{\partial E_y}{\partial \bar{y}} = \sum_{n=1}^{\infty}\left(\frac{-(n\pi)^2 H A_m}{L^2\left(e^{\frac{-2n\pi H}{L}}+1\right)}\right)\left(\cos(n\pi\bar{x})\right)\left(e^{\frac{n\pi H}{L}(\bar{y}-2)} + e^{\frac{-n\pi H}{L}\bar{y}}\right) \tag{137}$$

For the particular case of uniform interdigitated electrode arrays $w_1 = w_2 = w$, the dimensionless parameters (38) and (39) become

$$\alpha_1 = \frac{w}{2L} \tag{138}$$

$$\alpha_2 = \frac{g + \left(\frac{w}{2}\right)}{L} \tag{139}$$

The subtraction and summation of these parameters yield:

$$\alpha_2 - \alpha_1 = \frac{g}{L} \tag{140}$$

$$\alpha_1 + \alpha_2 = \frac{\left(\frac{w_1}{2}\right)}{L} + \frac{g + \left(\frac{w_1}{2}\right)}{L} = \frac{g + w}{L} \tag{141}$$

Since $w_1 = w_2$

$$\frac{g + w_1}{L} = \frac{g + \frac{w_1}{2} + \frac{w_2}{2}}{L} = 1 \tag{142}$$

The Fourier's constants become:

$$A_0 = V_0(\alpha_1 + \alpha_2 - 1) = 0 \tag{143}$$

$$A_m = \left(\frac{2V_0}{m\pi}\right)\left(\left(1 - \frac{1}{\left(1 + \left(\frac{1}{m(\alpha_2 - \alpha_1)}\right)^2\right)}\right)(sin(m\pi\alpha_2) + sin(m\pi\alpha_1)) + \frac{(1 + e^{\pi})}{\left(m\pi(\alpha_2 - \alpha_1) + \frac{\pi}{m(\alpha_2 - \alpha_1)}\right)(e^{\pi} - 1)}(cos(m\pi\alpha_1) - cos(m\pi\alpha_2))\right) \tag{144}$$

The solution in (124) becomes:

$$\varphi(\bar{x}, \bar{y}) = \sum_{n=1}^{\infty} \frac{A_m}{\left(e^{\frac{-2n\pi H}{L}} + 1\right)}(\cos(n\pi\bar{x}))\left(e^{\frac{n\pi H}{L}(\bar{y}-2)} + e^{\frac{-n\pi H}{L}\bar{y}}\right) \tag{145}$$

3.4. Validation of the results

Comparable solution for the electric potential (124) is proposed in [1]. The boundary conditions used in the present work are different from the ones used in [1] where potential between the adjacent electrodes was assumed linear and the condition on the upper part of the separation chamber was replaced by the condition.

$$\varphi(x, \infty) = 0 \tag{146}$$

The proposed solution in [1] is valid only for the case of uniform electrode array (equal size electrodes) while the present model provides solution for both uniform and non-uniform electrodes. Moreover, the potential profile between the adjacent electrodes was assumed in [1] while in the present work the potential distribution in the gap was found by solving the governing equation of the electric potential. In order to investigate the difference between the proposed solution in [1] and the current work, a comparison study for both solutions with finite element results is shown in Figure 3.8.

The electrodes width and the gap between adjacent electrodes are varying between few micrometers to close to one hundred micrometers. If the minimum width is taken as 5 μm and the maximum is 100 μm and the same values considered for the gap, the constant β will have values that are less than 0.5. Using the solution proposed in [1] will result in an error that reaches 26% (Figure 3.8). Error increases for small values of β because the solution in [1] ignores the Neumann boundary condition at the upper part of the microchannel. The present solution is valid for any size of chamber and for both uniform and non-uniform interdigitated electrode array. The results of the present work show better accuracy compared to the numerical results from the solution proposed in [1] as shown in Figure 3.8.

The present model is more versatile and more accurate than that in [1] and it represents a significant contribution toward the understanding of the DEP phenomena with application to living cell separation.

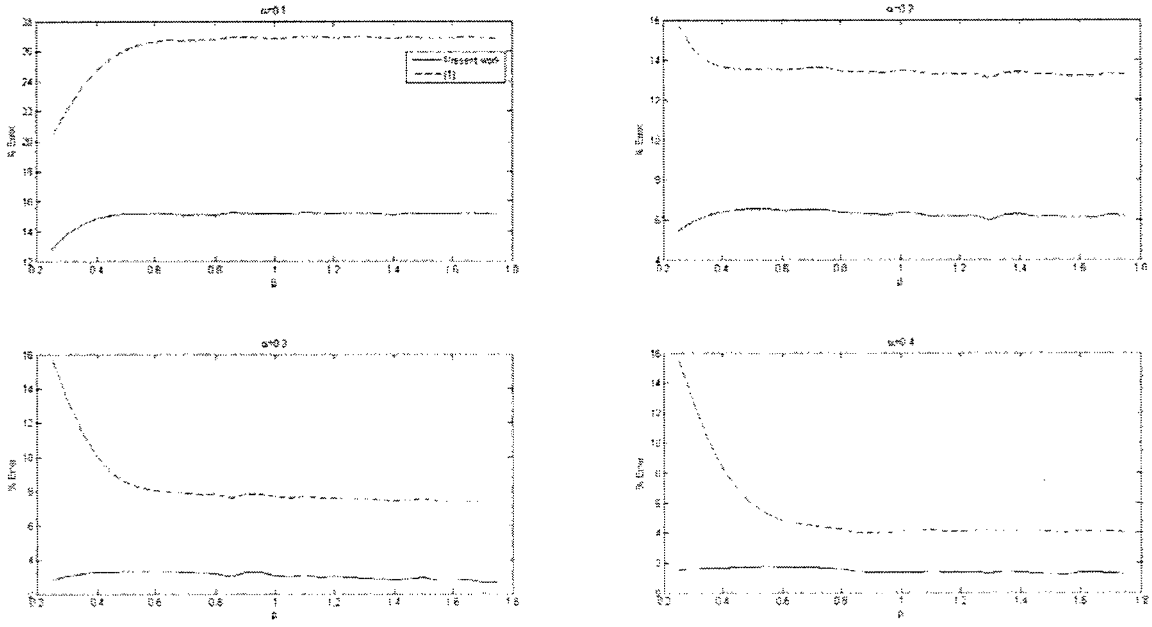

Figure 3.8: Error comparison between the solution proposed in [1] and the present work at different α and L=100 μm

The error plots in Figure 3.8 have been established based on the following procedure.

The dimensionless parameter β was taken equal to $\frac{H}{2(w+g)}$ and the mean square root error was evaluated based on the results produced by the proposed model (continuous line) vs. the model proposed in [1].

$$\% \, Error = 100 \times \sqrt{\frac{\sum_1^n(\text{Numerical} - \text{Analytical})^2}{\sum_1^n(\text{Numerical})^2}} \tag{147}$$

The word "numerical" is used for the numerical results using finite element method and "analytical" is the present solution or the solution proposed in [1]. From

Figure 3.8 it is clear that the proposed model is much more accurate than the solution proposed by [1] particularly if the β value is less than one.

3.5. The effect of the electrodes and the gap size

In order to facilitate the understanding of the effect of the electrodes size and gap between the adjacent electrodes, electric potential is plotted with various gap and electrode size. Based on the previous designs of equal size electrode-gap that is proposed in the literature, the length of the unit segment is assumed to be 100 μm and different gap distance is considered [33].

Figures 3.9 and 3.10 show the electric potential profile for different electrode width and fixed gap of 25 μm. Figure 3.9 is for the case $w_2 > w_1$ in which the electrode (w_2) holds the positive potential while Figure 3.10 is for $w_2 < w_1$. The profile of the electric potential for fixed gap of 50 and 75 μm and different size of electrodes are shown in Figure 3.11 and Figure 3.12.

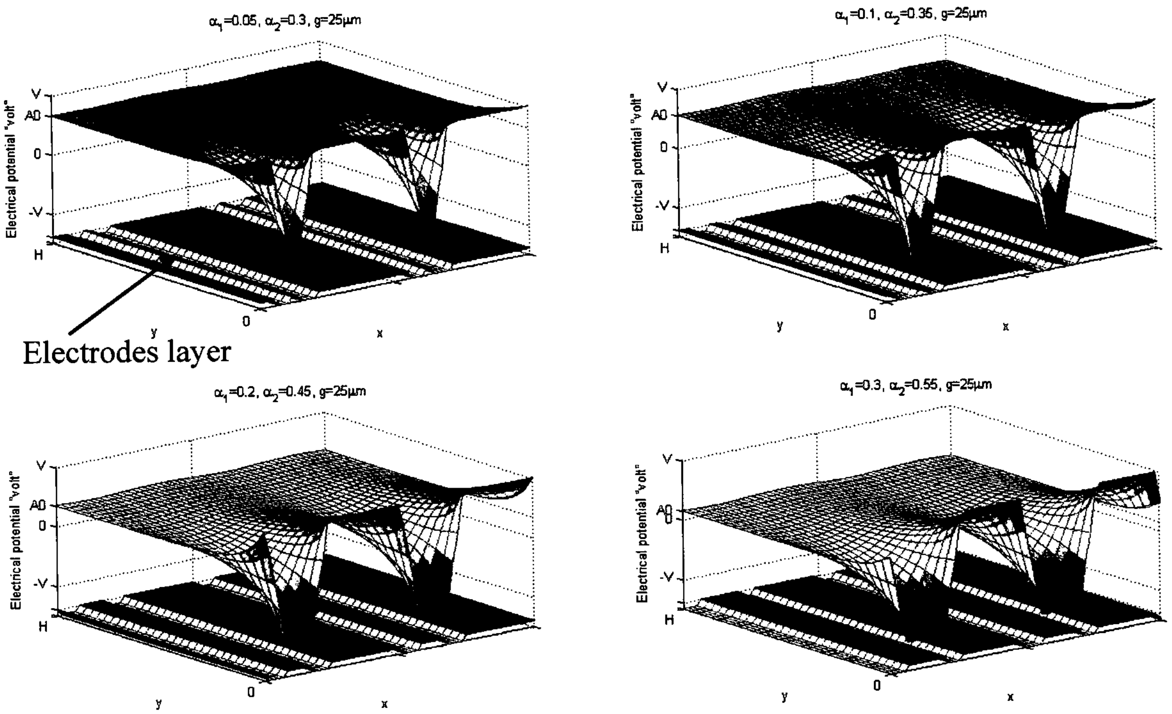

$\alpha_1=0.05, \alpha_2=0.3, g=25\mu m$

$\alpha_1=0.1, \alpha_2=0.35, g=25\mu m$

Electrodes layer

$\alpha_1=0.2, \alpha_2=0.45, g=25\mu m$

$\alpha_1=0.3, \alpha_2=0.55, g=25\mu m$

Figure 3.9 : Electric Potential profile for different electrodes size and fixed gap of 25 μm ($w_2 > w_1$)

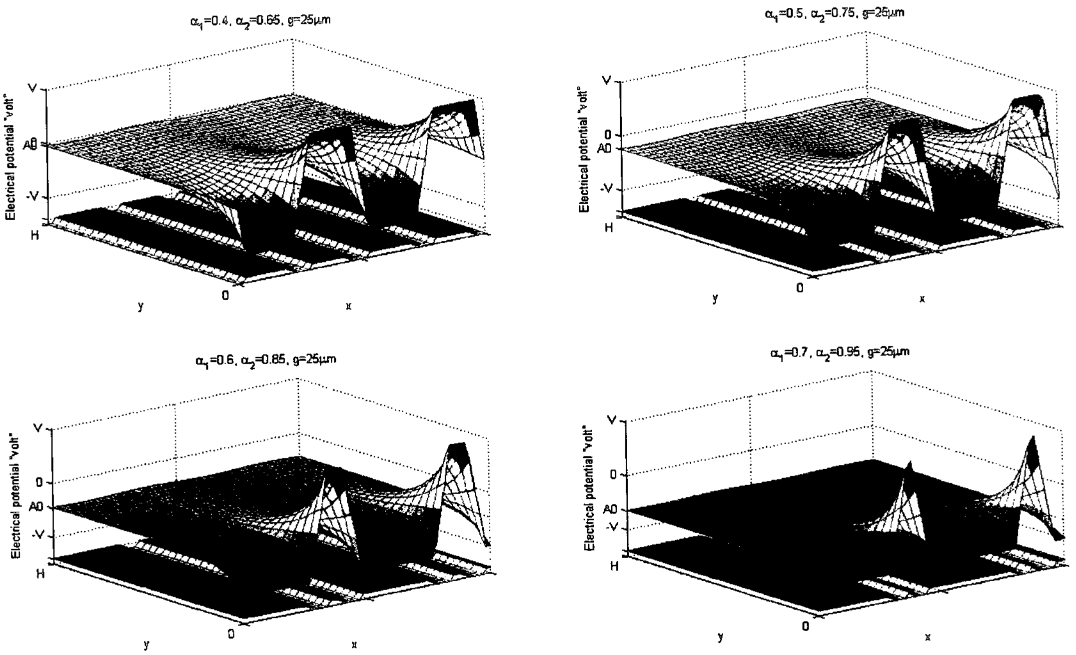

Figure 3.10: Electric Potential profile for different electrodes size Electrodes and fixed gap of 25 μm ($w_2<w_1$)

The effect of the gap size on the potential profile is shown in Figure 3.13, where the gap between the electrodes has been taken 25, 50 and 75 μm. In all the illustrated figures, the length of the unit cell has been kept constant (L=100 μm).

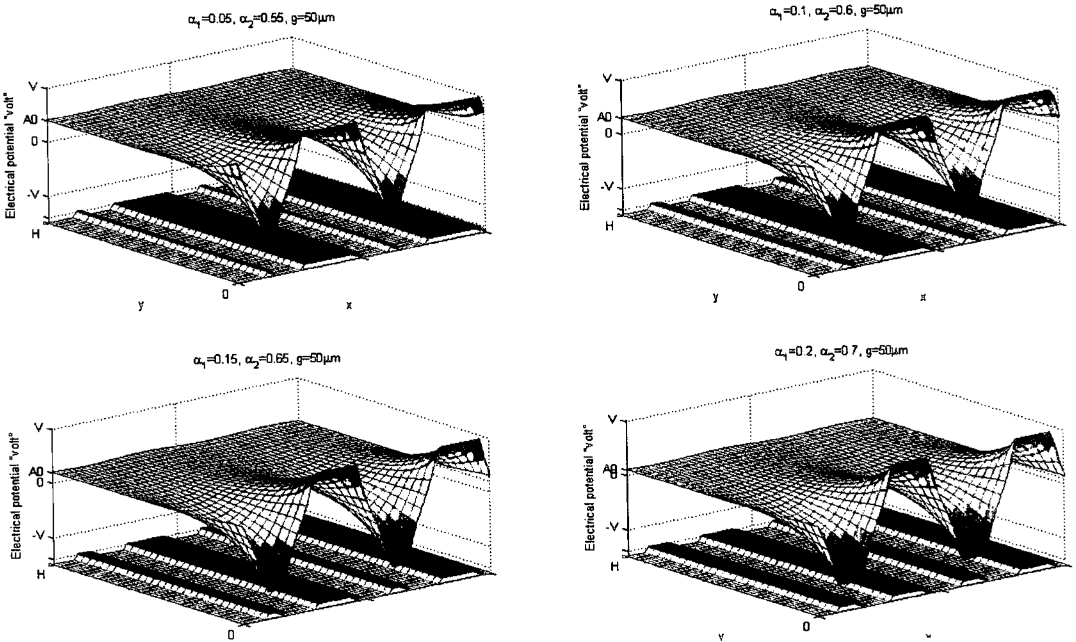

Figure 3.11: Electric Potential profile for different electrodes size and fixed gap of 50 μm

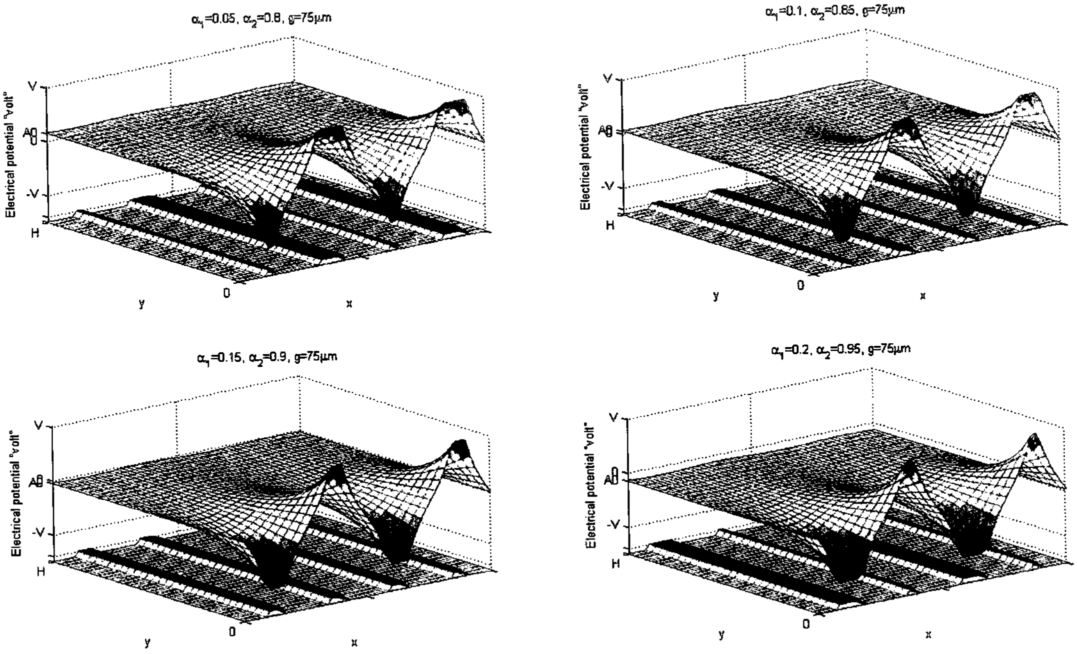

Figure 3.12: Electric potential profile for different electrode size and fixed gap of 75 µm

The sizes of the electrodes and the gaps have been found to affect the distribution and the profile of the electric potential. However, more simulations for the electric field and the gradient of E^2 have to be discussed to understand the effect of the electrodes and gap size on the DEP force.

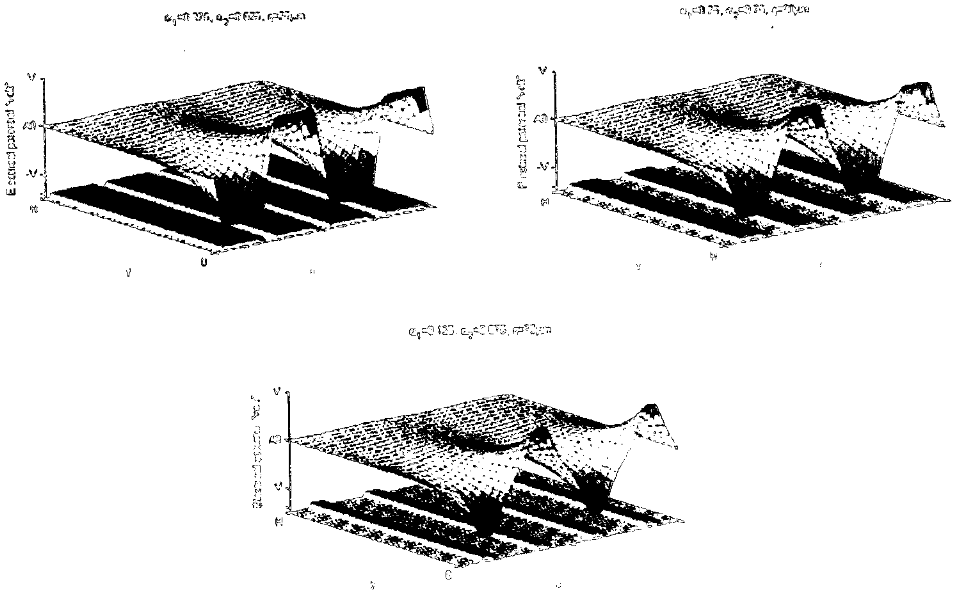

Figure 3.13 : Electric potential profile for equally size electrodes and different gap.

The electric vector field for different sizes of electrodes and fixed gap are shown in Figure 3.14 to 3.16. The figures illustrate the vector plot of the electric filed for different size of electrodes and gap of 25, 50 and 75 μm, respectively, while for the particular case $w_1 = w_2$ the electric vector field is shown in Figure 3.17. The unit length was kept constant and equal to 100μm in all the simulations.

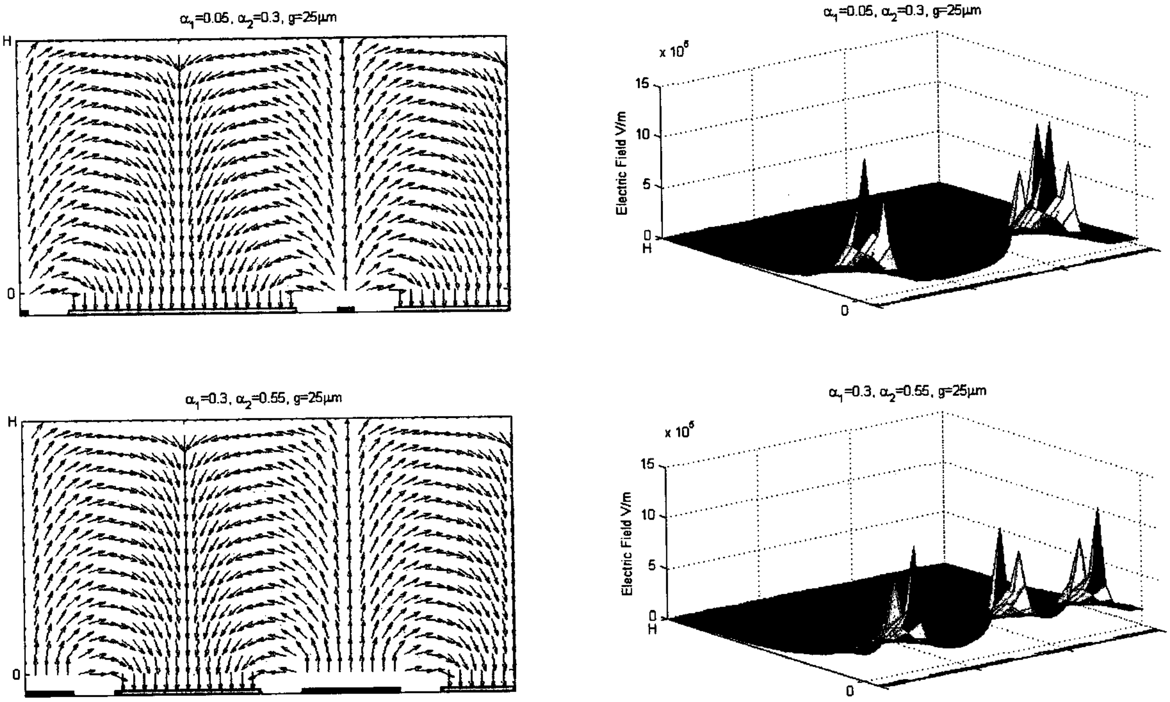

Figure 3.14: Electric field normalized vector plot and strength for different electrodes size with a gap of 25 μm

The electric field reaches its maximum value at the edge of the electrodes. For the case of different size electrodes, the electric field is much higher close to the small electrode and reaches a very small value at midpoint of the large electrode as clearly seen in illustrated figures.

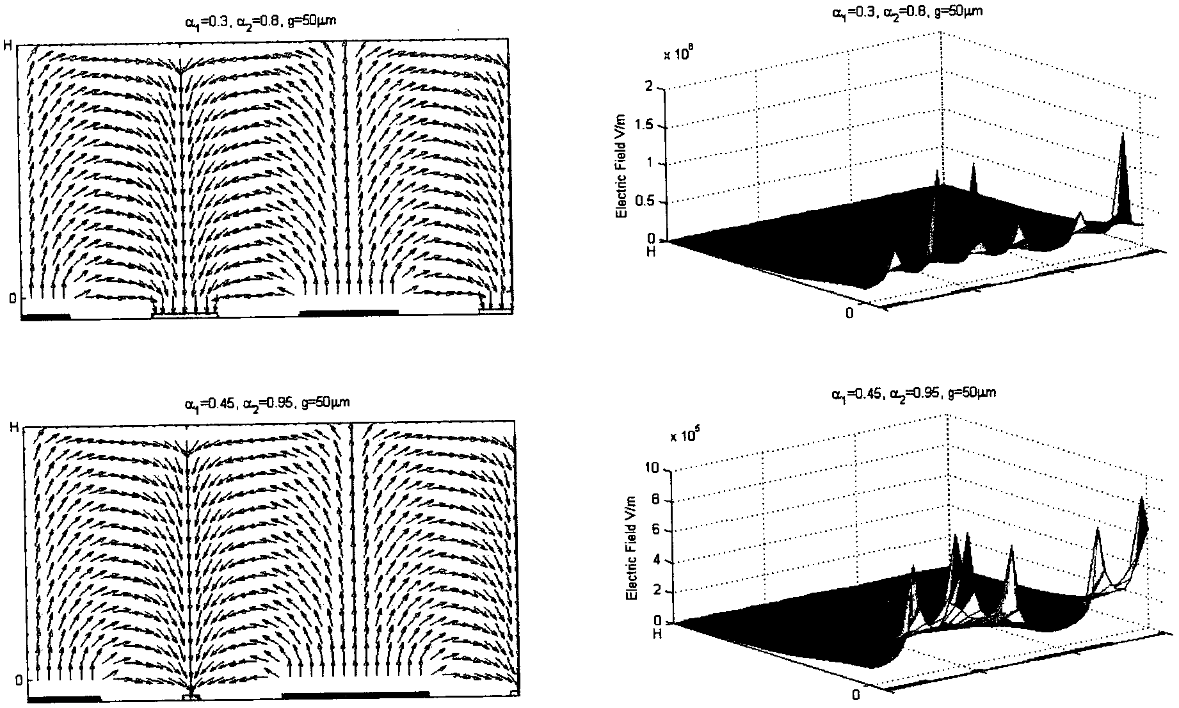

Figure 3.15: Electric field normalized vector plot and strength for different electrodes size with a gap of 50 μm

For small-large electrodes configuration ($\alpha_1 \sim 0 \; or \; \alpha_2 \sim 1$) the electric field can be considered high all over the small electrode and low on the large electrodes except at the edges. As a result, the cells that experience pDEP will be attracted toward the small electrode and the cells that experience nDEP will congregate around the midpoint of the large electrode where the electric field is minimal.

For equal size electrodes, the value of the electric field on the electrodes is identical as shown in Figure 3.17. Changing the gap between the electrode while keeping the unit length constant and equals to 100 μm, one can observe that the value of the electric field along the gap is decreasing with increasing the gap distance.

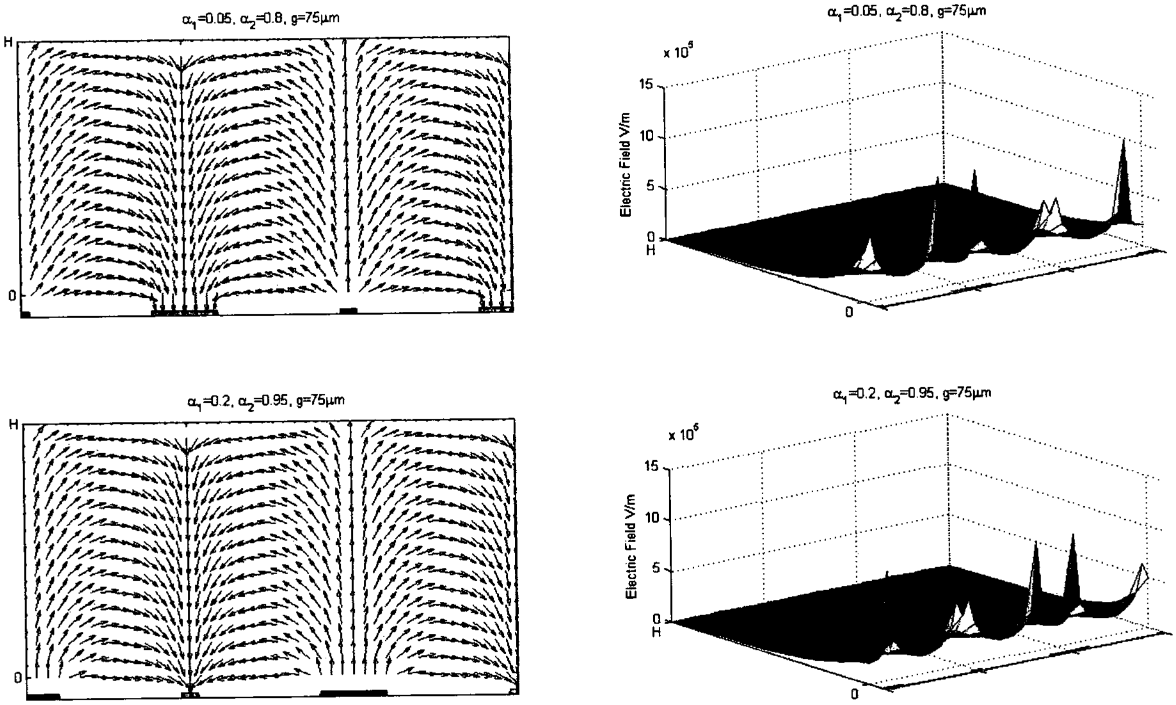

Figure 3.16: Electric field normalized vector plot and strength for different electrodes size with a gap of 75 μm

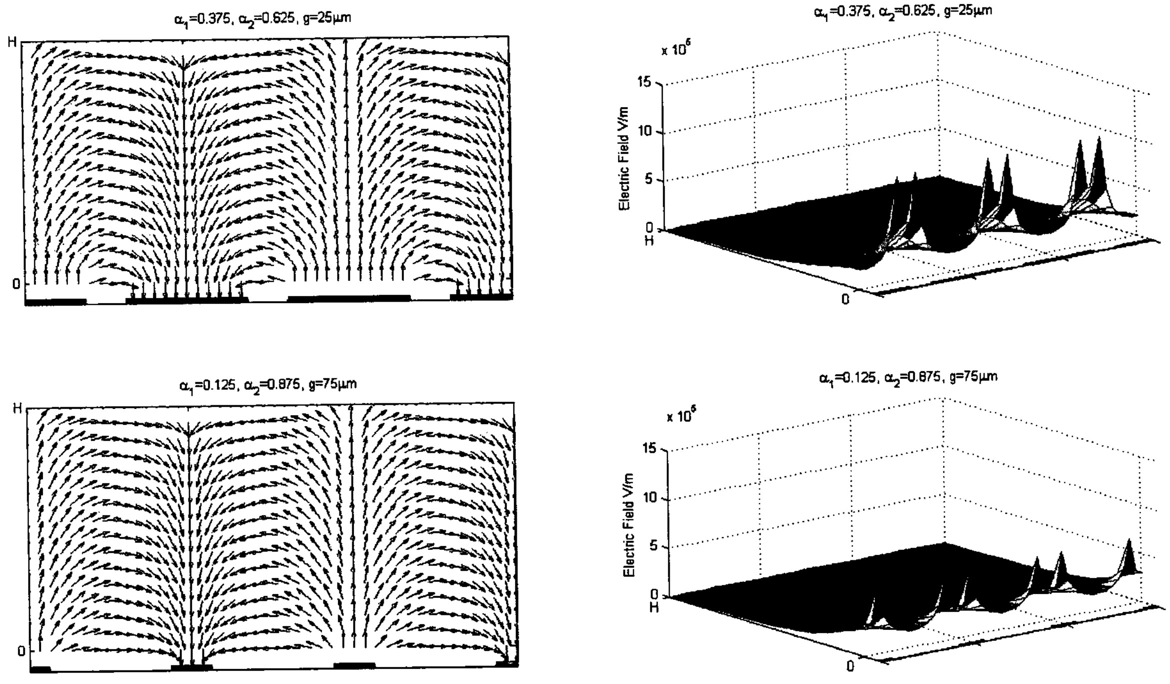

Figure 3.17: Electric field normalized vector plot and strength for same electrodes size with a different gap

The vector plots of ∇E^2 for different size of electrodes and fixed unit length of 100μm are shown in Figure 3.18 to 3.21. The gap between the electrodes is kept constant and equals to 25μm in Figure 3.18 while in Figure 3.19 and Figure 3.20 the gap between the electrodes increased to 50μm and 75μm, respectively.

The DEP force is proportional linearly with the gradient term ∇E^2 . From the Figures 3.18, 3.19 and 3.20 one can see that the DEP force reaches its maximum value at the edge of the electrodes and decreases towards the center of the electrodes or the center of the gap. For high ratio of electrodes ($\alpha_1 \sim 0$ or $\alpha_2 \sim 1$), the DEP force is large all round the small electrode and it is weak around the big electrode except at the edge similar to the profile of the electric field.

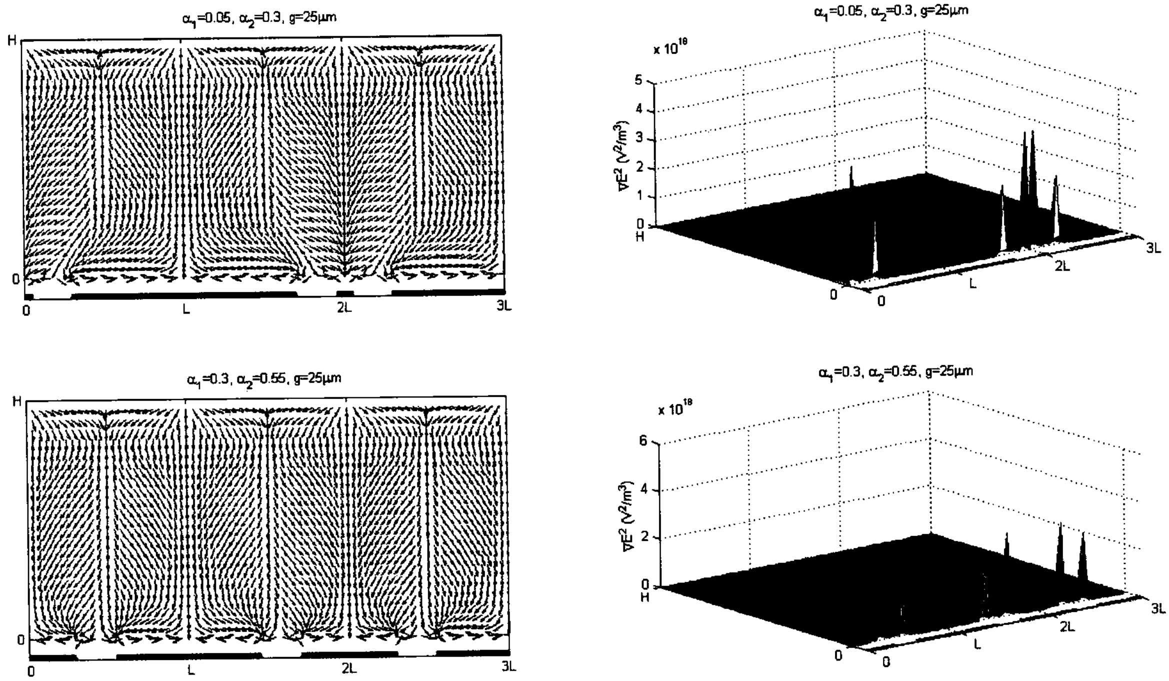

Figure 3.18: ∇(E.E) normalized vector plot and strength for different size of electrodes and fixed gap of 25μm

At the same applied voltage and unit length, the ∇E^2 absolute value was found to be decreasing with increasing gap between the electrodes. Smaller gap is suggested to increase the DEP force in the gap between the electrodes.

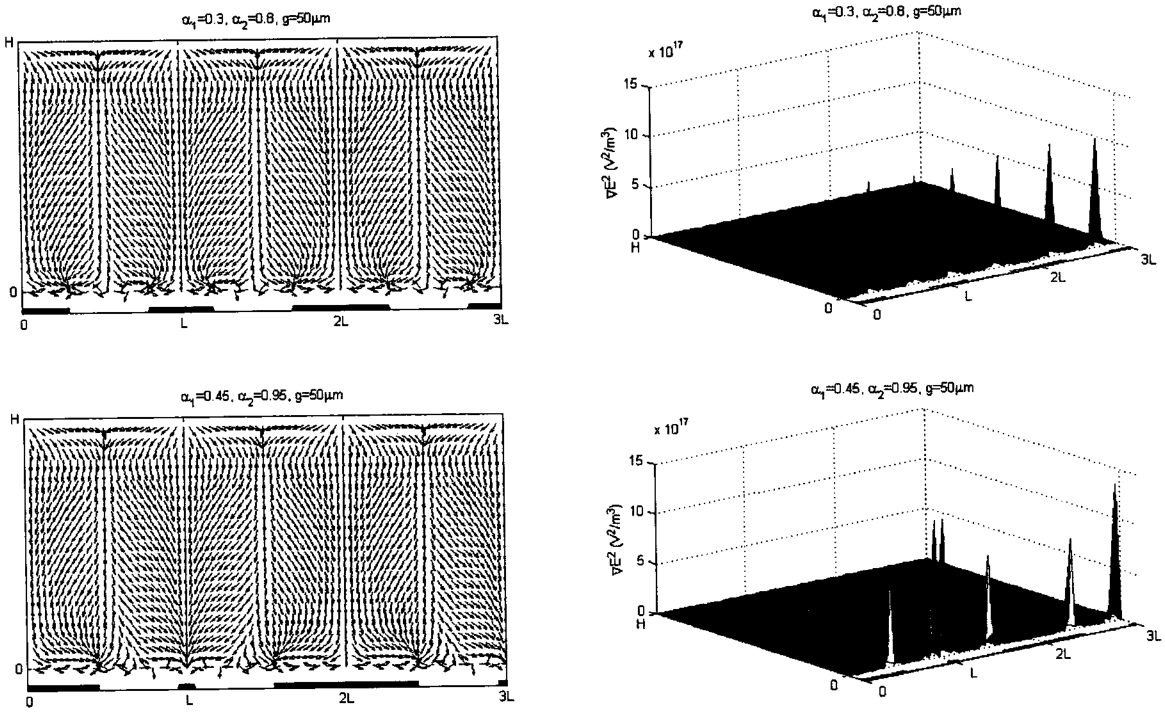

Figure 3.19: ∇(E.E) normalized vector plot and strength for different size of electrodes and fixed gap of 50 μm

Based on the previous discussion, DEP migration separation is considered one of the applications of different size electrodes. Different size electrodes create two different regions inside the separation chamber; low and high electric field regions. By studying Figures 3.18 , 3.19 and 3.22, one can observe that the best gap-electrode combination for DEP migration is to use small gap and high size ratio between the electrodes. High DEP force presents all around the small electrode and in the gap between the adjacent electrodes. The cells will be attracted toward the small electrode in case of pDEP (Figure 3.20) and repel from it in case of nDEP (Figure 3.21). The center point of the large electrode represents the weakest area of DEP force where the cells under nDEP will gather.

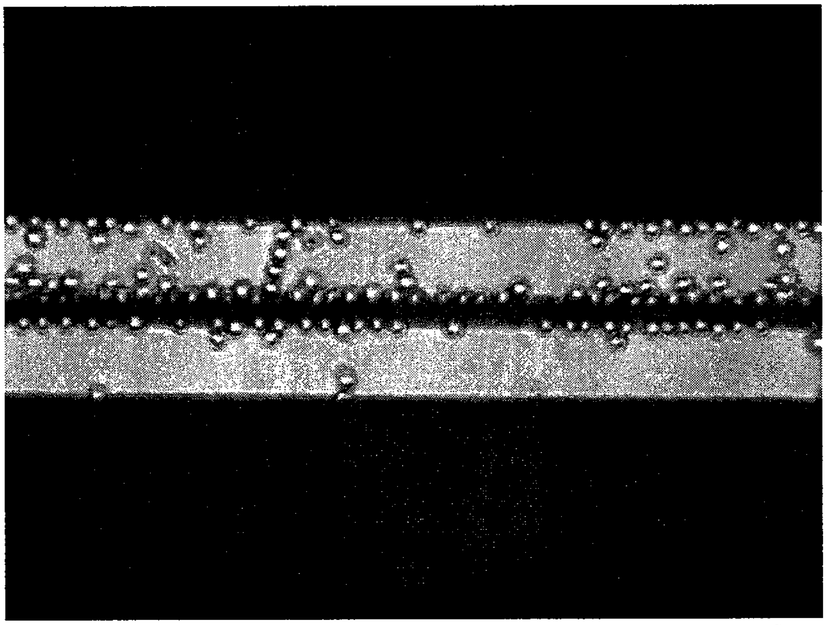

Figure 3.20: Cells experience pDEP accumulating around the small electrode.

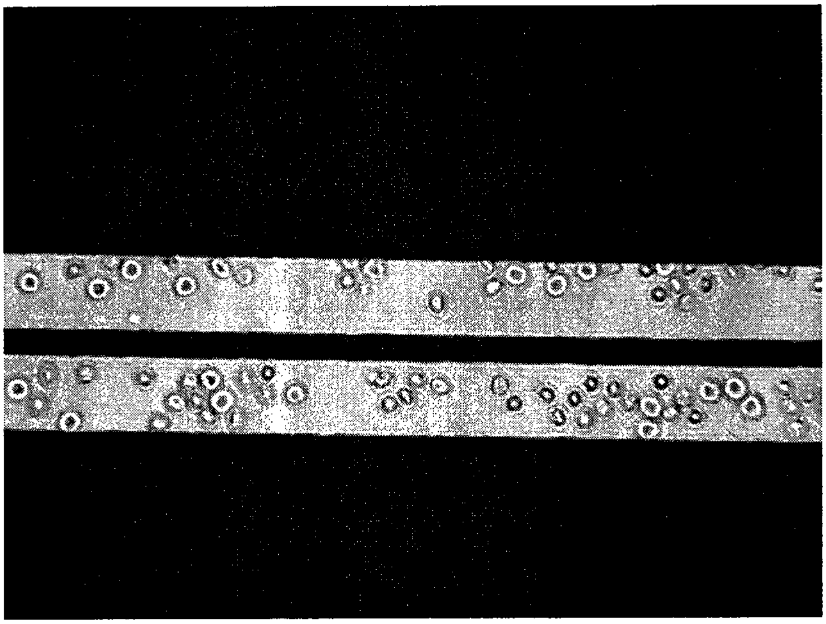

Figure 3.21: Cells experience nDEP accumulating in the gap between the electrodes.

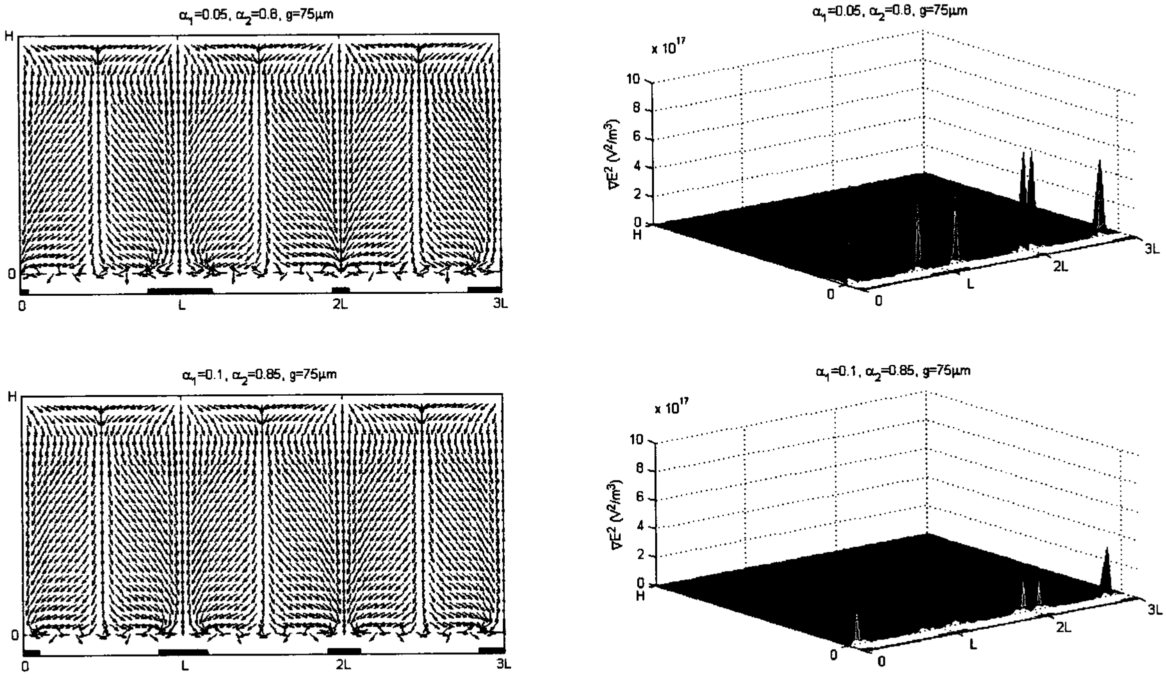

Figure 3.22: $\nabla(E.E)$ normalized vector plot and strength for different size of electrodes and fixed gap of 75 μm

For equal size electrodes and different gap the gradient of E^2 is shown in Figure 3.23. Small gap size creates trap like regions which can be used to trap cell using pDEP while large gap distance create low DEP regions where the cells with nDEP response will gather. Based on the simulation discussed, the DEP force increases with decreasing the size of the electrodes or the gap size. For high DEP force application small electrode size is recommended.

Figure 3.24 shows the log-log plot for the gradient of E^2 as a function of the electrode size. The gap size is taken equal to the electrode width. The log-log plot shows linear relation between the electrode-gap size and the DEP force.

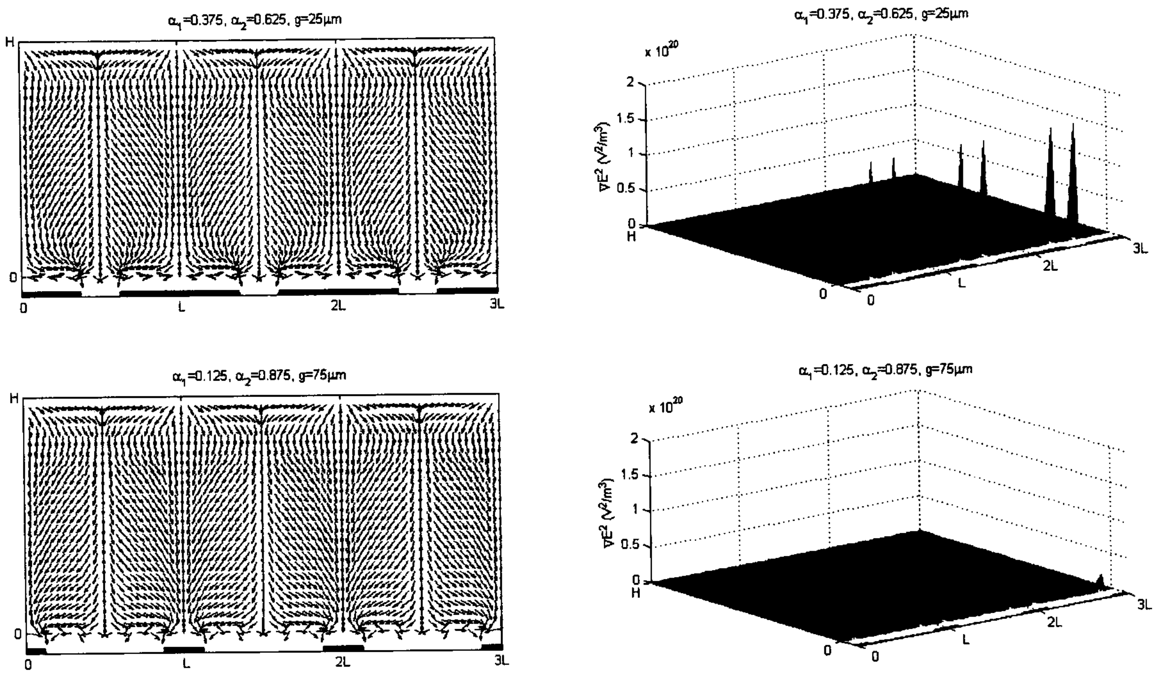

Figure 3.23: ∇(E.E) normalized vector plot and strength for same size electrodes and different gap

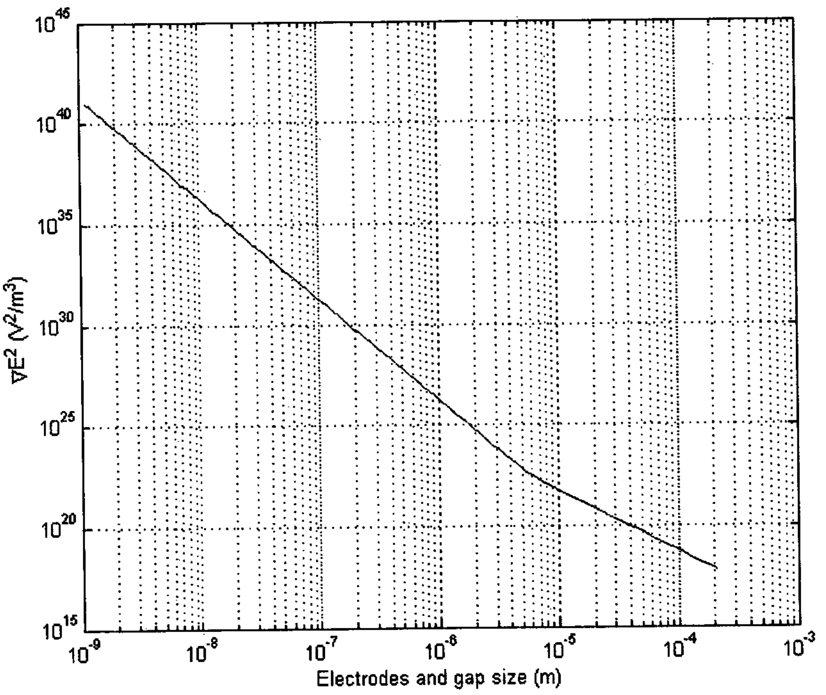

Figure 3.24: Logarithmic graph for ∇(E.E) strength at the edge of the electrode with the same electrode-gap size (V=10 volts, H=150 μm)

3.6. Configurations of the electrodes in the chamber

There are three possible configurations for the deposited layer of electrodes in the separation chamber. The electrodes might be along the flow direction, perpendicular or with an angle to the flow stream (Figure 3.25). Each configuration is used for a specific DEP application. In order to understand the effect of the orientation of the electrodes to the flow direction on the separation process, one has to understand the effect of the electrodes configuration on the cell movement.

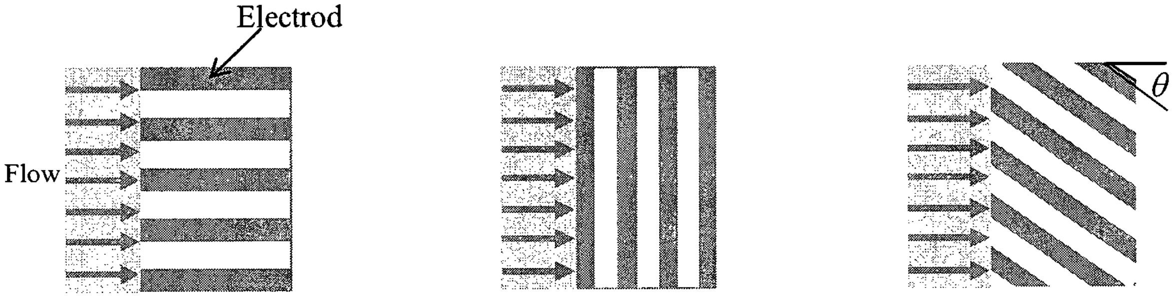

Figure 3.25: Electrodes configuration

The position of the cell over the electrodes layer is bounded by three main locations; on the electrode, in the gap and on the edge between them. For the case where the electrodes are parallel to the flow direction, the main forces on the cell inside the unit segment are shown in Figure 3.26 assuming pDEP response.

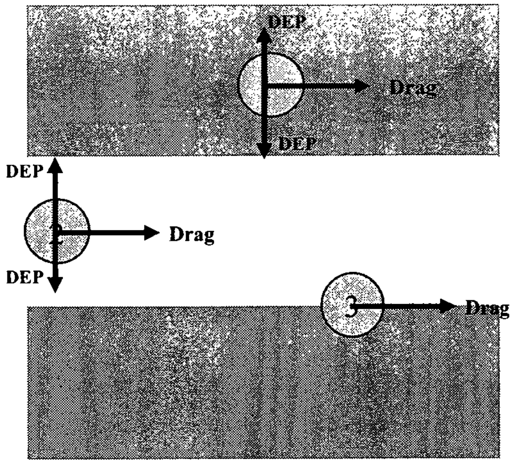

Figure 3.26 : Free body diagram for the cell inside the unit segment where the electrodes are parallel to the flow stream

When the cell is moving over the electrodes (Figure 3.26 case 1), the resultant DEP force is an attraction force toward the edge of the electrode normal to the flow direction. The resultant force from the drag and the DEP force will deflect the direction of the cell and move it closer to the edge. On the other hand, cell moving in the gap (Figure 3.26 case 2) will experience a resultant DEP force attracting it toward the electrode edge. Similar movement in the direction of the edge as in case 1 is expected. However, cell moving on the electrode edge will experience high DEP attraction force toward the edge normal to the plane of the electrodes layer.

Cells in motion under similar configuration will move toward the edge of the electrodes. The movement of the cells due to the drag force will not be interrupted by DEP force. The DEP force component normal to the plane of the electrodes layer will attract the cells to flow close to the electrodes. This configuration is recommended for DEP-FFF and DEP migration. Maximizing the DEP force increases the performance of the DEP-FFF separation process. In order to increase the DEP force, electrodes and gap size has to be minimized as possible.

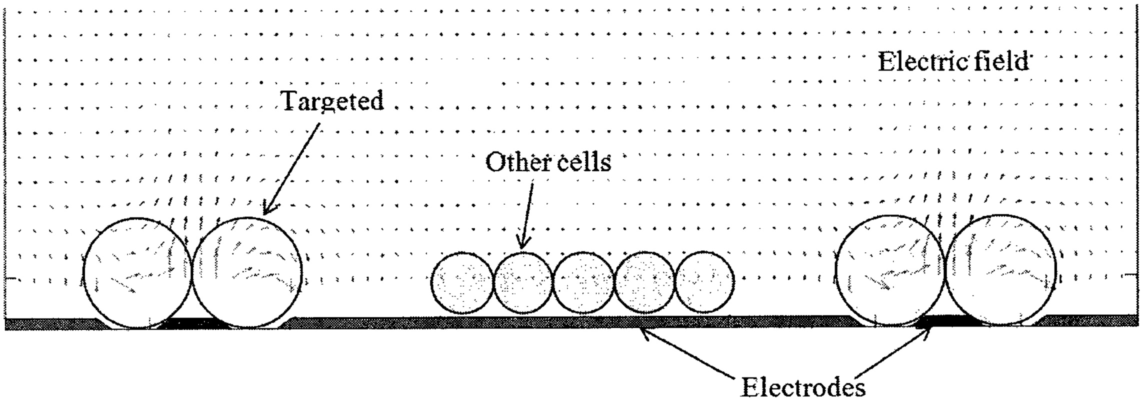

Figure 3.27: DEP migration using interdigitated electrodes.

For DEP migration process, the chamber has to be divided into two regions. One region with high electric field attracts cells that experience pDEP and low electric field region where cells under nDEP will be collected. The two regions chamber is achieved using different electrode widths. High ratio of electrodes size and small gap is the ideal design for this application. The distance between two large electrodes should be at least larger than the diameter of two cells (Figure 3.27). This implies that the summation of two gaps and one small electrode is equal at least to double the diameter of the targeted cells.

For DEP migration the width of the small electrode is suggested to be equal to the diameter of the targeted cells while gap is equal to the radius of these cells. Since the cells under nDEP will be collected around the midpoint of the large electrodes, the width of this electrode should fit all these cells. If 50 % of the large electrode is assumed to have low electric field, the width of the electrode should be at least double the diameter of the cell multiplied by number of cells on the electrode. The number of the cells on the electrodes is proportional to the ratio between the two types of cells.

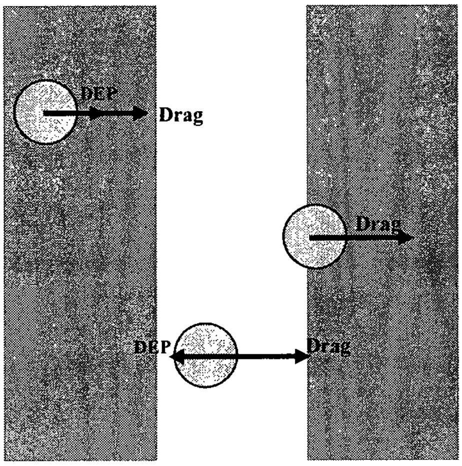

Figure 3.28: Free body diagram for the cell inside the unit segment where the electrodes are normal to the flow stream

For the second configuration where the electrodes direction is normal to the flow stream, the free body diagram is shown in Figure 3.28. When the cell is over the electrode or in the gap, the DEP effect is an attraction force toward the nearest edge, though the cell will experience high attraction force normal to the plane of the electrode when it is over the edge. The moment the cell passes the edge of the electrode it will experience a DEP force toward the edge and against the drag force. If this DEP force is greater than the drag force, cell will be trapped over the electrodes by the DEP force. Otherwise cell will continue moving with the stream. As a result, this configuration is recommended for DEP retention.

For DEP retention application the electrodes should stop the movement of the targeted cell and trap them in the separation chamber. Increasing the DEP force will increase the catching performance of the device. Minimizing the electrodes and the gap will increase the DEP force created by the device. However, the size of the electrodes and the gap should ensure enough places for the cells to settle on the edge (Figure 3.29). Equal electrodes and gap size that are equal to the targeted cell diameter is believed to be the best dimensions for this configuration.

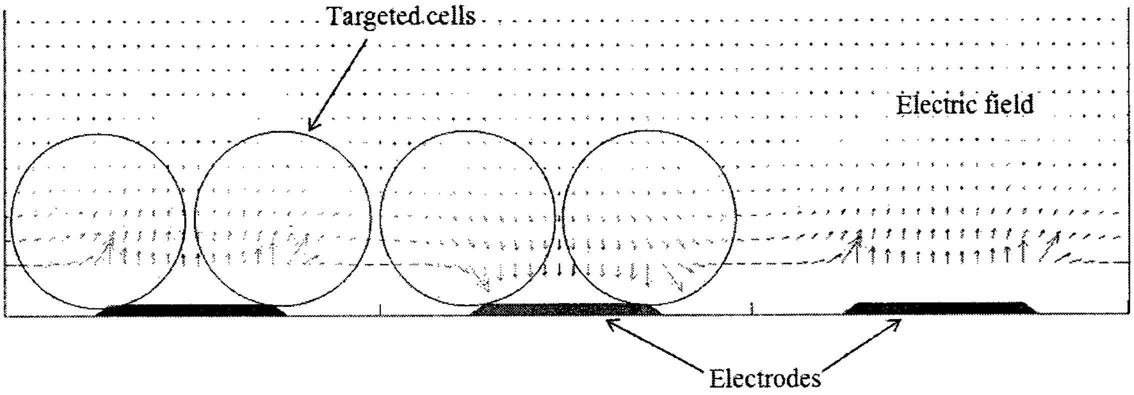

Figure 3.29 : DEP retention using interdigitated electrodes

The last configuration for the electrodes is with an angle to the flow stream (Figure 3.30). When the cell is over the electrode or in the gap, the cell will experience weak DEP force toward the closest point of the electrode edge. The resultant force from this force and the drag force will deflect the movement of the cell (Figure 3.30).

When the cell is over the edge it will experience high attraction force toward the edge and perpendicular to the plane that contains the electrodes. Due to the drag force the cell will continue moving with the stream. As the cell passes the electrode, it will experience high attraction force toward the electrodes. The resultant force from DEP force and the drag force F_R is with direction close to the direction of the electrodes (Figure 3.30 case c).

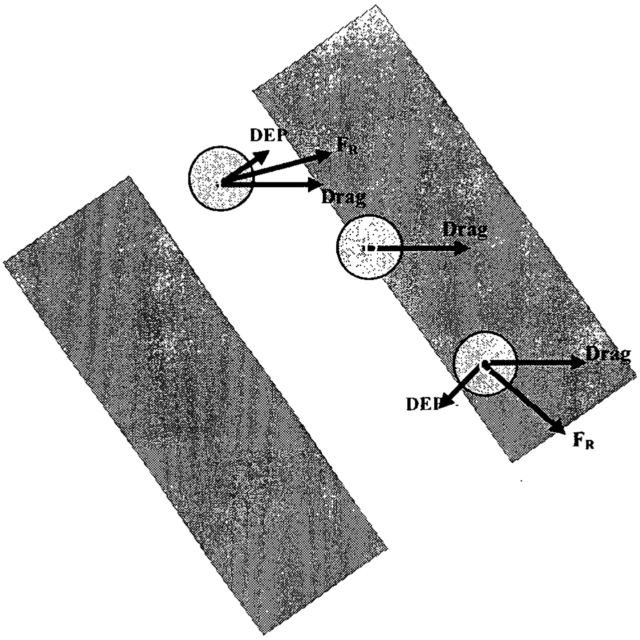

Figure 3.30: Free body diagram for the cell inside the unit segment where the electrodes are inclined with an angle to the flow stream

Increasing the DEP force will deflect the cell closer to the direction of the electrodes. DEP force is increased by decreasing the size of the electrodes and the gap. Electrodes and gap are suggested to be as small as possible to increase the DEP attraction force. This configuration is used for continuous DEP deflection separation method.

3.7. Moving dielectrophoresis

One of the most recent development of the dielectrophoretic phenomena is called moving dielectrophoresis which involves the real-time fractionation and transportation of cells achieved by sequentially energizing the electrodes present in the microchannel as shown in Figure 3.31 [87]. The mechanism involved in the energizing of the adjacent electrodes that generates the cell advancement is in this case the positive dielectrophoresis (pDEP). The entire process is illustrated in the Figure 3.31. The electrodes are placed at the bottom and at the top part of the microchannel; the bottom electrode is a single electrode covering the entire lower part of the channel while the one in the top includes a series of adjacent electrodes of length d at a gap g between them.

The work presented in this thesis seems to be the first approximate solution using Fourier series for the electrical potential, electric field and DEP force that exists in the microchannel in the case of moving dielectrophoresis applications.

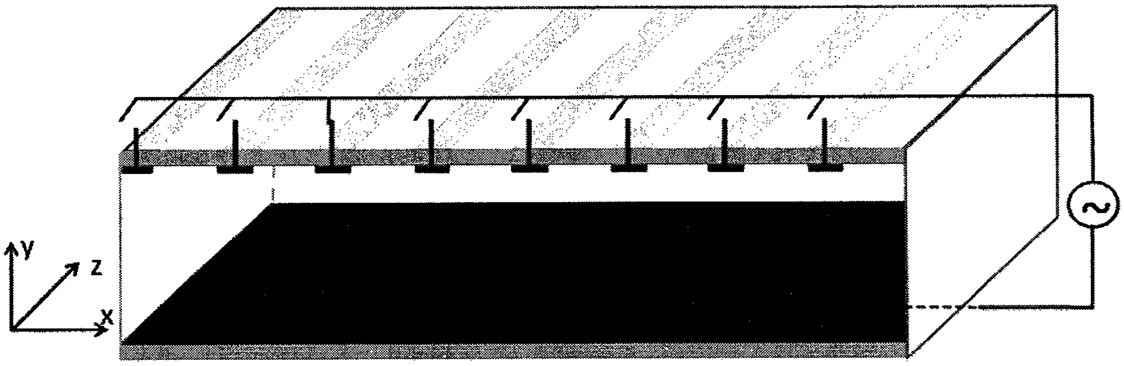

Figure 3.31: Schematic diagram showing the experimental arrangement electrodes used for moving dielectrophoretic devices. Series of finite size electrodes are patterned on the upper part of the channel and single electrode covers the bottom part of the channel.

The problem definition, boundary conditions and full solution of the present problem is found in Appendix A. However, part of the analytical formulation and results are discussed in this chapter.

Based on the nature of the boundary conditions and using the separation of variables technique, the present work assumes the solution as a superposition of two solutions that satisfy Laplace equation; linear part and a harmonic form as follows.

$$\varphi(\bar{x},\bar{y}) = A + B\bar{x} + C\bar{y} + D\bar{x}\bar{y} + F(\bar{x})G(\bar{y}) \tag{148}$$

The profile of the electric potential inside the unit segment used for the formulation was found as:

$$\varphi(\bar{x},\bar{y}) = A_0\bar{y} + \sum_{n=1}^{\infty} \frac{A_m}{\left(e^{\frac{KH}{L}} - e^{\frac{-KH}{L}}\right)} \left(\cos(n\pi\bar{x})\right) \left(e^{\frac{n\pi H}{L}\bar{y}} - e^{\frac{-n\pi H}{L}\bar{y}}\right) \tag{149}$$

The electric field is calculated as follows:

$$E(\bar{x},\bar{y}) = E_x\boldsymbol{i} + E_y\mathbf{j} \tag{150}$$

where i is the unit vector in $\bar{x}$-direction, j is the unit vector in $\bar{y}$-direction, E_x and E_y are the components of the electric field vector:

$$E_x(\bar{x},\bar{y}) = \sum_{n=1}^{\infty} \frac{A_m n\pi}{L sinh\left(\frac{n\pi H}{L}\right)} \sin(n\pi\bar{x}) sinh\left(\frac{n\pi H}{L}\bar{y}\right) \tag{151}$$

$$E_y(\bar{x},\bar{y}) = \frac{-A_0}{H} - \sum_{n=1}^{\infty} \frac{n\pi A_m}{L sinh\left(\frac{n\pi H}{L}\right)} cos(n\pi\bar{x}) cosh\left(\frac{n\pi H}{L}\bar{y}\right) \tag{152}$$

Dielectrophoretic force acting on particle or cell in the channel is given as:

$$F_{DEP} = \pi\varepsilon_0\varepsilon_{\mathrm{m}}\mathrm{r}^3\mathrm{Re}[\mathrm{f_{CM}}]\left(\xi_{DEP_x}\boldsymbol{i} + \xi_{DEP_y}\boldsymbol{j}\right) \tag{153}$$

where $\xi_{\mathrm{DEP}_\mathrm{x}}$ and $\xi_{\mathrm{DEP}_\mathrm{y}}$ are the components of $\nabla|\mathrm{E}|^2$ vector and are given as follows:

$$
\begin{aligned}
\xi_{DEP_x}(\bar{x},\bar{y}) = {} & 2\left(\sum_{n=1}^{\infty}\frac{A_m n^2\pi^2}{L^2 sinh\left(\frac{n\pi H}{L}\right)}\cos(n\pi\bar{x}) sinh\left(\frac{n\pi H}{L}\bar{y}\right)\right) \\
& \left(\sum_{n=1}^{\infty}\frac{A_m n\pi}{L sinh\left(\frac{n\pi H}{L}\right)}\sin(n\pi\bar{x}) sinh\left(\frac{n\pi H}{L}\bar{y}\right)\right) \\
& +2\left(\sum_{n=1}^{\infty}-\frac{A_m n^2\pi^2}{L^2 sinh\left(\frac{n\pi H}{L}\right)} sin(n\pi\bar{x}) cosh\left(\frac{n\pi H}{L}\bar{y}\right)\right) \\
& \left(\frac{A_0}{H}+\sum_{n=1}^{\infty}\frac{n\pi A_m}{L sinh\left(\frac{n\pi H}{L}\right)} cos(n\pi\bar{x}) cosh\left(\frac{n\pi H}{L}\bar{y}\right)\right)
\end{aligned}
\tag{154}
$$

$$
\begin{aligned}
\xi_{DEP_y}(\bar{x},\bar{y}) = {} & 2\left(\sum_{n=1}^{\infty}\frac{A_m n^2\pi^2}{L^2 sinh\left(\frac{n\pi H}{L}\right)} sin(n\pi\bar{x}) cosh\left(\frac{n\pi H}{L}\bar{y}\right)\right) \\
& \left(\sum_{n=1}^{\infty}\frac{A_m n\pi}{L sinh\left(\frac{n\pi H}{L}\right)} sin(n\pi\bar{x}) sinh\left(\frac{n\pi H}{L}\bar{y}\right)\right) \\
& +2\left(\sum_{n=1}^{\infty}\frac{A_m n^2\pi^2}{L^2 sinh\left(\frac{n\pi H}{L}\right)} sin(n\pi\bar{x}) sinh\left(\frac{n\pi H}{L}\bar{y}\right)\right) \\
& \left(\frac{A_0}{H}+\sum_{n=1}^{\infty}\frac{n\pi A_m}{L sinh\left(\frac{n\pi H}{L}\right)} cos(n\pi\bar{x}) cosh\left(\frac{n\pi H}{L}\bar{y}\right)\right)
\end{aligned}
\tag{155}
$$

3.8. Validation of the moving dielectrophoresis results

The results obtained by the method presented above are compared to those produced by a commercial FEA code and with experimental results. The results obtained using the commercial software (COMSOL) [169] are used as a reference for comparing the present solution. The analytical results show good agreement with the numerical data as illustrated in Figure 3.32.

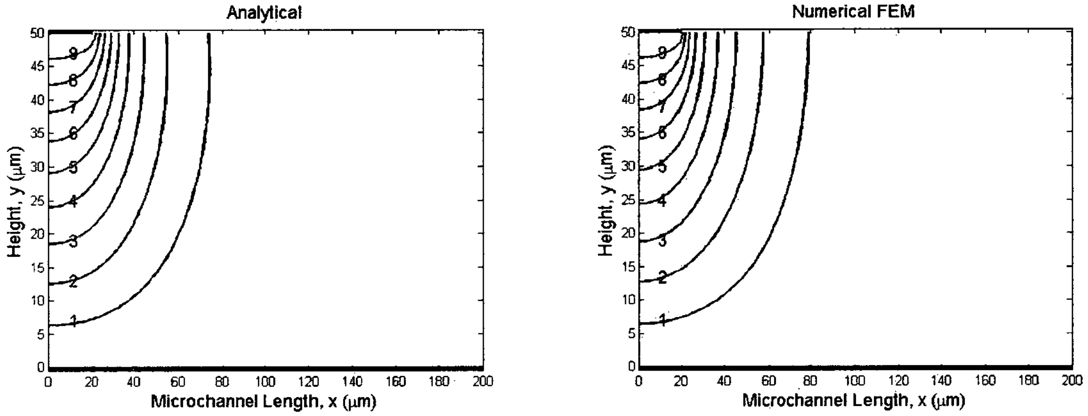

Figure 3.32: Comparison of analytical results and numerical simulations for the electric potential. Numerical simulations were obtained by finite element methods using COMSOL Multiphysics^{TM}. The contour plots of electric potential in the microchannel are shown for analytical and numerical results respectively. The thick lines at the top and bottom of the figures represent the electrodes and calculation were performed using (V_0=10 Volts, d=40μm, and H=50μm).

Contour plot of DEP force using the analytical solution is shown in Figure 3.33 a). The results show that dielectrophoretic force has a large value all around the finite size electrode and especially at its edge where it reaches its maximum on a semi circular shape. At the same time there is a second peak value for the DEP force close to the ground electrode and parallel to the force created by the finite-sized one as shown in Figure 3.33 a).

In order to see the response of the living cells to the DEP manipulation, erythrocytes cells suspended in the sucrose/dextrose low conductivity medium described in section 6.3 were injected into the test device. An AC signal of 1 MHz and 20 Volts peak to peak was applied to the electrodes. Red blood cells experienced a DEP phenomenon and gathered all around the finite size electrode with the higher density of cells at its edge. At the same time a second cluster of cells accumulates at the bottom part of the channel as shown in Figure 3.33 b). Overlapping the contour plot of the dielectrophoretic force and the experimental results in Figure 3.33 c), an excellent agreement can be observed.

The presented analytical formulations for DEP applications can be used to create path lines for the cells movement in the separation microdevice and help in design DEP such devices. This investigation aims to reach a separation of malignant cells from blood with accuracy of 100% or close to that value. The designs, simulation and fabrication of the cells separation device are discussed in the next chapter. Path lines for the cells movement were derived based on the numerical results in order to improve the separation microdevice.

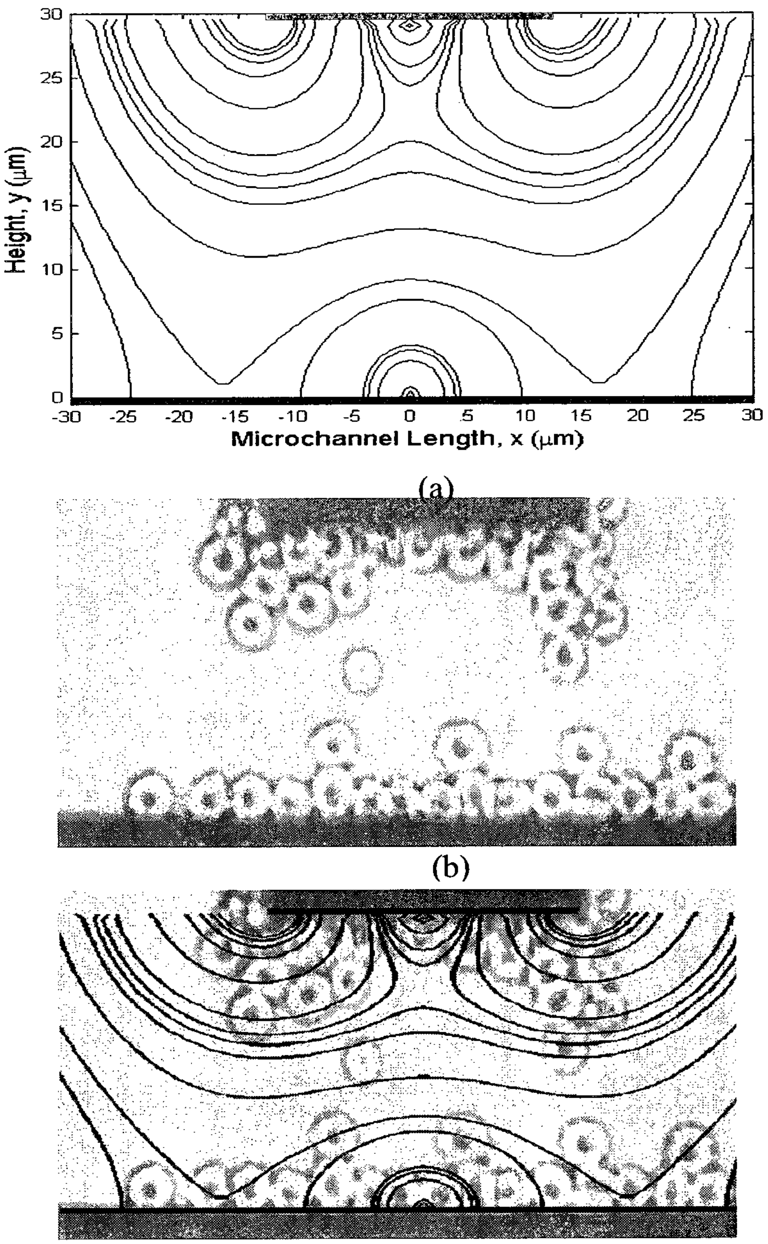

(a)

(b)

(c)

Figure 3.33: (a) Contour plot of $\nabla(E.E)$ using the determined solution (the upper finite electrode and the bottom electrode shown as thick lines); (b) Experimental results showing the behavior of red blood cell to DEP force; (c) Overlapping of the analytical solution with the experimental results.

3.9. Summary

Analytical solution for electric field and DEP over non-uniform interdigitated electrodes was presented in this chapter. Moreover, mathematical formulation for DEP force on cells for moving dielectrophoretic "traveling DEP" phenomenon was derived. Novel method to approximate the potential profile between adjacent electrodes was reported and the two presented analytical solution are based on Fourier series.

Excellent agreement was found by comparing the derived solution with numerical and experimental results. Comparing one of the present solutions with previous work shows that the derived mathematical formulation is more accurate than the previous work found in the literature. The reported DEP force expressions can be used to create models for cell movement in DEP based microdevices and represents a significant contribution towards the understanding of the DEP phenomena with application to living cell separation.

Chapter 4 : Designs, Simulation and Fabrication of the Cell Separation Device

4.1. Introduction and rationale

The main objective of the present research is to model, design, fabricate and test a microchannel device for cell separation and study the effect of the exposure to the separation electric field on the living cells. The separation is based on dielectrophoresis phenomena and it can be used for biomedical applications. Moreover, studying the effect of the dielectrophoretic separation on human living cells and investigating the change of the bio-marker in cells due to their labeling with nanotubes is also part of the present work.

Continuous feasible separation of specific line of viable cells from blood using micro-technology has not yet been achieved with 100% accuracy. The present proposed devices have been used to separate targeted cells from the whole blood sample continuously based on DEP deflecting method. The parallel configuration of the proposed separation device allows separation speed that would enable effective point of care tests.

Several microfluidic based microdevices have been designed, built and tested in order to improve the separation process. The final version of the separation microdevice is capable of separating malignant cells continuously from blood cells suspended in medium with high accuracy that is close to 100%. The small size of the microfluidic microdevice makes it possible for such system to be implemented in point of care devices.

All cell separation devices must comply specific requirements and conditions which are imposed on the practical design. Thus, the device requires an input and one or more outputs. The device needs to be fabricated from bio-compatible materials and enable sterilization. The flow cross section and the average flow speed of the fluid must be selected to satisfy the separation speed requirement. When integrated with multiple function systems, the flow as well as the power field should be integrated within the entire system.

The materials of the separation device should not alter the cells so that these cells could be used for further studies. The device should include microelectrodes layer with specific dimensions and configuration built from biocompatible material. All cells that flow through the microdevice must experience the DEP force created by the electrode layer in order to be separated. Therefore, the microdevice needs to include a microchannel above the electrodes layer with width equal to or less than the width of the electrodes layer.

DEP force above the electrodes decreases exponentially along the channel height as proved in chapter 3. The force reaches its maximum value close to the electrodes at the bottom of the channel and its minimum value at the upper part of the channel far from the electrodes layer. Thus, the height of the channel should be as small as possible in order for the cells to be affected by the DEP force. Keeping in mind the diameter of the targeted cells is around 16 μm (Table 1.1) the height of the channel has to be at least in the range of 25μm in order to prevent clogging of cells.

The separation device should have the ability to be integrated in point of care devices or other such test systems. Thus, the microdevice should be useful for several tests which require cleaning and sterilization of the system. The materials used for microchannel and electrodes should not be altered under high pressure and temperature during sterilization and as part of integrated system the device should enable fast and accurate separation. Therefore, separation of cells suspended in few milliliters of medium has to be performed within minutes.

This chapter discusses in the first sections the design, modeling and numerical simulation of the DEP force generated by the electrodes. The second part of the chapter presents the fabrication process of the separation microdevice.

4.2. Design of the electrodes layer

General schematic diagram for a design used for continuous separation of cells is shown in Figure 4.1. Electrodes with a certain configuration are positioned at a selected angle with the direction of flow of cells as illustrated in Figure 4.1.

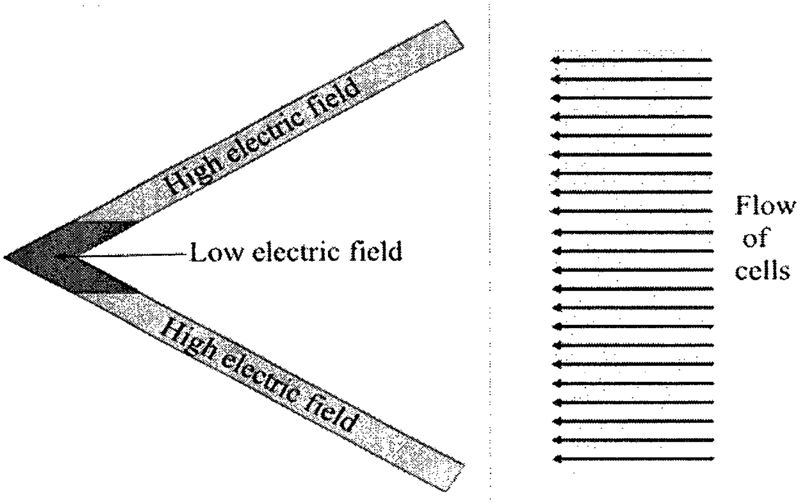

Figure 4.1: General schematic diagram of the initial design.

The electrodes layer is located on the lower side of the separation chamber due to the fabrication constrains. Cells passing over or close to the electrodes experience DEP phenomena. The applied frequency and the conductivity of medium shall ensure weak pDEP for targeted cells and nDEP for other blood cells.

The forces acting on the cells in the separation device are the buoyancy, gravitational, fluid drag and DEP force as illustrated in Figure 4.2.

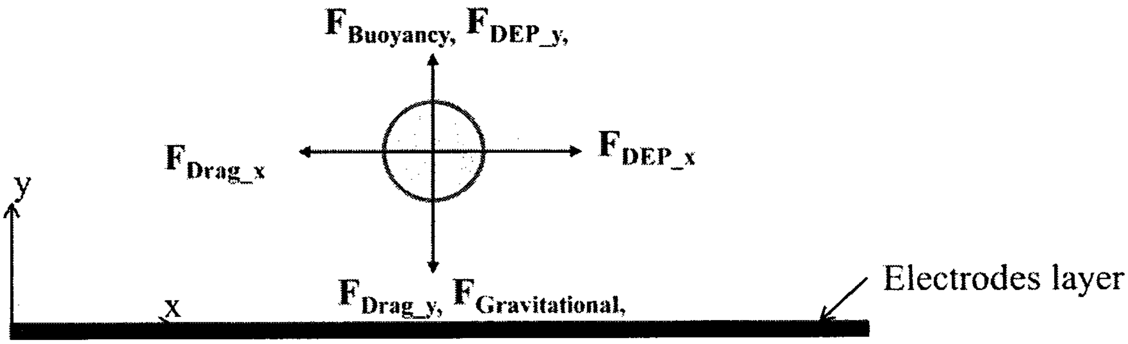

Figure 4.2: Components of forces acting on cell in the separation device.

The buoyancy, gravitational, the vertical components of DEP and drag force influence the vertical motion of cells in the microchannel. The cell movement on horizontal plane is controlled by the horizontal components of the drag and DEP forces.

The horizontal resultant force on a cell passing close to the electric field is illustrated in Figure 4.3. When the cell approaches the electrodes high nDEP force acts on the cell and influences its direction of movement. As a result, such cells move at a distance from the electric field parallel to the electrodes as shown in Figure 4.5 a. The velocity of the fluid would ensure that the resultant force acting on the cell will prevent the blood cells from passing the high electric field generated by the electrodes and those electrodes would act as a barrier to such cells.

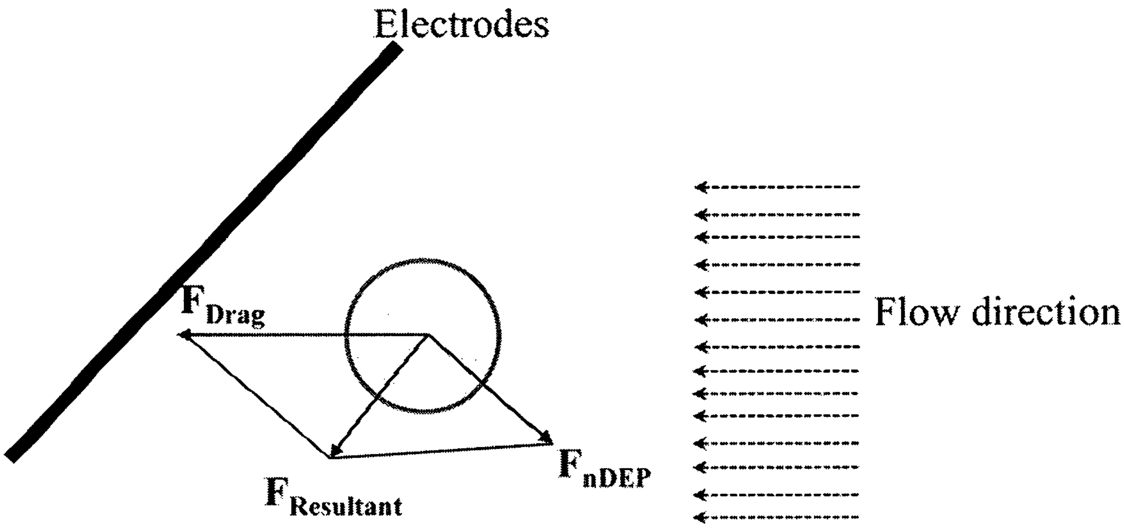

Figure 4.3: Components of forces acting on blood cell at the bottom of the separation device.

Free malignant circulating cells and larger cells in general which experience weak pDEP will have a resultant force as illustrated in Figure 4.4. The weak pDEP force generated by the electrodes has small effect on the direction of movement of targeted cells at the bottom part of the separation device.

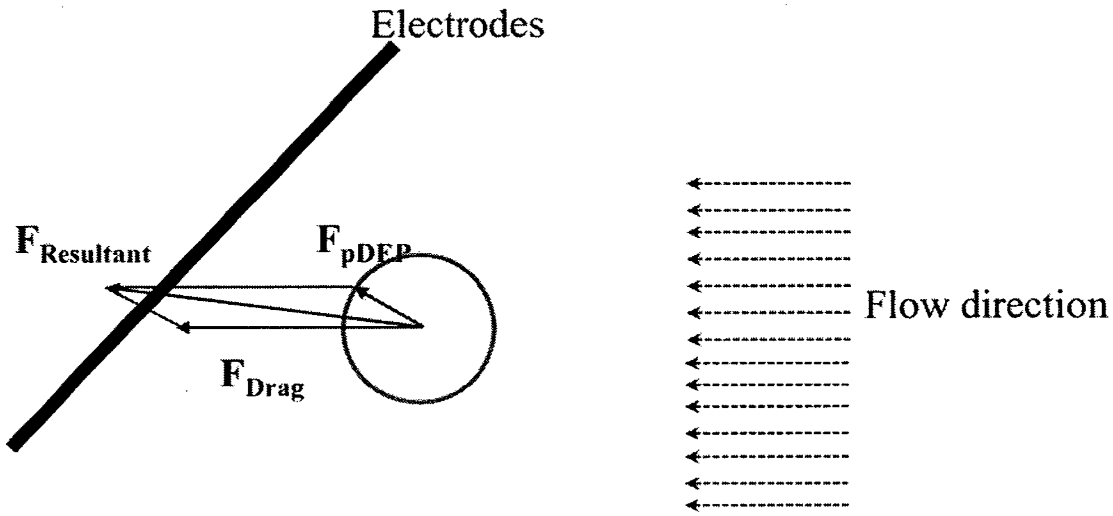

Figure 4.4: Components of forces acting on targeted cell at the bottom of the separation device

Targeted cells will pass the electric field that is created by the electrodes with insignificant deflection in their motion as illustrated in Figure 4.5 b. Such cells should experience fluid drag force that is higher than the pDEP force in order not to be captured by the high electric field. The expected movement path lines of cells under both nDEP and pDEP phenomena are shown in Figure 4.5.

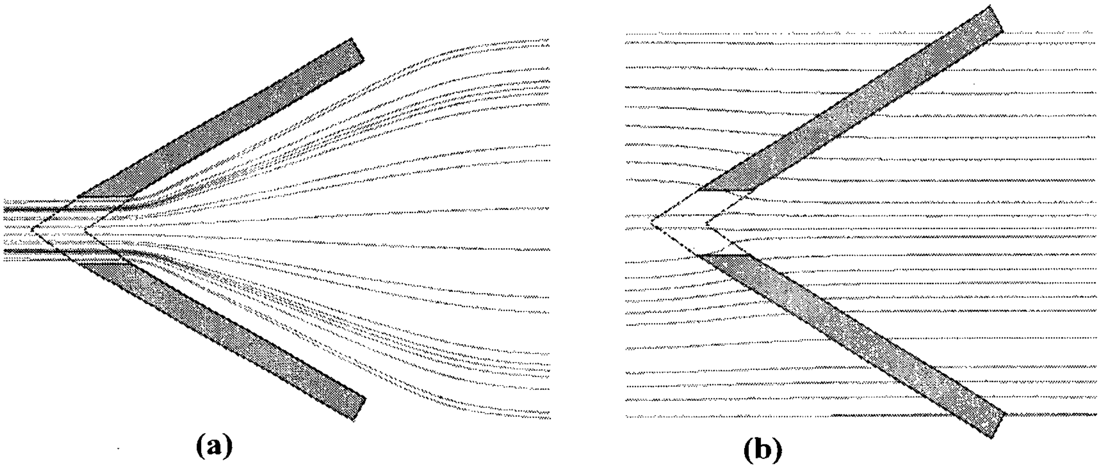

Figure 4.5: schematic diagram shows the expected path lines of cells in the separation device (a) blood cells under nDEP and (b) targeted cells under pDEP .

As an example, separation of human promyelocytic leukemia cells (HL-60) from blood in a medium with a conductivity of 10 mS/m has to be performed at frequencies theoretically ranging between 25.9-28.7 kHz (Table 1.1). This is because the cross over frequency of HL-60 cells is 25.9 kHz while it is 69.3 kHz for Erythrocytes, 47.3 kHz for Lymphocytes, 28.7 kHz for Granulocytes and 32.1 kHz for Monocytes cells. If the frequency of the applied AC potential is in the range 25.9-28.7 kHz the HL-60 cells will experience pDEP while blood cells will experience nDEP. The most favorable AC frequency is 25.9 kHz because HL-60 cells will experience the weakest pDEP possible while blood cells experience strong nDEP. Path lines of HL-60 cells in the separation device will be similar to Figure 4.5 b while blood cells which experience nDEP will follow the paths in Figure 4.5 a.

Interdigitated comb-like electrodes have been used because the phenomenon occurs at the edge of the electrodes where the electric field and charge accumulation increases. Numerical simulations show that the electric field created by interdigitated electrodes is higher than the one created by parallel straight electrodes with the same gap distance. Moreover, the simulations prove that the DEP force between the electrodes increases by decreasing the distance between the electrodes as illustrated in Figure 4.6.

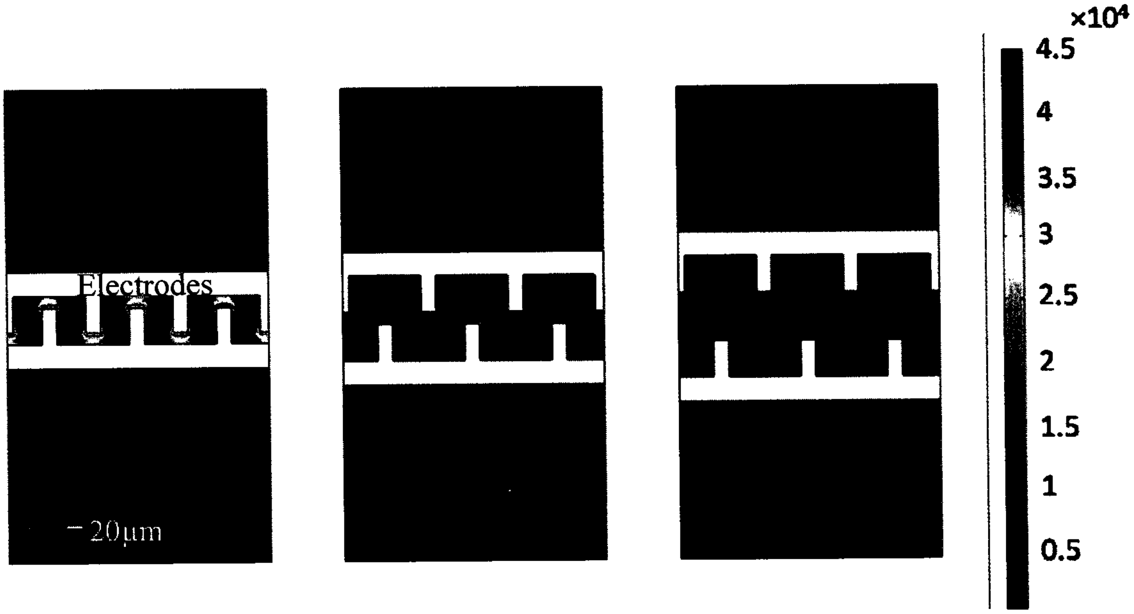

Figure 4.6: Numerical simulation for the electric field between interdigitated electrodes with different gap where values are in V/m (V=20 Volts peak-to-peak).

The distribution of the electric field between different size electrodes is demonstrated in Figure 4.7. The simulation analysis confirms that the strength of the electric field is higher between small electrodes. Therefore, interdigitated electrodes with small electrodes and small gaps have been used in the present design. Moreover, increasing the gap between adjacent electrodes creates weak electric field regions. Presence of these regions in the design may enable blood cells to pass the electrodes and not to be separated.

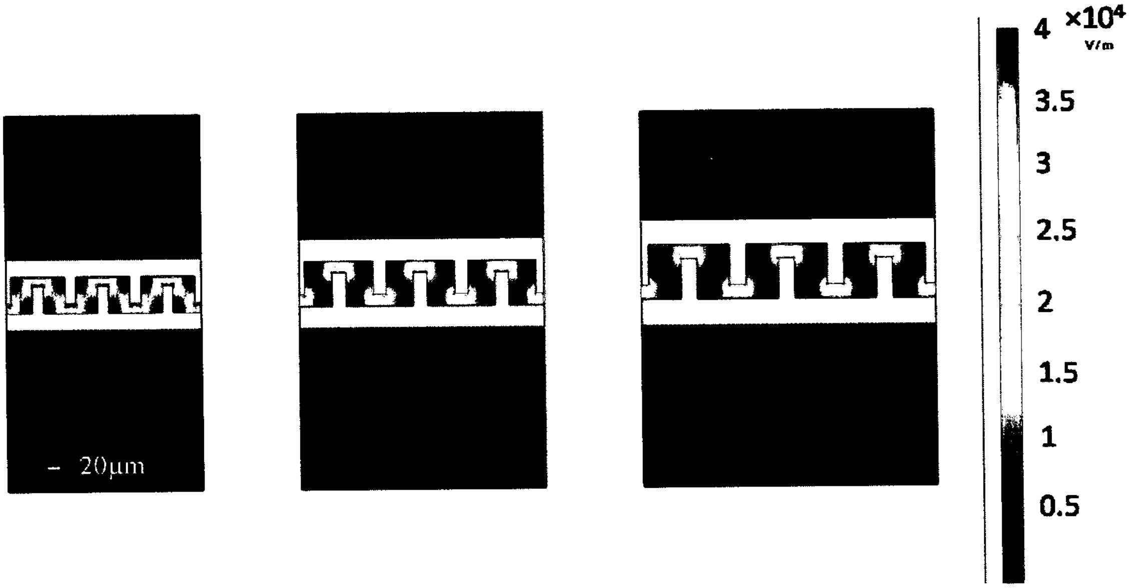

Figure 4.7: Numerical simulation for the electric field between different size interdigitated electrodes (V=20 Volts peak-to-peak).

Due to fabrication constraints the electrodes have been designed with 20µm width with a gap of 30µm. Finite element simulation of electric field between interdigitated electrodes with the selected dimensions shows that the electrodes create barrier-like DEP force as shown in Figure 4.8.

Figure 4.8: Numerical simulation for the distribution of DEP force between interdigitated electrodes (20µm electrodes, 30µm gap and 20 Volts peak-to-peak applied potential).

The pattern of the electrodes as used in the initial design is shown in Figure 4.9. In order to increase the accuracy of the separation process, parallel configuration of the design has been used as illustrated.

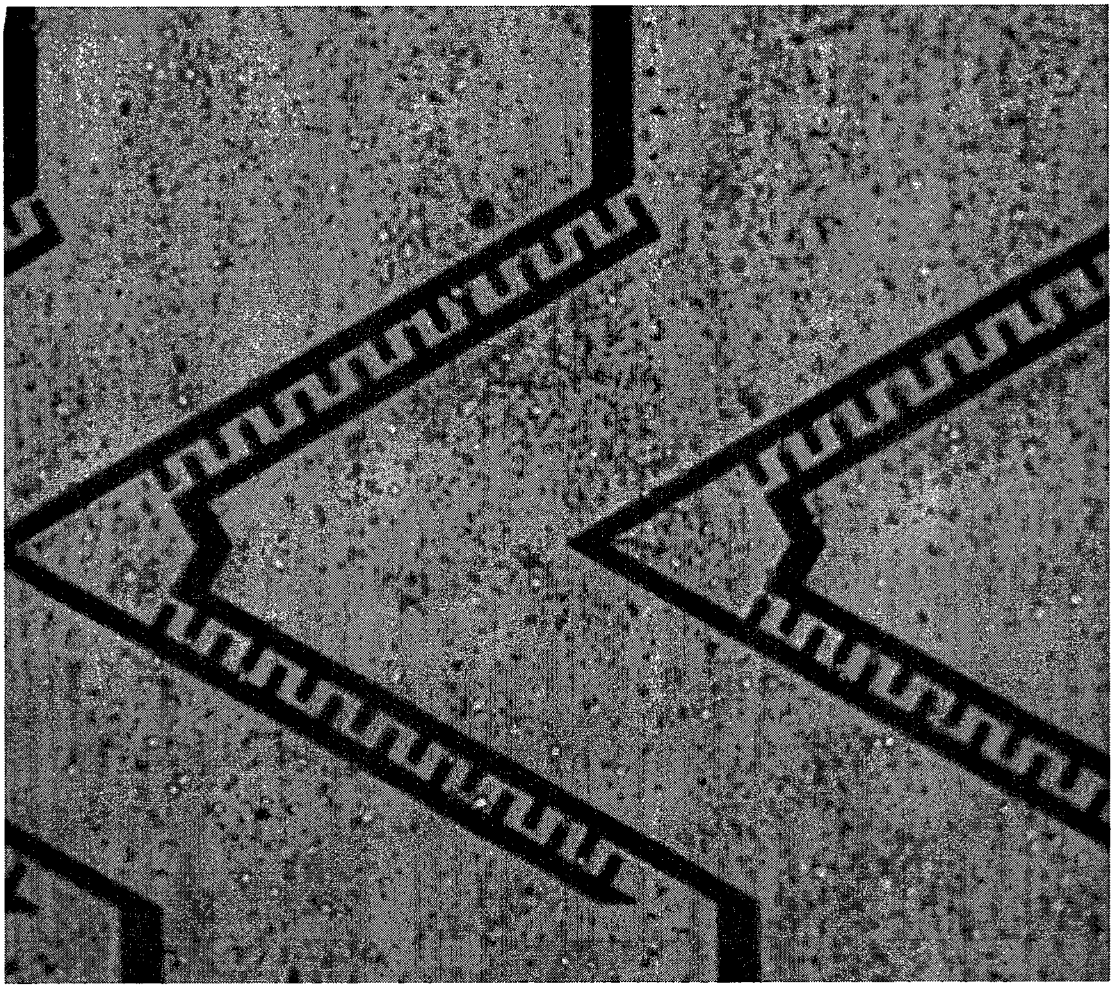

Figure 4.9: The initial design as used in the separation device showing the repeated patterns of electrodes.

The angle between the direction of the cells flow and the inclination of electrodes was taken to be 15°, 30° and 45° in order to study effect of the inclination of electrodes on the separation process. The experimental results confirmed the expected results obtained from simulations. Separation of malignant cells MDA231 from blood is shown in Figure 4.10. The blood cells experienced nDEP and then deflected their direction of movement to flow with the electrodes direction. MDA231 cells experienced pDEP and crossed the electrodes without deflecting their direction of movement as the blood cells did (Figure 4.10).

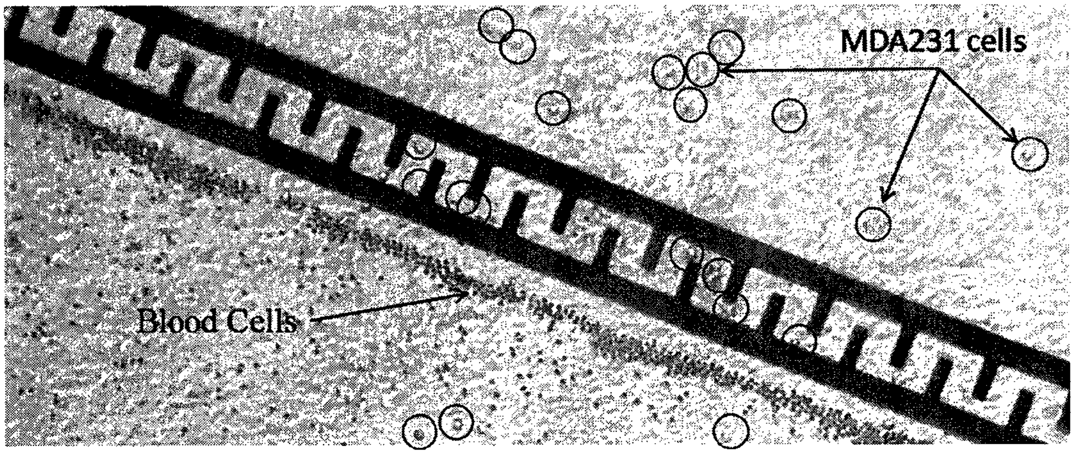

Figure 4.10: Separation of MDA231 cells from blood cells experimentally using the preliminary design of separation device

The initial design has been successfully used to separate targeted cells from blood sample but not close to 100% which this research is targeting.

The resolution issue is quite sensitive and the expected number of free malignant circulating cells in 1 cm^3 of blood specimen could range from 5 to 20,000 cells. The low count is associated with a low probability of existence of seeds of malignant cells colonies which might flow to tumors. However, the count is extremely important in patients who went through chemo-therapy as cells count will be very much related to the prognostics of the evaluation of the illness in the patient. Thus, the target for any practical device is to separate at a resolution of 100% or close to that value.

The malignant cells pass from the mid part of the device and continue their movement along with the blood cells which have not been held by the electric field. Targeted cells passing the mid part of the device are shown in Figure 4.11. The reason for the targeted cells not deflecting from their movement is the weak electric field at that part of the electrodes and the high drag force which acts on the cells due to the fluid speed. Thus, this problem can be solved by decreasing the speed of flow or by modifying the electrode pattern. This investigation aims to reach a separation speed that enables point of care tests. Therefore, reducing the speed of the flow may not to be feasible solution. An improvement to the design has to be made to prevent the targeted cells from flowing with blood cells at the mid part of the design.

The three different angles of inclination of the initial design have been experimentally studied. Results show that lower fluid speed is required as the inclination angle of the electrodes increases in order to reach the desired separation accuracy.

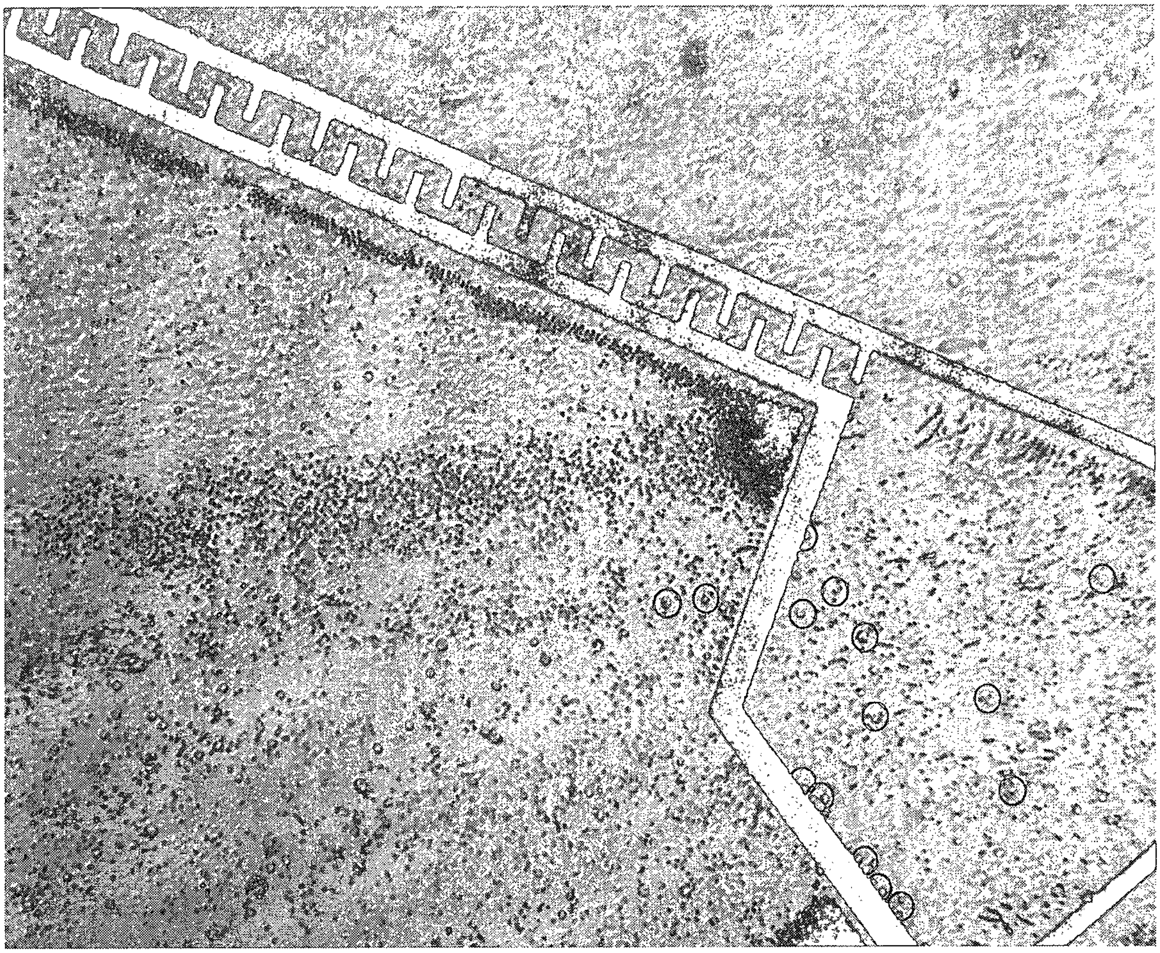

Figure 4.11: Separation of MDA231 cells from blood showing the MDA231 cells (in circles) passing the mid part of the separation device

The second pattern of the electrodes contains two parts as shown in Figure 4.12. Low frequency AC potential is applied on part 1 of the electrodes to ensure nDEP response for both malignant and blood cells. Both cell lines deflect their direction of movement to move close to the electrode as they pass close to part 1 of the electrodes as shown in Figure 4.13.

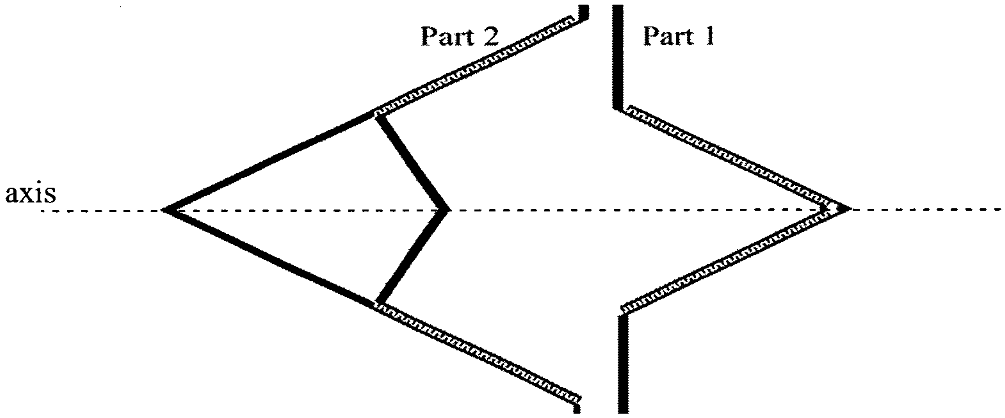

Figure 4.12: Schematic diagram for the second design configuration of electrodes used for continuous separation of cells.

The frequency of the applied AC potential on the electrodes on part 2 of the design ensures nDEP for the blood cells and weak pDEP for the targeted cells. Therefore, movement of targeted cells will not be affected by the configuration of part 2 of the electrodes design while blood cells will deflect their direction of movement to flow close to the axis of the design where the electric field is minimal. The flow path lines for blood cells (a) and the targeted cells (b) are shown in Figure 4.13.

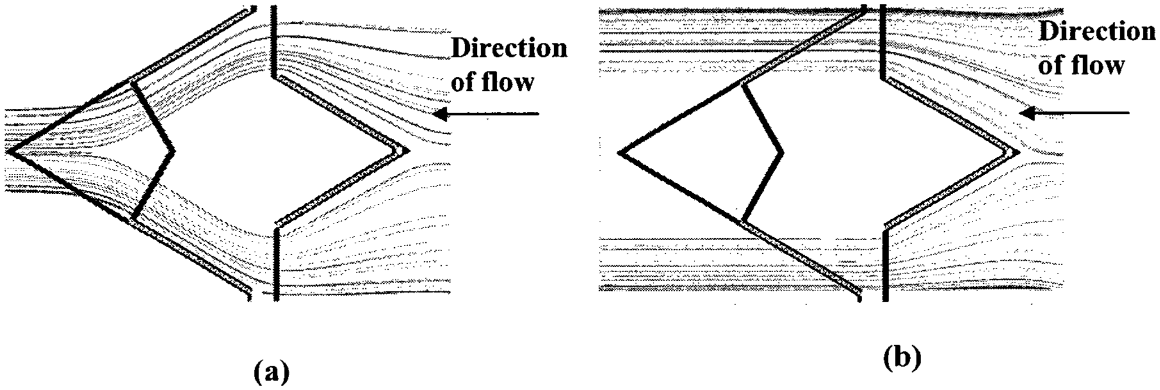

Figure 4.13: Schematic diagram shows the expected path lines of cells in the second design. (a) for blood cells and (b) for targeted malignant cells.

Using the second pattern of the electrodes in the separation device improved the separation process as will be further discussed in chapter 6. The targeted malignant cells in the second design pass the first part of the electrodes which deflect the cells movement due to presence of nDEP. Including part one of the second design has the objective of preventing the targeted cells from flowing in the mid part of the second part and therefore to be separated. The accuracy of the separation process reached close to 100% at low speeds but there might be a possibility to increase the separation speed by modifying the configuration of part 2 of the second design.

The exact estimate of the accuracy of the separation is difficult to be evaluated as the mix of the targeted cells and blood cells is carried out based on statistical estimates. The direct observation is mostly used to evaluate if targeted cells which are large in size are following the flow of the blood cells. When they are not observed, the estimation of the separation rate of 100% seems reasonable.

Existence of the electrodes in the mid portion of the part two creates weak electric field. This electric field causes the blood cells to accumulate at the corner of the mid part as shown in Figure 4.14. Reduction of the electric field in this part of the design might speed up the flow of the blood cells. Therefore, a modification of the design was performed.

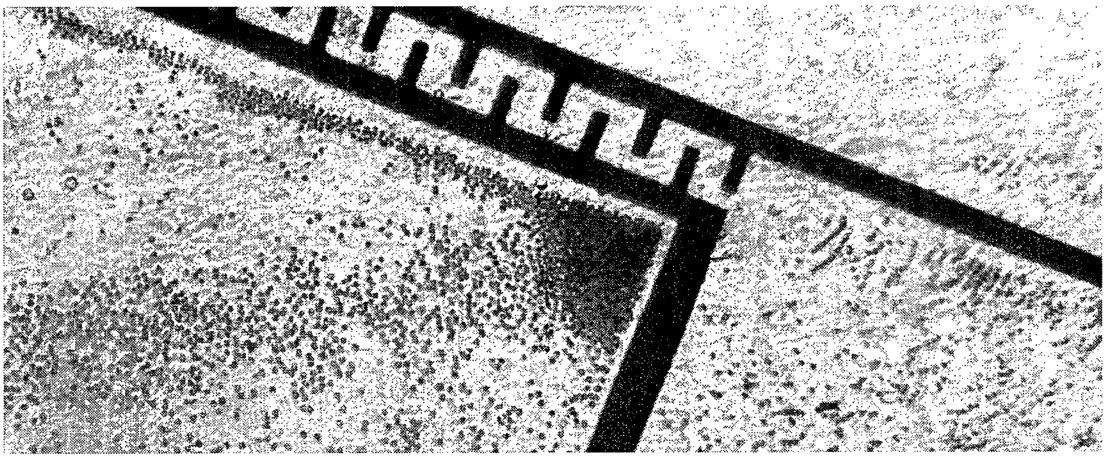

Figure 4.14: Separation of MDA231 cells from blood showing the accumulation of blood cells at the corner of the electrodes.

In the improved version of the second design the electrodes in mid part 2 of the design at the location where the blood cells pass have been removed as illustrated in Figure 4.15. Absence of any electrodes in the path line of blood cells eliminates any DEP forces on the cells' path. This enhances the separation process and the movement of cells in that specific portion of the design and the separation process could perform faster. The effect of the modification in the second design is discussed in details in chapter 6.

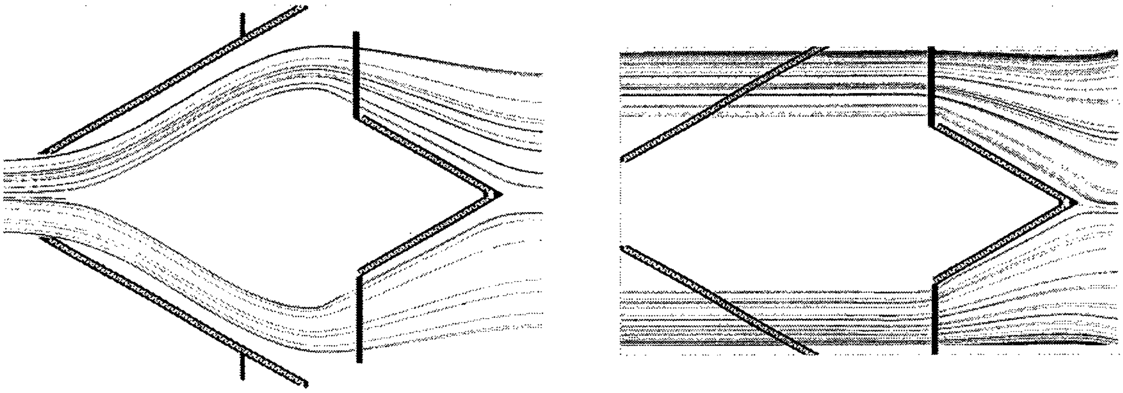

Figure 4.15: Schematic diagram shows the expected path lines of cells in the improved version of design 2.

Study of the effect of DEP manipulation on living cells represents one of the objectives of the present work. Several patterns of electrodes have been designed to investigate DEP manipulation on cells including parallel electrodes, castellated electrodes and interdigitated electrodes as illustrated in Figure 4.16.

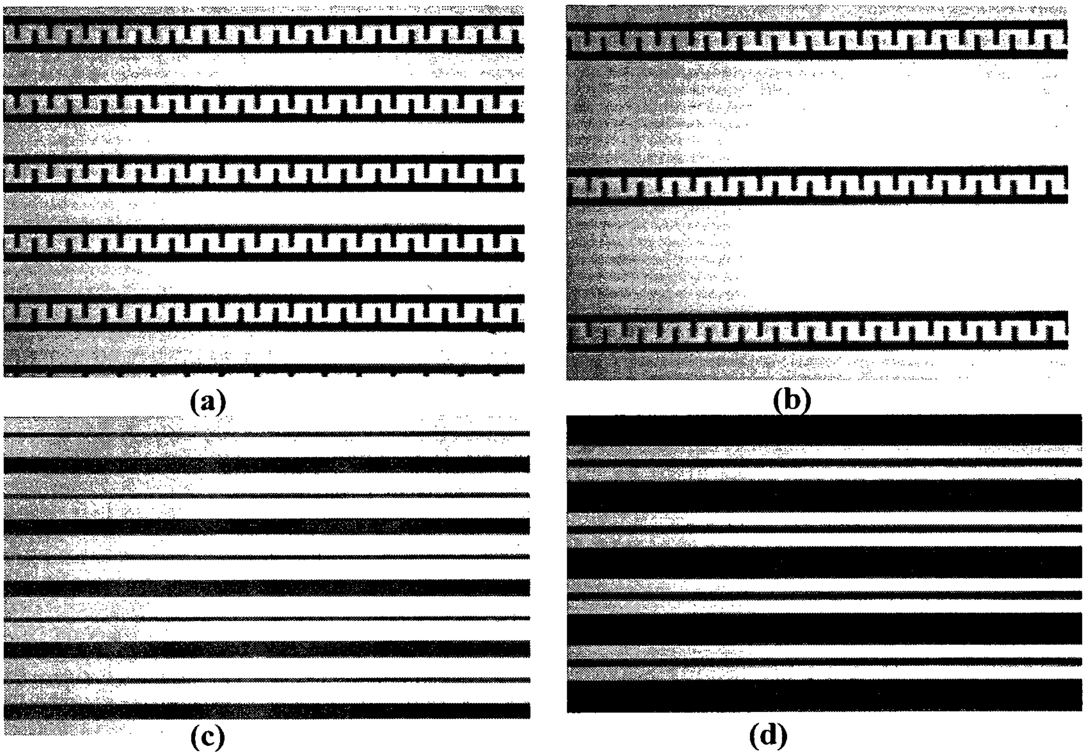

Figure 4.16: Different patterns of electrodes that have been used in studying the effect of DEP manipulation. (a) Interdigitated comb-like electrodes for pDEP manipulation, (b) Interdigitated comb-like electrodes for nDEP manipulation, (c) and (d) Parallel interdigitated straight electrodes.

The sizes of the gap and electrodes have been varied in the designs between 20μm and 200μm in order to study both effects pDEP and nDEP on cells. The 200μm has been chosen to be the maximum gap in order to have all the cells affected by the DEP manipulation. The effects of single-wall carbon nanotubes on the electrical properties of cells as a change in their membrane capacitance have been studied using the same designs as shown in Figure 4.16. These findings are discussed in detail in chapter 5.

4.3. Numerical simulation for the DEP force

The dielectrophoretic force exerted on a living cell under non-uniform electric field and immersed in a medium is given by equation (19) in chapter 3 as:

$$\boldsymbol{F}_{DEP} = \pi\varepsilon_0\varepsilon_m r^3 Re[f_{CM}]\nabla|\boldsymbol{E}|^2 \tag{156}$$

where ε_0 is the vacuum dielectric constant, ε_m is the suspending medium dielectric constant, r is the particle radius, $Re[f_{CM}]$ is the real part of Clausius-Mossotti factor and E represents the peak electric field. $\nabla|E|^2$ is the only term of DEP force expression that is affected by the electrode size and configuration. Distribution and intensity of the gradient of electric field squared ($\nabla|\boldsymbol{E}|^2$) influences the attraction and repulsion of cells toward electric field due to DEP phenomena. Numerical simulations show that the size of the electrodes and gap affect the distribution and strength of electric field. Different configuration and sizes of electrodes are required for different applications. Continuous separation devices require small size electrodes and gap in order to create higher strength electric field. Therefore, in the present work, small electrodes and gaps in the range of 20μm are used to deflect the cells to the desired direction in the separation device.

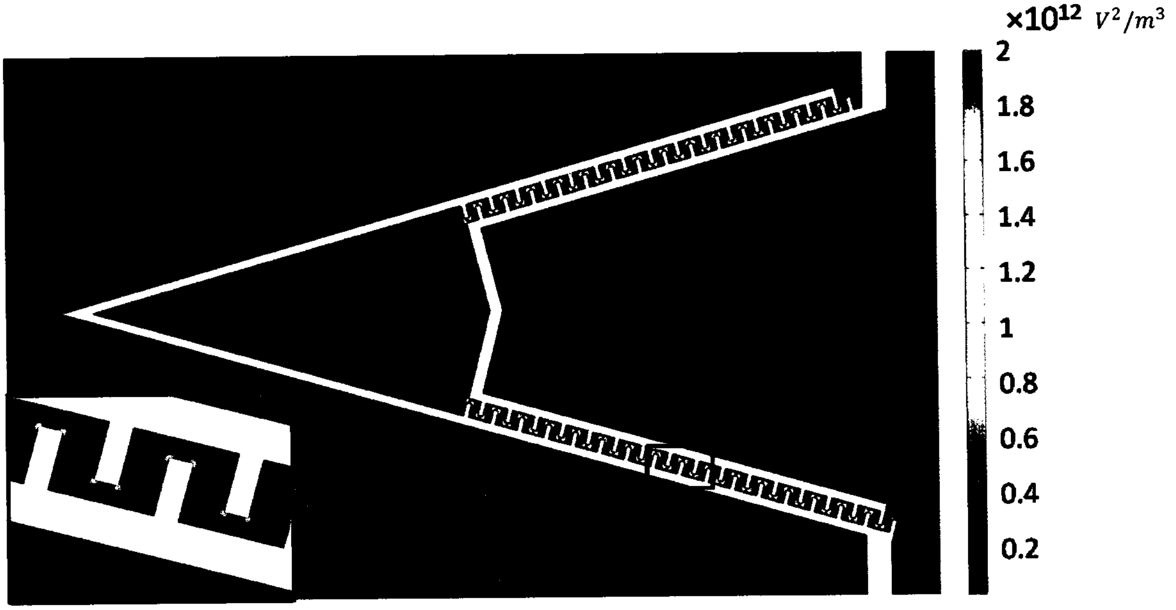

Figure 4.17: Numerical simulation using COMSOL for the first design shows the distribution and strength of ∇(E.E) (20 volts peak-peak)

COMSOL multiphysics and MATLAB software were used in the formulation of the numerical simulation. The finite element analysis of the gradient of the squared electric field distribution and the intensity found for the initial design and is shown in Figure 4.17. The angle between the direction of the cell flow and the electrode inclination was selected as 15°.

The numerical simulations further show similarity in the distribution and strength of electric field for different inclination angles of the electrodes in the initial design. $\nabla|\boldsymbol{E}|^2$ distribution for the first design is illustrated in Figure 4.18. The angle of inclination of the electrodes was further selected as 30° and 45°, respectively. The sizes of electrodes and gap are assumed to be the same for all analyzed versions of the initial design. The inclination angle of the electrodes affects the distribution of DEP force in the separation device. The electrode patterns create barrier-like electric field making the same angle as the electrodes.

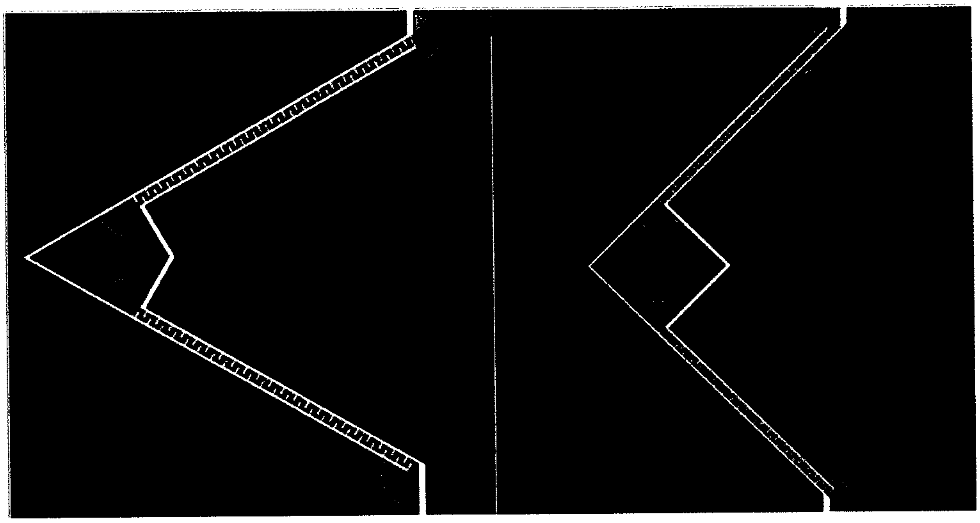

Figure 4.18: Numerical simulation of the first design shows the distribution of DEP force (inclination of electrodes are 30° and 45° respectively). Red color where ∇(E.E) is greater than 10^8 V^2/m^3 and blue color otherwise where DEP force is weak.

Blood cells that flow close to the electric field experience strong repulsion nDEP force in the direction shown in Figure 4.19. The fluid drag force acts on the cell against the direction of the fluid flow. Blood cell will pass the electric field if the force component $F_{Drag}\,sin(\theta)$ is higher than the nDEP force created by the electrodes where θ is the inclination angle of the electrodes.

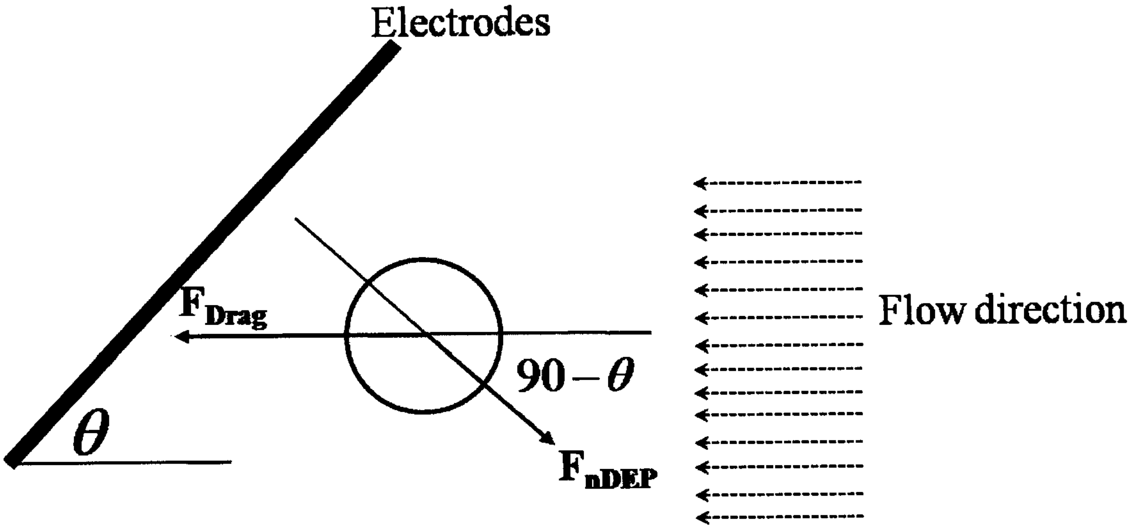

Figure 4.19: Schematic diagram shows the forces act on the blood cell as it flow close to the electrodes.

For spherical cell moving in a viscous medium the fluid drag force acting on the cell is given as:

$$\boldsymbol{F}_{Drag} = 6\pi\mu_f rK^*v \tag{157}$$

where μ_f is the fluid viscosity, r is the cell radius, K^* is a correction factor for the fluid drag force and v is the cell velocity [170, 171]. The maximum speed that the blood cells can have in order not to pass the electrodes at the limit drag is equal to nDEP:

$$F_{Drag}\, sin(\theta) = nDEP \tag{158}$$

Equation (158) can be written as:

$$6\pi\mu_f rK^*vsin(\theta) = nDEP \tag{159}$$

Solving equation (159) for v yields:

$$v = \frac{nDEP}{6\pi\mu_f rK^*sin(\theta)} \tag{160}$$

Equation (160) proves the effect of the inclination of the electrodes on the speed of the separation process. The higher the inclination angle, slower is the separation speed required to stop blood cells not to pass the electrodes.

Numerical simulation of the electric field for the second design is shown in Figure 4.20. Results confirm that the modified version of the second design has lower DEP force along the path of blood cells. Removal of the electrodes from the path of blood cell in the modified design version enhances the speed of the separation process. This has been confirmed experimentally and further discussed in chapter 6.

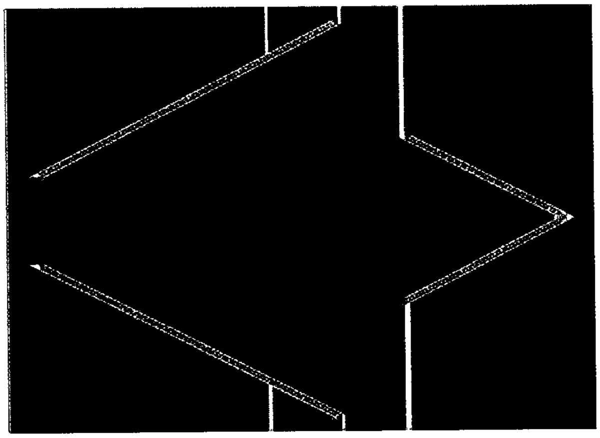

Figure 4.20: Numerical simulation shows the distribution of DEP force for the second electrodes pattern. Red color where ∇(E.E) is greater than 10^8 V^2/m^3 and blue color otherwise where DEP force is weak.

Different configurations of electrodes have been designed to investigate the effects of DEP manipulation on living cells. Same designs have been used to study the effect of single-wall carbon nanotubes on cells. The different patterns of electrodes have been designed keeping in mind that the sizes of gap and electrodes should ensure enough space for all cells to be affected by the DEP force. Therefore, the microdevice should have enough area of high-field such that all targeted cells should experience pDEP and enough area of low-field for the cells which experience nDEP to gather in.

Interdigitated electrodes which consist of two staggered comb-like electrode structures have been used to study the effect of DEP manipulation. This type of configuration offers the desired distribution of electric field to observe both the pDEP and nDEP phenomena. The distribution of $\nabla|\boldsymbol{E}|^2$ generated by the applied potential through the electrodes is shown in Figure 4.21.

The calculated crossover frequency of cell line MDA231 suspended in a medium of 10 mS/m is found to be around 10 KHz (Table 1.1). Positive DEP phenomenon is expected if the applied AC signal is about 50 KHz. Numerical simulation shows that high values of $\nabla|E|^2$ exist at the tips of the electrodes as illustrated in Figure 4.21. Experimental results of the accumulation of cells at the tip of the electrodes is shown in Figure 4.22 a).

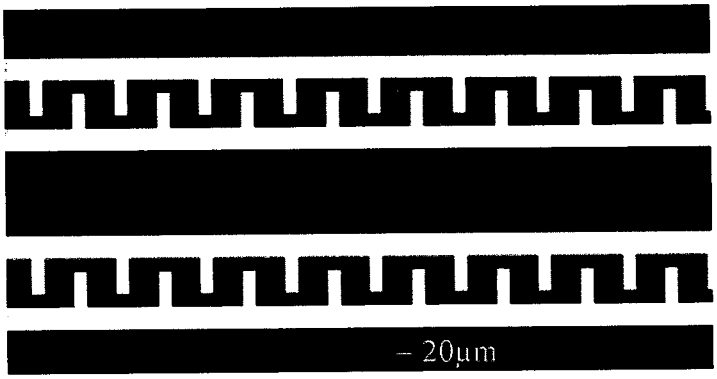

Figure 4.21: Distribution of strong (red) and weak (blue) DEP force using comb-like interdigitated electrodes.

The calculated crossover frequency of RBC suspended in a medium of conductivity 10 mS/m is around 69 KHz while the crossover frequencies of blood white cells are greater than 28 KHz (Table 1.1). Blood cells suspended in a medium of 10 mS/m and under 5 KHz, 20 volts peak-peak AC potential is expected to experience nDEP response. Based on the finite element simulation (Figure 4.21), cell will accumulate in the low field (blue) area where the gradient of the term $|E|^2$ is minimal. Figure 4.22 b) illustrates the experimental results showing the response of the blood cells under 5 KHz, 20 volts peak-to-peak AC potential.

The response of blood cells and MDA231 cells under 40 KHz, 20 volts peak-to-peak AC potential is shown in Figure 4.22 c). Blood cells experienced nDEP and accumulated between the electrodes where the electric field is minimal. MDA231 cells experienced pDEP at this frequency and gathered at the tips of the electrodes. Small circles are used to indicate the location of MDA231 cells.

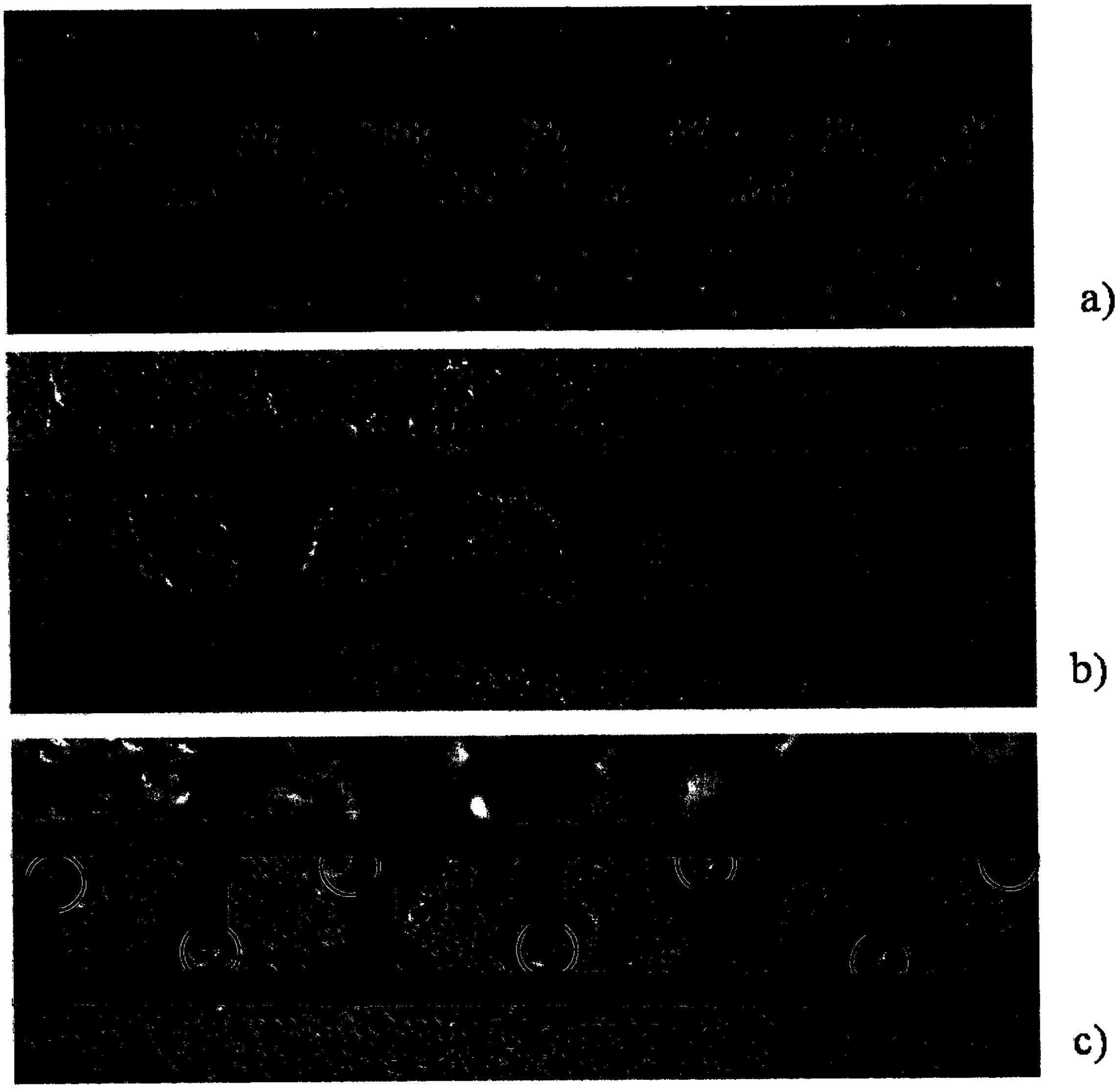

Figure 4.22: Experimental results show the response of blood and MDA231 cells to DEP phenomena. (a) MDA231 cells experience pDEP (b) Blood cells experience nDEP (c) Blood cells experience nDEP and MDA231 at the tip of the electrodes because of the pDEP phenomenon.

4.4. Fabrication of the chip

The separation microdevice consists of two main parts, upper part from PolyDiMethylSilooxane (PDMS) fabricated in the laboratory and lower part from glass as shown in Figure 4.23. Soda lime glass and quartz have been used as substrates. Soda lime glass is the most common commercial glass that is a mixture of silica, soda, and lime. Different patterns of electrodes were designed using AutoCAD and printed as photo-masks using high resolution printers (resolution 50,800 dpi) by a commercial supplier (Fineline Imaging, Colorado Springs, CO). The thickness of the deposited electrodes is 5800Å and the size of the glass substrate is up to 7”×7”.

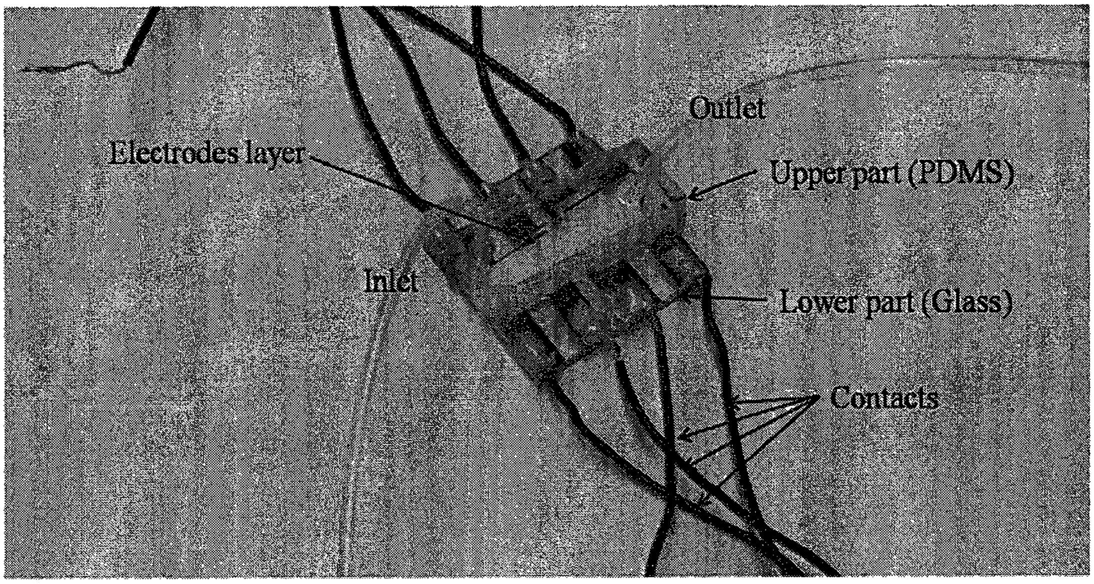

Figure 4.23: Separation device showing the PDMS upper part and the glass made substrate

The upper part of the separation device contains the microchannel which is made from PDMS following the normal procedure as shown in Figure 4.24. Sylgard 184 pre-polymer and curing agent are mixed with weight-ratio 10:1. Then the mixture is poured in the mold and degasified. After removing all the bubbles from the mixture by degasifying, the mixture is cured in an oven at 80°C for two hours. Finally after curing, the PDMS microchannel is peeled off from the mold.

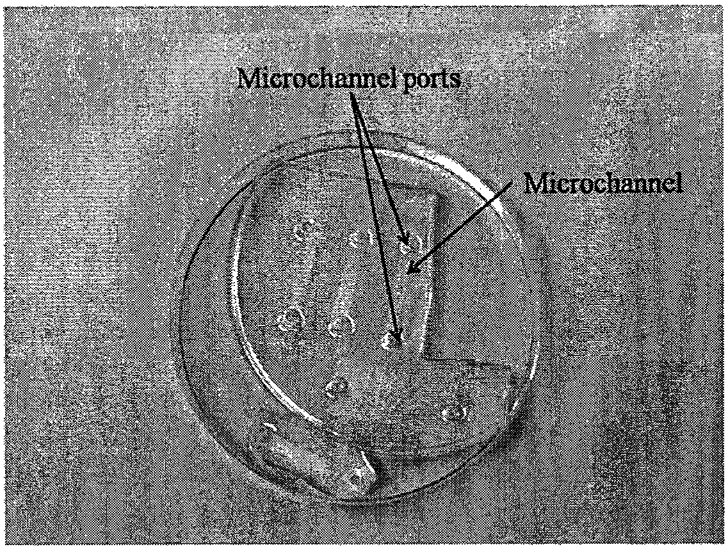

Figure 4.24: PDMS made microchannels

Molds have been built in the laboratory using the available facilities and material. Several attempts to create the PDMS molds have failed because of the non-compatibility between the materials used in the mold and PDMS. Smooth surface microchannels have been successfully built using 30μm thickness tape. The profile of the microchannel was made by cutting the tape to the desired shape (Figure 4.25).

0.2-10 μl pipette tips have been attached to the end of the microchannel mold to create the inlet and outlet of the blood sample. 0.25 mm internal diameter plastic tubes have been attached to the PDMS microchannel to form the inlet and outlet of the microchannel. PDMS was glued to the glass substrate using silicon based adhesive.

A simple device has been assembled to study the DEP manipulation on cells. The device consists of a small reservoir made out of glass, glass cover and a glass substrate where the electrodes are deposited (Figure 4.26).

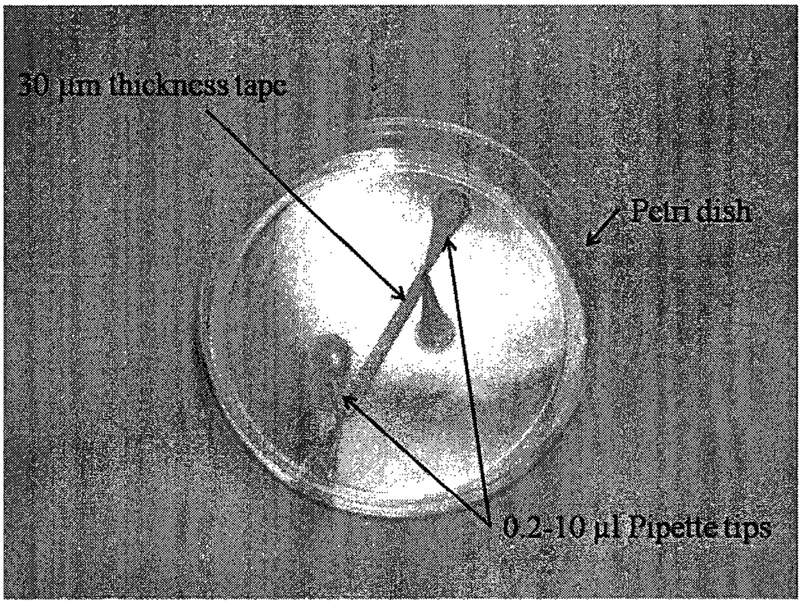

Figure 4.25: Mold fabrication for upper part PDMS microchannel.

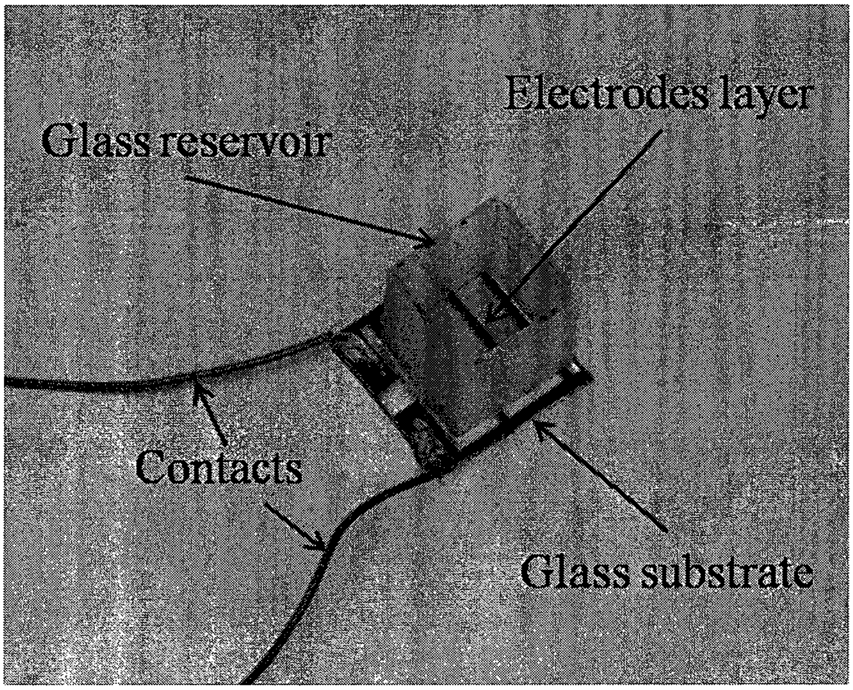

Figure 4.26: The device which used for DEP manipulation

This investigation has also been directed towards searching ways through which the separation speed could be enhanced. One possibility was seen as treating cells with Carbon Nano-Tubes (CNT). The modification in the electrical properties of the cells might enhance the capability of targeted cells to align with the high intensity electric field. However, such an approach would raise the problem of bio-compatibility of the CNTs with the living cells. This aspect is investigated in the next chapter.

4.5. Summary

This chapter discussed the design and fabrication of living cell separation device based on DEP phenomena. A novel microfluidic device for continuous separation is presented. Separation of cells is performed using DEP phenomena. The numerical analysis of the design has been validated by experimental investigations. The separation of malignant cells using the proposed device reached close to 100 % accuracy with a flow rate 0.1 mL/hr for a single device. Malignant cells MDA231 have been successfully separated from blood cells using the proposed device with the desired accuracy. The small size of the microdevice makes it possible to stack several devices in a single chip. Microchip with stacked devices is suggested to reach the desired volume flow rate for point-of-care tests.

Several test devices have been fabricated in the laboratory to investigate the effect of the DEP manipulation on living cells. Electrode layers have been deposited using high resolution printer for mask fabrication from a commercial source. Other parts of the device have been manufactured in the laboratory using the available instruments and materials.

Chapter 5 : The Effects of Carbon Nanotubes on Living Cells

5.1. Introduction

Carbon nanotubes (CNTs) offer exciting opportunities for science research and clinical applications. In recent years, CNTs research has been established as a highly interdisciplinary field to exploit their outstanding features. CNTs are believed to have a promising future in a variety of possible applications because of their unique physical properties [172]. Individual carbon nanotubes have tubular shapes that are few micrometers in length with a diameter close to one nanometer. They are categorized based on the number of graphite layers in single-walled carbon nanotubes (SWCNT) and multi-walled carbon nanotubes (MWCNT) [173].

Carbon nanotubes are regarded as non immunogenic and biocompatible materials which make them ideal for relevant biological and pharmacological studies. Using them for medical purposes can be an important key towards an early diagnostics and treatment of several ailments. These tiny fullerene structures are known to have unique propertiesin view of their high surface area compared to their size and the nanoscale hollow cavity. The CNT cavity has added advantage of being potential nanofluidic devices to deliver organic and inorganic material to cells such as drug [174], siRNA [175, 176] and proteins [177].

Recently there is a trend towards using carbon nanotubes for cancer diagnostics and treatment [173]. Single-wall and multi-wall nanotubes were used for sensing cancer cells in serum and tissues. Human prostate cancer cells impedance was measured using multi-wall nanotubes embedded in a polydimethylsiloxane (PDMS) channel [178]. Single-wall nanotubes with a multi-label secondary antibody-nanotube bioconjugates were combined to form an electrochemical sensor to detect the protein cancer biomarker [179].

Several techniques have been proposed and performed in order to selectively destroy the cancer cells. These include treatment of cells with carbon nanotubes and exposing them to radiofrequency field [180], laser at specific light intensities [181] and near-infrared light [182].

Toxicity of the carbon nanotubes on living organisms is not yet fully determined. They were found to be toxic in trials made in vivo, on the rat and mouse lung, and also in vitro [183, 184] which strongly supports their toxicity for human respiratory system. However, the small size, large surface area, and high reactivity of these materials are the main factors for potential toxicity [185]. Moreover, CNTs will have wide-spread applications in many technological fields, and hence worker/consumer exposure is likely to occur, posing emerging health concerns [185, 186]. Initial toxicological studies demonstrated that pulmonary deposition of SWCNT or multi-wall carbon nanotubes (MWCNT) causes acute pulmonary inflammation as well as chronic responses such as fibrosis [183, 184, 187-190] . These studies suggest that CNTs may induce toxicity in normal bronchial epithelial cells. However, how CNTs provoke susceptibility to the toxicity and pulmonary inflammation is not clear. Thus, genome-wide monitoring of gene expression is important to understand the extent of CNTs effect [186].

This chapter discusses the effect of CNTs on the living cells. Dielectrophoretic crossover frequency has been determined for CNT treated cells and non-treated cells in order to detect the change in the cell membrane capacitance due to treatment of CNTs. Moreover, cDNA array analysis using Affymetrix probe sets complementary to approximately

54,675 human genes have been carried to monitor the levels of expression within human normal bronchial epithelial cells treated with SWCNTs and unexposed cells. Comprehensive list of genes that are differentially expressed between SWCNTs- treated and their control cells were determined. The present chapter and the next chapter use significant number of abbreviations from biology. For convenience they are presented in page 124 of the thesis.

5.2. Single-walled and multi-walled carbon nanotubes suspension preparation

Single-walled carbon nanotubes with purity of 80-90% and multi-walled carbon nanotubes with purity of 60-70% have been obtained from (Sigma-Aldrich, Inc., Oakville, ON, Canada) in powder format; CNTs were dissolved and diluted to a concentration of 1 mg/ml stock in 1x phosphate-buffered saline (PBS). The particles have been vortexed for 1 min and then indirectly sonicated (Hielscher Ultrasonic, Ringwood, NJ, USA) for 10 min at 4 °C immediately prior to preparing treatment-dilution into serum-free and growth factor-free medium. The dilutions were again vortexed prior to being added to the cells at 60-70% confluence; the cells were incubated with a final concentration of 0.1 mg/ml SWCNT [191, 192].

5.3. Preparation of cells

MDA231 cell line has been obtained from the Centre for Experimental Therapeutics in Cancer, (Lady Davis Institute for Medical Research of the Sir Mortimer B. Davis-Jewish General Hospital, McGill University, Montréal, Canada). Primary human bronchial epithelial HNBE cells were obtained from (Lonza Group Ltd, Shawinigan, Qc, Canada). Cells were incubated in 30 ml tissue culture flasks (Falcon) and fed every 48h. HNBE cells fed with keratinocyte Serum-Free (KSF)-Medium supplemented with 5 mg/100 ml of bovine pituitary extract (BPE) (Invitrogen Canada Inc., Burlington, ON, Canada), whereas, MDA231 cells were fed with RPMI-1640 medium with 10% fetal bovine serum BPS and 1% penicillin. At 80-90% confluence, the cells were trypsinized with 0.05% Trypsin in 0.53 mM EDTA and reseeded at a ratio of 1:3. The HNBE cells had doubling times in approximately 4 days, being shorter in early passage than late passages prior to senescence after 8 passages.

5.4. Cell growth and viability analyses

HNBE cells (1 X 10^6/ml) were plated in 100-mm dishes in their regular media (untreated cells) or containing 0.1 mg/ml of SWCNTs for two days. Afterwards, cell morphology analysis was performed using an inverted phase-contrast microscope. For cell growth and viability assay the cells were collected by trypsinization, washed and counted after two days using trypan blue exclusion and hemocytometer. Cell morphology test was repeated three times, with the same results. Data represent the proliferation and viability test assessed by the morphology analysis of three independent experiments that is shown in Figure 5.1.

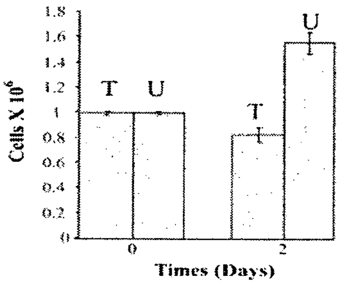

Figure 5.1: SWCNTs inhibit cell proliferation and affect cell viability of HNBE-treated cells (T) in comparison with their control untreated-cells (U)

SWCNTs found to be present in the cells cytoplasm provoke the conversion of cells from epithelial to fibroblast-like phenotype, and cause cell death [193]. In addition, cells become larger in appearance and more elongated, and show a decrease in cell-cell contact in comparison with control cells which display an epithelial morphology with high level of cell to cell contact as illustrated in Figure 5.2.

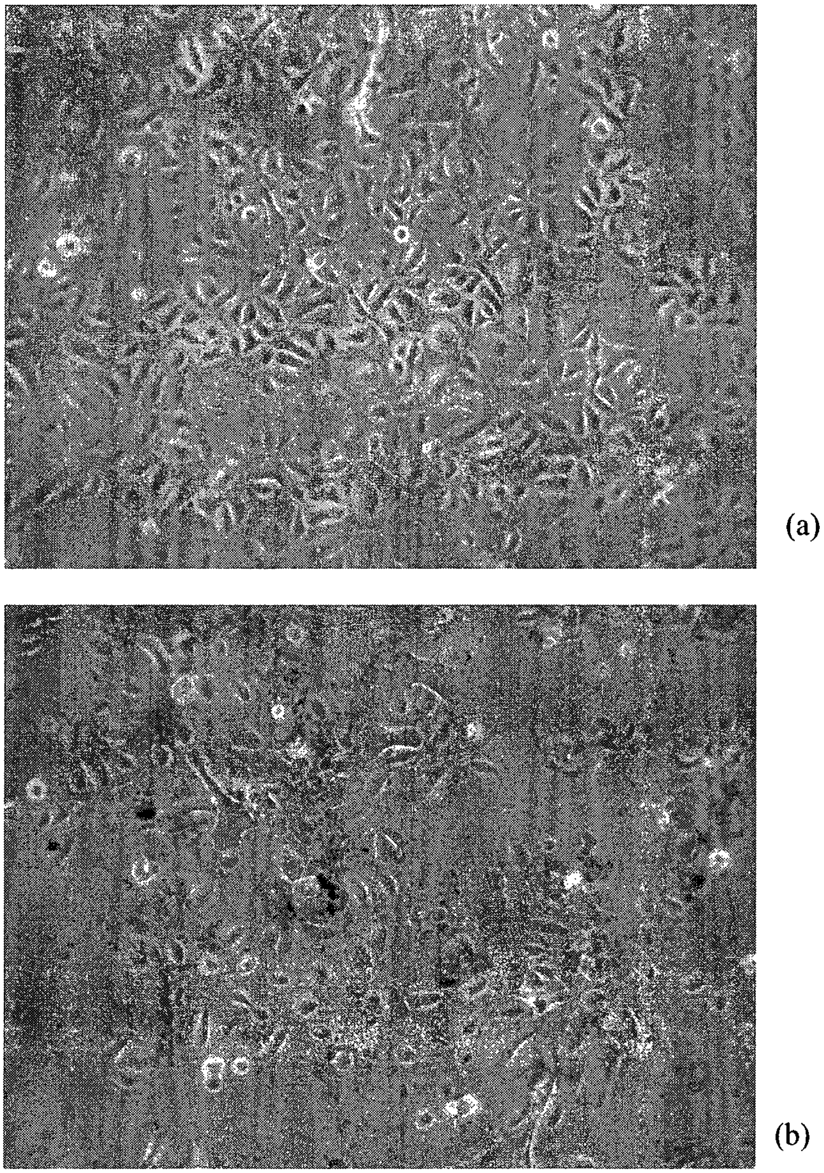

Figure 5.2: SWCNTs affect cell morphology of HNBE cells, HNBE-treated cells (b) in comparison with their control untreated-cells (a)

The effect of CNTs on the breast cancer cells MDA231 was more obvious. More nanotubes entering the cell cytoplasm were found in case of MDA231 cell line compared to the HNBE cells. Figure 5.3 shows clearly the effect of nanotubes on cell adhesion. Treating cells with SWCNTs decreases the cell to cell contact and increases the cells death rate.

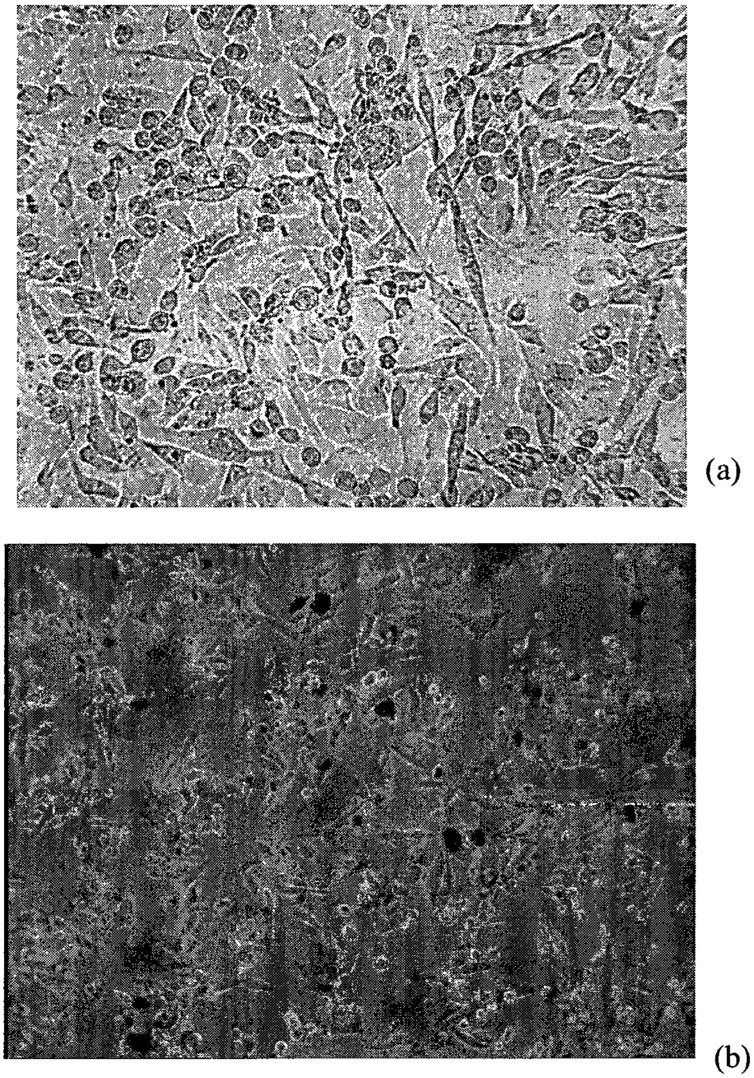

Figure 5.3: SWCNTs affect cell morphology of MDA231 cells, MDA231-treated cells (b) in comparison with their control untreated-cells (a)

The MDA231 treated cells detaching from the culturing flask were found to increase rapidly with time and detached cells form a complex form as shown in Figure

5.4. With a period of two weeks most of the cells (1 X 10^6) were detached from the dish and formed several clusters.

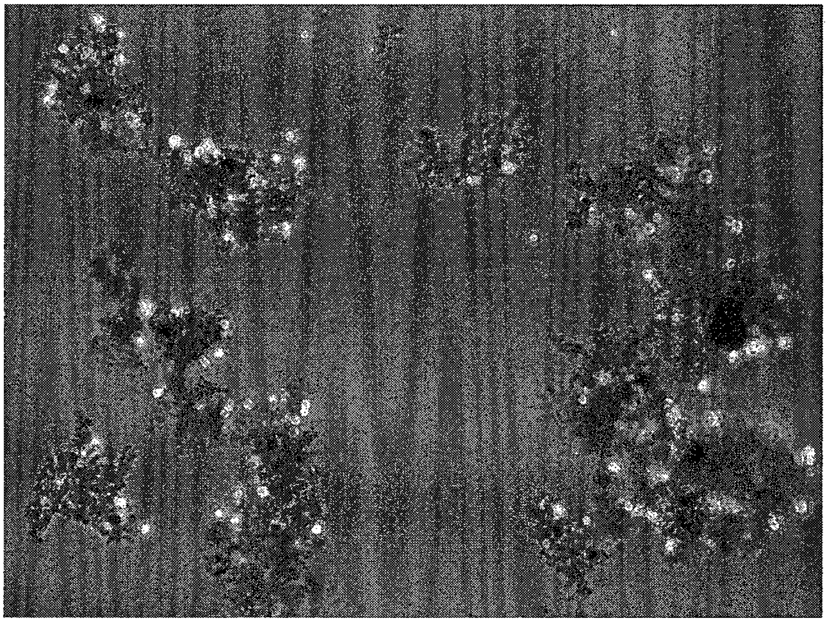

Figure 5.4: SWCNTs affect cell morphology of MDA231 cells, MDA231-treated cells after two week of SWCNTs treatment.

The crossover frequency f_0 of the cell can be expressed in the equation 3.23 as:

$$f_0 = \frac{\sigma_M}{\sqrt{2}\pi r C_{mem}} \quad \textbf{(161)}$$

where σ_M is the conductivity of medium, r is the radius of the cell and C_{mem} is the membrane capacitance of the cell. The effect of the SWCNTs of the membrane capacitance of MDA231 cells have been studied experimentally using DEP phenomena. The crossover frequencies of treated and non treated cells with nanotubes have been investigated using comb-like interdigitated electrodes. Difference in crossover frequency between treated and non-treated cells could not be observed. As a result, one can conclude that SWCNTs has no effect or slight effect on the cells membrane capacitance that could not be noticeable experimentally.

5.5. Microarray process

Microarray is a complex instrument containing a platform with thousands of spots for gene analysis. Microarray facilitates the identification in gene expression for tens of thousands of genes rather than few tens for the classical methods. Tens of thousands of fixed locations on glass polymer substrate are called spots. Millions of identical DNA molecules or fragments are fixed in the spots where each set of molecules identify a single mRNA molecule.

Microarray is mostly used to compare gene expression in two different samples. Two samples of the same cells treated differently or under different conditions may have change in the gene expression. For example, cells in dish #1 were seeded normaly following the standard procedure while cells in dish #2 were seeded similar to dish #1 but with adding substance A to the medium. In this case the cells in dish #1 are called control cells and cells in dish #2 are the treated cells. The effect of substance A on the gene expression of the cells can be studied using microarray. Microarray is performed by labeling the mRNA of both samples (control and treated) with different colors (assuming green for the control and blue for the treated). Then, the microarray is excited by laser beam and scanned in wavelength range suitable for the two selected colors. The emitted amount of fluorescence from each spot is proportional to the quantity of the nucleic acid bound in it. Therefore, from the intensity and color of the emitted fluorescence, thousands of data points are generated representing information about the gene expression in the sample. Comparison study for the gene expression in the two samples indicates the effect of substance A on the cells [194, 195].

5.6. PCR process

Polymerase Chain Reaction (PCR) is a laboratory technique that allows producing millions of copies of predetermined DNA sequence by using two specific fragments of DNA that called primers. The primers indicate the specific part of nucleic acid molecule that require to be amplified. Primers are designed such that they include particular sequences of nucleotide that hybridize with the opposite DNA strand. After the DNA is hybridized, double strand is formed by the primer and the complementary part of the targeted DNA.

Primers are designed with two strands one for each strand of the targeted DNA. Repeating the PCR hybridization cycles helps DNA amplification process. The repeated process of DNA amplification starts by denaturized DNA to loosen and split the DNA double strands. This process is achieved by heating the DNA sample at a temperature of 94°C for specific time that is usually more than 30 seconds and less than 5 minutes. Next step is the hybridization of the primers and the specific parts of DNA. This process is reached by lowering the temperature of the DNA sample. Hybridization temperature is usually in the range 40°C-65°C.

The last step in the PCR cycle is the strand replication. The temperature is raised to 72°C which is the optimum temperature for thermo-stable DNA to replicate. The cycle is repeated a number of times in order to duplicate the previous strands formed in the previous cycle [196, 197].

5.7. RNA isolation and microarray analysis

RNA is a biologically important type of molecule that is similar to DNA. Total RNA was extracted with TRIZOL (Invitrogen Canada Inc., Burlington, ON, Canada) according to the manufacturer's instructions. Biotinylated probes for microarray analysis were prepared using 10 µg of total RNA as described below. The total RNA was mixed with 100 pM of T7- (T) 24 primer (Genosys, San Diego, CA, USA) and denatured for 10 min at 70°C, then chilled on ice. First strand cDNA synthesis was performed using Superscript II reverse transcriptase (Life Technologies, Toronto, ON, Canada) and second strand synthesis was performed using DNA polymerase I, E *coli* DNA ligase and RNase H (Invitrogen Canada Inc., Burlington, ON, Canada). The biotinylated probe was prepared from the entire cDNA reaction using the ENZO Bioarray High Yield RNA Transcript Labeling Kit (ENZO Diagnostics, Toronto, ON, Canada). Incubating the purified probe in 1x fragmentation buffer for 35 min at 95°C reduced the average probe length. Hybridization was performed at 45°C for 20 h using 15µg of biotinylated probe.

Following hybridization, the non-specifically bound probe was removed by 10 low stringency washes and four high stringency washes performed using a GeneChip Fluidics Station 400 (Affymetrix, San Diego, CA, USA). Specifically bound probe was detected by incubating the arrays with SAPE (streptavidin phycoerythrin, Molecular Probes) and scanning the chips using a GeneArray Scanner (Hewlett-Packard, San Diego, CA, USA). The scanned images were analyzed using the GeneChip Analysis Suite 3.3 (Affymetrix, San Diego, CA, USA); and the statistical analysis of Microarray data was performed using FlexArray software (www.affymetrix.com).

5.8. Microarray results

The cDNA array technique has been used to identify genes that are differentially expressed in HNBE-SWCNTs-treated cells in comparison to their wild type (untreated) cells. Figure 5.5 shows the scatter plot of the differential expression of the 54,675 genes in HNBE-treated and untreated cells. Overall, we identified 14,294 genes out of 54,675, which are regulated differently between matched treated and untreated cells.

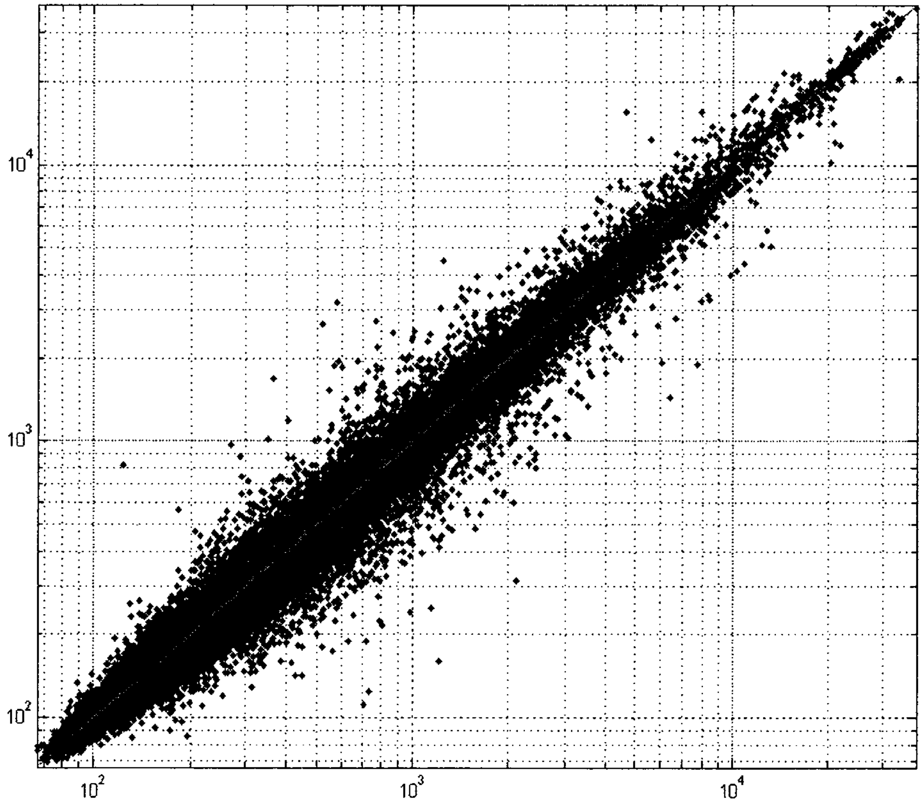

Figure 5.5: Representative scatter plot cDNA microarray analysis of HNBE SWCNTstreated and untreated cells. HNBE-SWCNTs treated cells, 0.1 mg/ml for 48 h, (y axis) and untreated (x axis) of each sample were labeled and hybridized to the cDNA microarray.

Totally 7,029 genes, with intensity ratios between 1.0 and 8.0, were up-regulated, while 79,265 genes were down-regulated with ratios between -8.0 and -1.0. Thus, 12.8%

of the 54,675 genes were over expressed and 13.2% were under expressed in the SWCNTs treated cells. It is therefore notable that the expression levels of 74% of all genes studied in this experiment did not differ between SWCNTs-treated and untreated cells.

The altered genes included those associated with cell cycle, apoptosis, cell survival, cell adhesion, signal transduction and transcription regulator. Representative list of the altered genes is listed in Tables 5.1 and 5.2.

Table 5.1: Representative list of over-expressed genes in HNBE SWCNTs-treated cells versus untreated cells.

Average Ratio of 2 experiments	GenBank accession no.	Gene name	Function
1.112	AA971429	CASP 8	Cell apoptosis
1.914	NM014330	Protein phosphatase 1	Cell apoptosis
2.877	NM001674	Activating transcription factor 3	Cell apoptosis
1.121	N36774	TNFRSF1A	Cell apoptosis
2.760	AJ277151	Tumor necrosis factor receptor 4	Cell apoptosis
1.658	BC006196	Tumor necrosis factor receptor 9	Cell apoptosis
2.179	NM002546	Tumor necrosis factor receptor 11b	Cell apoptosis
1.816	AF246998	Tumor necrosis factor receptor 19	Cell apoptosis
2.453	NM001252	Tumor necrosis factor 7	Cell apoptosis
1.781	AI936516	Tumor necrosis factor 8	Cell apoptosis
1.664	AF053712	Tumor necrosis factor11	Cell apoptosis
3.079	BC033638	Caspase 1	Cell apoptosis
2.932	BE467978	Caspase 4	Cell apoptosis
2.084	AL833692	Caspase 11	Cell apoptosis
3.639	BF433388	BCL 2	Cell apoptosis
2.404	AI498359	BCL2-like 2	Cell apoptosis
1.391	NM019096	GTP binding protein 2	Cell signaling
2.628	NM020525	Interleukin 22	Cell signaling
2.376	NM003856	Interleukin 1 receptor-like 1	Cell signaling
2.561	AF003934	Growth differentiation factor 15	Cell signaling
2.537	AL110232	Transcription factor EC	Transcription regulator
2.075	AB028021	Forkhead box A2	Transcription regulator
2.701	BC005161	Inhibin, beta E	Cell growth
1.454	BF342661	Microtubule-associated protein 2	Cell structure

In general, most of the genes that are over-expressed in SWCNTs-treated cells encode for cell apoptosis, signal transduction and transcription regulator, while those genes that are under-expressed are involved in cell adhesion and motility, cell proliferation and survival as can be seen from Tables 5.1 and 5.2.

Table 5.2: Representative list of under-expressed genes in HNBE SWCNTs-treated cells versus untreated cells.

Average Ratio of 2 experiments	GenBank accession no.	Gene name	Function
-1.463	AA481656	Protocadherin 1	Adhesion
-1.097	NM018937	Protocadherin beta 3	Adhesion
-3.929	BC000019	Cadherin 6 type 2	Adhesion
-2.800	NM004934	Cadherin 18 type 2	Adhesion
-2.529	BC015877	Cadherin 19 type 2	Adhesion
-2.008	AW593060	Cadherin 20, type 2	Adhesion
-2.974	NM004389	Catenin alpha 2	Adhesion
-4.422	U96136	Catenin delta 2	Adhesion
-1.898	AA668763	Leupaxin	Signaling & Adhesion
-2.069	AA749101	Interferon 1	Signaling & Adhesion
-1.795	NM020242	Kinesin family member 15	Signaling
-2.716	AF002985	Chemokine 11	Signaling
-1.475	NM152364	Repetin	Extracellular matrix
-3.665	AK057680	Matrix metallopeptidase 2	Extracellular matrix
-1.910	NM002423	Matrix metallopeptidase 7	Extracellular matrix
-1.627	NM004994	Matrix metallopeptidase 9	Extracellular matrix
-1.389	U38321	Matrix metallopeptidase 19	Extracellular matrix
-1.747	NM022718	Matrix metallopeptidase 25	Extracellular matrix
-1.619	BE350145	Collagen VI alpha 1	Extracellular matrix
-1.789	U29343	Hyaluronan-mediated motility receptor	Cell motility
-3.122	AB046400	Serpin peptidase inhibitor 4	Cell survival
-1.458	N90191	Cyclin B1	Cell cycle
-1.556	AW183154	Kinesin family member 14	Cell cycle
-1.652	NM005733	Kinesin family member 20A	Cell cycle
-2.105	AA810156	Nuclear fragile X2	Cell cycle

5.9. Reverse Transcription (RT) - Polymerase Chain Reaction (PCR)

The present work focused on selected groups of altered genes involved in apoptosis, cell cycle, cell survival, cell adhesion and cell motility; therefore, the expression of nineteen selected genes from these groups by RT-PCR have been investigated. These genes included Rho GTPase-26, Microtubule-2, GTP binding protein-2, Protein phosphatase-1, Interleukin receptor-1, Inhibin beta-E, Growth differentiation factor-15, Forkhead a2, Activating transcription factor-3, Serpin peptidase inhibitor-4, Chemokine 11, Interferon-1, Kinesins (14, 15 and 20A), Leupaxin, Cyclin-B1, Repetin and Hyaluronan-mediated motility receptor

RT-PCR amplifications have been performed using primer sets for Rho GTPase-26, Microtubmule-2, GTP binding protein-2, Protein phosphatase-1, Interleukin receptor-1, Inhibin beta-E, Growth differentiation factor-15, Forkhead a2, Activating transcription factor-3, Serpin peptidase inhibitor-4, Chemokine 11, Interferon-1, Kinesins (14, 15 and 20A), Leupaxin, Cyclin-B1, Repetin, Hyaluronan-mediated motility receptor and GAPDH genes (Table 5.3). GAPDH was used to control the amounts of cDNA generated from each sample. Synthesis of the first-strand cDNA was carried out using a cDNA kit for RT-PCR (MBI Fermentas, Toronto, ON, Canada). One fifth of the RT product was amplified for 30 cycles (1 min at 95°C, 1 min at 58°C, and 1 min at 72°C) followed by an extension of 7 min at 72°C. RT-PCR amplification products were analyzed on a 1% agarose gel stained with ethidium bromide; the RT-PCR analysis was repeated three times for each gene.

The total RNA used in this study was obtained from treated and untreated cells harvested from 2 separate experiments conducted under the same conditions and representing passage numbers 3 from two different batches of the same cell line. As expected from the array analysis, Rho GTPase 26, Microtubule-2, GTP binding protein-2, Protein phosphatase-1, Interleukin receptor-1, Inhibin beta-E, Growth differentiation factor-15, Forkhead a2 and Activating transcription factor-3, were found to be up-regulated; whereas Serpin peptidase inhibitor10 4, Chemokine-11, Interferon-1, Kinesins (14, 15 and 20A), Leupaxin, Cyclin-B1, Repetin and Hyaluronan-mediated motility receptor were down-regulated in SWCNTs-treated cells versus untreated cells at the RNA level. The results of RT-PCR is shown in Figure 5.6.

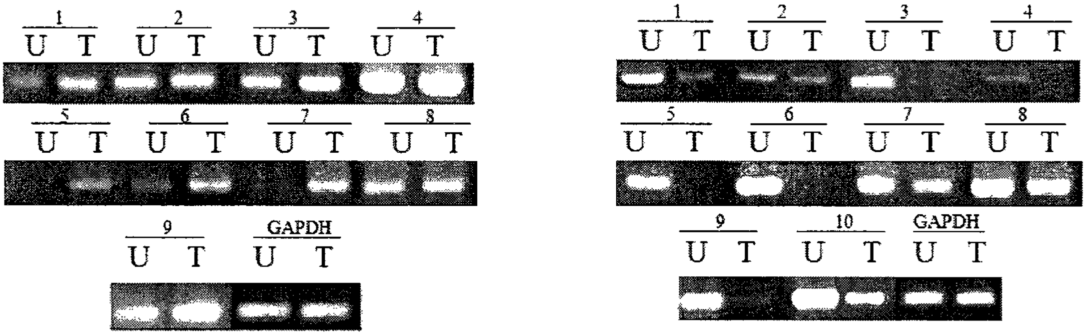

Figure 5.6: . Validation of microarray data by RT-PCR. This analysis was performed using HNBE SWCNTs-treated cells and their corresponding HNBE-untreated cells (U: untraded cells; T: treated cells).

RT-PCR was used to amplify fragments of Rho GTPase-26, Microtubule-2, GTP binding protein-2, Protein phosphatase-1, Interleukin receptor-1, Inhibin beta-E, Growth differentiation factor-15, Activating transcription factor-3, Forkhead a2 and (gene number 1 to 9, respectively) which confirm the up-regulation results obtained by the microarray (A); whereas Serpin peptidase inhibitor-4, Chemokine-11, Interferon-1, Kinesins (14, 15 and 20A), Leupaxin, Cyclin-B1, Repetin and Hyaluronan-mediated motility receptor (gene number 1 to 10, respectively) were reconfirmed to be down-regulated in SWCNTs-treated cells in comparison with untreated (control) cells (B). GAPDH gene amplified from the same samples shows similar loading in each lane.

RT-PCR amplifications for the samples have been repeated three times to confirm the obtained results. Quantification test for RT-PCR was performed using ImageJ program thus confirming the Microarray data and initial RT-PCR analysis. Figure 5.7 shows the quantification results of the RT-PCR results where the height of the columns represents the average value of the band intensity of the three samples.

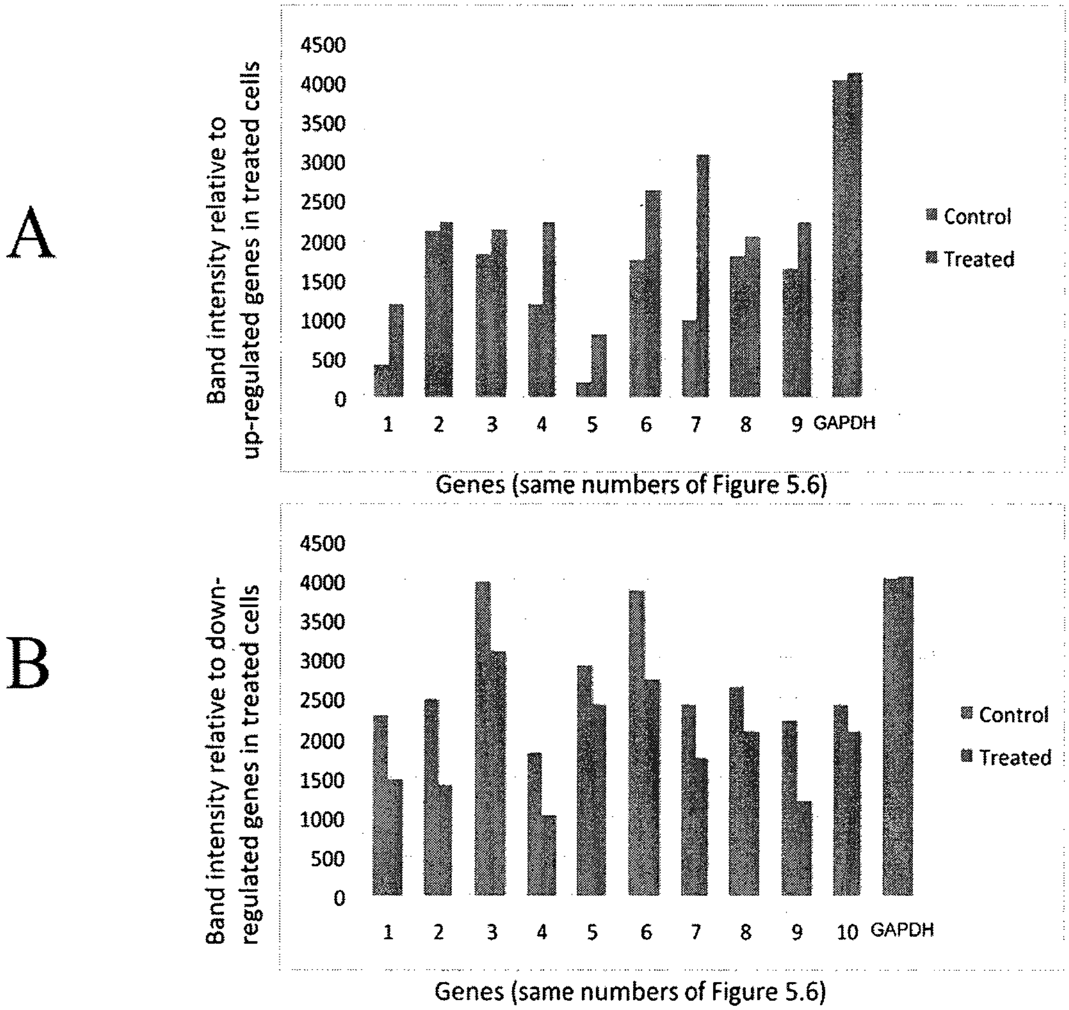

Figure 5.7: RT-PCR quantifications based on three separate experiments for the 19 selected genes. The results confirm the up and down-regulation genes (A and B, respectively) of the Microarray data and initial RT-PCR analysis.

Table 5.3: Primer sets used for RT-PCR amplification

Gene name	Primers
Rho GTPase activating protein-26	5'-GGT CTG TTG CAG GGT TTG TT-3'
	5'-CTT CTG GCC TGT CAA AAA GC-3'
Microtubule- 2	5'-AAA GCT GAT GAG GGC AAG AA-3'
	5'-GGC CCC TGA ATA AAT TCC AT-3'
GTP binding protein-2	5'-TTA CAG CGA CTC ACG GAC AG-3'
	5'-TCT TGC TGA CCA CGA TGA AG-3'
Protein phosphatase-1	5'-GTG TAT TGG CCA GGA GAG GA-3'
	5'-GGC CTT CAA GAA AGC ACT TG-3'
Interleukin receptor-1	5'-AAG GAG TTT GCC TAC GAG CA-3'
	5'-TTT CTG GGA ATT TTG CTT GG-3'
Inhibin beta-E	5'-TTG CTG CCT CTT TCC ATT CT-3'
	5'-CAT CCG TCT TGA CCA CAT TG-3'
Growth differentiation factor-15	5'-GAG GTG CAA GTG ACC ATG TG-3'
	5'-AAT GAG CAC CAT GGG ATT GT-3'
Activating transcription factor-3	5'-TCG GAG AAG CTG GAA AGT GT-3'
	5'-TCT GGA GTC CTC CCA TTC TG-3'
Forkhead-a2	5'-ACC ACT ACG CCT TCA ACC AC-3'
	5'-GGG GTA GTG CAT CAC CTG TT-3'
Serpin peptidase inhibitor-4	5'-CCA CAG AAA AAG CTG CAA CA-3'
	5'-GTT TGA CTT TCC ACC CAG GA-3'
Chemokine-11	5'-GCT TCC CCA TGT TCA AAA GA-3'
	5'-TAA GCC TTG CTT GCT TCG AT-3'
Interferon-1	5'-GAG GAA CAT GAG GTG GCT GT-3'
	5'-ATG AGG ATG CCC AGA ATC AG-3'
Kinesin family member-14	5'-CCA ATG CTA TCA GCA GCA AA-3'
	5'-TGT AAT GTC GGG TTC CCA TT-3'
Kinesin family member-15	5'-TCT TTG CAA AAA GCG AAC CT-3'
	5'-ACT GGT CGG GAA TGA AGT TG-3'
Kinesin family member-20A	5'-CTT CCG TGA CAG CAA GTT GA-3'
	5'-TCC TTG ATG AAC GAG TGC AG-3'
Leupaxin	5'-CTG CTC CCA TCC TGG ATA AA-3'
	5'-AGT CCC CAC AAA CAA AGC AC-3'
Cyclin-B1	5'-GGC CAA AAT GCC TAT GAA GA-3'
	5'-AGA TGT TTC CAT TGG GCT TG-3'
Repetin	5'-AGC CAA CAT CAC CAA CAC AA-3'
	5'-CCA CAT GGA CCT TCC TGA CT-3'
Hyaluronan-mediated motility receptor	5'-TGG AAG CAA GGC TAA ATG CT-3'
	5'-ACC TGC AGC TTC ATC TCC AT-3'
GAPDH	5'-TGC ACC ACC AAC TGCTTAGC-3'
	5'-GGCATGGACTGTGGTCATGAG-3'

5.10. Discussion

This investigation appears to be the first Microarray study on the effect of SWCNTs on human normal bronchial epithelial cells. In the present study, the significant changes in the expression of 14,294 genes, with 7,029 genes being up-regulated and 7,265 being down-regulated have been identified. The majority of these genes are discovered for the first time as targets of SWCNTs exposure in human normal bronchial cells. While, it has been previously reported that SWCNT can provoke alveolar macrophage activation, chronic pulmonary inflammation and granuloma formation in mouse models [198], the investigators of this study used Affymetrix microarrays to explore the molecular effects on the macrophages when exposed to SWCNT. They found that SWCNT is able to activate various transcription factors such as nuclear factor kappaB (NF-kappaB) and activator protein 1 (AP-1) which can lead to the induction of protective and anti-apoptotic gene expression in these cell models. In this study, NF-kappaB has been found to be slightly down-regulated in HNBE-SWCNTs-treated cells; however, the AP-1 gene was not found on our list of genes. Although, the present preliminary data shows that SWCNTs provoke cell apoptosis of human normal bronchial epithelial cells through Activating transcription factor-3 and transcription factor-15 and probably other transcription factors such as Activating transcription factor-2 and 7. On the other hand, further study examined the effect of SWCNTs on HEK293 cell line, human embryonic kidney cancer cells using a small oligo-based microarray analysis related to cell cycle, cell apoptosis and signal transduction [199]; the study identified genes such as (Cyclin-A1 and 2 , Cyclin-C , Cyclin-D1 and 3, Cyclin-G1 and 2, Cdk2, 3, 4 and 6 of cell cycle and P16, 12Bax, Hrx, Bak-1, P53 and TGF-bR1 of cell apoptosis as well as Mad 2, Jak-1, Ttk, Tyk-2,Pa2g-4 and Early growth response-1 of signal transduction group) as being differentially expressed in SWCNTs-treated in comparison with untreated HEK293 kidney cancer cells. Herein this work reports for the first time a complete list of gene targets of SWCNTs in human normal bronchial epithelial cells; while, deregulation of the majority of genes reported in the previous study [199] on human embryonic kidney cells has been confirmed. Moreover, in this study we show for the first time that Protein phosphatase-1 is over-expressed in HNBE SWCNTs-treated cells compared to untreated cells. This gene plays an important role in growth arrest and DNA damage and it is known to be correlated with cell survival [200-202] .

Moreover, Activating transcription factor-3 gene was found to be up-regulated in SWCNTs-treated cells. This gene was reported to have a significant role in cell apoptosis and carcinogenesis [203, 204]. In addition, the interleukin receptor-1 is over-expressed in HNBE SWCNTs-treated cells, which participates in cell signaling of airway inflammation through its activation by interleukin-33 [205, 206]. On the other hand, treatment of HNBE cells with SWCNTs induces a down-regulation of Hyaluronan-Mediated Motility Receptor gene which is involved in cell motility and cell growth [207, 208]. Other important genes are reported to be down-regulated, in this study, in SWCNTs-treated cells compared to untreated cells. This includes Chemokine11 gene which is part of cell signaling and motility [209, 210]. Kinesin family members (14, 15 and 20A,) all found to be under-expressed in HBNE-treated cells. These genes are correlated with cell proliferation, cell cycle and trafficking [211-213]. Accordingly, this study is the first investigation to categorize the gene targets of SWCNTs in primary human normal lung cells using microarray analysis.

Any method of separation that could alter the genetics of the targeted cells is not useful. One could draw the conclusion that DEP is valuable as a method as it does not alter the cells genetics. In the next chapter, findings related to the genetics modifications of cells due to exposure to AC electric field along with results of experiments are presented.

5.11. Summary

Identification of differential gene expression between HNBE SWCNTs-treated cells and their wild type (control) cells is the basis for a comprehensive understanding of the effect of SWCNTs in human lung cells, as these differences are likely to represent the coordinated alteration of critical pathways involved in the regulation of cell proliferation, apoptosis and cell survival. The reason why the present study used human normal bronchial epithelial cells is because using HNBE cells would be the best way to study the effect of SWCNTs in human normal lung cells. Therefore, we treated HNBE cells with 0.1 mg/ml of SWCNTs for 48 hours, as described in the "Methods" section. In the absence of treatment, HNBE cells displayed an epithelial phenotype, and formed monolayer well-organized cells. In contrast, and as indicated in Figure 5.2 SWCNTs-treatment led to a phenotypic conversion from epithelial to fibroblast-like phenotype. Cells became more elongated and larger in appearance, and showed a decrease in cell to cell contact in comparison with untreated cells; this is accompanied by an inhibition of cell proliferation and cell death (Figure 5.1), while showing SWCNTs presence within their cytoplasm.

The comprehensive identification and profiling of gene expression affected by SWCNTs in human normal bronchial epithelial cells as reported in this study will help to understand the mechanism of the effect of SWCNTs in human health especially for the respiratory system. As other studies for new equipment and substances such as cell-phones and microwaves have noted [214-216], this systematic approach toward gene identification is believed to be useful in the discovery of the real effect of new materials and/or technologies on human health.

Chapter 6 : Material, Method and Results

6.1. Introduction

This chapter presents the results of separation process of malignant cells (MDA231) from blood sample using the microdevice presented in chapter 4. The preparations of cells and suspension medium, experimental setup and separation accuracy are also discussed. Furthermore, the effects of the separation process on the genes expression in MDA231 cell line have been studied. Microarray data for cells suspended in low conductivity (between 10-50 mS/m) sucrose/dextrose medium for fifty minutes without any electrical exposure and under the influence of pDEP and nDEP is presented.

6.2. Suspension medium

The low conductivity medium that was used in the experiments has been prepared in the laboratory by adding 8.5% (w/v) sucrose plus 0.3 % (w/v) dextrose to distilled water. Medium was filtered and then sterilized in order to avoid any contamination of the living cells during the separation. The conductivity of the medium was adjusted to the desired conductivity (5 to 20 mS/m) by adding a small quantity of Trypsin in 0.53 mM EDTA. Addition of 700µL of Trypsin to 100mL of sucrose/dextrose medium provides a conductivity of 10 mS/m.

6.3. Cells preparation

Breast cancer cells line MDA231 cells have been used as malignant cells in the present work. The cells were obtained from “Lady Davis Institute for Medical Research” of the Sir Mortimer B. Davis-Jewish General Hospital, Department of Oncology, Human

Genetics and Medicine, McGill University Montreal. Cells were cultured in 75 cm^2 flask and fed with RPMI 1640 (5% FBS and 1% penicillin) every 48 hours. At 80-90% confluence, the cells were washed with phosphate buffered saline (PBS), trypsinized with 0.05% Trypsin in 0.53 mM EDTA and reseeded at a ratio of 1:4.

Blood cells and erythrocytes were suspended in the low conductivity sucrose/dextrose medium described in section 6.2. Blood samples have been obtained from a donor. The blood was diluted and used in the experiments or treated with EDTA as anticoagulant in order to separate erythrocytes cells. Ficoll-Paque Plus product containing 5.7% w/v FicollTM PM400 and 9% w/v diatrizoate sodium was mixed with blood anterior and diluted two times with phosphate buffered saline plus (PBS+) and 2% fetal bovine serum (2% FBS). The complex solution was centrifuged at room temperature (19-25^{o}C) for 30 minutes at 400 x g with brake off. The upper plasma layer was isolated without disturbing the interface between FicollTM and plasma. Subsequently red blood cells layer was removed and suspended in a medium that is suitable for DEP manipulations.

6.4. Specimens preparation

Different specimens of living cells were used in the experiments. Erythrocytes cells suspended in sucrose/dextrose low conductivity medium were used to validate the analytical solution presented in chapter three. Moreover, specific number of MDA231 cells was mixed with diluted blood and then separated using the proposed microdevice in order to investigate the performance of the device and the accuracy of the separation process.

The blood specimens used in the separation microdevice were prepared by diluting 200 μl of blood into 3 ml of the sucrose/dextrose low conductivity medium. MDA231 cells were added to the specimens as malignant cells with ratio of 1 to 100 cells per 100,000 blood cells with the purpose of studying the efficiency of the microdevice to separate malignant cells. The separation device was fed with cells specimens using single syringe pump. The pump uses pressure difference to create flow that is controlled through a keypad interface.

The genes modifications of the three different specimens (control, pDEP and nDEP) were compared in order to look into the effect of DEP manipulation on living cells. The three specimens were prepared as it follows:

6.4.1. Control specimens

a. Liquid media covering cells were removed using the aspirator.
b. MDA231 cells were washed with 5-10 ml of phosphate buffered saline (PBS) and then PBS was removed from the flask using the aspirator.
c. Cells were trypsinized by adding 3 ml of 0.05% Trypsin in 0.53 mM EDTA to the flask and incubate for 5 minutes or until they detach from the flask.
d. Cells were removed from the incubator and checked under the microscope to ensure detaching of cells from the flask
e. 8 ml of RPMI1640 medium was added to the Trypsin and then carefully been mixed.
f. Cells were counted using the hemocytometer.

g. 3 million cells were transferred into 15 mL centrifuge tube and centrifuged for 4 min at 500 g.

h. After centrifugation, liquid medium is removed using the aspirator while the cell pellet remains at the base of the tube.

i. Cells were suspended in the sucrose/dextrose conductivity medium described as in section 6.2 with conductivity of 10 mS/m.

j. Cells were kept in the medium for 50 minutes inside the clean room shown in Figure 6.1 to avoid any contamination and then centrifuged for 4 min at 500 g.

k. After centrifugation, sucrose/dextrose medium was removed using the aspirator keeping the cell pellet at the base of tube.

l. Cells were lyzed by adding 350μl of RLT buffer. RLT buffer is used for lysis of cells and tissues before RNA isolation.

6.4.2. pDEP specimens

i. Steps (a-i) were performed similar to the control specimen.

j. Cells suspended in the medium were fed into the DEP device shown in Figure 4.26.

k. 20 volts peak-to-peak with frequency of 100 kHz has been applied to the cells in order to achieve pDEP phenomenon. Aggregation of cells at the tips of the electrodes was observed.

l. The process was performed in the clean room to prevent any contamination and cells were kept under the pDEP phenomenon for fifty minutes.

m. Cells were collected from the microdevice and then it was washed for 5 minutes with sucrose/dextrose medium to remove the cells which accumulate in the device.

n. Cells were collected in 15 mL tube then centrifuged for 4 min at 500 g.

o. After centrifugation, sucrose/dextrose medium was removed using the aspirator keeping the cell pellet at the base of tube.

p. Finally, cells were lyzed by adding 350μl of RLT buffer.

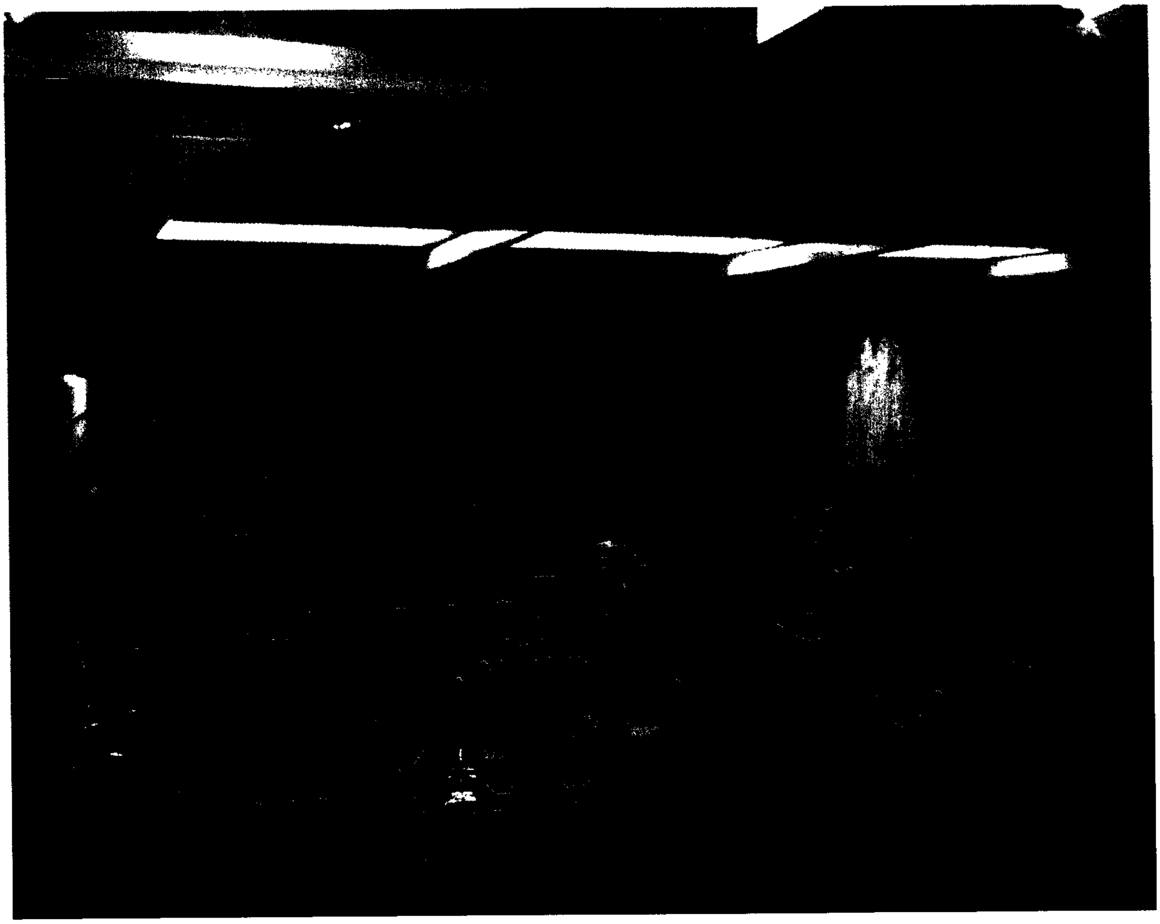

Figure 6.1: The clean room in the laboratory where the experiments were performed

6.4.3. nDEP specimens

The nDEP specimens were prepared similar to the pDEP specimen except step (c) where the AC applied frequency was set to 10 kHz to ensure nDEP phenomenon.

6.5. Experimental setup

The experimental setup is shown in Figure 6.2 and it consists of the followings:

1- Syringe pump to provide the desired flow rate of the specimen.
2- Syringe contains the blood specimen.
3- Two function generators supply the microdevice with the required AC signal.
4- The separation microdevice
5- Inverted microscope
6- Digital camera to record the image of the separation process.
7- Computer to visualize the separation of malignant cells.

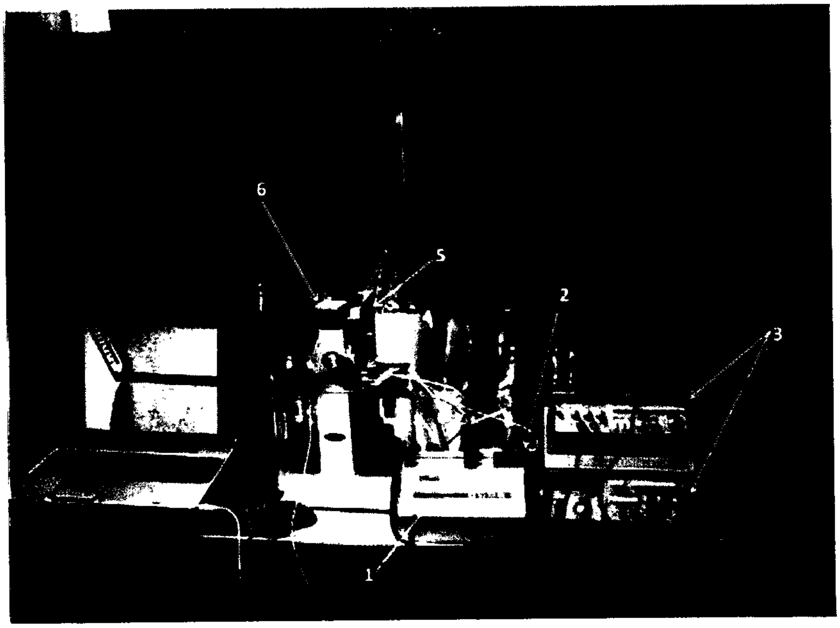

Figure 6.2: Illustration of the experimental setup

6.6. Separation of malignant cells from blood

Separation of MDA231 cells from blood was performed using the microdevice illustrated in Figure 4.15. MDA231 cells were mixed with diluted blood as described in section 6.4. Experimental results for the separation process matched the path lines of cells described in Figure 4.15. The first function generator provided part one of the electrodes pattern with 20 volts peak-to-peak potential and 10 kHz frequency. The applied frequency ensures nDEP phenomena for both blood and MDA231 cells. Therefore, blood and MDA231 cells were repelled from the electrodes as they move close to them as shown in Figure 6.3.

The average velocity of the flow was studied to indicate the maximum flow rate possible such that cells will not cross the electric field generated by the electrodes. The minimum flow rate possible by the available syringe pump is 0.02 μl/hr while the cross section of the microfluidic part of the device is 50μm height ×10,000 μm width. Thus, the minimum average velocity possible was close to 11 μm/s.

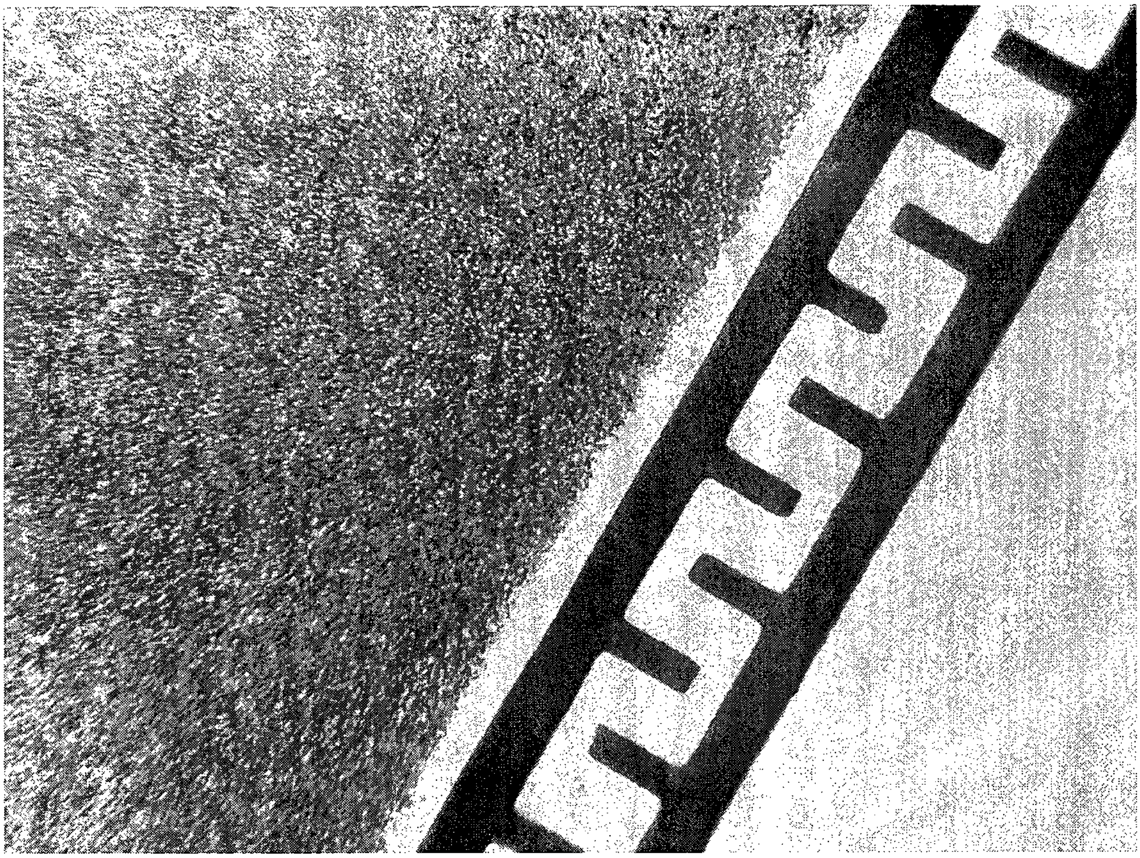

Figure 6.3: Cells as they pass close to part one of the electrodes layer.

The experimental results show that as smaller the flow rate is more adequate the separation process. However, increasing the flow speed up to 80μm/s causes some cells to cross the DEP barrier-like created by the electrodes as shown in Figure 6.4. The highest flow speed possible such that cells will not pass the electrodes in the first part of the design was found to be in range of 50 μm/s. thus, the maximum flow rate possible to reach the desired separation accuracy is 0.1 ml/hr. Parallel device would enable multiplication of this rate.

The path lines of blood cells found experimentally matched the ones found analytically in chapter 4. Cells were divided into two separate streams one in each side of the microchannel. The right side stream is shown in Figure 6.5.

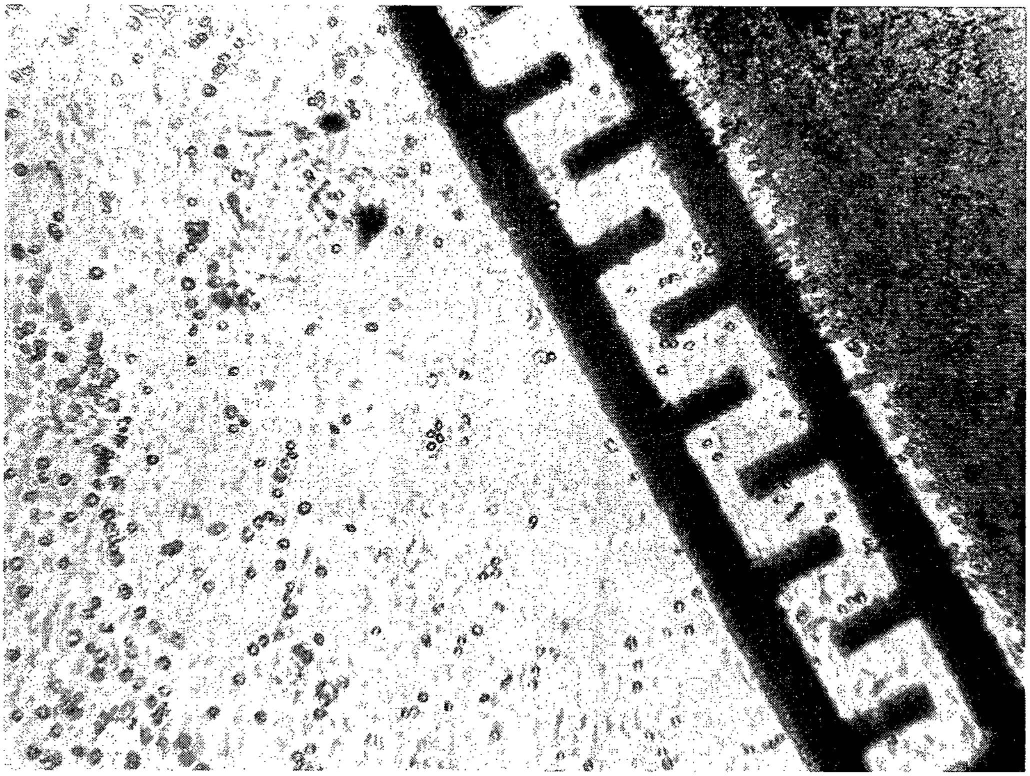

Figure 6.4: Cells crossed the electric field on the first part of the separation device due to the high flow rate.

The second function generator provided part two of the electrodes patterns with 20 volts peak-to-peak potential and 35 kHz frequency that ensure nDEP for blood cells and weak pDEP for MDA231 cells. The trajectory of MDA231 cells found experimentally is similar to that predicted through modeling in chapter 4. Blood cells passed close to part two of the electrodes patterns and deflected their direction of movement parallel to the electrodes whereas MDA231 cells crossed the electrodes and continued their movement as shown in Figure 6.6.

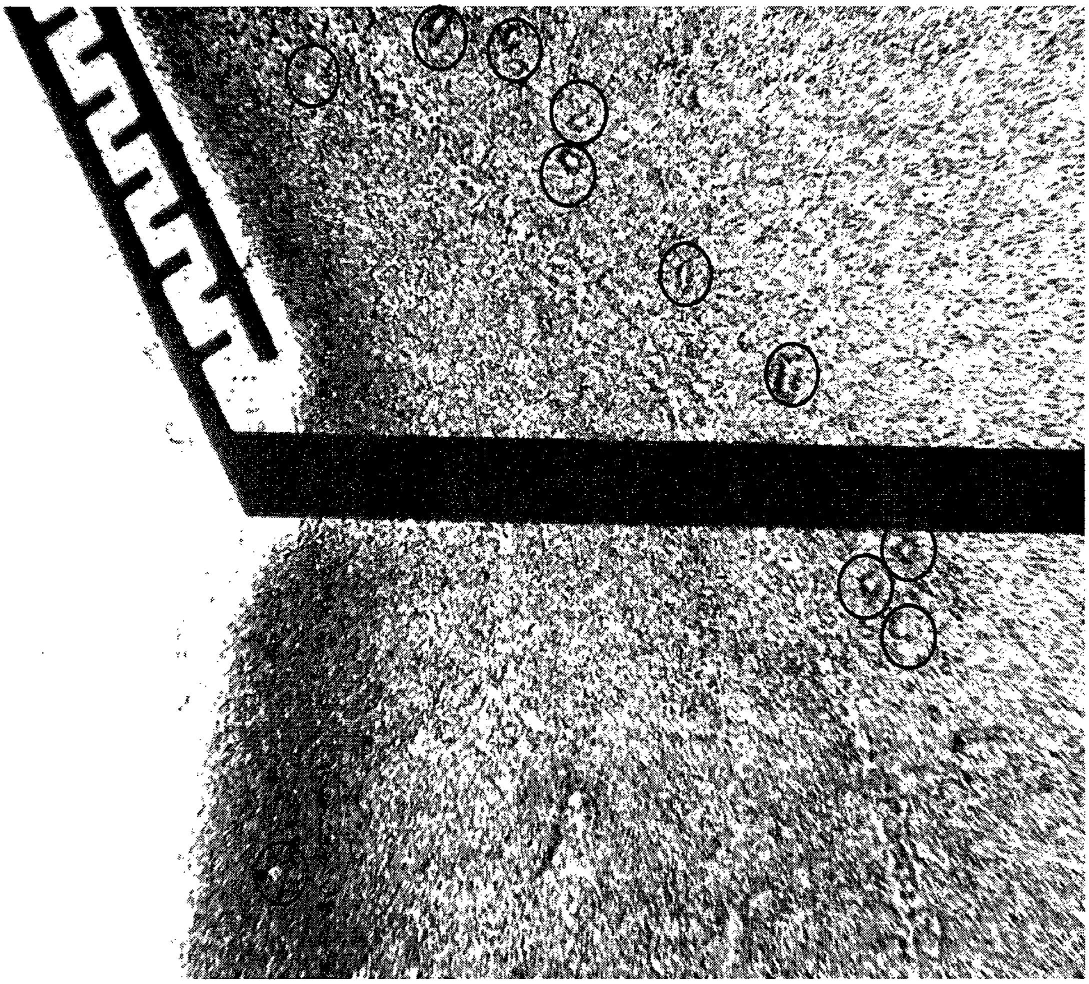

Figure 6.5: Right side stream of cells after crossing part one of the electrodes patterns. Circles were used to indicate the location of MDA231 cells in the stream

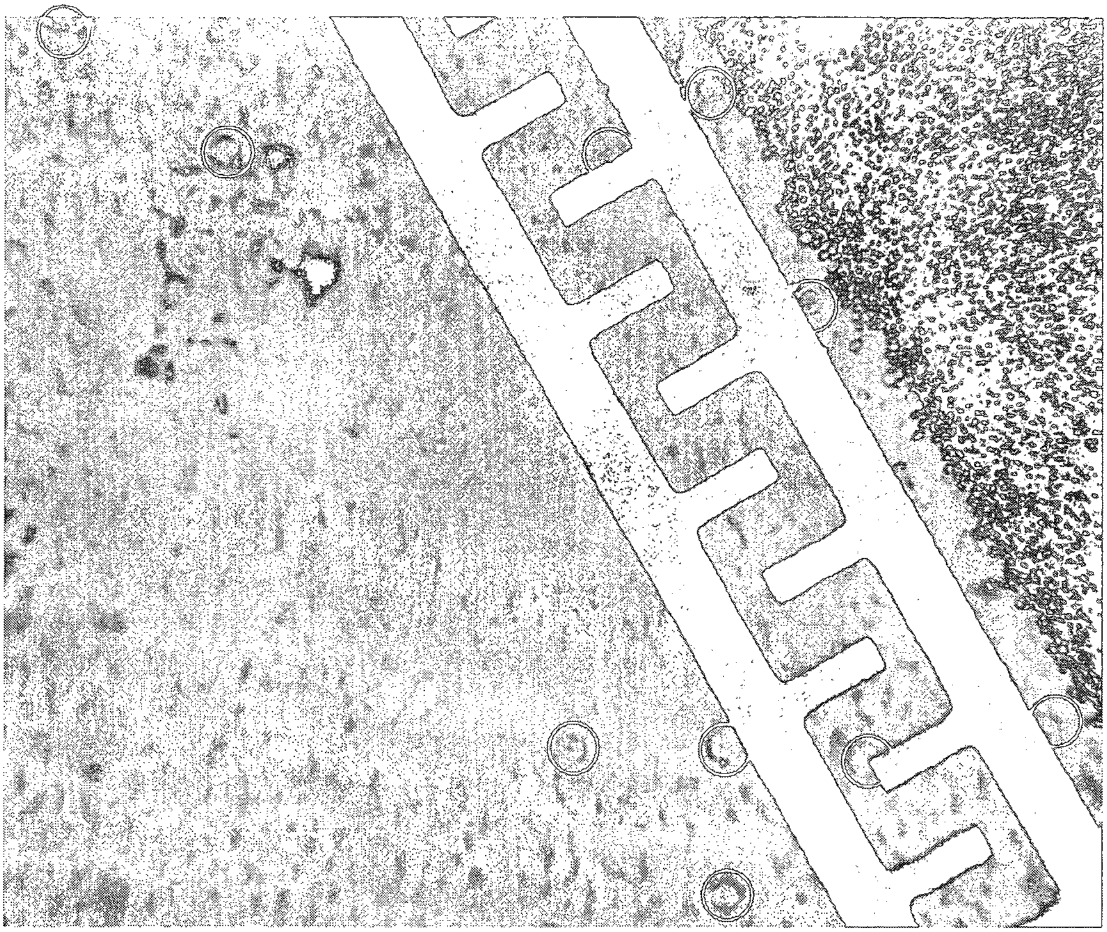

Figure 6.6: Blood and MDA231 cells as they cross part two of the electrodes. Circles were used to indicate the location of MDA231 cells

An exact measurement for the accuracy of the separation process was not possible to achieve by simple counting of the malignant cells before and after the separation process. Such process requires precise counting of cells. If flow cytometry would be used for the first counting, there is little chance that the cells will remain alive during the separation by DEP. Meanwhile, the available counting method is through the Hemocytometer which provides statistical estimation of number of cells and not the exact number. Therefore, exact counting of cells required more precise techniques that at the time were not available.

However, this work is targeting 100% accuracy or close to that value. Therefore, no targeted cell should flow within the blood stream at the outlet. The low conductivity medium and the blood stream at the outlet are shown in Figure 6.7. Experimental results show that targeted cells flow in a separate stream from the blood stream as shown in Figure 6.6 and no MDA231 cells were observed in the blood stream. As a result, 100% accuracy seems to be achievable with such a device.

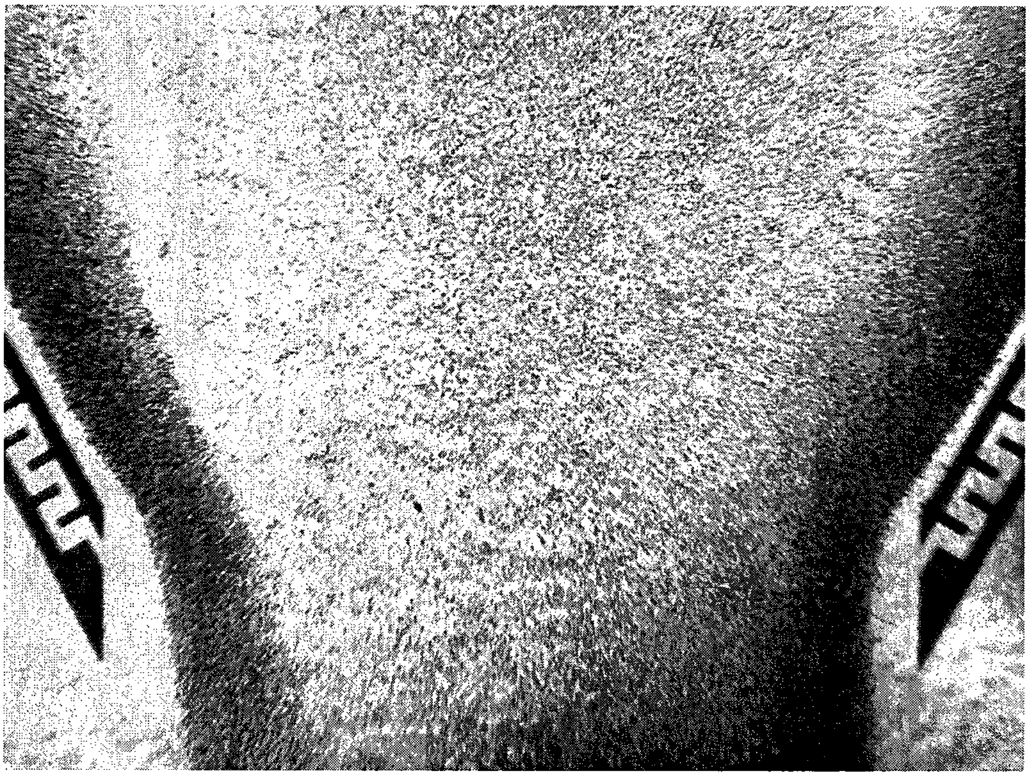

Figure 6.7: Blood cells stream at the blood outlet. No presence of MDA231 cells in the stream can be observed.

The small size of the presented microdevice makes it possible to stack several in a single microfluidic chip in order to reach a flow rate that enables point of care tests. Moreover, it is possible to increase the separation speed by repeating the same design on the glass substrate to increase the device cross section. For example, stacking of 10 devices each of cross section 50 μm × 10 cm creates a chip with a small size that is capable of separating malignant cells from 1ml of diluted blood in less than 7 minutes. Thus, it is believed that the targeted accuracy and speed of separation has been achieved. Moreover, such devices could be fabricated on polymers, under the cost of the device corresponding to disposable device.

6.7. Effect of DEP on living cells

The effect of AC field long term exposure on living cells has been reported to affect the cells growth and proliferation [218]. Moreover, no effect on MDA231 cells viability was found through experiments after 1 hr of exposure to 50 kHz and 20 volts peak-to-peak AC field. The one hour period was chosen because the separation process is performed usually in few minutes up to less than 1 hr. MDA231 cells were suspended in the low conductivity medium as described in section 6.3 with a conductivity of 10mS/m. Culturing of the cells after DEP manipulation reveals no difference between cells before and after the exposure.

Full understanding of the AC field exposure on living cells required complete study for gene changes due to DEP manipulation. A complementary DNA microarray multiplex technology has been used to identify the changes in gene expressions occur due to DEP manipulation. The alternations in six thousand seven hundred fifty-four genes were studied. The effects of both phenomena pDEP and nDEP on living cells have been investigated. MDA231 cells were kept in the test device for fifty minutes under the influence of DEP phenomena as described in section 6.4. The genes changes in MDA231 cells in the pDEP samples were compared to the gene change in the control cells.

Moreover, genes expressions for cells that experienced nDEP have been matched up to the control cells as well.

a. Effect of pDEP manipulation on living cells

The scatter plot of the differential expression of 6,754 genes in MDA231 cells that experienced pDEP and control cells is shown in Figure 6.8. Six hundred fifty four genes were found to be slightly up regulated with fold change between 1.3 and 2.78 while nine hundred seventy five genes were found to be down regulated. A fold change of 1.5 means that a specific gene is found 50% more in the experimental specimen comparing to the control. The fold change of down regulated genes falls between -2.38 and -1.3. As a result, only 10% of the studied genes were over expressed while 14% were under expressed in MDA231 cells that experienced pDEP. One can notice that the majority of the 6,754 genes in this test did not differ due to pDEP manipulation.

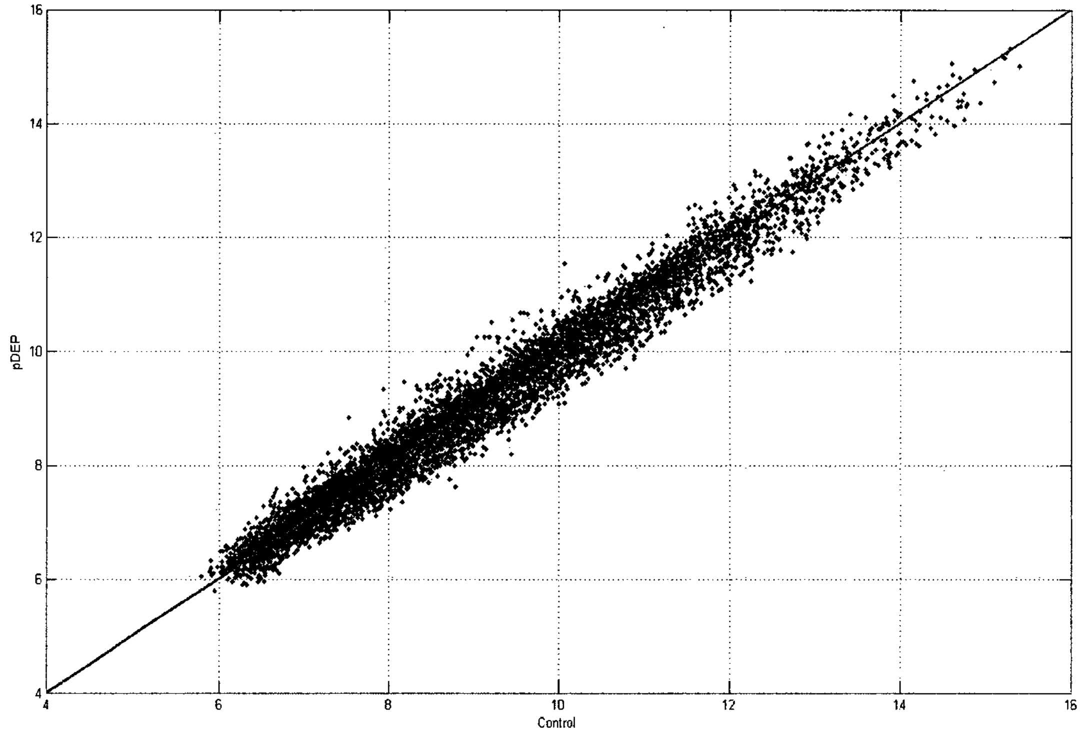

Figure 6.8: : Representative scatter plot cDNA microarray analysis of MDA231 influenced by pDEP and the control cells. MDA231 cells experienced pDEP for 50minutes (y axis) and control cells kept in the low conductivity medium for same period (x axis) of each sample were labeled and hybridized to the cDNA microarray

b. Effect of nDEP manipulation on living cells

The effects of nDEP manipulation on living cells were investigated in the same technique as to pDEP. The scatter plot of the differential expression of all the studied genes in MDA231 cells that were kept for fifty minutes under nDEP force and control cells is shown in Figure 6.9. Two thousand six hundred and sixteen genes have been found over expressed. The fold change of these genes falls between 1.3 and 7.36 while 2417 genes were found to be under expressed with fold change between -14.78 and -1.3. Thus, 39% of the six thousand seven hundred fifty-four genes were up regulated and 36% were down regulated. The expression levels of 25% of the studied genes did not differ due to the effect of nDEP force on the cells.

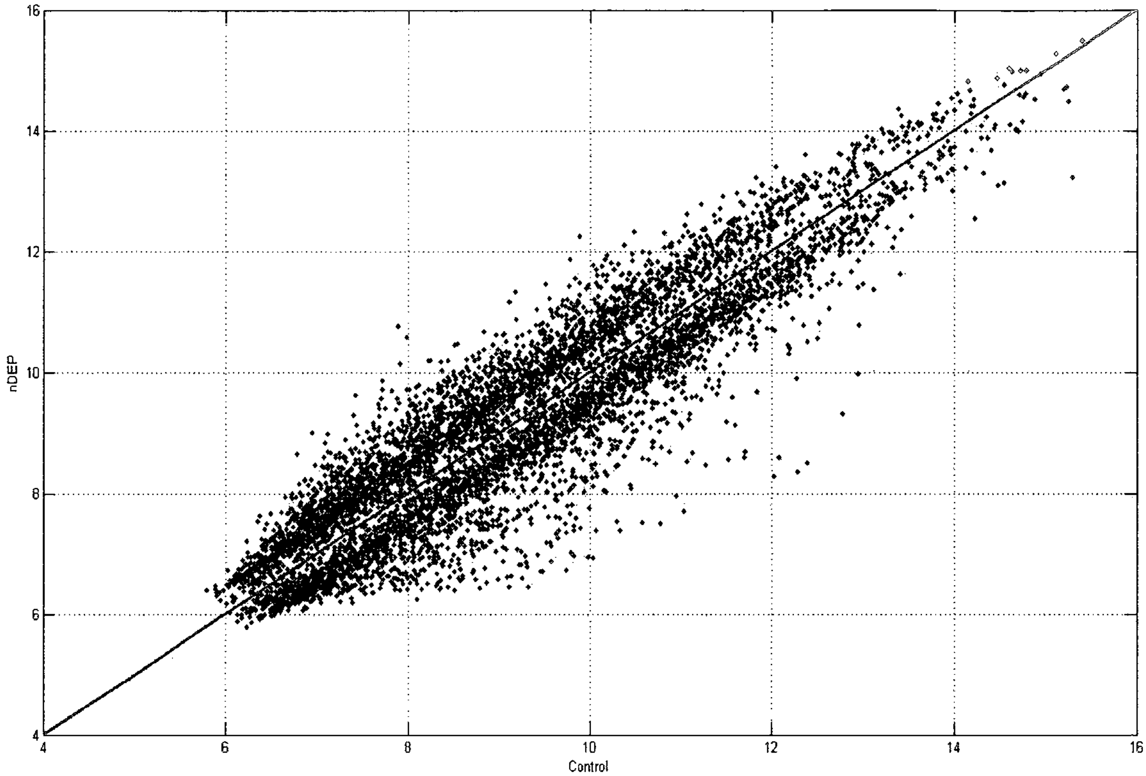

Figure 6.9: Representative scatter plot cDNA microarray analysis of MDA231 influenced by nDEP and the control cells. MDA231 cells experienced nDEP for 50 minutes (y axis) and control cells kept in the low conductivity medium at the same period of time (x axis) of each sample were labeled and hybridized to the cDNA microarray

In contrast to cells that experienced pDEP, majority of the genes in MDA231 cells were altered due to the exposure to the low frequency AC field where cells experienced nDEP phenomena as shown in Figure 6.10. Moreover, the fold changes for pDEP treated cells falls between -2.38 and 2.78 while in case of nDEP specimen is between -14.78 and 7.36.

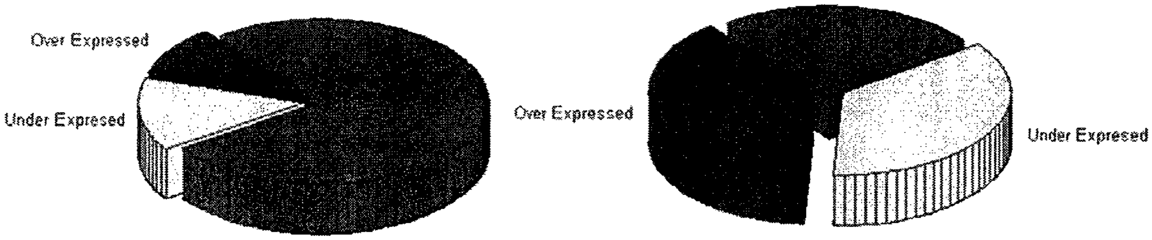

Figure 6.10: Pie charts show the ratio of altered genes for pDEP and nDEP specimens respectively.

The altered genes include those associated with mitosis, proteolysis, cell proliferation, cell division, growth factor, transcription factor, peptidase activity, sensory perception, cell adhesion, cell signaling, signal transduction, cell-matrix adhesion and transcription factor activity. Representative list of the over-expressed genes is listed in Table 6.1 while under expressed genes are in Table 6.2.

Table 6.1: Representative list of over-expressed genes in nDEP specimens versus control.

Fold change	GenBank accession no.	Gene name	Function
2.87793	NM012120	CD2-associated protein	Mitosis
2.30912	NM199246	cyclin G1	Mitosis
2.07076	NM018136	asp (abnormal spindle) homolog, microcephaly associated (Drosophila	Mitosis
2.00701	NM004354	cyclin G2	Mitosis
1.82493	NM018685	anillin, actin binding protein	Mitosis
2.41006	NM001010853	peptidase M20 domain containing 2	Proteolysis
1.57049	NM015239	ATP/GTP binding protein 1	Proteolysis
1.44618	NM001873	carboxypeptidase E	Proteolysis
1.3729	NM023083	calpain 10	Proteolysis
2.38729	NM006016	CD164 molecule, sialomucin	cell proliferation
3.25048	NM004064	cyclin-dependent kinase inhibitor 1B	cell proliferation
2.12144	NM004804	cytosolic iron-sulfur protein assembly 1 homolog (S. cerevisiae)	cell proliferation
2.10466	NM004071	CDC-like kinase 1	cell proliferation
1.9397	NM030762	basic helix-loop-helix family, member e41	cell proliferation
2.87793	NM012120	CD2-associated protein	cell division
1.77874	NM033379	cell division cycle 2, G1 to S and G2 to M	cell division
1.7471	NM013367	anaphase promoting complex subunit 4	cell division
1.70901	NM003503	cell division cycle 7 homolog (S. cerevisiae)	cell division
1.61844	NM003903	cell division cycle 16 homolog (S. cerevisiae)	cell division
1.61295	NM018451	centromere protein J	cell division
2.85132	NM014679	centrosomal protein 57kDa	growth factor
2.18777	NM001204	bone morphogenetic protein receptor	growth factor
1.65792	NM001752	catalase	growth factor
1.54226	NM000076	cyclin-dependent kinase inhibitor 1C	growth factor
2.6547	NM016631	chromosome 21 open reading frame 66	Transcription factor
2.67115	NM000383	autoimmune regulator	Transcription factor
2.11255	NM005171	activating transcription factor 1	Transcription factor
1.83665	NM013354	CCR4-NOT transcription complex, subunit 7	Transcription factor
2.41006	NM001010853	peptidase M20 domain containing 2	Peptidase activity
2.1185	NM001304	carboxypeptidase D	Peptidase activity
2.08833	NM018394	abhydrolase domain containing 10	Peptidase activity
1.63574	NM005186	calpain 1, (mu/l) large subunit	Peptidase activity

Generally, most of the up-regulated genes in MDA231 cells due to the exposure to the 10 kHz AC frequency field are for mitosis, proteolysis, cell proliferation, cell division, growth factor, transcription factor and peptidase activity whereas the down-regulated genes are involved in sensory perception, cell adhesion, cell signaling, signal transduction, cell-matrix adhesion and transcription factor activity as shown in Table 6.2.

Table 6.2: Representative list of under-expressed genes in MDA231 cells that experienced nDEP phenomenon versus control cells

Fold change	GenBank accession no.	Gene name	Function
- 1.4366	NM020321	amiloride-sensitive cation channel 3	Sensory perception
-1.5113	NM139030	CD151 molecule (Raph blood group)	Sensory perception
-1.54767	NM004935	cyclin-dependent kinase 5	Sensory perception
-2.59148	NM199004	arrestin, beta 2	Sensory perception
-7.83586	NM001681	ATPase, Ca++ transporting, cardiac muscle, slow twitch 2	Cell adhesion
-4.4927	NM001001392	CD44 molecule (Indian blood group)	Cell adhesion
-2.17619	NM201414	amyloid beta (A4) precursor protein	Cell adhesion
-2.14746	NM005158	cadherin-like 24	Cell adhesion
-1.59985	NM016174	cerebral endothelial cell adhesion molecule	Cell adhesion
-2.78065	NM001784	CD97 molecule	Cell signaling
-2.24884	NM001200	bone morphogenetic protein 2	Cell signaling
-1.51564	NM004335	bone marrow stromal cell antigen 2	Cell signaling
-8.18455	NM000064	complement component 3	Signal transduction
-7.85659	NM001660	ADP-ribosylation factor 4	Signal transduction
-3.55567	NM006449	CDC42 effector protein (Rho GTPase binding) 3	Signal transduction
-3.40821	NM212460	ADP-ribosylation factor-like 4A	Signal transduction
-3.25076	NM001018159	NEDD8 activating enzyme E1 subunit 1	Signal transduction
-2.69307	NM199002	Rho guanine nucleotide exchange factor	Signal transduction
- 1.32495	NM001706	B-cell CLL/lymphoma 6	cell-matrix adhesion
- 1.32887	NM016446	chromosome 9 open reading frame 127	cell-matrix adhesion
-1.36479	NM003815	ADAM metallopeptidase domain 15	cell-matrix adhesion
- 4.4927	NM001001392	CD44 molecule (Indian blood group)	cell-matrix adhesion
- 2.54958	NM001040619	activating transcription factor 3	Transcription factor activity
-2.388	NM003670	basic helix-loop-helix family, member e40	Transcription factor activity
-2.29442	NM004364	CCAAT/enhancer binding protein (C/EBP), alpha	Transcription factor activity
-1.72648	NM001675	activating transcription factor 4 (tax-responsive enhancer element B67)	Transcription factor activity

6.8. Discussion

This investigation seems to be the first Microarray study on the effect of AC field exposure on living cells. The cell line MDA231 was taken as a model in the present work. Insignificant changes in the genes expressions have been found due to the exposure to 100 kHz AC field of potential 20 volts peak-to-peak. At the same time as, considerable changes in the expression of 75% of the studied genes, with 39% of the genes being over-expressed and 36% being under-expressed have been found due to the exposure to 10 kHz AC field of potential 20 volts peak-to-peak. Important genes are reported to be altered by the exposure to AC electric field. Represented list for these genes is listed in Tables 6.1 and 6.2.

The present study shows that it is preferable to perform the separation of cells at high AC frequency in range of 100 kHz. This is possible by increasing the conductivity of medium to change the crossover frequency of the targeted cells. The crossover frequency of several cell lines suspended in sucrose/dextrose medium with conductivity 10 and 20 mS/m is shown in Figure 6.11 (a) and (b) respectively. This method should enable the re-culture of cells after separation ensuring minimal gene modification during separation process.

It was experimentally found that working at low frequency that is less than 1 kHz causes chromium corrosion and water electrolyzing and both phenomena happen faster at higher potential and lower frequency. Moreover, corrosion and electrolyzing are found to be at higher frequency with higher conductivity of medium. Figure 6.12 shows the corrosion of the electrodes layer for one of the designs that was used in the experiments.

In conclusion, this study is the first investigation to classify the gene targets of DEP manipulation using microarray analysis. Moreover, further investigations about the effect of the conductivity of medium on the separation of cells and corrosion of the microdevice have to be performed.

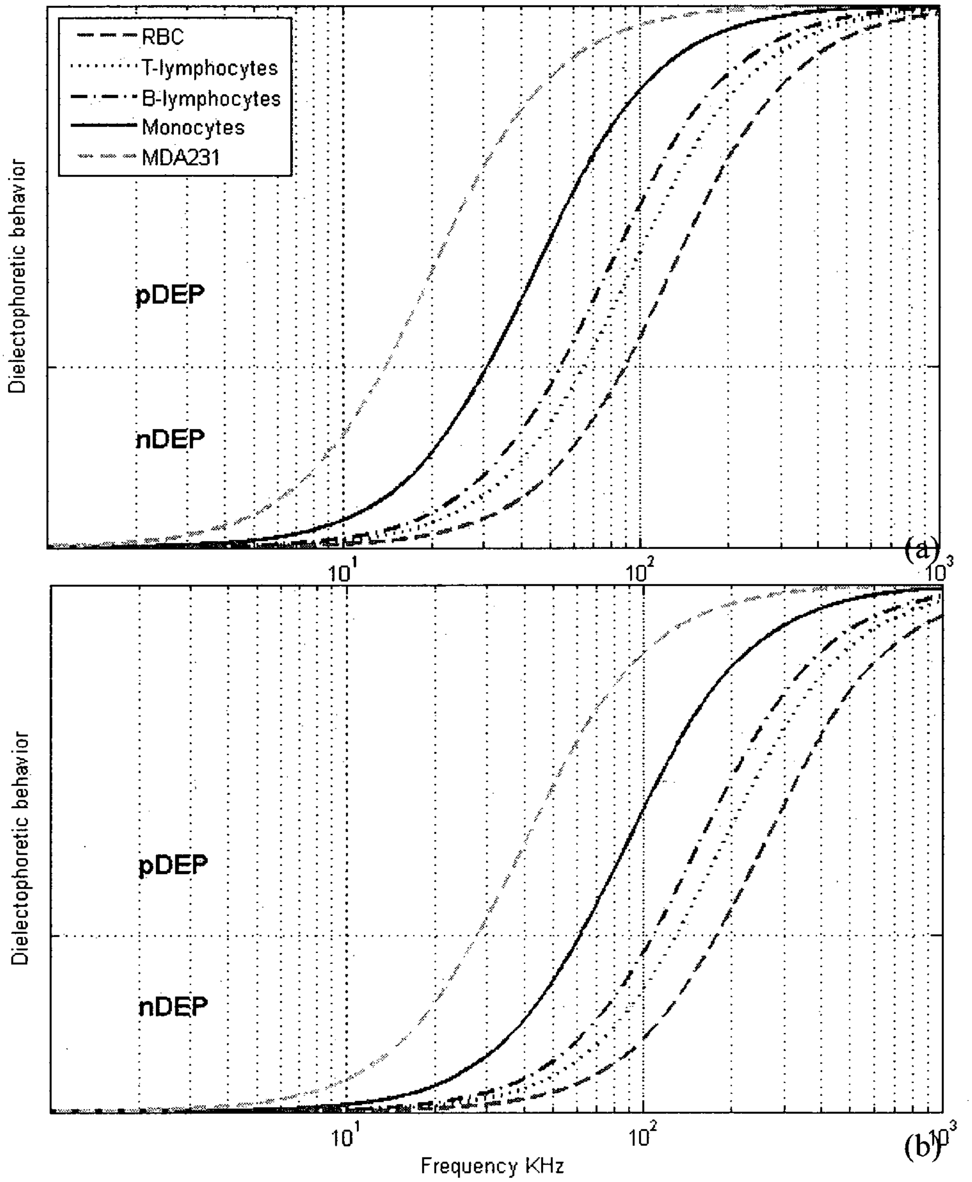

Figure 6.11: Cross over frequency for several cell lines, (a) for conductivity of medium of 10 mS/m and (b) 20 mS/m.

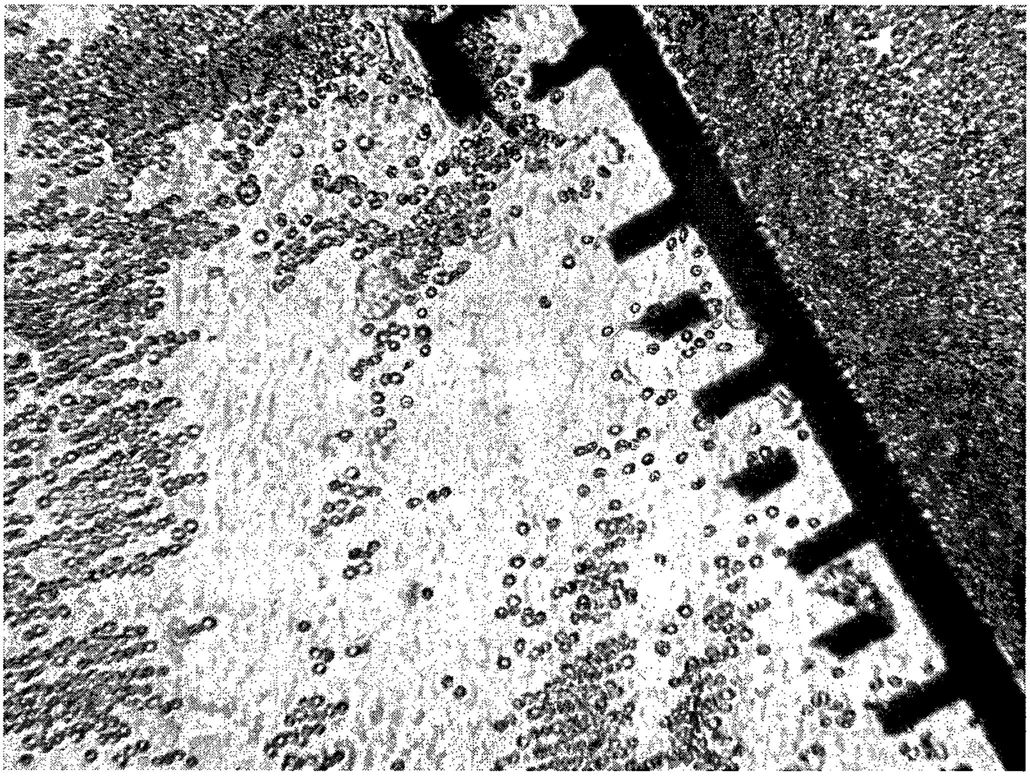

Figure 6.12: Corrosion of the chromium electrodes layer. Conductivity of medium is 20 mS/m, frequency is 200Hz and potential of 20 volts peak-to-peak.

6.9. Summary

In this chapter the experimental results of the separation process was discussed. Separation of MDA231 cells from diluted blood has been achieved with the desired accuracy that is close to 100%. The experimental results were matched with the analytical ones that were discussed in chapter 4. Excellent agreement between the experimental results and the expected path lines of the cells was found. The small size of the presented device and the ability to stack several layers of the design makes it possible to reach flow rate that enables point of care tests.

The second part of the chapter discussed the effect of DEP manipulation of living cells. The changes in genes expression due to the exposure to AC field of 10 kHz and 100 kHz were investigated using microarray analysis. The exposure of living cells to low frequency AC field was found to alter 75% of the genes compared to only 24% in case of high AC frequency. Moreover, the fold change of the altered genes was higher in case of low frequency AC field. As a result, higher AC frequency in range of 100 kHz is recommended for DEP applications in order to not affect the cells.

Chapter 7 : Summary, Contributions and Future Work

7.1. Summary and conclusion of the research study

Cancer is considered to be the second cause of death in the United states of America and other parts of the world [219]. The findings presented in this work are believed to be an important step forward towards developing a microfluidic device that can be implemented in point-of-care systems for early detection of cancer. Same type of device could be used in the follow up of patients that have been treated from cancer.

The first chapter of the thesis reviews the open literature on separation of living cells and particles, blood cells and fluid behavior in microsystems and the fabrication of microfluidic devices. The next chapter discussed the pressure driven flow in microchannels. The fluid flow behavior in trapezoidal, semi circular and rectangular microchannels has been investigated. Rectangular cross sectional microchannels were found to be the best fit among the studied microchannels for rapid separation of cells.

Analytical solutions for electric field and dielectrophoretic force for interdigitated and moving dielectrophoresis were driven using Fourier series in chapter three. The derivation of DEP force generated by non-uniform interdigitated electrode array is presented in the first part of the chapter. The derived expression has been compared with numerical results and previously proposed solution existents in the open literature. Results show that the present model is more versatile and more accurate than the precedent work and it represents a significant contribution toward the understanding of the DEP phenomena with application to living cell separation.

The recently introduced moving dielectrophoresis as a method of moving cells in microchannel was considered in the second part of chapter three. An analytical solutions using Fourier series were presented for the electric field distribution and dielectrophoretic force generated inside of a microchannel. Comparison for the results with numerical and experimental data shows excellent agreement.

Numerical simulation of DEP force, modeling and fabrication of the cells separation device were discussed in chapter four. Few iterations were performed to achieve the final microfluidic device. The new microdevice for continuous separation of living cells is presented. The device separates malignant cells from blood based on DEP phenomena. Path lines of malignant cells and blood cells have been found based on the numerical results and confirmed experimentally. The final microfluidic chip is capable to separate malignant cells from blood continuously with a flow rate of 0.1 ml/hr.

Treatment of cells with carbon nanotubes to enhance the separation speed was investigated in chapter five. CNTs were found not to affect the cells membrane capacitance. Bio-compatibility of the CNTs with the living cells has been studied using microarray analysis. CNTs were found to alter important genes that were reported in the chapter.

The method of separation, cells and medium preparation and experimental setup were explained in chapter six. The experimental results matched the path lines of cells found in chapter four. Separation reached 100% accuracy based on direct screening of the separation process. The changes in genes expressions occur due to the exposure of MDA231 cells to 10 kHz (where cells experienced nDEP) and 100 kHz AC field (where the studied cells experienced pDEP) have been studied using microarray analysis. Cells under nDEP found to have significant change in genes expressions compared to cells under pDEP phenomenon.

This work presented a novel microfluidic device for separation malignant cells from blood with high accuracy. The device is based on DEP phenomena which also found to have a little effect on living cells if the applied frequency in range of 100 kHz. The presented device can be implemented in point-of-care systems for early detection of cancer.

7.2. Contributions

In this thesis, a method of separation malignant cells from blood is presented. The first contribution is the analytical solution for non-uniform interdigitated electrodes presented in chapter three. Fourier based solution for moving dielectrophoresis is another contribution derived in chapter three. Both analytical formulations are presented for the first time and can be used to derive models for cells movement in DEP based microdevices.

The influence of the geometry on DEP separation device found is the third contribution of this work. DEP force was found to be higher between smaller size gap and electrodes. Different applications of DEP devices required different size of electrodes. The effect of the electrodes and gap size on different applications of DEP was discussed in chapter three.

The fourth contribution is the new separation microfluidic device is presented in chapter four. Small size microdevice for continuous separation of living cells was proposed. Numerical and analytical results matched the experimental separation data which supported the efficiency of the device.

The fifth contribution is represented by the results of the study of carbon nanotubes effect on human normal epithelial cells. For the first time a complete list of gene targets of SWCNTs in human normal bronchial epithelial cells was reported. The presented gene identification is believed to be helpful in the discovery of the real effect of new materials and technologies on human health.

The sixth contribution represents the finding of full microarray study on the effect of nDEP and pDEP manipulation of cells. Changes in genes expressions due to the exposure to AC field of 10 kHz and 100 kHz are presented in chapter 6. For the first time the altered genes due to DEP manipulation are reported. Low AC field frequency in range of 10 kHz was found to alter 75 % of the genes while high frequency in range of 100 kHz affects only 24% of the studied genes.

The rest of this thesis includes experimental work on cell separation and validation of the analytical results using living cells which represent a contribution to the research area.

7.3.Areas of future research

The present work uses single layer of electrodes in the separation device. Two layers of electrodes are expected to improve the separation process and increase the separation speed. In addition, further studies and systematic optimization are needed on the configuration of the electrodes.

The effects of DEP manipulation on normal healthy living cells need to be investigated. Moreover, continuous separation of malignant cells from real blood that is taken from patients is required. Furthermore, one needs to optimize the method of stacking several microfluidic devices in order to enable point-of-care tests.

Increasing the separation speed by repeating the presented design as shown in Figure 7.1 needs to be studied. The distance between first design and the next one should be optimized in order not to allow any targeted cells from passing the electrodes barrier. Cells passing at a distance above the electrodes experience weak DEP force. Therefore, cells need to move close to the electrode layer for better separation speed and accuracy. The distance between the electrodes should be optimized such that cells have enough time to flow close to the electrodes.

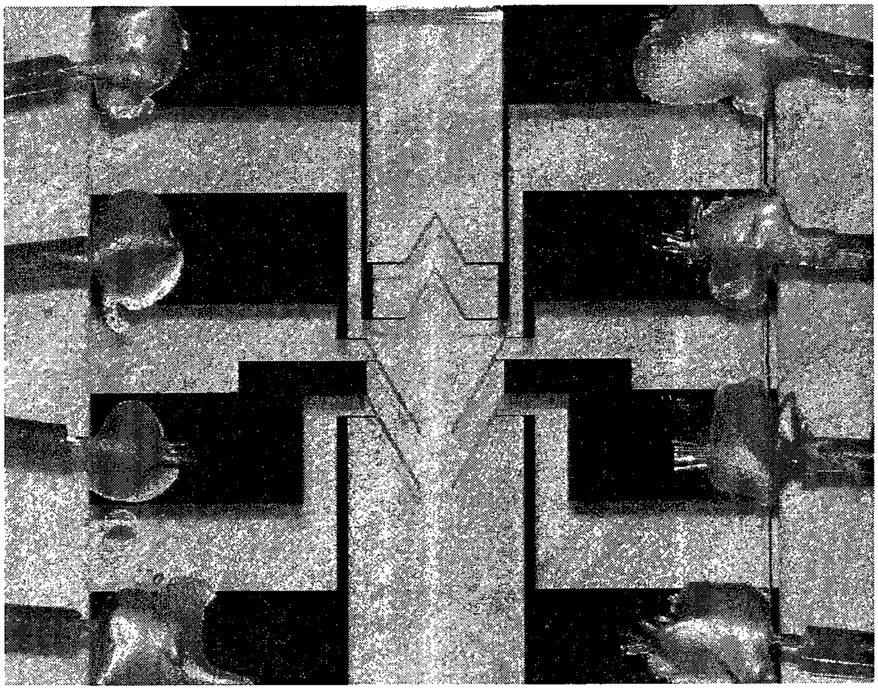

Figure 7.1: Repeating the electrodes patterns in order to increase the separation accuracy and speed

The influence of the conductivity of medium on the separation accuracy and speed needs to be determined at different AC field frequencies. Moreover, DEP manipulation techniques in high conductivity of medium including cells food without having any corrosion of electrodes or water electrolysis are needed.

Chromium electrodes with size greater than 10 µm have been used in the present work. Nanoscale electrodes or electrodes in size of less than 1 µm or using other metals for electrodes layer is also an area for future work.

Appendix A

Analytical Formulation of Electric Field and Dielectrophoretic Force for Moving Dielectrophoresis Using Fourier Series

A.1. Abstract

Electrokinetics manipulation and separation of living cells employing microfluidic devices require good knowledge of the strength and distribution of electric field in such devices. AC dielectrophoresis is performed by generating non uniform electric field using microsize electrodes. Among the several applications of dielectrophoretic phenomenon the present study considers the recently introduced phenomenon of moving dielectrophoresis. An analytical solution using Fourier series is presented for the electric field distribution and dielectrophoretic force generated inside a microchannel. The potential at the upper part of the microchannel has been found by solving the governing equation of the electric potential with specific boundary conditions. The solutions for the electric field and dielectrophoretic force show excellent agreement with the numerical results. Microdevices were fabricated and experiments were carried out with living cells confirming and validating the analytical solutions.

A.2. Introduction

Electrokinetics phenomenon is extensively used in applications dealing with both the separation and the transport of biological molecules and particles in microchannels. Two relevant electrokinetics techniques used in the lab-on-a-chip applications are the electrophoresis and dielectrophoresis phenomena. Electrophoresis represents the movement of charged particles due to the influence of the uniform electric field while dielectrophoresis (DEP) [31] is the motion of neutral, polarisable particles subjected to a non-uniform electric field. The magnitude and the direction of the force experienced by particles in the DEP situation depends on the amplitude and frequency of the applied AC electric field and the dielectric properties of the particle and its medium of submersion [31].

Dielectrophoretic phenomenon has been extensively used in microdevices for living cell manipulation [27, 36-38] because they use the natural properties of those cells. Moreover, dielectrophoresis is considered one of the fastest noninvasive separation techniques which is a critical requirement for any lab assay. In addition, cell separation using dielectrophoretic phenomenon holds promise for other biological applications especially concerning disease diagnostics [39, 46]. As an illustrative application different types of cells including yeast cells, lymphocytes and cancer cells [27, 69, 82] have been separated from a mixture using DEP based microdevices.

In order to compute the DEP force acting on a cell, a formulation for the electric field should take into consideration the various configurations of electrodes required by the dielectrophoretic applications. The specific case regarding the presence of interdigitated electrodes for cell separation and the recently introduced moving dielectrophoresis must be included in these studies. Several approximate solutions for the potential and DEP force over interdigitated electrodes have been reported in the open literature. These solutions are based on Fourier series [1, 222, 223], Green's function [65, 224], Green's theorem [225], Schwarz-Christoffel mapping method [226, 227] or other numerical methods [228, 229]. Fourier series and Green's theorem approximation solutions assume the potential to be linear between adjacent electrodes. The solution proposed in [223] includes the Neumann boundary conditions at the upper part of the chamber but the potential in the gap between adjacent electrodes is assumed to be linear. However, Schwarz-Christoffel mapping requires a more complex approach demanding, for example, the calculation of several elliptical integrals. One of the most recent developments of the dielectrophoretic phenomenon is called moving dielectrophoresis [87] due to the fact that the real-time fractionation and transportation of cells is achieved by sequentially energizing the electrodes present in the microchannel as shown in Figure A-1.a. The mechanism involved in the energizing of the adjacent electrodes that generates the cell advancement. This process is illustrated in Figure A-1.b. The entire lower part of the channel forms a single electrode while the one on the upper part includes a series of adjacent electrodes of length d at a gap of g between them.

An analytical expression for electric potential, electric field and DEP force for moving DEP was reported using Wiener–Hopf method [230]. The analytical solution treated the microchannel into two separate domains where the electric potential, electric field and DEP force were described using different formulation in each domain. In the present work another simple formulation is proposed, for electric potential, electric field and DEP force using Fourier series. The new expressions for the three parameters have the advantage that can be applied over the entire microchannel domain using a single formula.

To the authors knowledge this work presents an alternative methodology to find a solution for the electric potential, the electric field and the DEP force for moving dielectrophoresis applications, by using Fourier series. The following section presents the theory of the electric field and electric potential with the associated physical structure and boundary conditions.

A.3. Theory

The expression of dielectrophoretic force acting on a spherical polarisable cell placed in a non-uniform electrical field and immersed in a medium is given by the equation [42, 71].

$$F_{DEP} = \pi \varepsilon_0 \varepsilon_m r^3 Re[f_{CM}] \nabla |E|^2 \quad (162)$$

where ε_0 is the vacuum dielectric constant, ε_m is the suspending medium dielectric constant, r is the particle radius, Re$[f_{CM}]$ is the real part of Clausius-Mossotti factor and E represents the applied electric field.

In order to develop the model for the movement of the cell in the microchannel, the dielectrophoretic force must be known. Therefore a mathematical formulation for the distribution of the electric field between the electrodes has to be identified.

In order to generate the relation, we consider the expression of the electric field given by Gauss's law as follows:

$$\nabla . \boldsymbol{E} = \frac{\rho}{\varepsilon_0} \quad (163)$$

where ρ is the total electric charge density. In the present case the charge density including both the free and the bounded charge is zero. Equation (163) becomes:

$$\nabla . \boldsymbol{E} = 0 \quad (164)$$

The quasi-electrostatic form of Maxwell's equation relates the electric field with the electric potential in the following formulation:

$$\boldsymbol{E} = -\nabla \varphi \quad (165)$$

where φ represents the electric potential.

Substitution of equation (165) into (164) yields:

$$\frac{\partial^2\varphi}{\partial x^2}+\frac{\partial^2\varphi}{\partial y^2}+\frac{\partial^2\varphi}{\partial z^2}=0 \tag{166}$$

Under the assumption that the width of the microchannel is sufficiently large, the system is simplified to the schematic illustrated in Figure A-2 where Laplace equation (166) becomes:

$$\frac{\partial^2\varphi}{\partial x^2}+\frac{\partial^2\varphi}{\partial y^2}=0 \tag{167}$$

The following boundary conditions are taken into consideration:

1. The finite-size upper electrode is energized at a potential V_0.
2. The upper part of the channel is insulated; change of potential across the upper part of the considered segment is set to zero.
3. The bottom electrode is grounded.
4. The change in potential at the right side, which is theoretically at infinity, is assumed to be zero. The right side of the unit segment is assumed to be at a finite distance L from the left extremity of the considered unit segment.
5. The unit segment is symmetrical about y-axis (left side).

The boundary conditions applied for the Laplace equation (167) are:

$$\varphi(x,H)=V_0 \qquad 0\le x\le\frac{d}{2} \tag{168}$$

$$\frac{\partial\varphi}{\partial y}(x,H)=0 \qquad \frac{d}{2}\le x\le L \tag{169}$$

$$\varphi(x,0)=0 \tag{170}$$

$$\frac{\partial\varphi}{\partial x}(L,y)=0 \tag{171}$$

$$\frac{\partial\varphi}{\partial x}(0, y) = 0 \tag{172}$$

To normalize the equation with respect to the specific coordinates, the following dimensionless parameters are assumed:

$$\bar{x} = \frac{x}{L} \tag{173}$$

$$\bar{y} = \frac{y}{H} \tag{174}$$

Substituting equations (173) and (174) into (167) yields:

$$\frac{\partial^2\varphi}{L^2\partial\bar{x}^2} + \frac{\partial^2\varphi}{H^2\partial\bar{y}^2} = 0 \tag{175}$$

Using the non-dimensional parameters in equations (173) and (174), the boundary conditions become:

$$\varphi(\bar{x}, 1) = V_0 \qquad 0 \leq \bar{x} \leq \frac{d}{2L} \tag{176}$$

$$\frac{\partial\varphi}{\partial\bar{y}}(\bar{x}, 1) = 0 \qquad \frac{d}{2L} \leq \bar{x} \leq 1 \tag{177}$$

$$\varphi(\bar{x}, 0) = 0 \tag{178}$$

$$\frac{\partial\varphi}{\partial\bar{x}}(1, \bar{y}) = 0 \tag{179}$$

$$\frac{\partial\varphi}{\partial\bar{x}}(0, \bar{y}) = 0 \tag{180}$$

Equations (177) can be written in the form:

$$\varphi(\bar{x}, 1) = \varphi_g(\bar{x}) \qquad \frac{d}{2L} \leq \bar{x} \leq 1 \tag{181}$$

where $\varphi_g(\bar{x})$ represent the electrical potential distribution function at the top part of the microchannel from the edge of the finite-size electrode to the right side of the considered segment.

With all the equations modeling the dielectrophoretic phenomena and the boundary conditions the next paragraphs describe the solution of these equations using Fourier series to determine the exact value of the electric filed and electric potential within the environment of the complete structure.

A.4. Solution of the governing equations by Fourier series

Based on the nature of the boundary conditions and using the separation of variables technique, the present work assumes the solution to be superposition of two solutions that satisfy Laplace equation; linear part and a harmonic form as follows,

$$\varphi(\bar{x},\bar{y}) = A + B\bar{x} + C\bar{y} + D\bar{x}\bar{y} + F(\bar{x})G(\bar{y}) \tag{182}$$

where A, B, C and D are constants. Since the electrode at the bottom part of the channel is grounded, the constants A and B are assumed to be zero.

Following the separation of variables technique the subsequent formulation is obtained:

$$\varphi(\bar{x},\bar{y}) = C\bar{y} + D\bar{x}\bar{y} + (a_0\cos(K\bar{x}) + a_1\sin(K\bar{x}))\left(b_0 e^{\frac{KH}{L}\bar{y}} + b_1 e^{\frac{-KH}{L}\bar{y}}\right) \tag{183}$$

Substituting the boundary conditions (178), (179) and (180) in (183) yields:

$$\varphi(\bar{x},\bar{y}) = C\bar{y} + \sum_{n=1}^{\infty} \mathrm{C_n}(\cos(K\bar{x}))\left(e^{\frac{KH}{L}\bar{y}} - e^{\frac{-KH}{L}\bar{y}}\right) \tag{184}$$

where $\mathrm{C_n}$ is a constant and $K = n\pi$.

The nature of the potential at the upper part of the microchannel requires solving Laplace's equation between the edge of the finite electrode and the right side of the unit segment represented in Figure A-3. To overcome the analytical solution of equation (184, a new potential function is created with new coordinates and set of boundary conditions.

This interesting technique will permit the solution of Laplace equation with this new potential function:

$$\frac{\partial^2\varphi_g}{\partial x_g^2}+\frac{\partial^2\varphi_g}{\partial {y_g}^2}=0 \tag{185}$$

$$\varphi_g(0,y_g)=V_0 \qquad\qquad y_g\leq T_h \tag{186}$$

$$\varphi_g(\infty,y_g)=0 \tag{187}$$

where $\mathrm{T_h}$ is the thickness of the electrodes layer and $\mathrm{x_g}$, $\mathrm{y_g}$ are the coordinates inside the considered domain (Figure A-3). Since the electrodes are deposited on an insulated layer the following boundary condition is implied:

$$\frac{\partial\varphi_g}{\partial y_g}(x_g,0)=0 \tag{188}$$

In order to use dimensionless coordinates in equation (185), the following dimensionless parameters are proposed:

$$\bar{x}_g=\frac{x_g}{H} \tag{189}$$

$$\bar{y}_\mathrm{g}=\frac{y_g}{\mathrm{T_h}} \tag{190}$$

The dimensionless form of equation (185) and its boundary conditions are:

$$\frac{\partial^2\varphi_g}{H^2\partial\bar{x}_g^2}+\frac{\partial^2\varphi_g}{T_h^2\partial{\bar{y}_g}^2}=0 \tag{191}$$

$$\varphi_g(0,\bar{y}_g)=V_0 \qquad\qquad \bar{y}_g\leq 1 \tag{192}$$

$$\varphi_g(\infty,\bar{y}_g)=0 \tag{193}$$

$$\frac{\partial\varphi_g}{\partial\bar{y}_g}(\bar{x}_g,0)=0 \tag{194}$$

Using the separation of variables principle, the solution of equation (191) is assumed to take the form:

$$\varphi_g(\bar{x}_g, \bar{y}_g) = F_g(\bar{x}_g) G_g(\bar{y}_g) \tag{195}$$

Following the standard procedure of separation of variables the solution becomes:

$$\varphi_g(\bar{x}_g, \bar{y}_g) = \left(C_{1g} e^{(K_g \bar{x}_g)} + C_{2g} e^{(-K_g \bar{x}_g)}\right)\left(C_{3g} cos\left(\frac{T_h K_g}{H} \bar{y}_g\right) + C_{4g} sin\left(\frac{T_h K_g}{H} \bar{y}_g\right)\right) \tag{196}$$

where C_{1g}, C_{2g}, C_{3g} and C_{4g} are constants and K_g is the separation constant as function of n. Substituting the boundary condition (193) and (194) yields:

$$\varphi_g(\bar{x}_g, \bar{y}_g) = \sum_{n=1}^{\infty} C_{5g} e^{-K_g \bar{x}_g} cos\left(\frac{T_h K_g}{H} \bar{y}_g\right) \tag{197}$$

where C_{5g} is a constant. A new substitution for the boundary conditions (192) gives:

$$V_0 = \sum_{n=1}^{\infty} C_{5g} cos\left(\frac{T_h K_g}{H} \bar{y}_g\right) \tag{198}$$

The dimensionless variable $\bar{y}_g$ ranges between 0 and 1. The maximum value for the term $\cos\left(\frac{T_h K_g}{H} \bar{y}_g\right)$ is 1 while the minimum value is $\cos\left(\frac{T_h K_g}{H}\right)$. The cosine term in equation (198) can be neglected if the value of the term approaches 1. This work assumes zero thickness for the deposited electrodes. Therefore solving equation (198) for C_{5g} gives:

$$C_{5g} = \frac{V_0}{2^n} \tag{199}$$

As a result, the potential distribution at the upper part of the microchannel is written as:

$$\varphi(\bar{x}\ \ ,1) = V_0 \qquad 0 \le \bar{x} \le \frac{d}{2L} \tag{200}$$

$$\varphi_g\left(\bar{x}_g, 1\right) = \sum_{n=1}^{\infty} \frac{V_0}{2^{\mathrm{n}}} e^{-n\beta\,\bar{x}_g} \qquad \frac{d}{2L} \ \le \bar{x} \le 1 \tag{201}$$

where $n\beta = K_g$ and β is a constant to be determined. The two boundary conditions (200) and (201) can be joined as one boundary condition using the Fourier cosine series as follows:

$$\varphi(\bar{x}, 1) = A_0 + \sum_{m=1}^{\infty} A_m cos(m\pi\bar{x}) \qquad 0\ \le \bar{x} \le 1 \tag{202}$$

where:

$$A_0 = V_0 \left[R + \sum_{m=1}^{\infty} \frac{H}{2^m mL\beta} \right] \tag{203}$$

$$A_m = 2V_0 \left[\frac{sin(m\pi R)}{m\pi} + \sum_{n=1}^{\infty} \frac{n\beta L cos(m\pi R) - m\pi H sin(m\pi R)}{2^n H(\beta^2 n^2 L^2 + m^2\pi^2 H^2)} \right] \tag{204}$$

Substituting of the boundary condition (202) in equation (184) gives:

$$C = A_0 \tag{205}$$

$$C_n = \frac{A_m}{\left(e^{\frac{n\pi H}{L}} - e^{\frac{-n\pi H}{L}}\right)} \tag{206}$$

The profile of the electric potential inside the unit segment used for the formulation is given by the equation:

$$\varphi(\bar{x}, \bar{y}) = A_0\bar{y} + \sum_{n=1}^{\infty} \frac{A_m}{sinh\left(\frac{n\pi H}{L}\right)} \left(\cos(n\pi\bar{x})\right) sinh\left(\frac{n\pi H}{L}\bar{y}\right) \tag{207}$$

Using the Gaussian surface shown in dashed line in Figure A-2 the following equality is found.

$$H\int_0^1 A_0\bar{y}+\sum_{n=1}^{\infty}\frac{A_m}{sinh\left(\frac{n\pi H}{L}\right)}\cos(n\pi R)sinh\left(\frac{n\pi H}{L}\bar{y}\right)d\bar{y}=H\int_0^{\infty}\sum_{n=1}^{\infty}\frac{V_0}{2^{\mathrm{n}}}e^{-n\beta\bar{x}_g}\,d\bar{x}_g \tag{208}$$

The arrangement of equation (47) gives:

$$\left(A_0+\sum_{n=1}^{\infty}\frac{A_mL}{n\pi Hsinh\left(\frac{n\pi H}{L}\right)}\cos(n\pi R)\left(sinh\left(\frac{n\pi H}{L}\bar{y}\right)-1\right)\right)-\sum_{n=1}^{\infty}\frac{V_0}{2^{\mathrm{n}}n\beta}=0 \tag{209}$$

Equation (209) was solved using MATLAB™ in order to determine the value of the constant β at different microchannel height. Figure A-4 shows the variation of the constant β as the microchannel height changes. No relation between the constant β and the distance d was found for value of length L that is greater than 5H.

A.5. Electric field and dielectrophoretic force

The electric field is calculated using equation (165) as follows:

$$E(\bar{x},\bar{y})=E_x\boldsymbol{i}+E_y\mathbf{j} \tag{210}$$

where **i** and **j** are unit vectors along the $\bar{x}$ and $\bar{y}$ directions, respectively. E_x and E_y are the components of the electric field vector:

$$E_x(\bar{x},\bar{y})=\sum_{n=1}^{\infty}\frac{A_m n\pi}{Lsinh\left(\frac{n\pi H}{L}\right)}\sin(n\pi\bar{x})sinh\left(\frac{n\pi H}{L}\bar{y}\right) \tag{211}$$

$$E_y(\bar{x},\bar{y})=\frac{-A_0}{H}-\sum_{n=1}^{\infty}\frac{n\pi A_m}{Lsinh\left(\frac{n\pi H}{L}\right)}cos(n\pi\bar{x})cosh\left(\frac{n\pi H}{L}\bar{y}\right) \tag{212}$$

Equation (162) implies that the dielectrophoretic force acting on particle or cell in the channel is proportional to the gradient of electric field intensity. Therefore, the gradient of electric field intensity can be expressed as a combination of vector components

$$F_{DEP} = \pi\varepsilon_0\varepsilon_m r^3 \mathrm{Re}[f_{CM}]\left(\xi_{DEP_x}\boldsymbol{i} + \xi_{DEP_y}\boldsymbol{j}\right) \tag{213}$$

where ξ_{DEP_x} and ξ_{DEP_y} are the components of $\nabla|E|^2$ vector created by the electrodes and are given as follows:

$$\begin{aligned}\xi_{DEP_x}(\bar{x},\bar{y}) = {} & 2\left(\sum_{n=1}^{\infty}\frac{A_n n\pi}{L\sinh\left(\frac{n\pi H}{L}\right)}\sin(n\pi\bar{x})\sinh\left(\frac{n\pi H}{L}\bar{y}\right)\right)\left(\sum_{n=1}^{\infty}\frac{A_n n^2\pi^2}{L^2\sinh\left(\frac{n\pi H}{L}\right)}\cos(n\pi\bar{x})\sinh\left(\frac{n\pi H}{L}\bar{y}\right)\right) \\ & - 2\left(\frac{A_0}{H} + \sum_{n=1}^{\infty}\frac{n\pi A_n}{L\sinh\left(\frac{n\pi H}{L}\right)}\cos(n\pi\bar{x})\cosh\left(\frac{n\pi H}{L}\bar{y}\right)\right)\left(\sum_{n=1}^{\infty}\frac{A_n n^2\pi^2}{L^2\sinh\left(\frac{n\pi H}{L}\right)}\sin(n\pi\bar{x})\cosh\left(\frac{n\pi H}{L}\bar{y}\right)\right)\end{aligned} \tag{214}$$

$$\begin{aligned}\xi_{DEP_y}(\bar{x},\bar{y}) = {} & 2\left(\sum_{n=1}^{\infty}\frac{A_n n\pi}{L\sinh\left(\frac{n\pi H}{L}\right)}\sin(n\pi\bar{x})\sinh\left(\frac{n\pi H}{L}\bar{y}\right)\right)\left(\sum_{n=1}^{\infty}\frac{A_n n^2\pi^2}{L^2\sinh\left(\frac{n\pi H}{L}\right)}\sin(n\pi\bar{x})\cosh\left(\frac{n\pi H}{L}\bar{y}\right)\right) \\ & + 2\left(\frac{A_0}{H} + \sum_{n=1}^{\infty}\frac{n\pi A_n}{L\sinh\left(\frac{n\pi H}{L}\right)}\cos(n\pi\bar{x})\cosh\left(\frac{n\pi H}{L}\bar{y}\right)\right)\left(\sum_{n=1}^{\infty}\frac{A_n n^2\pi^2}{L^2\sinh\left(\frac{n\pi H}{L}\right)}\cos(n\pi\bar{x})\sinh\left(\frac{n\pi H}{L}\bar{y}\right)\right)\end{aligned} \tag{215}$$

Figure A-5 shows the contour plot for the electric potential in the unit segment. Figures A-6 and A-7 show the contour plot of the magnitude of the electric field and the gradient of the term $|E|^2$ respectively calculated using the present solution Comsol Multiphysics^{TM}. The illustrations show that electric field reaches its maximum value at the edge of the finite upper electrode. However, maximum DEP force occurs also at the edge of the upper electrode and it decreases rapidly with the distance from the electrode. The analytical formulation of DEP force presented in this paper can be used in developing models for particles and cells movement in microchannel.

A.6. Validation of the results

The results obtained by the above method are compared to those produced by a commercial FEA code. The results obtained using the commercial software are assumed to be close to the exact solution. The analytical results were calculated using MATLAB and the number of terms included in the solution is chosen to be 500 and L value was set to be $10H$. The calculations of electric potential, electrical field and the gradient of $(E.E)$ term were performed using the same number of terms (m=n=500). However, including more terms in the solution causes no change in the results up to four significant digits.

(a) Numerical results

The present solution for the electric potential which described by equation (207) is compared to that found using finite element method software (COMSOL Multiphysics). The analytical results show very good agreement with the numerical data as illustrated in Figures A-5. The mesh size used in the numerical solution was set to be less than 1 μm. Figure A-6 shows the contour plot for the magnitude of the electric field calculated using equations (210-212) compared to the numerical results. The analytical results agree very well with the numerical data.

Figure A-7 shows the analytical contour plots of the magnitude of the gradient of $(E.E)$ term calculated using equations (213-215) compared with the numerical simulation. FEM results show a jagged gradient even with a mesh size that is less than 0.5 μm. This is due to the numerical differentiation used by the software. The results of the analytical solution agree with the numerical simulations and provide smooth gradient for the expression of DEP force. Accordingly, the analytical solution provides more accurate and smoother results for higher order terms like DEP force.

This work assumed the right side of the unit segment to be at a finite distance L from the left extremity. This assumption was validated by observing the change in electric potential as L value changes at different selected points in the domain. Figure A-8 shows the variation in the potential for nine points selected in various locations. These points were selected in order to cover the entire domain. The results show that with the assumption of L value to be more than $5H$ does not influence the results up to 6 significant figures. These results confirm the hypothesis of a finite distance used in this work.

(b) Experimental data

(i) Chip Design and Fabrication

The microdevice used to verify the analytical solution experimentally consists of two main parts: an upper part made of PolyDiMethylSilooxane (PDMS) and a lower part made of glass. For the purpose of validation of the analytical solution several finite-size electrodes of 25 μm spaced by a gap of 50 μm have been deposited on a glass substrate (and not to use the dielectrophoretic phenomenon). The distance between the ground electrode and the finite-size electrode was chosen to be 30 μm (Figure A-9). On the PDMS upper part of the microdevice a microchannel was included having a cross section of 30 μm height and 50 μm width. The PDMS element was fabricated following the normal procedure. Sylgard 184 pre-polymer and curing agent were mixed with weight-ratio 10:1. The mixture was poured in the mold and degasified. After removing all the bubbles from the mixture by degasifying, the mixture was cured in an oven at 80°C for two hours. Finally after curing, the PDMS microchannel was removed from the mold.

Quartz glass substrate was used. Electrodes pattern was designed using AutoCAD and printed using high resolution printers (resolution 50,800 dpi) from a commercial partner (Fineline Imaging, Colorado Springs, CO).

(ii) Cell Preparation

Human blood was obtained from a donor from “Lady Davis Institute for Medical Research” of the Sir Mortimer B. Davis-Jewish General Hospital, Department of

Oncology, Human Genetics and Medicine, McGill University, Montreal, and was treated with EDTA as anticoagulant. In order to separate erythrocytes cells from blood Ficoll-Paque Plus product containing 5.7% w/v FicollTM PM400 and 9% w/v v diatrizoate sodium was mixed with blood anterior diluted two times with phosphate buffered saline plus (PBS+) and 2% fetal bovine serum (2% FBS). The complex solution was mixed at room temperature (19-25°C) for 30 minutes at 400 x g with brake off. The upper plasma layer was isolated without disturbing the interface between FicollTM and plasma. Subsequently the red blood cell layer was removed and suspended in a solution of 8.5% (w/v) sucrose plus 0.4 % (w/v) dextrose buffer that provides a low conductivity medium for the dielectrophoretic phenomenon. Conductivity of medium has been adjusted to 15 mS/m by adding a small quantity of Trypsin in 0.53 mM EDTA.

(iii) Experimental Results

Contour plot of DEP force using the analytical solution is shown in Figure A-10.a. The results show that dielectrophoretic force has a large value all around the finite size electrode and especially at its edge where it reaches its maximum on a semi circular shape. At the same time there is a second peak value for the DEP force close to the ground electrode and parallel to the force created by the finite-sized one as shown in Figure A-10.a.

In order to see the response of the living cells to the DEP manipulation, erythrocytes cells suspended in the sucrose/dextrose low conductivity medium were injected into the test device. An AC signal of 1 MHz and 20 Volts peak to peak was applied to the electrodes. Red blood cells experienced a DEP phenomenon and gathered all around the finite size electrode with the higher density of cells at its edge. At the same time a second cluster of cells accumulated at the bottom part of the channel as shown in Figure A-10 b. Overlapping the contour plot of the dielectrophoretic force and the experimental results in Figure A-10.c, an excellent agreement can be observed.

A.7. Conclusion

Laplace equation has been solved using Fourier series in order to provide an analytical expression for DEP force acting on a particle in the case of moving dielectrophoretic phenomenon. The electric potential at the upper part of the microchannel has been found by solving the governing equation with the specified assumptions. Non homogeneous boundary conditions at the upper part of the electrode have been combined in a single expression using Fourier series. Comparison with finite element results and experimental validation show very good agreement with the computed solution.

The assumption of finite length for the unit segment was validated and the results show that there is no improvement in the accuracy of the solution up to 6 significant figures for a value of the parameter L that is larger than 5H. Moreover, the presented analytical solution shows that the channel height is inversely proportional with the magnitude of the DEP force, as illustrated in Figure A-11.

Analytical expressions for the electric field and the DEP force have been obtained for the case of moving dielectrophoresis. The reported solution can play a novel role in subsequent microfluidics applications regarding manipulation of living cells suspended in liquid phase.

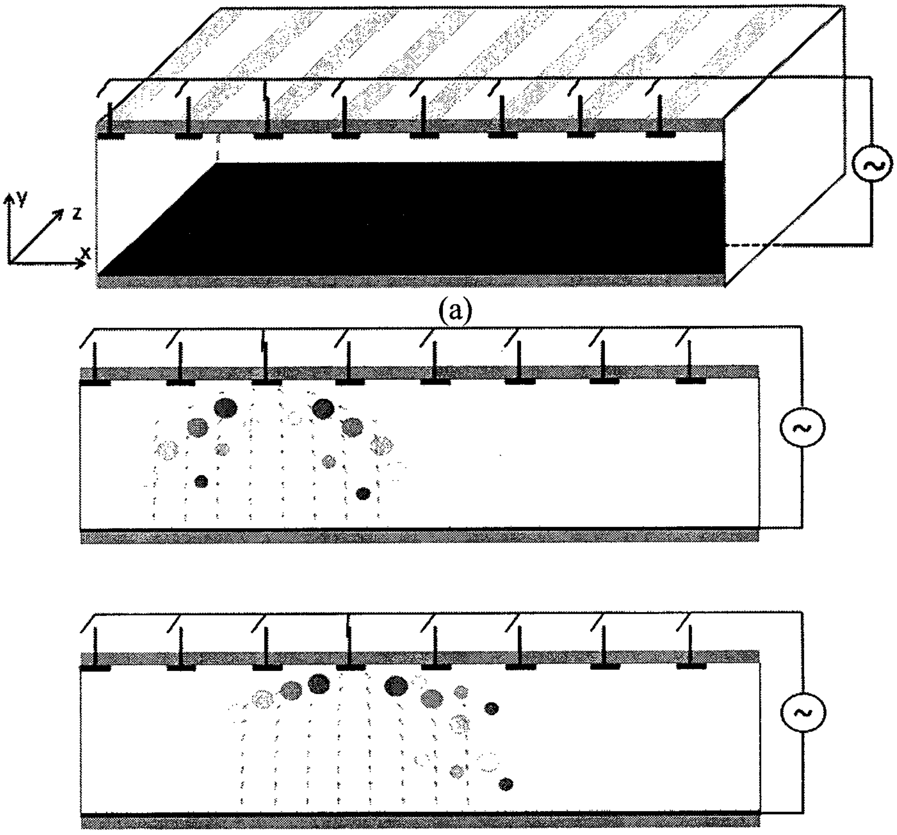

Figure A- 1: Schematic diagram showing the experimental arrangement electrodes used for moving dielectrophoretic devices. Series of finite size electrodes are patterned on the upper part of the channel and single electrode covers the bottom part of the channel. Energizing one of the finite size electrodes "third from the left" influences the movement of cells toward the electrode. (b) 2D schematic diagram showing the cells displacement under the influence of moving dielectrophoresis. The circles represent cells. Small cells were assumed to experience nDEP while large cells experience pDEP. Movement of cells is illustrated using different intensity of the color: a darker nuance represents a more recent position on the trajectory of the cell. In the first part of the diagram only the third finite-size electrode is actuated while in the second part only the fourth electrode. Sequential energizing of the electrodes causes the cells to move in the microchannel due to the dielectrophoretic phenomenon.

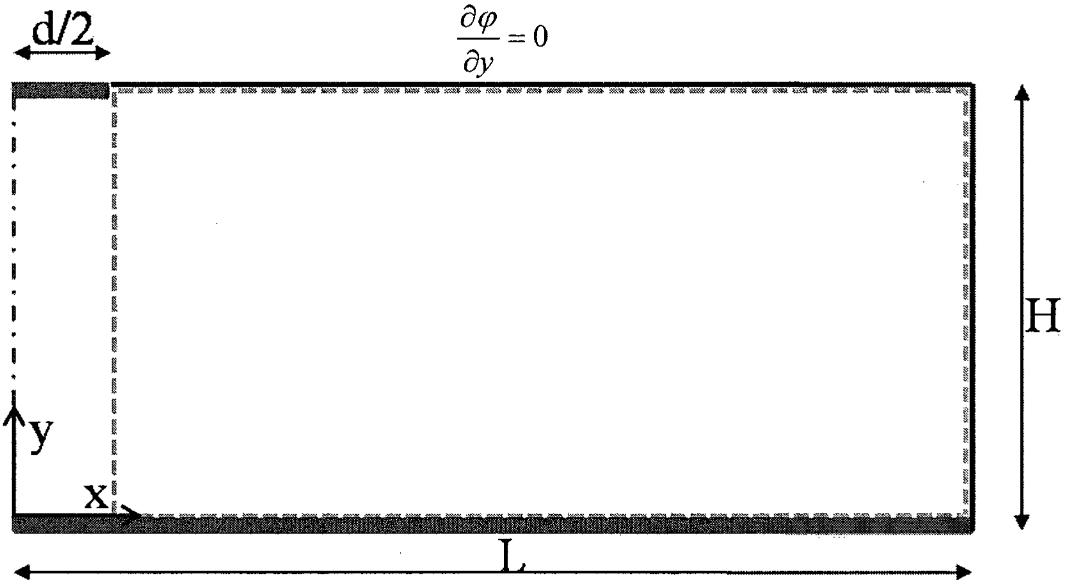

Figure A- 2: Illustration of the geometry of the unit segment and the boundary conditions used in the analytical solution. The unit segment consists of a finite size electrode of length *d/2* with a potential of V_0 and a grounded single electrode covers the entire bottom part. The Gaussian surface used in the solution is shown as dashed line.

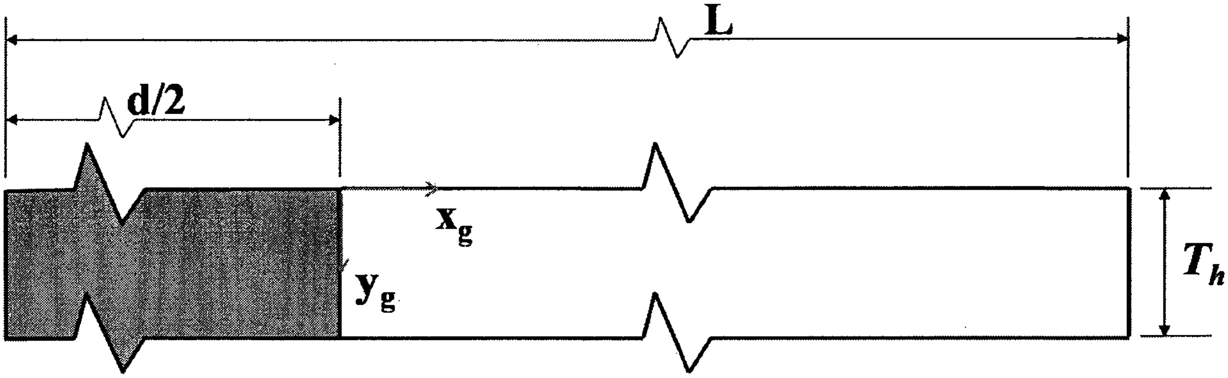

Figure A- 3: Schematic diagram includes the upper part of the microchannel showing the energized electrode and the coordinate system used in the solution to indicate the potential distribution at the upper part of microchannel.

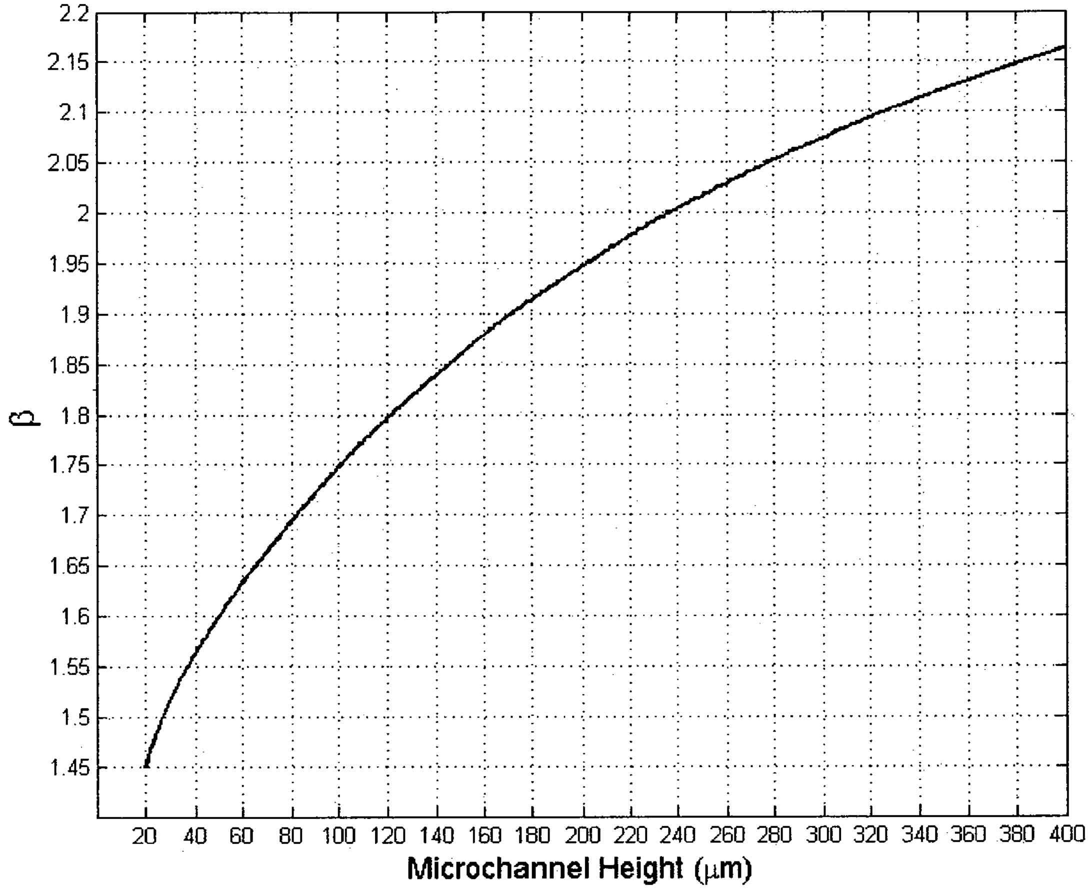

Figure A- 4: The variation of the constant β with the microchannel height H. The constant β is used to describe the potential function at the upper part of the microchannel between the edge of the finite size electrode and the right end of the unit segment. The value of β was calculated up to three significant digits using MATLAB based on equation (48) with (m=n= 500 terms).

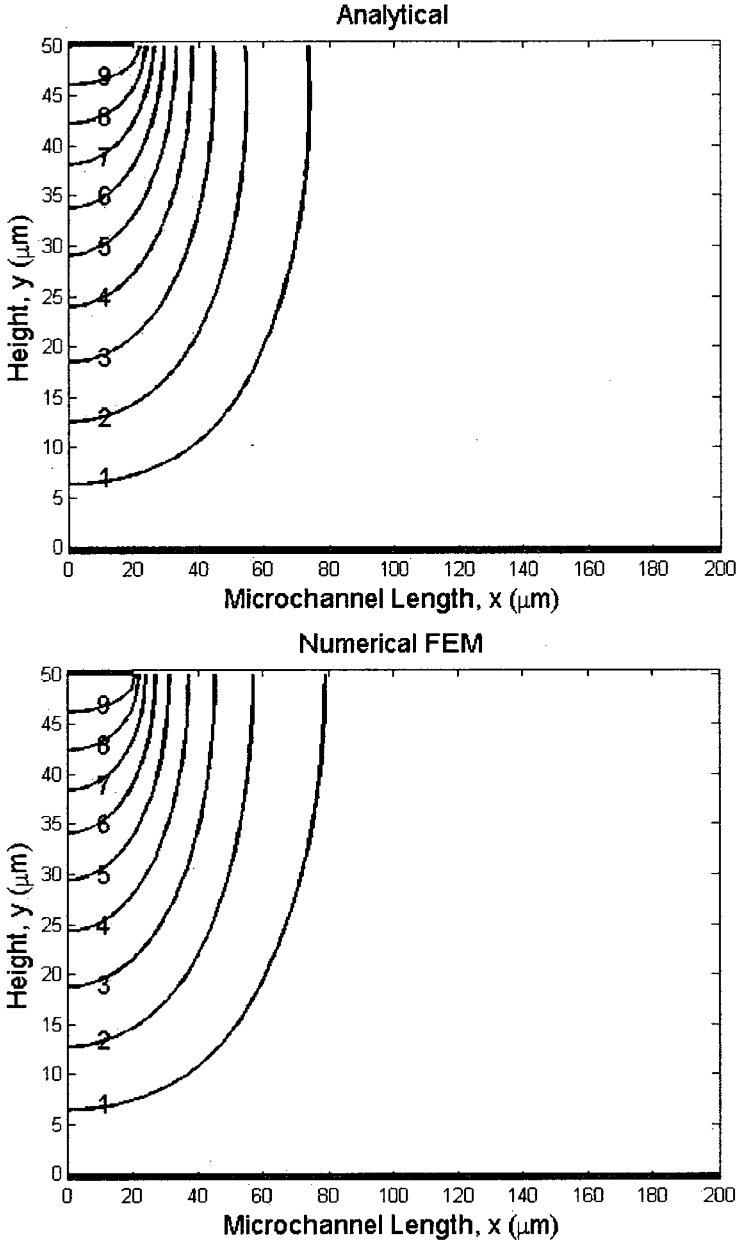

Figure A- 5: Comparison of analytical results and numerical simulations for the electric potential. Numerical simulations were obtained by finite element methods using COMSOL Multiphysics^{TM}. The contour plots of electric potential in the microchannel are shown for analytical and numerical results respectively. The thick lines at the top and bottom of the figures represent the electrodes and calculation were performed using (V_0=10 Volts, d=40μm, and H=50μm).

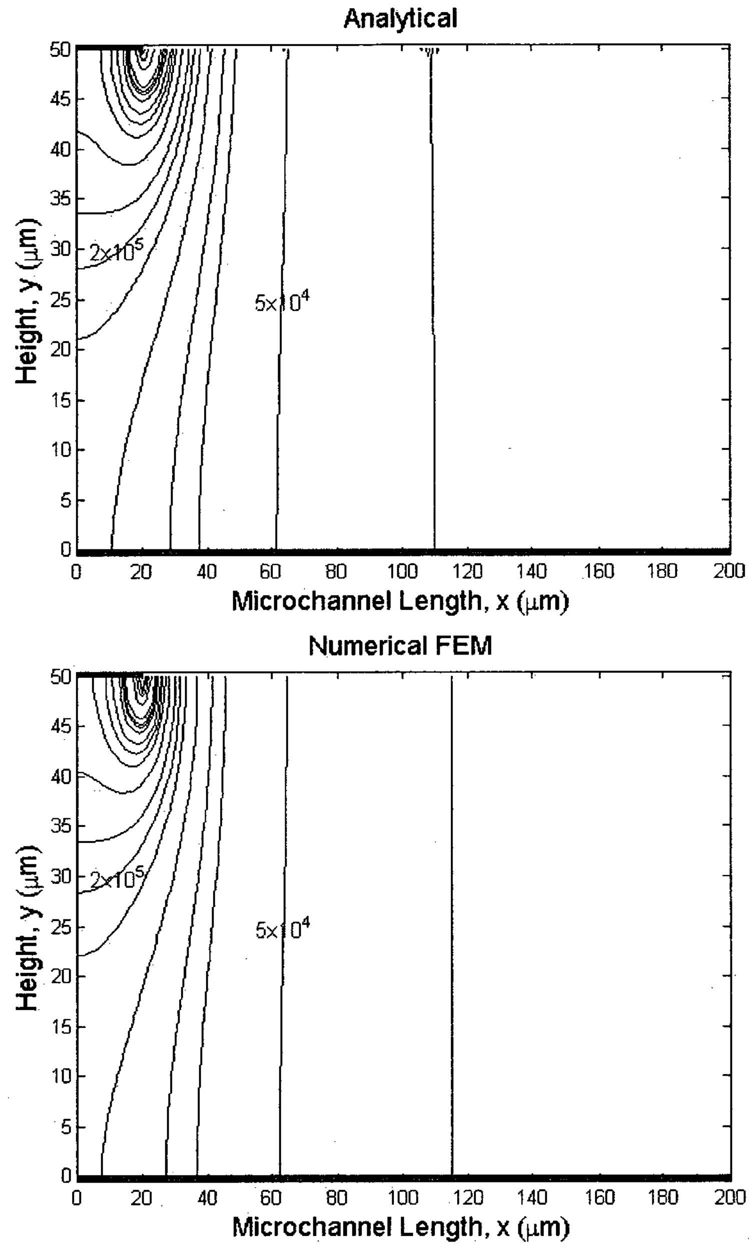

Figure A- 6: Comparison of analytical results and numerical simulations for the magnitude of electric filed. The contour plots of electric field in the microchannel for the same contour levels are shown for analytical and numerical results respectively. Calculations were performed with the same values used to calculate the electric

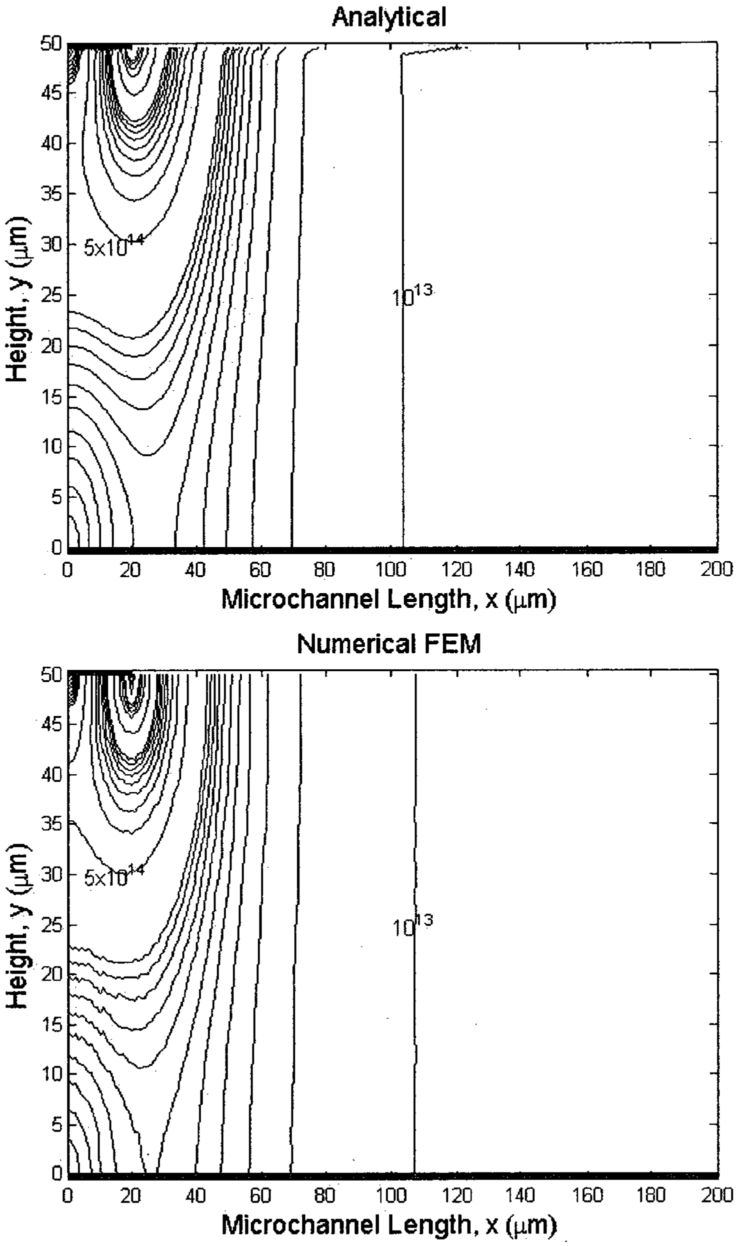

Figure A- 7: Comparison of analytical results and numerical simulations for the magnitude of the gradient of *(E.E)* The contour plots of the gradient of (*E.E*) in the microchannel for the same contour levels are shown for analytical and numerical results respectively. Calculations were performed with the same values used to calculate the electric potential.

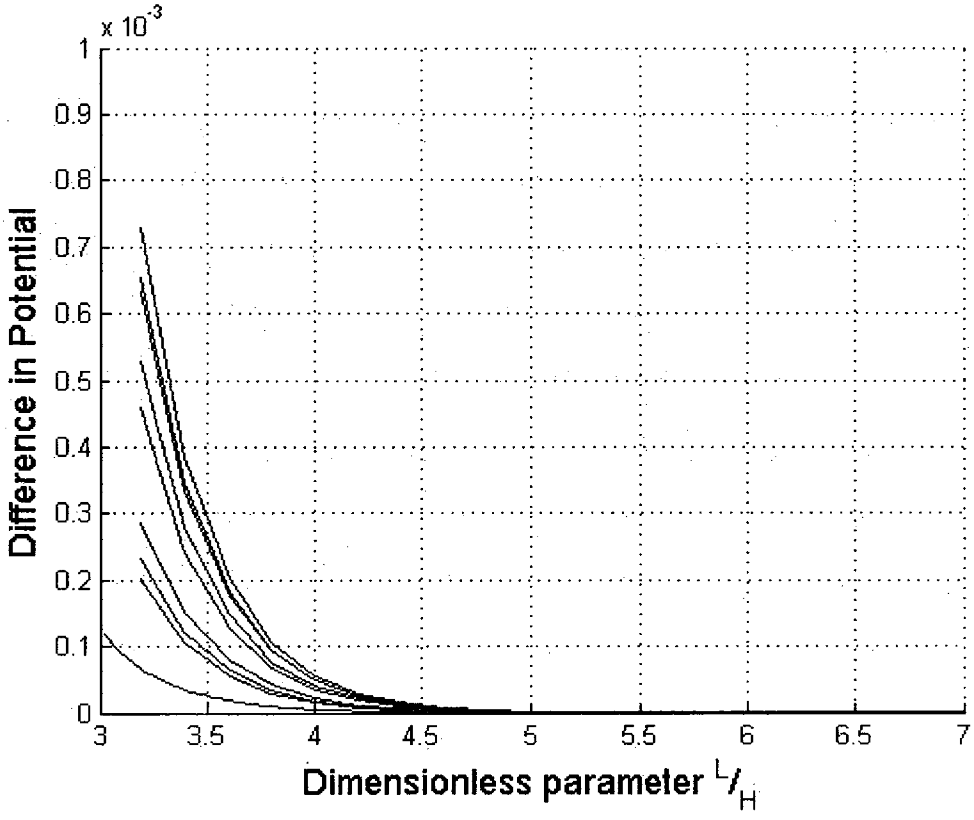

Figure A- 8: The variation in the electric potential at specific points as the parameter $\frac{L}{H}$ changes. The variation in potential for nine points located at different location in the channel is shown.

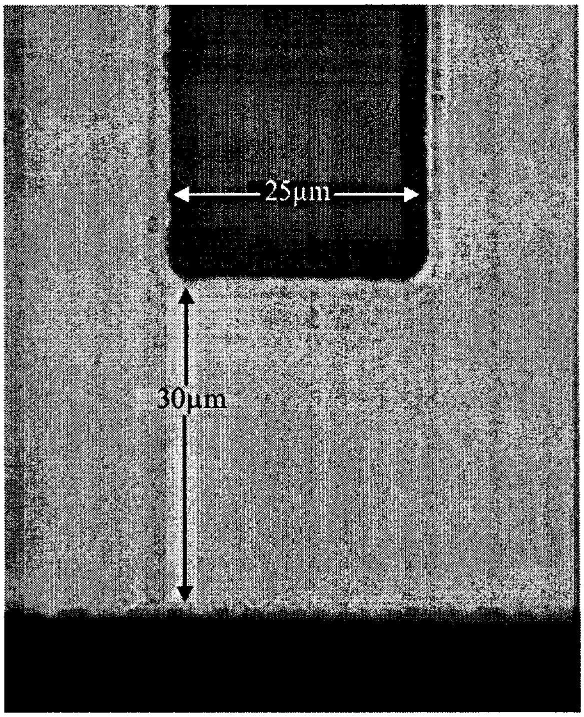

Figure A- 9: Electrodes pattern used in the experiment for experimental validation of the analytical results. The electrodes layer was designed using AutoCAD and printed using high resolution printers from a commercial partner. The finite size electrode (top) and the grounded electrode (down) are shown.

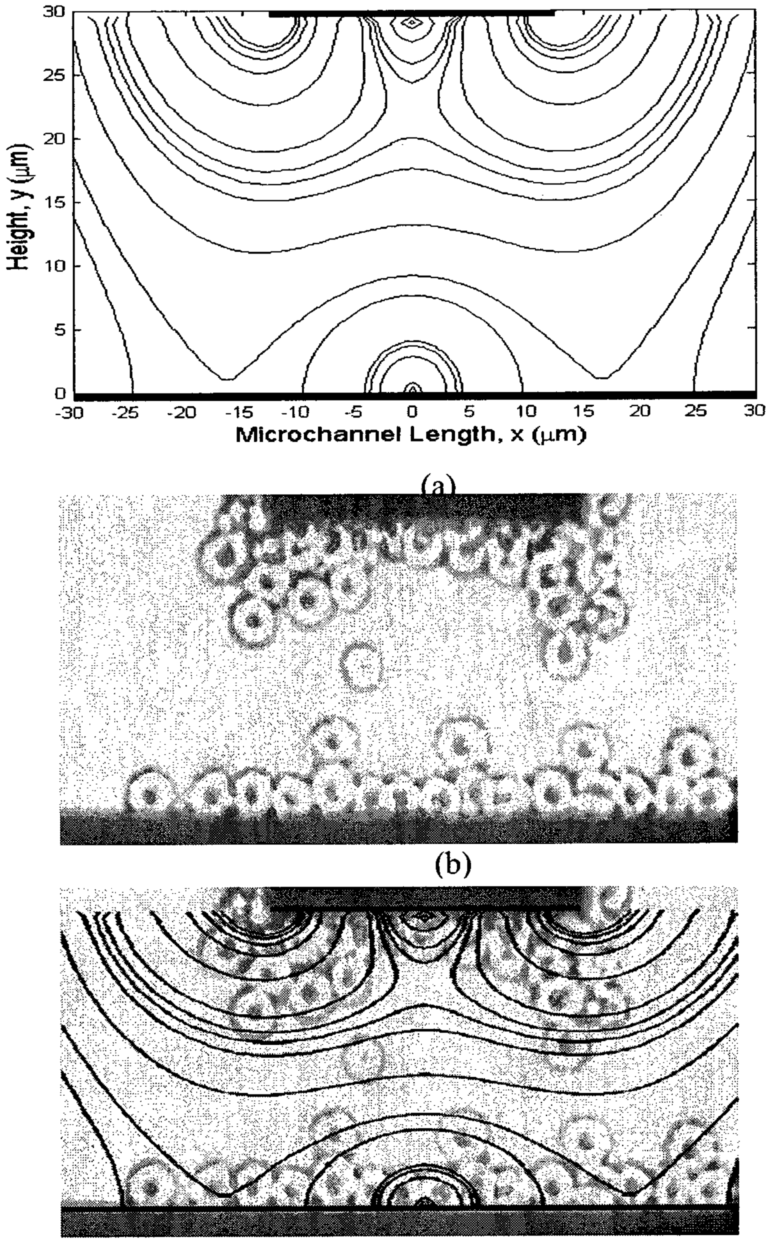

(a)

(b)

(c)

Figure A- 10: Comparison of analytical results and experimental data. (a) Contour plot of the magnitude of gradient of (*E.E*) using the analytical solution (the upper finite electrode and the bottom electrode shown as thick lines); (b) Experimental results showing the behavior of red blood cell to DEP force; (c) Overlapping of the analytical solution with the experimental results.

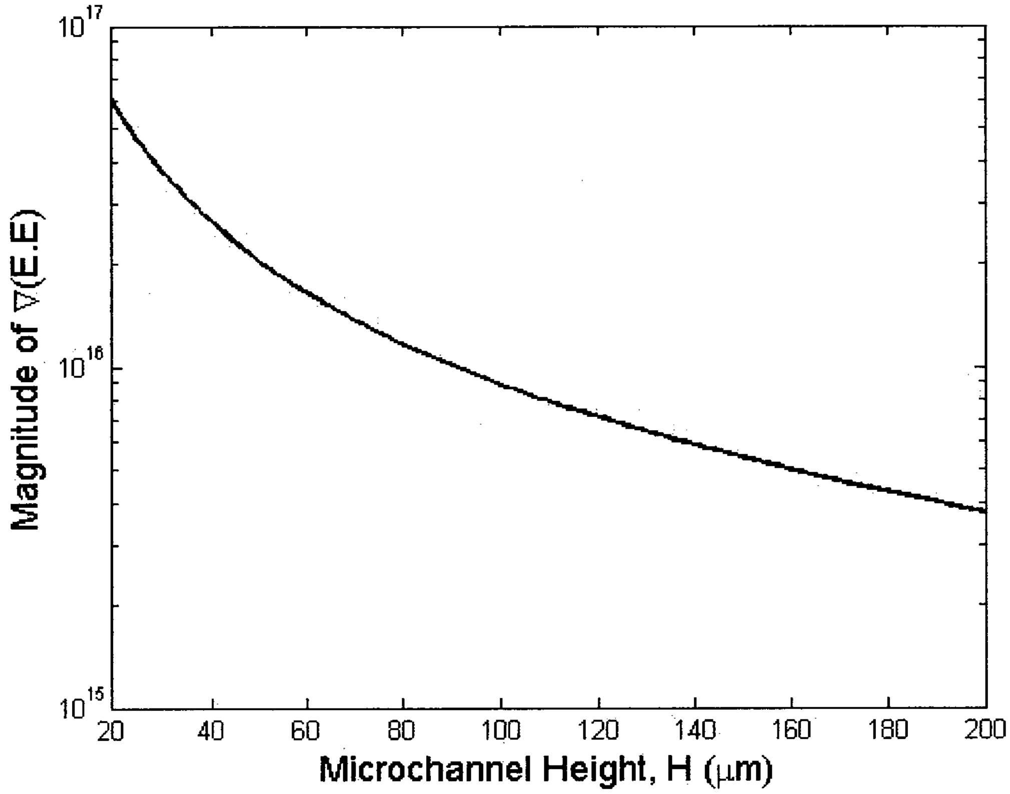

Figure A- 11: The variation of the magnitude of the gradient of (*E.E*) at a selected point that is close to the edge of the finite size electrode calculated using the analytical solution. Values are in (Volts^2/m^3) and the point is selected to be 5 μm below the edge of the finite size electrode. Similar behavior was found for several points at different locations in the unit segment.

References:

1. Morgan, H., et al., *The dielectrophoretic and travelling wave forces for interdigitated electrode arrays: Analytical solution using Fourier series.* Journal of physics D: applied physics, 2001. **34**: p. 1553-1561.

2. Erickson, D. and D. Li, *Integrated microfluidic devices.* Analytica chemica acta, 2004. **507**(1): p. 11-26.

3. Andersson, H. and A. Van den Berg, *Microfluidic devices for cellomics: a review.* Sensors and actuators B: chemical, 2003. **92**(3): p. 315-325.

4. Tüd s, A.J., G.A.J. Besselink, and R.B.M. Schasfoort, *Trends in miniaturized total analysis systems for point-of-care testing in clinical chemistry.* Lab on a chip, 2001. **1**(2): p. 83-95.

5. Tay, F.E.H., *Microfluidics and BioMEMS applications.* 2002: Kluwer Academic Pub.

6. Das, C.M., et al., *Dielectrophoretic segregation of different human cell types on microscope slides.* Analytical chemistry, 2005. **77**(9): p. 2708-2719.

7. Yang, S., A. Ündar, and J.D. Zahn, *Blood plasma separation in microfluidic channels using flow rate control.* American society for artificial internal organs, 2005. **51**(5): p. 585-590.

8. Sun, Y., et al., *Combining nanosurface chemistry and microfluidics for molecular analysis and cell biology.* Analytica chimica acta, 2009. **650**(1): p. 98-105.

9. Yi, C., et al., *Microfluidics technology for manipulation and analysis of biological cells.* Analytica chimica acta, 2006. **560**(1-2): p. 1-23.

10. Arifin, D.R., L.Y. Yeo, and J.R. Friend, *Microfluidic blood plasma separation via bulk electrohydrodynamic flows.* Biomicrofluidics, 2007. **1**: p. 014103-13.

11. Yang, S., A. Ündar, and J.D. Zahn, *A microfluidic device for continuous, real time blood plasma separation.* Lab on a chip, 2006. **6**(7): p. 871-880.

12. Blattert, C., et al. *Microfluidic blood/plasma separation unit based on microchannel bend structures.* Microtechnology in medicine and biology. 2005. **23**(3):P. 38- 41.

13. Blattert, C., et al. *Separation of blood in microchannel bends.* Engineering in medicine and biology society. 2004. San Francisco, CA, USA.

14. Park, J., et al. *Continuous plasma separation from whole blood using microchannel geometry.* Microtechnology in medicine and biology. 2005. Oahu, Hawaii.

15. Seo, J., et al., *Separation of blood cells and plasma in microchannel.* The 13th international conference on solid-state sensors, 2005. Seoul, Korea.

16. He, B., L. Tan, and F. Regnier, *Microfabricated filters for microfluidic analytical systems.* Analytical chemistry, 1999. 71(7): p. 1464-1468.

17. Crowley, T.A. and V. Pizziconi, *Isolation of plasma from whole blood using planar microfilters for lab-on-a-chip applications.* Lab on a chip, 2005. **5**(9): p. 922-929.

18. Sumida, E., et al., *Platelet separation from whole blood in an aqueous two-phase system with water-soluble polymers.* Journal of pharmacological sciences, 2006. **101**(1): p. 91-97.

19. Yamada, M., M. Nakashima, and M. Seki, *Pinched flow fractionation: continuous size separation of particles utilizing a laminar flow profile in a pinched microchannel.* Analytical chemistry, 2004. **76**: p. 5465-5471.

20. Takagi, J., et al., *Continuous particle separation in a microchannel having asymmetrically arranged multiple branches.* Lab on a chip, 2005. **5**(7): p. 778-784.

21. Feng, J., *A Bio-MEMS device for separation of breast cancer cells from peripheral whole blood.* 2003. Thesis, 2004. Beijing, China.

22. Miltenyi, S., et al., *High gradient magnetic cell separation with MACS.* Cytometry, 1990. **11**(2): p. 231-238.

23. McCloskey, K.E., J.J. Chalmers, and M. Zborowski, *Magnetic cell separation: characterization of magnetophoretic mobility.* Analytical chemistry, 2003. **75**(24): p. 6868-6874.

24. Han, K.H. and A.B. Frazier, *Continuous magnetophoretic separation of blood cells in microdevice format.* Journal of applied physics, 2004. **96**: p. 5797-5802.

25. Han, K.H., J.P. Landers, and A.B. Frazier. *Continuous paramagnetophoretic microseparator for blood cells.* Transducers, solid-state sensors, actuators and microsystems. 2003. Boston, United States.

26. Liu, C., L. Lagae, and G. Borghs, *Manipulation of magnetic particles on chip by magnetophoretic actuation and dielectrophoretic levitation.* Applied physics letters, 2007. **90**: p. 184109-12.

27. Gascoyne, P.R.C., et al., *Dielectrophoretic separation of cancer cells from blood. IEEE transactions on industry applications*, 1997. **33**(3): p. 670-678.

28. Becker, F.F., et al., *Separation of human breast cancer cells from blood by differential dielectric affinity.* Proceedings of the national academy of sciences, 1995. **92**(3): p. 860-864.

29. Li, Y. and K. Kaler, *Dielectrophoretic fluidic cell fractionation system.* Analytica chimica acta, 2004. **507**(1): p. 151-161.

30. Pohl, H.A., *Continuous dielectrophoretic cell classification method.* 1982, Google Patents: United States.

31. Pohl, H.A., *Dielectrophoresis : the behavior of neutral matter in nonuniform electric fields.* 1978, Cambridge ; New York: Cambridge University Press.

32. Gordon, J.E., Z. Gagnon, and H.C. Chang, *Dielectrophoretic discrimination of bovine red blood cell starvation age by buffer selection and membrane cross-linking.* Biomicrofluidics, 2007. **1**: p. 044102-5.

33. Chen, D.F., H. Du, and W.H. Li, *Bioparticle separation and manipulation using dielectrophoresis.* Sensors and actuators A: physical, 2007. **133**(2): p. 329-334.

34. Lewpiriyawong, N., C. Yang, and Y.C. Lam, *Dielectrophoretic manipulation of particles in a modified microfluidic H filter with multi-insulating blocks.* Biomicrofluidics, 2008. **2**: p. 034105-11.

35. Demierre, N., et al., *Focusing and continuous separation of cells in a microfluidic device using lateral dielectrophoresis.* Sensors and actuators: B. chemical, 2008. **132**(2): p. 388-396.

36. Huang, Y. and R.P. Holzel, *Differences in the AC electrodynamics of viable and non-viable yeast cells determined through combined dielectrophoresis and electrorotation studies.* Physics in medicine and biology, 1992. **37**(7): p. 1499-1517.

37. Pethig, R., et al., *Positive and negative dielectrophoretic collection of colloidal particles using interdigitated castellated microelectrodes.* Journal of physics D: applied physics, 1992. **25**: p. 881-888.

38. Markx, G.H., et al., *Dielectrophoretic characterization and separation of micro-organisms.* Microbiology, 1994. **140**(3): p. 585-591.

39. Pethig, R. and G.H. Markx, *Applications of dielectrophoresis in biotechnology.* Trends in biotechnology, 1997. **15**(10): p. 426-432.

40. Iliescu, C., et al., *A 3-D dielectrophoretic filter chip.* Electrophoresis, 2007. **28**(7):p. 1107-1114.

41. Srinivasan, V., V.K. Pamula, and R.B. Fair, *An integrated digital microfluidic lab-on-a-chip for clinical diagnostics on human physiological fluids.* Lab on a chip, 2004. **4**(4): p. 310-315.

42. Gascoyne, P.R.C. and J. Vykoukal, *Particle separation by dielectrophoresis.* Electrophoresis, 2002. **23**(13): p. 1973 - 1983.

43. Cen, E.G., et al., *A combined dielectrophoresis, traveling wave dielectrophoresis and electrorotation microchip for the manipulation and characterization of human malignant cells.* Journal of microbiological methods, 2004. **58**(3): p. 387-401.

44. Yang, J., et al., *Cell separation on microfabricated electrodes using dielectrophoretic/gravitational field-flow fractionation*. Analytical chemistry, 1999. **71**(5): p. 911–918.

45. Yang, J., et al., *Dielectric properties of human leukocyte subpopulations determined by electrorotation as a cell separation criterion*. Biophysical journal, 1999. **76**(6): p. 3307-3314.

46. Huang, Y., et al., *Dielectrophoretic cell separation and gene expression profiling on microelectronic chip arrays*. Biochimica et biophysica acta, 1997. **1323**: p. 240-252.

47. Auerswald, J. and H.F. Knapp, *Quantitative assessment of dielectrophoresis as a micro fluidic retention and separation technique for beads and human blood erythrocytes*. Microelectronic engineering, 2003. **67**: p. 879-886.

48. Wei, M.T., J. Junio, and H.D. Ou-Yang, *Direct measurements of the frequency-dependent dielectrophoresis force*. Biomicrofluidics, 2009. **3**: p. 012003-08.

49. Kua, C.H., et al., *Review of bio-particle manipulation using dielectrophoresis*. Innovation in manufacturing systems and technology, 2005.

50. Wang, X.B., et al., *Dielectrophoretic manipulation of cells with spiral electrodes*. Biophysical journal, 1997. **72**(4): p. 1887-1899.

51. Yu, L., et al., *Sequential field-flow cell separation method in a dielectrophoretic chip with 3-D electrodes*. Journal of microelectromechanical systems, 2007. **16**(5): p. 1120-1129.

52. Iliescu, C., et al., *Bidirectional field-flow particle separation method in a dielectrophoretic chip with 3D electrodes*. Sensors and actuators: B. chemical, 2008. **129**(1): p. 491-496.

53. Borgatti, M., et al., *Separation of white blood cells from erythrocytes on a dielectrophoresis (DEP) based 'Lab-on-a-chip' device*. International journal of molecular medicine, 2005. **15**: p. 913–920.

54. Bocchi, M., et al., *Dielectrophoretic trapping in microwells for manipulation of single cells and small aggregates of particles*. Biosensors and bioelectronics, 2009. **24**(5): p. 1177-1183.

55. Yu, C., et al., *A three-dimensional dielectrophoretic particle focusing channel for microcytometry applications*. Journal of microelectromechanical systems, 2005. **14**(3): p. 480-487.

56. Chu, H., I. Doh, and Y.H. Cho, *A three-dimensional (3D) particle focusing channel using the positive dielectrophoresis (pDEP) guided by a dielectric structure between two planar electrodes*. Lab on a chip, 2009. **9**(5): p. 686-691.

57. Morgan, H. and N.G. Green, *Dielectrophoretic manipulation of rod-shaped viral particles*. Journal of electrostatics, 1997. **42**(3): p. 279-293.

58. Lapizco-Encinas, B.H., et al., *Insulator-based dielectrophoresis for the selective concentration and separation of live bacteria in water*. Electrophoresis, 2004. **25**(10/11): p. 1695-1704.

59. Docoslis, A., et al., *A novel dielectrophoresis-based device for the selective retention of viable cells in cell culture media*. Biotechnology and bioengineering, 1997. **54**(3): p. 239-250.

60. Vahey, M.D. and J. Voldman, *An equilibrium method for continuous-flow cell sorting using dielectrophoresis*. Analytical chemistry, 2008. **80**(9): p. 3135-3143.

61. Broche, L.M., et al., *Early detection of oral cancer–Is dielectrophoresis the answer?*. Oral oncology, 2007. **43**(2): p. 199-203.

62. Cheng, J., et al., *Isolation of cultured cervical carcinoma cells mixed with peripheral blood cells on a bioelectronic chip*. Analytical chemistry 1998. **70**: p. 2321-2326.

63. Markx, G.H., P.A. Dyda, and R. Pethig, *Dielectrophoretic separation of bacteria using a conductivity gradient*. Journal of biotechnology, 1996. **51**(2): p. 175-180.

64. Xu, C., et al., *Dielectrophoresis of human red cells in microchips*. Electrophoresis, 1999. **20**(9): p. 1829-1831.

65. Li, H. and R. Bashir, *Dielectrophoretic separation and manipulation of live and heat-treated cells of Listeria on microfabricated devices with interdigitated electrodes*. Sensors and actuators B: chemical, 2002. **86**(2-3): p. 215-221.

66. Lu, Y., et al., *Controllability of non-contact cell manipulation by image dielectrophoresis (iDEP)*. Optical and quantum electronics, 2005. **37**(13): p. 1385-1395.

67. Tsukahara, S., T. Sakamoto, and H. Watarai, *Positive dielectrophoretic mobilities of single microparticles enhanced by the dynamic diffusion cloud of ions*. Langmuir, 2000. **16**(8): p. 3866-3872.

68. Voldman, J., et al., Holding *forces of single-particle dielectrophoretic traps*. Biophysical journal, 2001. **80**(1): p. 531-541.

69. Doh, I. and Y.H. Cho, *A continuous cell separation chip using hydrodynamic dielectrophoresis (DEP) process*. Sensors and actuators A: physical, 2005. **121**(1): p. 59-65.

70. Li, Y., et al., *Continuous dielectrophoretic cell separation microfluidic device*. Lab on a chip, 2007. **7**(2): p. 239-248.

71. Holmes, D., N.G. Green, and H. Morgan, *Microdevices for dielectrophoretic flow-through cell separation*. Engineering in medicine and biology magazine, IEEE, 2003. **22**(6): p. 85-90.

72. Pommer, M.S., et al., *Dielectrophoretic separation of platelets from diluted whole blood in microfluidic channels*. Electrophoresis, 2008. **29**(6): p. 1213-1218.

73. Han, K.H. and A.B. Frazier, *Lateral-driven continuous dielectrophoretic microseparators for blood cells suspended in a highly conductive medium*. Lab on a chip, 2008. **8**(7): p. 1079-1086.

74. Lin, J.T.Y. and J.T.W. Yeow, *Enhancing dielectrophoresis effect through novel electrode geometry.* Biomedical microdevices, 2007. **9**(6): p. 823-831.

75. Chen, D. and H. Du, *A dielectrophoretic barrier-based microsystem for separation of microparticles.* Microfluidics and nanofluidics, 2007. **3**(5): p. 603-610.

76. Pysher, M.D. and M.A. Hayes, *Electrophoretic and dielectrophoretic field gradient technique for separating bioparticles.* Analytical chemistry, 2007. **79**(12): p. 4552-4557.

77. Chen, K.P., et al., *Insulator-based dielectrophoretic separation of small particles in a sawtooth channel.* Electrophoresis, 2009. **30**(9): p. 1441-1448.

78. Wang, X.B., et al., *Separation of polystyrene microbeads using dielectrophoretic/gravitational field-flow-fractionation.* Biophysical journal, 1998. **74**(5): p. 2689-2701.

79. Guglielmi, L., et al., *Mouse embryonic stem cell sorting for the generation of transgenic mice by sedimentation field-flow fractionation.* Analytical chemistry, 2004. **76**(6): p. 1580-1585.

80. Müller, T., et al., *Microdevice for cell and particle separation using dielectrophoretic field-flow fractionation.* Journal of liquid chromatography and related technologies, 2000. **23**(1): p. 47-59.

81. Huang, Y., et al., *Introducing dielectrophoresis as a new force field for field-flow fractionation.* Biophysical journal, 1997. **73**(2): p. 1118-1129.

82. Wang, X.B., et al., *Cell separation by dielectrophoretic field-flow-fractionation.* Analytical chemistry, 2000. **72**(4): p. 832-839.

83. Yang, J., et al., *Differential analysis of human leukocytes by dielectrophoretic field-flow-fractionation.* Biophysical journal, 2000. **78**(5): p. 2680-2689.

84. Vykoukal, J., et al., *Enrichment of putative stem cells from adipose tissue using dielectrophoretic field-flow fractionation.* Lab on a chip, 2008. **8**(8): p. 1386-1393.

85. Leu, T.S. and C.Y. Weng, *Dynamics of dielectrophoretic field-flow fractionation (DEP-FFF) based micro sorter for cell separation.* Modern physics letters B, 2009. **23**(3): p. 389-392.

86. Petersen, E., et al., *DNA migration and separation on surfaces with a microscale dielectrophoretic trap array. Physical review letters*, 2007. **98**(8): p. 88102-4.

87. Kua, C.H., et al., *Dynamic cell fractionation and transportation using moving dielectrophoresis.* Analytical chemistry, 2007. **79**: p. 6975–6987.

88. Fiedler, S., et al., *Dielectrophoretic sorting of particles and cells in a microsystem.* Analytical chemistry, 1998. **70**(9): p. 1909-1915.

89. Tornay, R., et al., *Dielectrophoresis-based particle exchanger for the manipulation and surface functionalization of particles.* Lab on a chip, 2008. **8**(2): p. 267-273.

90. Wang, L., et al., *Dielectrophoresis switching with vertical sidewall electrodes for microfluidic flow cytometry.* Lab on a chip, 2007. **7**(9): p. 1114-1120.

91. Christensen, T.B., et al., Sample *preparation by cell guiding using negative dielectrophoresis.* Microelectronic Engineering, 2007. **84**(5-8): p. 1690-1693.

92. Hu, X., et al., *Marker-specific sorting of rare cells using dielectrophoresis.* Proceedings of the national academy of sciences, 2005. **102**(44): p. 15757-15761.

93. Heeren, A., et al., *Manipulation of micro-and nano-particles by electro-osmosis and dielectrophoresis.* Microelectronic engineering, 2007. **84**(5-8): p. 1706-1709.

94. Taff, B.M. and J. Voldman, *A scalable addressable positive-dielectrophoretic cell-sorting array.* Analytical chemistry, 2005. **77**(24): p. 7976–7983.

95. Muller, T., et al., *The potential of dielectrophoresis for single-cell experiments.* Engineering in medicine and biology magazine, IEEE, 2003. **22**(6): p. 51-61.

96. Pethig, R., R.S. Lee, and M.S. Talary, *Cell physiometry tools based on dielectrophoresis.* Journal of the association for laboratory automation, 2004. **9**(5): p. 324-330.

97. Lagally, E.T., S.H. Lee, and H.T. Soh, *Integrated microsystem for dielectrophoretic cell concentration and genetic detection.* Lab on a chip, 2005. **5**(10): p. 1053-1058.

98. Ramadan, Q., et al., *Simultaneous cell lysis and bead trapping in a continuous flow microfluidic device.* Sensors and actuators B: chemical, 2006. **113**(2): p. 944-955.

99. Cheng, I.F., H.C. Chang, and D. Hou, *An integrated dielectrophoretic chip for continuous bioparticle filtering, focusing, sorting, trapping, and detecting.* Biomicrofluidics, 2007. **1**: p. 021503-15.

100. Hunt, T.P., D. Issadore, and R.M. Westervelt, *Integrated circuit/microfluidic chip to programmably trap and move cells and droplets with dielectrophoresis.* Lab on a chip, 2008. **8**(1): p. 81-87.

101. Baaijens, J.P.W., A.A. Van Steenhoven, and J.D. Janssen, *Numerical analysis of steady generalized newtonian blood flow in a 2D model of the carotid artery bifurcation.* Biorheology, 1993. **30**: p. 63-63.

102. Krafczyk, M., et al., *Analysis of 3D transient blood flow passing through an artificial aortic valve by Lattice–Boltzmann methods.* Journal of biomechanics, 1998. **31**(5): p. 453-462.

103. Tsubota, K., et al., *A particle method for blood flow simulation,–application to flowing red blood cells and platelets.* Journal of the earth simulator, 2006. **5**: p. 2-7.

104. Kikuchi, Y., *Effect of leukocytes and platelets on blood flow through a parallel array of microchannels: micro-and macroflow relation and rheological measures of leukocyte and platelet activities.* Microvascular research, 1995. **50**(2): p. 288-300.

105. Dobbe, J.G.G., et al., *Analyzing red blood cell-deformability distributions*. Blood cells, molecules and diseases, 2002. **28**(3): p. 373-384.

106. Zhang, J., P.C. Johnson, and A.S. Popel, *Red blood cell aggregation and dissociation in shear flows simulated by lattice Boltzmann method*. Journal of biomechanics, 2008. **41**(1): p. 47-55.

107. Jovtchev, S., et al., *Factors determining the electro-optical behaviour of red blood cells*. Colloids and surfaces A: physicochemical and engineering aspects, 2002. **209**(2-3): p. 257-265.

108. Jovtchev, S., et al., *Role of electrical and mechanical properties of red blood cells for their aggregation*. Colloids and surfaces A: physicochemical and engineering aspects, 2000. **164**(2-3): p. 95-104.

109. Berliner, S., et al., *The degree of red blood cell aggregation on peripheral blood glass slides corresponds to inter-erythrocyte cohesive forces in laminar flow*. Thrombosis research, 2004. **114**(1): p. 37-44.

110. Deuling, H.J. and W. Helfrich, *Red blood cell shapes as explained on the basis of curvature elasticity*. Biophysical journal, 1976. **16**(8): p. 861-868.

111. Backman, L., *Shape control in the human red cell*. Journal of cell science, 1986. **80**: p. 281-298.

112. Grebe, R., H. Wolff, and H. Schmid-Schönbein, *Influence of red cell surface charge on red cell membrane curvature*. Pflügers archiv european journal of physiology, 1988. **413**(1): p. 77-82.

113. Gedde, M.M., E. Yang, and W.H. Huestis, *Shape response of human erythrocytes to altered cell pH*. Blood, 1995. **86**(4): p. 1595-1599.

114. Rasia, M. and A. Bollini, *Red blood cell shape as a function of medium's ionic strength and pH*. Biochimica et biophysica acta, 1998. **1372**(2): p. 198-204.

115. Bransky, A., et al., *An automated cell analysis sensing system based on a microfabricated rheoscope for the study of red blood cells physiology*. Biosensors and bioelectronics, 2006. **22**(2): p. 165-169.

116. Kikuchi, Y., Q.W. Da, and T. Fujino, *Variation in red blood cell deformability and possible consequences for oxygen transport to tissue*. Microvasc Research, 1994. **47**(2): p. 222-231.

117. Carola, R., J.P. Harley, and C.R. Noback, *Human anatomy and physiology*. 1990: McGraw-Hill Companies.

118. Van De Graaff, K.M., *Human anatomy*. 1998: WCB/McGraw-Hill.

119. Lee, S.H., et al., *Microfluidic chip for biochemical reaction and electrophoretic separation by quantitative volume control*. Sensors and actuators B: chemical, 2005. **110**(1): p. 164-173.

120. Tjerkstra, R.W., et al., *Etching technology for chromatography microchannels.* Electrochimica acta, 1997. **42**(20-22): p. 3399-3406.

121. Lee, K.B. and L. Lin, Surface *micromachined glass and polysilicon microchannels using MUMPs for BioMEMS applications.* Sensors and actuators A: physical, 2004. **111**(1): p. 44-50.

122. Liu, J.S., et al., *Electrostatic bonding of a silicon master to a glass wafer for plastic microchannel fabrication.* Journal of materials processing technology, 2006. **178**(1-3): p. 278-282.

123. Chien, R.D., *Micromolding of biochip devices designed with microchannels.* Sensors and actuators A: physical, 2006. **128**(2): p. 238-247.

124. Waddell, E.A., L.E. Locascio, and G.W. Kramer, *UV Laser micromachining of polymers for microfluidic applications.* Journal of the association for laboratory automation, 2002. **7**(1): p. 78-82.

125. Lee, J. and C.J.C. Kim. *Liquid micromotor driven by continuous electrowetting.* IEEE micro electro mechanical systems, MEMS. 1998. Heidelberg, Germany.

126. Pollack, M.G., A.D. Shenderov, and R.B. Fair, *Electrowetting-based actuation of droplets for integrated microfluidics.* Lab on a chip, 2002. **2**(2): p. 96-101.

127. Pollack, M.G., R.B. Fair, and A.D. Shenderov, *Electrowetting-based actuation of liquid droplets for microfluidic applications.* Applied physics letters, 2000. **77**: p. 1725-1726.

128. Nguyen, N.T. and S.T. Wereley, *Fundamentals and applications of microfluidics.* 2002: Artech House.

129. Robinson, L., et al., *Electrochemical wettability switches gate aqueous liquids in microfluidic systems.* Lab on a chip, 2006. **6**(10): p. 1277-1278.

130. Kim, C.J., *Micropumping by electrowetting,* ASME international mechanical engineering congress and exposition. 2001: New York, United States.

131. Zhang, Y., et al., *Electroosmotic flow in irregular shape microchannels.* International journal of engineering science, 2005. **43**(19-20): p. 1450-1463.

132. Das, S. and S. Chakraborty, *Analytical solutions for velocity, temperature and concentration distribution in electroosmotic microchannel flows of a non-Newtonian bio-fluid.* Analytica chimica acta, 2006. **559**(1): p. 15-24.

133. Chen, X.Y., et al., *Developing pressure-driven liquid flow in microchannels under the electrokinetic effect.* International journal of engineering science, 2004. **42**(5-6): p. 609-622.

134. Li, D., *Electro-viscous effects on pressure-driven liquid flow in microchannels.* Colloids and surfaces A: physicochemical and engineering aspects, 2001. **195**(1-3): p. 35-57.

135. Meisel, I. and P. Ehrhard, *Electrically-excited (electroosmotic) flows in microchannels for mixing applications*. European journal of mechanics-B/fluids, 2006. **25**(4): p. 491-504.

136. Bayraktar, T. and S.B. Pidugu, *Characterization of liquid flows in microfluidic systems*. International journal of heat and mass transfer, 2006. **49**(5-6): p. 815-824.

137. Gad-el-Hak, M., *The fluid mechanics of microdevices-the freeman scholar lecture*. Journal of fluids engineering, 1999. **121**: p. 5-33.

138. Obot, N.T., *Toward a better understanding of friction and heat/mass transfer in microchannels-a literature review*. Nanoscale and microscale thermophysical engineering, 2002. **6**(3): p. 155-173.

139. Sharp, K.V. and R.J. Adrian, *Transition from laminar to turbulent flow in liquid filled microtubes*. Experiments in fluids, 2004. **36**(5): p. 741-747.

140. Wu, P. and W.A. Little, *Measurement of friction factors for the flow of gases in very fine channels used for microminiature Joule-Thomson refrigerators*. Cryogenics, 1983. **23**(5): p. 273-277.

141. Wu, P. and W.A. Little, *Measurement of the heat transfer characteristics of gas flow in fine channel heat exchangers used for microminiature refrigerators*. Cryogenics, 1984. **24**(8): p. 415-420.

142. Zhuo, L., et al., *Experimental and numerical studies of liquid flow and heat transfer in microtubes*. International journal of heat and mass transfer, 2007. **50**(17-18): p. 3447-3460.

143. Mohiuddin Mala, G. and D. Li, *Flow characteristics of water in microtubes*. International journal of heat and fluid flow, 1999. **20**(2): p. 142-148.

144. Judy, J., D. Maynes, and B.W. Webb, *Characterization of frictional pressure drop for liquid flows through microchannels*. International journal of heat and mass transfer, 2002. **45**(17): p. 3477-3489.

145. Morini, G.L., *Laminar-to-turbulent flow transition in microchannels*. Nanoscale and microscale thermophysical engineering, 2004. **8**(1): p. 15-30.

146. Guo, Z.Y. and Z.X. Li, *Size effect on microscale single-phase flow and heat transfer*. International journal of heat and mass transfer, 2003. **46**(1): p. 149-159.

147. Yang, C. and D. Li, *Electrokinetic effects on pressure-driven liquid flows in rectangular microchannels*. Journal of colloid and interface science, 1997. **194**(1): p. 95-107.

148. Yang, C. and D. Li, *Analysis of electrokinetic effects on the liquid flow in rectangular microchannels*. Colloids and surfaces A: physicochemical and engineering aspects, 1998. **143**(2-3): p. 339-353.

149. Wang, C., et al., *Characterization of electroosmotic flow in rectangular microchannels*. International journal of heat and mass transfer, 2007. **50**(15-16): p. 3115-3121.

150. Hrnjak, P. and X. Tu, *Single phase pressure drop in microchannels.* International journal of heat and fluid flow, 2007. **28**(1): p. 2-14.

151. Baviere, R., et al., *Experimental characterization of water flow through smooth rectangular microchannels.* Physics of fluids, 2005. **17**: p. 098105-10.

152. Qu, W. and I. Mudawar, *Experimental and numerical study of pressure drop and heat transfer in a single-phase micro-channel heat sink.* International journal of heat and mass transfer, 2002. **45**(12): p. 2549-2565.

153. Yun, K.S. and E. Yoon, *Micro/Nanofluidic device for single-cell-based assay.* Biomedical microdevices, 2005. **7**(1): p. 35-40.

154. Wu, H.Y. and P. Cheng, *Friction factors in smooth trapezoidal silicon microchannels with different aspect ratios.* International journal of heat and mass transfer, 2003. **46**(14): p. 2519-2525.

155. Cao, B., G.W. Chen, and Q. Yuan, *Fully developed laminar flow and heat transfer in smooth trapezoidal microchannel.* International communications in heat and mass transfer, 2005. **32**(9): p. 1211-1220.

156. Hao, P.F., F. He, and K.Q. Zhu, Flow *characteristics in a trapezoidal silicon microchannel.* Journal of micromechanics and microengineering, 2005. **15**(6): p. 1362-1368.

157. Weilin, Q., G. Mohiuddin Mala, and L. Dongqing, *Pressure-driven water flows in trapezoidal silicon microchannels.* International journal of heat and mass transfer, 2000. **43**(3): p. 353-364.

158. Yang, J. and D.Y. Kwok, *Microfluid flow in circular microchannel with electrokinetic effect and Navier's slip condition.* Langmuir, 2003. **19**(4): p. 1047-1053.

159. Kyle, R.A. and M.A. Shampo, *Agostino Bassi.* Journal of the american medical association, 1979. **241**(15): p. 1584.

160. Zborowski, M., et al., *Continuous cell separation using novel magnetic quadrupole flow sorter.* Journal of magnetism and magnetic materials, 1999. **194**(1): p. 224-230.

161. Gascoyne, P.R.C., et al., *Cell separation by conventional dielectrophoresis combined with field-flow fractionation.* Biophysical journal, 1996. **70**: p. A333.

162. Liu, B.C., T.I. Chen, and C.H. Liu. *A cell separation chip using micro-structures filter and multi-frequencies dielectrophoresis.* Solid-state sensors, actuators and microsystems. 2005. Seoul, Korea.

163. Holmes, D. and H. Morgan, *Cell sorting and separation using dielectrophoresis.* Institute of physics conference series, electrostatics. 2004. Edinburgh, United Kingdom.

164. Yoichiro, I. and S. Kazufusa, *A new continuous-flow cell separation method based on cell density: Principle, apparatus, and preliminary application to separation of human buffy coat.* Journal of clinical apheresis, 2001. **16**(4): p. 186-191.

165. Vettore, L., M.C. De Matteis, and P. Zampini, *A new density gradient system for the separation of human red blood cells.* American journal of hematology, 1980. **8**(3). p. 291-297.

166. Wigzell, H. and B. Andersson, *Cell separation on antigen-coated columns: elimination of high rate antibody-forming cells and immunological memory cells.* Journal of experimental medicine, 1969. **129**(1): p. 23-36.

167. Lapizco-Encinas, B.H. and M. Rito-Palomares, *Dielectrophoresis for the manipulation of nanobioparticles.* Electrophoresis, 2007. **28**(24). p. 4521 – 4538.

168. Kubisz, L., et al., *The effect of temperature on the electric conductivity of poly (dimethyl siloxane) ferromagnetic gel.* Journal of physics: condensed matter, 2008. **20**: p. 204118.

169. Multiphysics, C., *COMSOL Multiphysics.* 2006.

170. Weinbaum, S., *A strong interaction theory for the creeping motion of a sphere between plane parallel boundaries. Part 2. Parallel motion.* Journal of fluid mechanics, 1980. **99**(part 4): p. 766-783.

171. Kua, C.H., et al., *Cell motion model for moving dielectrophoresis.* Analytical chemistry, 2008. **80**(14): p. 5454-5461.

172. Service, R.F., *Nanotoxicology: nanotechnology grows up.* Science, 2004. **304**(5678): p. 1732-1734.

173. Teker, K., et al., *Applications of carbon nanotubes for cancer research.* Nanobiotechnology, 2005. **1**(2): p. 171-182.

174. Bianco, A., K. Kostarelos, and M. Prato, *Applications of carbon nanotubes in drug delivery.* Current opinion in chemical biology, 2005. **9**(6): p. 674-679.

175. Liu, Z., et al., *siRNA delivery into human T cells and primary cells with carbon-nanotube transporters.* Angewandte chemie international edition, 2007. **46**(12): p. 2023 - 2027.

176. Zhang, Z., et al., *Delivery of telomerase reverse transcriptase small interfering RNA in complex with positively charged single-walled carbon nanotubes suppresses tumor growth.* Clinical cancer research, 2006. **12**(16): p. 4933-4939.

177. Kam, N.W.S., et al., *Nanotube molecular transporters: internalization of carbon nanotube-protein conjugates into mammalian cells.* Journal of the american chemical society, 2004. **126**(22): p. 6850-6851.

178. Yun, Y., et al., *Electrochemical impedance measurement of prostate cancer cells using carbon nanotube array electrodes in a microfluidic channel.* Nanotechnology, 2007. **18**(46): p. 465505-465505.

179. Yu, X., et al., *Carbon nanotube amplification strategies for highly sensitive immunodetection of cancer biomarkers.* Journal of the american chemical society, 2006. **128**(34): p. 11199-11205.

180. Gannon, C.J., et al., *Carbon nanotube-enhanced thermal destruction of cancer cells in a noninvasive radiofrequency field.* Cancer, 2007. **110**(12): p. 2654-2665.

181. Panchapakesan, B., et al., *Single-wall carbon nanotube nanobomb agents for killing breast cancer cells.* Nanobiotechnology, 2005. **1**(2): p. 133-139.

182. Kam, N.W.S., et al., *Carbon nanotubes as multifunctional biological transporters and near-infrared agents for selective cancer cell destruction.* Proceedings of the national academy of sciences, 2005. **102**(33): p. 11600-11605.

183. Muller, J., et al., *Respiratory toxicity of multi-wall carbon nanotubes.* Toxicology and applied pharmacology, 2005. **207**(3): p. 221-231.

184. Lam, C.W., et al., *Pulmonary toxicity of single-wall carbon nanotubes in mice 7 and 90 days after intratracheal instillation.* Toxicological sciences, 2004. **77**(1): p. 126-134.

185. Donaldson, K., *Resolving the nanoparticles paradox.* Nanomedicine, 2006. **1**(2): p. 229-234.

186. Tsuji, J.S., et al., *Research strategies for safety evaluation of nanomaterials, part IV: Risk assessment of nanoparticles.* Toxicological sciences, 2006. **89**(1): p. 42-50.

187. Warheit, D.B., et al., *Comparative pulmonary toxicity assessment of single-wall carbon nanotubes in rats.* Toxicological sciences, 2004. **77**(1): p. 117-125.

188. Shvedova, A.A., et al., *Unusual inflammatory and fibrogenic pulmonary responses to single-walled carbon nanotubes in mice.* The american journal of physiology - lung cellular and molecular physiology, 2005. **289**(5): p. 698-708.

189. Mangum, J.B., et al., Single-*walled carbon nanotube (SWCNT)-induced interstitial fibrosis in the lungs of rats is associated with increased levels of PDGF mRNA and the formation of unique intercellular carbon structures that bridge alveolar macrophages in situ.* Particle and fibre toxicology, 2006. **3**(1): p. 15-28.

190. Li, Z., et al., Cardiovascular *effects of pulmonary exposure to single-wall carbon nanotubes.* Environmental health perspectives, 2007. **115**(3): p. 377-382.

191. Simon-Deckers, A., et al., *In vitro investigation of oxide nanoparticle and carbon nanotube toxicity and intracellular accumulation in A549 human pneumocytes.* Toxicology, 2008. **253**(1-3): p. 137-146.

192. Tabet, L., et al., *Adverse effects of industrial multiwalled carbon nanotubes on human pulmonary cells.* Journal of toxicology and environmental health part A, 2009. **72**(2): p. 60-73.

193. Tombler, T.W., et al., *Reversible electromechanical characteristics of carbon nanotubes under local-probe manipulation.* Nature, 2000. **405**(6788): p. 769-772.

194. Causton, H.C., J. Quackenbush, and A. Brazma, *Microarray gene expression data analysis: a beginner's guide.* 2003: Wiley-Blackwell.

195. Russell, S., L.A. Meadows, and R.R. Russell, *Microarray technology in practice*. 2008: Academic Press.

196. van Pelt-Verkuil, E., A. van Belkum, and J.P. Hays, *Principles and technical aspects of PCR amplification*. 2008: Springer Verlag.

197. Weissensteiner, T., H.G. Griffin, and A.M. Griffin, *PCR technology: current innovations*. 2004: CRC.

198. Chou, C.C., et al., *Single-walled carbon nanotubes can induce pulmonary injury in mouse model*. Nano letters, 2008. **8**(2): p. 437-445.

199. Cui, D., et al., *Effect of single wall carbon nanotubes on human HEK293 cells*. Toxicology letters, 2005. **155**(1): p. 73-85.

200. Brush, M.H. and S. Shenolikar, *Control of cellular GADD34 levels by the 26S proteasome*. Molecular and cellular biology, 2008. **28**(23): p. 6989-7000.

201. Harding, H.P., et al., *Ppp1r15 gene knockout reveals an essential role for translation initiation factor 2 alpha (eIF2a) dephosphorylation in mammalian development*. Proceedings of the national academy of sciences, 2009. **106**(6): p. 1832 -1837.

202. Morton, E., et al., *Identification of the growth arrest and DNA damage protein GADD34 in the normal human heart and demonstration of alterations in expression following myocardial ischaemia*. International journal of cardiology, 2006. **107**(1): p. 126-129.

203. Yin, X., J.W. DeWille, and T. Hai, *A potential dichotomous role of ATF3, an adaptive-response gene, in cancer development*. Oncogene, 2007. **27**(15): p. 2118-2127.

204. Huang, X., X. Li, and B. Guo, *KLF6 induces apoptosis in prostate cancer cells through up-regulation of ATF3*. Journal of biological chemistry, 2008. **283**(44):29795-29801.

205. Hayakawa, H., et al., *Soluble ST2 blocks interleukin-33 signaling in allergic airway inflammation*. Journal of biological chemistry, 2007. **282**(36): p. 26369-26380.

206. Schmitz, J., et al., *IL-33, an interleukin-1-like cytokine that signals via the IL-1 receptor-related protein ST2 and induces T helper type 2-associated cytokines*. Immunity, 2005. **23**(5): p. 479-490.

207. Greiner, J., et al., *Receptor for hyaluronan acid–mediated motility (RHAMM) is a new immunogenic leukemia-associated antigen in acute and chronic myeloid leukemia*. Experimental hematology, 2002. **30**(9): p. 1029-1035.

208. Hamilton, S.R., et al., *The hyaluronan receptors CD44 and Rhamm (CD168) form complexes with ERK1, 2 that sustain high basal motility in breast cancer cells*. Journal of biological chemistry, 2007. **282**(22): p. 16667-16680.

209. Proost, P., et al., *Proteolytic processing of CXCL11 by CD13/aminopeptidase N impairs CXCR3 and CXCR7 binding and signaling and reduces lymphocyte and endothelial cell migration.* Blood, 2007. **110**(1): p. 37-44.

210. Satish, L., et al., *Interferon-inducible protein 9 (CXCL11)-induced cell motility in keratinocytes requires calcium flux-dependent activation of μ-calpain.* Molecular and cellular biology, 2005. **25**(5): p. 1922-1941.

211. Madhavan, J., et al., *KIF14 and E2F3 mRNA expression in human retinoblastoma and its phenotype association.* Molecular vision, 2009. **15**: p. 235-240.

212. Taniuchi, K., et al., *Down-regulation of RAB6KIFL/KIF20A, a kinesin involved with membrane trafficking of discs large homologue 5, can attenuate growth of pancreatic cancer cell.* Cancer research, 2005. **65**(1): p. 105-112.

213. Miki, H., et al., *All kinesin superfamily protein, KIF, genes in mouse and human.* Proceedings of the national academy of sciences, 2001. **98**(13): p. 7004-7011.

214. Belyaev, I.Y., et al., *Exposure of rat brain to 915 MHz GSM microwaves induces changes in gene expression but not double stranded DNA breaks or effects on chromatin conformation.* Bioelectromagnetics, 2006. **27**(4). p. 295-306.

215. Qutob, S.S., et al., *Microarray gene expression profiling of a human glioblastoma cell line exposed in vitro to a 1.9 GHz pulse-modulated radiofrequency field.* Radiation research, 2006. **165**(6): p. 636-644.

216. Paparini, A., et al., *No evidence of major transcriptional changes in the brain of mice exposed to 1800 MHz GSM signal.* Bioelectromagnetics, 2008. **29**(4). p. 312-323.

217. Cailleau, R., M. Olivé, and Q.V.J. Cruciger, *Long-term human breast carcinoma cell lines of metastatic origin: preliminary characterization.* In vitro cellular and developmental biology-plant, 1978. **14**(11): p. 911-915.

218. Wang, X., J. Yang, and P.R.C. Gascoyne, *Role of peroxide in AC electrical field exposure effects on Friend murine erythroleukemia cells during dielectrophoretic manipulations.* biochimica et biophysica acta-general subjects, 1999. **1426**(1): p. 53-68.

219. McGinnis, J.M. and W.H. Foege, *Actual causes of death in the United States.* Journal of the american medical association, 1993. **270**(18): p. 2207-2214.

220. Jemal, A., et al., *Cancer statistics*, 2009. CA: A Cancer Journal for Clinicians, 2009. **59**(4): p. 225-232.

221. Smith, R.A., V. Cokkinides, and H.J. Eyre, *American Cancer Society guidelines for the early detection of cancer*, 2006. CA: A cancer journal for clinicians, 2006. **56**(1): p. 11-25.

222. Morgan, H., et al., *The dielectrophoretic and travelling wave forces generated by interdigitated electrode arrays: analytical solution using Fourier series.* Journal of physics D: applied physics, 2001. 34(10): p. 1553-1561.

223. Chang, D.E., S. Loire, and I. Mezi, *Closed-form solutions in the electrical field analysis*. Journal of physics D: applied physics, 2003. **36**: p. 3073-3078.

224. Clague, D.S. and E.K. Wheeler, *Dielectrophoretic manipulation of macromolecules: The electric field*. Physical review E, 2001. **64**(2): p. 26605-08.

225. Wang, X., et al., *A theoretical method of electrical field analysis for dielectrophoretic electrode arrays using Green's theorem*. Journal of physics D: applied physics, 1996. **29**: p. 1649-1660.

226. Sun, T., H. Morgan, and N.G. Green, *Analytical solutions of Ac electrokinetics in interdigitated electrode arrays: electric field, dielectrophoretic and traveling-wave dielectrophoretic forces*. Physical review E, 2007. **76**(4): p. 1-18.

227. Sun, T., H. Morgan, and N.G. Green. *Analytical solutions of the dielectrophoretic and travelling wave forces generated by interdigitated electrode arrays*. The 12th international conference on electrostatics. 2008. Oxford, United Kingdom.

228. Green, N.G., A. Ramos, and H. Morgan, *Numerical solution of the dielectrophoretic and travelling wave forces for interdigitated electrode arrays using the finite element method*. Journal of electrostatics, 2002. **56**(2): p. 235-254.

229. Chen, D.F., et al., *Numerical modeling of dielectrophoresis using a meshless approach*. Journal of micromechanics and microengineering, 2005. **15**: p. 1040-1048.

230. Kua, C. H., Y. C. Lam, et al., *Modeling of dielectrophoretic force for moving dielectrophoresis electrodes*. Journal of Electrostatics. 2008. **66**: p. 514–525.